IMMOBILISATION OF REDOX ACTIVE MOLECULES AS PRECURSORS FOR NANOWIRE SELF-ASSEMBLY

BY

Elena Campagnoli B. Sc. M. Sc.

A thesis presented at Dublin City University for the Degree of Doctor of Philosophy

Supervisor Prof. Robert J. Forster

School of Chemical Sciences

Dublin City University

September 2007

I hereby certify that the material, which I now submit for assessment on the program of study leading to the award of Doctor of Philosophy is entirely of my own work and has not been taken from the work of others, save and to the extent that such work has been cited and acknowledged within the text of my work

Signed Elena Compagnoni

I.D. 53126033

Date 5/09/07

Abstract

Spontaneously adsorbed monolayers of $[Co(ttp\text{-}CH_2\text{-}SH)_2](PF_6)_2$ have been formed on platinum microelectrodes by exposure to micromolar solutions of the complex in 0.1 M $TBABF_4$ in acetonitrile, ttp-CH_2-SH is 4′-(*p*-(thiolmethyl)-phenyl)-2,2′:6′,2′′-terpyridine. Resonance Raman spectroscopy on roughened polycrystalline platinum macro electrodes show that the molecule undergoes adsorption by sulphur atom onto the platinum surface. The monolayers show reversible and well defined cyclic voltammetry when switched between Co^{2+} and Co^{3+} forms, with a peak to peak splitting of 0.040±0.005 V up to $200Vs^{-1}$ and an FWHM of 0.138±0.010 V. Adsorption is *irreversible* leading to the maximum surface coverage, $6.3\pm0.3\times10^{-11}$ $molcm^{-2}$ for $2.5\leq[Co(ttp\text{-}CH_2\text{-}SH)_2]\leq10$ μM. The rate of monolayer formation appears to be controlled not by mass transport or interfacial binding but by surface diffusion of the complex. The surface diffusion coefficient is $5.5\pm1.1\text{x}10^{-7}$ cm^2s^{-1} indicating that prior to formation of an equilibrated monolayer, the adsorbates have significant mobility on the surface. The electron transfer process across the monolayer-electrode interface has been probed by high speed chronoamperometry and the standard heterogeneous electron transfer rate constant, k°, is approximately $3.06\pm0.03\text{x}10^4$ s^{-1}. The reorganization energy is. 18.5 $kJmol^{-1}$.

Self-assembled monolayers of pentanethiol-beta-cyclodextrins have been immobilised on gold polycrystalline macroelectrodes and electrochemically and spectroscopically characterised. The adsorption dynamics was followed by monitoring the change in capacitance during time and a surface diffusion process was found to be the rate determining step. The layers appear to have a mixed structure most likely between a hexagonal close-packed monolayer and a brick configuration. Blocking behaviour depends on the hydrophobicity of the solution phase redox active probe. Scan rate dependent cyclic voltammetry has been used to characterise the defect density within the assemblies. In general, the layers are stable enough in time and potential window to probe the host-guest properties of the immobilized cyclodextrin cavities. The modified gold electrodes were exposed to micromolar solutions of cobalt biphenylterpyridine, in order to electrochemically and spectroscopically characterise the inclusion process. The host-guest reaction occurred for the *in-situ* experiments and it was characterised in terms of equilibrium constant, $2.78\pm0.7\times10^{4}$ M^{-1}, and free Gibbs energy of inclusion, 25 kJ mol^{-1}. Finally, control experiments of the adsorption of the redox active probe onto the bare gold electrodes further confirmed the occurring of the inclusion.

TABLE OF CONTENTS

CHAPTER 1

CHAPTER 2

CHAPTER 3

ELECTRON TRANSFER DYNAMICS ACROSS PLATINUM/COBALT TERPYRIDINE THIOL INTERFACE 145

CHAPTER 5

CHAPTER 6

Chapter 1

Theoretical framework and Literature survey

Introduction

From high-speed molecular computers to optoelectronic switching, technological advances in speed and miniaturisation drive the search for novel materials with enhanced electronic properties. In particular, the semiconductor industry has seen a remarkable miniaturisation trend that nowadays, needs the utilisation of microelectronic circuit components with molecule or atom sizes[1]. The silicon industry is facing fundamental physical constraints (charge leakage, loss of the fundamental band structure) to further progress of Moore's Law[2]. Primarily, the etching technique, used in the production of silicon devices, is a top-down approach which is reaching its limits. Therefore, in order to produce molecule size circuits, an alternative route to pattern million of transistors, wires and other devices needs to be found[3]. Particularly, a bottom-up technology that uses atoms to build nanometre size molecules, which can be further arranged on a surface in a three-dimensional way is desired. An easy and well-known technology that fulfils these needs is the self-assembly technique, that allows dense monolayers of tailored molecules to be immobilised in a controlled and organised manner[2]. Depending on the nature of the immobilised molecule, wires, switches, rectifiers and storage devices can be built and characterised[4], as shown in Figure 1.1

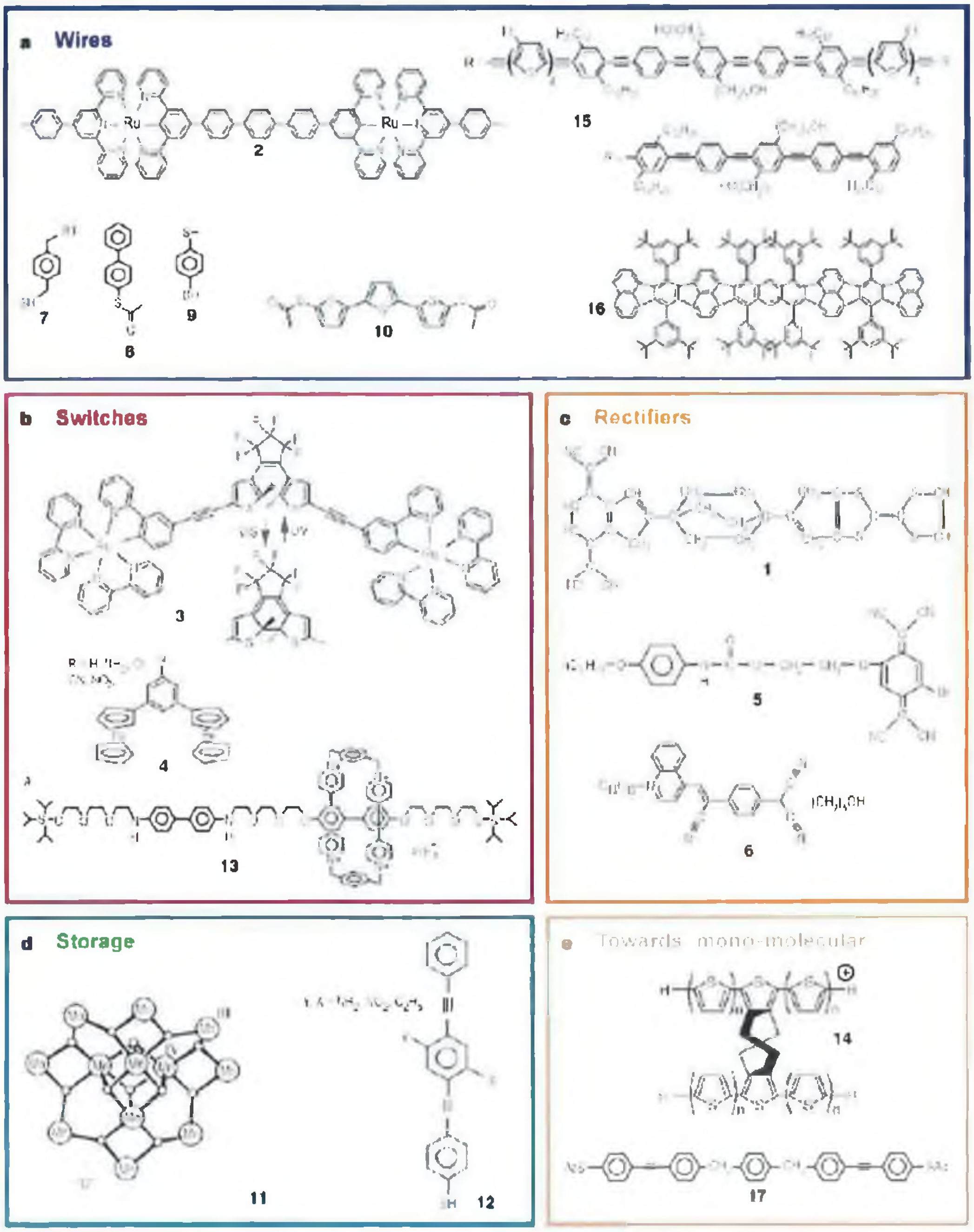

Figure 1.1 a) wires b) hybrid molecular switches, c) hybrid molecular rectifiers, d) storage, e) two molecules that show promise for mono-molecular electronics. Adapted from reference 3.

Using typical size organic molecules it is possible to fit 10^{14} molecule per cm^2 compared to a density occupation of 10^7-10^8 devices of the silicon industry[2]. Moreover, the self-assembly technique not only allows to produce a denser pattern to what contemporary chip-patterning techniques can achieve, but also produces systems where directional control of single electron transfer and efficient charge separation can be realised. Furthermore, the immobilised molecules can be functionalised and additional properties can be easily introduced. This is possible since the position and orientation of the single molecules within the monolayer can be controlled and characterised.

The present project is focused on the assembly and characterisation of molecules able to transfer electrons to and from an electrode surface, with a long term view towards producing molecular wires. Many studies in literature have reported different methods for the immobilisation and characterisation of electroactive systems through show self-assembly.

Bumm *et al.*[5] showed how single molecular wires had been inserted at grain boundaries within self-assembled monolayer of dodecanethiolate on gold. This technique permitted the isolation of single molecular wires from their neighbours which were then imaged by STM and electrically characterised. Qualitative results of the conductance levels showed that the molecular wires were more highly conducting than the surrounding alkanethiolate structures[6].

Chen *et al.*[7] developed a more controlled insertion of the molecular wires into an alkanethiol matrix, by applying controlled voltage pulses to an alkanethiolate SAM under a solution of molecular wires and triggering the insertion with the STM tip. The sulphur terminated conjugated oligomers showed a higher conductance compared to the insulating surrounding matrix.

Importantly, suitable candidates for molecular wires should connect two electrodes and therefore the capability of disulfide terminated molecules to bridge these surfaces in a perpendicular way is important. Single molecules of benzene-1,4-dithiol self-assembled onto two facing gold electrode surfaces of a mechanically controllable break junction showed to form a statically stable gold-sulphur-aryl-sulphur-gold system, allowing for direct observation of charge transport through the molecules[8].

Schiffrin *et al.* [9, 10] stepped a bit further by connecting gold nanoparticle to a gold surface via alkanethiol bispyridinium (viologen) and studied the electron transfer properties of such a system. Viologen was electrochemically active between the nanoparticles and the gold surface, and the films were air stable and did not show any degradation after thousands of cycles.

Another route followed in literature is the utilisation of the molecular recognition properties of a system. Mbyndio *et al.*[15] followed a biological route using DNA to guide the assembly of nanorods in precise arrangements. The approach links on sequence of single-stranded DNA to a nanorod and the other to a surface, allowing the complementary strands to find each other in solution and interact specifically.

It is clear, from the examples cited above, that the more studied and used system to self-assemble molecules on a surface is the chemisorption of sulphur terminated redox molecules on gold surfaces[17], which allow electrons to be transported thanks to their molecular structure.

Therefore, following the ideas of self-assembly and molecular recognition, this project focused on the self-assembly of complexes of transition metals which show different redox states, that are immobilised either covalently on a substrate (*e.g.* sulphur atom on a platinum substrate) or by non-covalent interactions between an electrochemically silent immobilised host and a redox active guest in solution (*e.g.* cyclodextrin host-guest interactions). Then, the immobilised molecules can be used to attach other molecules present in solution via chemical reaction (creation of disulfide bond, coupling reaction between amine and carboxylic acid) or via repetitive host-guest interactions, following a bottom up method.

The formation of the disulfide bond and in particular the use of the host-guest chemistry of cyclodextrins has several advantages, among which the most interesting is the possibility to select the guest molecule nature, thus, easily tuning the molecular wire properties[18]. In this way, complex synthetic reactions needed to covalently link several metal complexes as to create a supramolecule are avoided, and various lengths of molecular wires can be created and the direction of growth off a surface controlled. This represents a promising step compared to the immobilisation of rigid rod conjugated dithiols[19].

After the creation of such modified surfaces, the characterisation of their structures and electron transfer properties is of primary importance. Electrochemistry offers a simple and flexible way[21] to characterise the stability, the defect density, the electrochemical reactivity of the modified interface, even at microsecond timescales with the use of microelectrodes[20]. Moreover, Surface Enhanced Raman Spectroscopy (SERS) allows to further investigate the orientation of the molecules in the layers, in particular when an external potential is applied.

In this chapter, the contemporary theories used to describe the electrical double layer at an interface and the electron transfer processes are described. The formation and characterisation of self-assembled monolayers and the models describing the adsorption dynamics are considered. The electrochemical techniques that are commonly used to characterise the electron transfer activity of redox active monolayers and the fundamentals of Surface Enhanced Raman Spectroscopy are then described.

Chapter Two describes the synthesis and characterisation of the complexes and sulphur terminated β-cyclodextrins used in this study. Microelectrodes have been employed in the characterisation of the electron transfer and their construction and properties are given.

Chapter Three describes the characterisation in solution and as monolayer, of a cobalt terpyridine thiol terminated complex, adsorbed on platinum microelectrodes. The study of the adsorption dynamics is performed by electrochemistry in order to identify the rate determining step. The effect of the applied potential on the heterogeneous electron transfer rate constant and the contribution of the solvent dynamics on the charge transfer are discussed. Insights in the orientation of the molecules within the monolayer are obtained by SERS.

Chapter Four deals with the immobilisation and characterisation of thiol terminated β-cyclodextrins (β-CDs) confined on gold surfaces. The study of the adsorption dynamics is performed by electrochemistry as well as the characterisation in terms of surface coverage, defects, permeation of the layer and orientation of the molecules within the monolayer. Further insights in the spatial arrangement of the β-CDs in the monolayer as varying the applied potential from the OCP are obtained by SERS.

Chapter Five described the inclusion of a cobalt terpyridine biphenyl complex into the cavities of the immobilised β-CDs. Characterisation of the inclusion reaction is given in terms of thermodynamics parameters, as the free Gibbs energy of inclusion, equilibrium constant of the reaction and potential shifts of the included moiety respect to the solution values.

1.1. The electrode-solution interface

Modified and unmodified surfaces exhibit different interfacial properties, which can be used to characterise the system. In particular, the study of the double layer capacitance changes, following a monolayer deposition, gives information about defect density, ion penetration, solvation and stability of the layers.

Introduction

The solid/liquid interface (*e.g.* metal/solution interface) is an environment which has distinct and different reactive properties from those of the contacting bulk phases. Basically, the species present at the interface experience an anisotropic electric field, which arises from the breaking down of the symmetry and decays with the distance from the electrode. Thus, solvent dipoles can become oriented and a net ionic excess charge accumulates at the interface on the solvent side. This solvent charge induces the metal to accumulate an identical charge of opposite sign on its surface to reach a situation where the principle of electroneutrality is satisfied:

$$q_m = -q_s \tag{1.1}$$

Therefore, a charge separation is present at the metal-solution interface which produces a difference in potential. This arrangement of charges and dipole is called the *Electrical Double Layer*. The extension of the double layer is identified at the metal side within a distance of a few Angstrom and at the solution side as the layer of adsorbed solvent molecules and specifically adsorbed species.

A description of this distribution of charges has been given in several theories[21], which span from the simplest model of a *parallel plate capacitor,* suggested by Helmholtz[22], to more realistic and complicated models proposed by Gouy and Chapman,[23, 24] and Stern[25]. The power of the electrochemistry resides in the fact that an external voltage can be applied to the metal, in order to easily vary its potential and study the consequent electrical double layer rearrangement. The following theories can be then applied to the more specific electrode-electrolyte solution interfaces.

1.1.2 From the Helmholtz to Stern description

The idea of the parallel plate capacitor as a description of the electrical double layer is just a simple way to visualise the distribution of the charges at the interface. However, due to thermal agitation, it is highly unlikely that the charge accumulated on the solution side could reside on a singular plane. A compensating charge that diffuses in the solution is a more realistic view. The concept of a *diffuse double layer* was first introduced by Gouy and Chapman[21]. In this model, the solution charge is localised in a layer whose magnitude is the result of balanced electrostatic and thermal phenomena. The potential profile, when the thermal activation barrier is larger than the potential applied, follows an exponential decay:

$$\phi = \phi_0 \exp(-\kappa x) \tag{1.2}$$

where x is the distance from the electrode surface and κ is:

$$\kappa = \left[\left(e^2 / \varepsilon k_B T \right) \sum_i z_u^2 n_i^0 \right]^{1/2} \tag{1.3}$$

called the *Debye-Hückel parameter*[26] and has the units of reciprocal length. It follows that κ^{-1} has the units of length (m) and is usually called the *thickness of the double layer*. Since n_i^0 is proportional to the concentration of the electrolyte in solution, by increasing the concentration and the valence of the electrolyte, *i.e.* at higher ionic strengths, it is possible to decrease the value of κ^{-1} and, consequently, the thickness of the double layer, until the situation of the parallel plate capacitor is reached.

By means Equation 1.3, it is possible to calculate the double layer thickness for any electrolyte at different concentrations and use these calculations to understand experimental data. In Chapter 2, κ^{-1} values for acetonitrile solutions of $TBABF_4$ are be calculated and compared to the experimental data.

Gouy and Chapman derived their model by assuming that ions at the interface are point charges, without physical size and restrictions to the minimum approachable distance to the surface. Since ions have a finite size, and are usually solvated, this assumption is clearly not realistic. The ions cannot reach the surface and they can also be limited by solvent molecules adsorbed on the metal. This is particularly true for cations which exhibit a strong energy of solvation. The closest plane that ions can approach is, therefore, a result of different parameters as the ionic radius, the primary solution sheath and the strength of the electrostatic interaction.

Figure 1.2 shows the plane where the centres of solvated ions reside, at a distance x_2, usually called the *outer Helmholtz plane* (OHP). In this instance, the interaction is purely electrostatic and the chemical natures of the ions and the metal are assumed not to play an essential role. Those ions are said *non-specifically or physically adsorbed.* However, ions and neutral molecules can be adsorbed on the electrode surface by experiencing a more specific and stronger interaction with the charged surface than the electrostatic governing in the diffuse layer, for instance a chemical bond. In this situation, solvent dipoles previously adsorbed on the metal surface can be replaced by molecules whose solvent sheath has been stripped off. This situation gives rise to a *inner Helmholtz plane* (IHP) or *Stern surface,* at some distance x_1, from the metal surface, where the centres of these *specifically or chemically adsorbed* molecules are localised. It follows that, the weaker the solvation of the molecule the stronger will be its specific adsorption. The whole picture of the electrical double layer is shown in Figure 1.2 together with the potential profile.

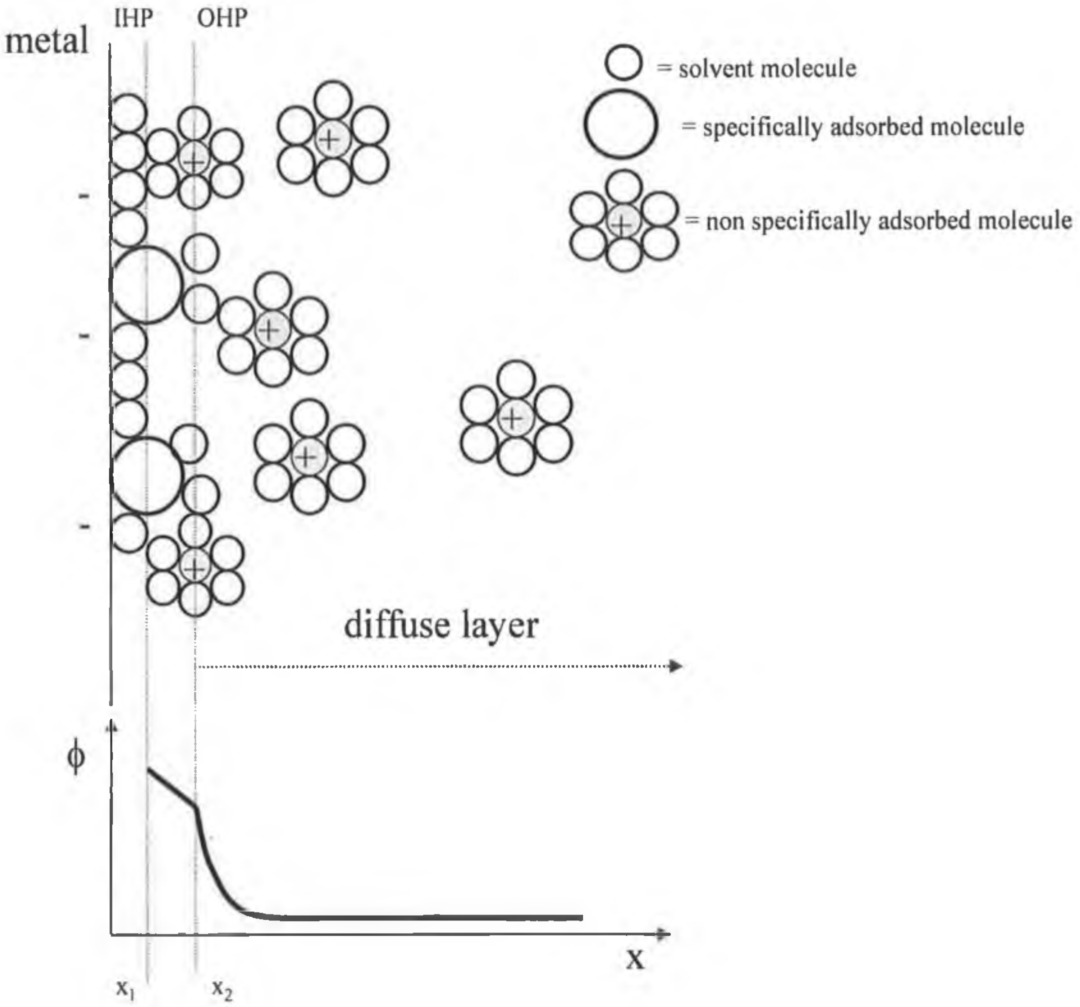

Figure 1.2 Schematic representation of the double layer under the Stern theory. IHP and OHP are inner and outer Helmholtz planes respectively, at a distance x_1 and x_2. At the bottom, the potential profile is represented. Within the IHP and OHP ϕ has a linear decay while in the diffuse layer is described by a single exponential decay.

1.2 Differential capacitance

If one considers the double layer as a parallel plate capacitor, it can be described by:

$$q = C_{dl}\phi \tag{1.4}$$

where q is the charge accumulated (C), ϕ is the potential present at the interface (V) and C_{dl} is the capacitance of the double layer (F).

Since the potential is applied by an external source of voltage, it is possible to step it over a range of values and, by measuring the charge accumulated at each step, obtain C_{dl}. For an ideal parallel plate capacitor, C_{dl} should be constant with a consequent linear relationship between q and ϕ. However, in real systems, an exact proportionality between q and ϕ is not found, since variation of the potential leads to solvent dipoles reorientation, specific adsorption or desorption of ions, which shield the double layer from the metal surface. However, it has been found that the variation of charge, dq, produced by a variation in the potential, dϕ, is itself a function of ϕ [21]. Thus, the derivative dq/dϕ is a better description of the process occurring at the interface, and is usually called as *the differential capacitance* C_d:

$$C_d = \frac{dq}{d\phi} \tag{1.5}$$

Forster[27, 28] reported on measurements of C_d by means of small amplitude potential step chronoamperometry, where the pulse amplitude was small enough to consider the measured capacitance as an approximate differential capacitance. Figure 1.3 shows the potential dependence of C_d for a clean (black dots) and anthraquinone modified (empty squares) mercury microelectrodes. Both the curves show minima for C_d, which corresponds to the PZC. However, the presence of the anthraquinone shifts the minimum at more negative potentials, due to a variation of the PZC of approximately 0.090V. In fact, adsorption of the negatively charged anthraquinone species causes the charge at the solution side of the interface to become non zero, which has to be balanced. Since the electrode is more polarisable than the solution the countercharge is induced there. Therefore, to regain the condition where no excess charge is present on the metal, the potential shifts to a more negative value so as the charge due to adsorbed anthraquinones is exactly counter balanced by an opposing excess charge in the diffuse layer.

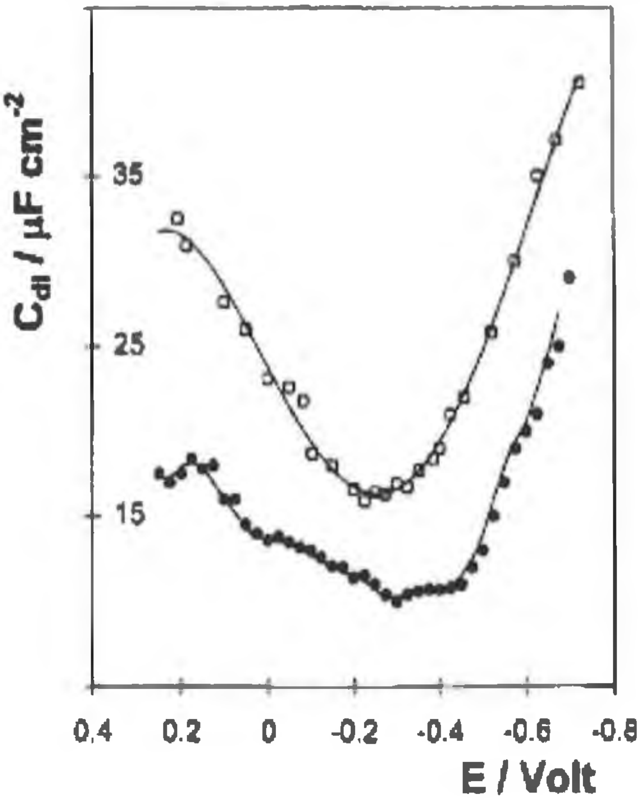

Figure 1.3 .Dependence of the double layer capacitance on the applied potential. The symbol ● represents data for a mercury microelectrode immersed in a solution containing 10μM anthraquinone 2,6-disulfonic acid and 10μM anthraquinone 1,5-disulfonic acid. The symbol □ represents data for a clean mercury microelectrode in the same electrolytic solution but without any dissolved anthraquinone. In both cases the supporting electrolyte is 0.05M $NaClO_4$ at pH of approximately 5.5. Adapted from reference 24.

1.2.1 Capacitance of an unmodified surface

As mentioned in the GC theory, the double layer can be thought as made of two contributions defined by the OHP. It follows that also the total C_d can be split in two different components [25], C_H and $C_{diffuse}$, *i.e.* two capacitors in series, representing the capacitance of the charges at the OHP and of the diffuse layer respectively.

Therefore, the typical rules for capacitors in series can be applied:

$$C_d^{-1} = C_H^{-1} + C_{diffuse}^{-1} \tag{1.6}$$

where

$$\begin{aligned} C_H &= \varepsilon_{sol}\varepsilon_0 / x_2 \\ C_{diffuse} &= f(\varepsilon, \varepsilon_o, \kappa, \phi) \end{aligned} \tag{1.7}$$

and ε_o is the permittivity of the free space and ε_{sol} is the solution dielectric constant, κ is the Debye-Hückel parameter and ϕ is the potential at the interface[21]. Equation 1.7 shows that while C_H behaves as a parallel plate capacitor and it is potential independent, $C_{diffuse}$ is potential dependent. Significantly, the differential capacitance is governed by the smallest of the two components. By increasing the ionic strength in the solution, the parameter κ increases and $C_{diffuse}$ becomes large. It follows that C_H is predominant in Equation 1.7, and the double layer is reduced to the Helmholtz parallel plate capacitor. Again, application of these equations to experimental data will be discussed in Chapter 2.

1.2.2 Capacitance of a modified interface

The same model of capacitors in series described for an unmodified surface, was proposed by Smith and White[29] for an electrode coated with a compact and completely insulating molecular electroactive film. Figure 1.4 shows the studied system and the proposed model.

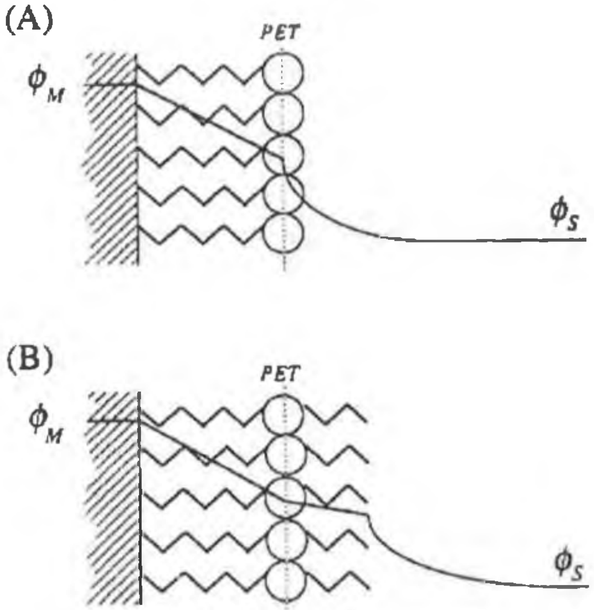

Figure 1.4. Scheme of irreversibly adsorbed electroactive films in contact with an electrolyte solution. The electroactive centres are indicated by open circles and separated from the surface by a dielectric film (zig-zag lines) of finite thickness. In A and B the interfacial potential profile is linear across the dielectric region between the metal and PET. In B a second dielectric layer extends a finite distance beyond the PET introducing a second linear potential decay. For both A and B the potential profile in solution is non-linear. Adapted from reference 25

Equations 1.6 and 1.7 still apply to the system, the only difference being the substitution of C_H, the double layer capacitance at the OHP, with C_{film}, the capacitance of the film:

$$C_d^{-1} = C_{film}^{-1} + C_{diffuse}^{-1} \tag{1.8}$$

$$C_{film} = \varepsilon_o \varepsilon_{film} / d$$

$$C_{diffuse} = f(\varepsilon_o, \varepsilon_{sol}, \kappa, \phi)$$

As before the total interfacial capacitance is governed by the smallest of the two components. In this situation, by reducing the thickness of the double layer, κ^{-1}, the capacitance of the film becomes dominant in the C_d expression. The film is thought to behave as a parallel plate capacitor, whose dielectric constant is controlled by the chains of the adsorbed molecules. Thus, since the adsorbed monolayer usually shows a lower dielectric constant than the electrolyte, monitoring the total interfacial capacitance, at high electrolyte concentrations, allows changes in the double layer structure to be probed. In fact, the switching from uncoated to coated alkanethiols gold electrodes produces a drop in the capacitance, which can be experimentally determined with electrochemical techniques.

For instance, Boubour *et al.*[30, 31] and Ruediger *et al.*[32] used ac impedance spectroscopy to characterise the double layer structure. In particular, Boubour studied the ionic permeability of alkanethiols adsorbed on gold electrodes using ac impedance spectroscopy in absence of an external redox probe. The layers behaved as ionic insulators, until a critical potential, V_c, was reached or exceeded. At potential more cathodic than V_c, SAMs of alkanethiols showed a significant change in the phase angle in the low frequency region associated with ion penetration, as shown in Figure 1.5:

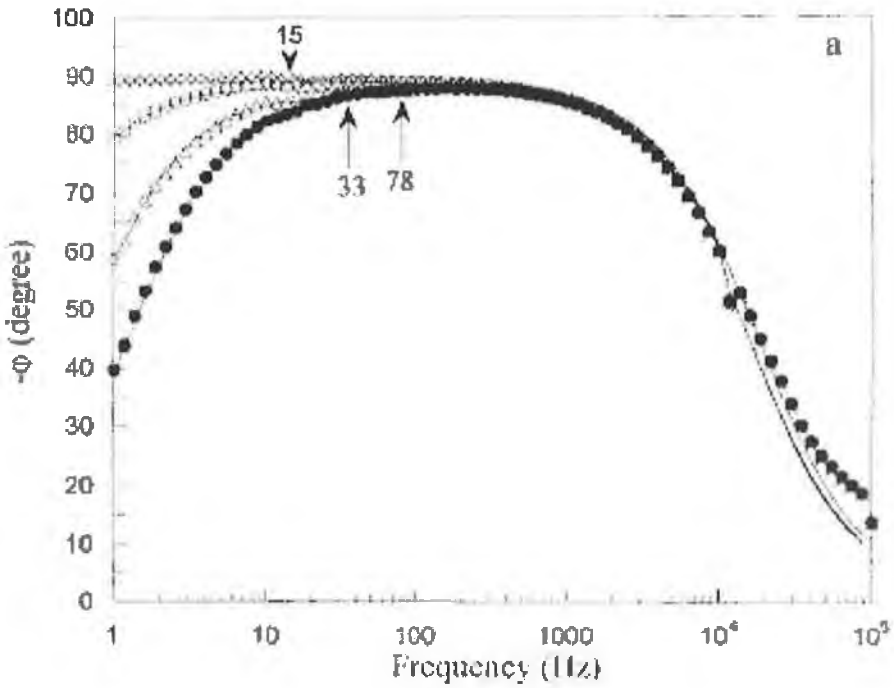

Figure 1.5. Bode plot of $CH_3(CH_2)_{11}S/Au$ SAM from 0.4 to -0.2V (×), -0.3V (○), -0.4V (Δ) and -0.5V (●) in 50mM K_2HPO_4, pH 7. Symbols are the experimental data and solid lines are the best fitting obtained by the corresponding equivalent circuit. Adapted from reference 26.

In several contributions[33, 34, 35, 36] cyclic voltammetry is used to probe the blocking behaviour of SAMs towards an external redox probe dissolved in the contacting electrolyte solution. Figure 1.6 shows how the presence of an adsorbed layer changes the profile of the CV of a reversible electroactive probe, increasing the peak-to-peak separation and rendering the electron transfer reaction more difficult.

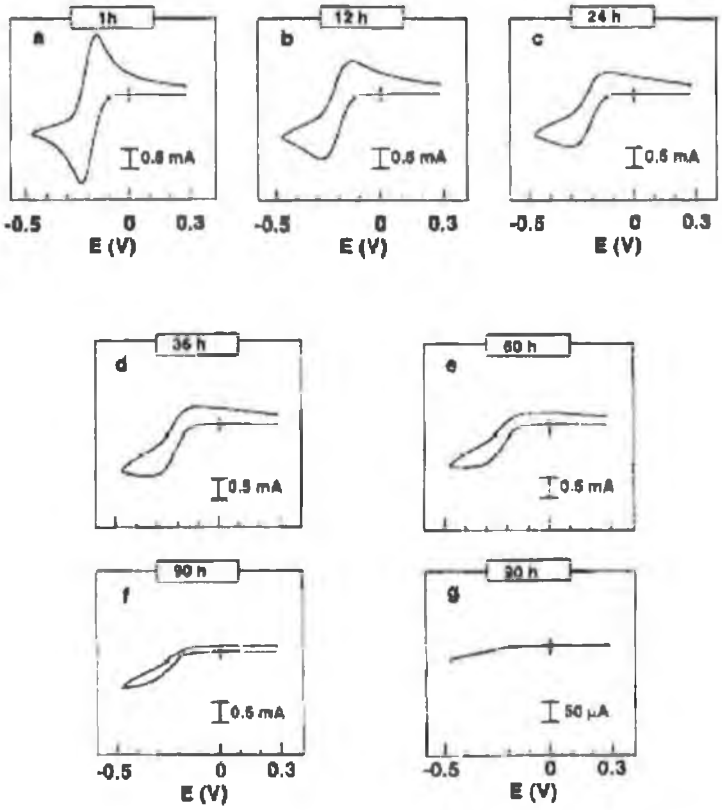

Figure 1.6. Cyclic voltammograms of 5 mM $Ru(NH_3)_6^{3+}$ obtained using nanoporous SAM-electrodes fabricated by immersing a gold surface in ethanol solutions containing hexadecanethiols for the time period indicated in each frame. The data were obtained at 0.1 $Vmin^{-1}$ in an aqueous electrolyte solution containing 1M KCl. All data, except frame g, were obtained with the same electrode. Adapted from reference 29.

Finally, Walsh *et al.*[37] used chronoamperometry to probe the double layer structure dependence on the electrolyte concentration, as shown in Figure 1.7:

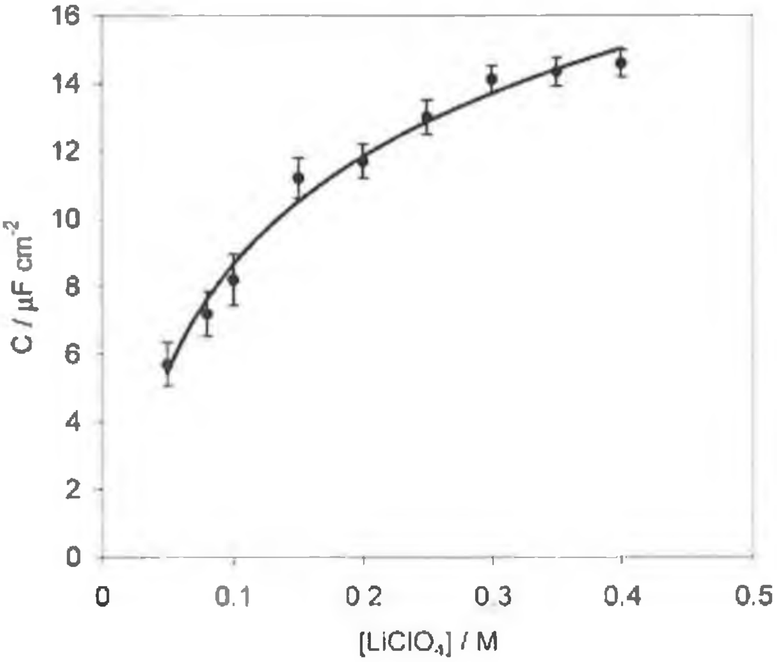

Figure 1.7. Dependence of the differential capacitance in $LiClO_4$ concentration for spontaneously adsorbed monolayers of $[Os(bpy)_2\text{-}4\text{-}bptCl]^+$ on a 12.5 μm radius platinum microelectrode. Potential step size is 0.025V, from 0.400 to 0.425V vs. Ag/AgCl. Adapted from reference 33.

In particular, the differential capacitance of platinum microelectrodes modified with osmium complex monolayers were determined, showing clearly that the total differential capacitance is sensitive to the electrolyte concentration up to 0.3M, after which is dominated by the monolayer contribution. Moreover, the limiting differential capacitance was significantly larger than that expected for a monolayer completely impermeable to the electrolyte, suggesting that the monolayer was partially solvated at high electrolyte concentrations.

In conclusion, probing the double layer capacitance as a function of the electrolyte concentration helps to characterise the monolayer structure in terms of permeability (defect free), thickness of the layer and dielectric properties. Further discussion on the characterisation of the monolayer properties in terms of capacitance is reported in the next section.

1.3. Self-assembled monolayers on electrodes

1.3.1 Definition of Self-Assembled Monolayer

There is an increasing interest in the properties of modified electrodes that can be used in a wide range of technologies at nanometre-scale. Self-assembled and spontaneously adsorbed monolayers provide an easy method to change, in a controlled way, the chemical composition and physical structure of a surface[36].

A single layer of highly organised and close packed molecules on a substrate surface on a large scale is defined as a *monolayer*[36]. The assembly of molecules on a substrate is defined *self-assembly* when the process is spontaneous and consequent to the simple exposition of the substrate to a homogeneous solution or vapour of the molecules[17].

Self-assembled monolayers (SAMs) show both a strong bond between the substrate and the molecules, by means of a specific atom or moiety, and additional lateral interactions among the molecules themselves that stabilise the monolayer. Other methods are used to produce monolayers on a substrate and among them the most popular is the Langmuir-Blodgett (LB)[17].

1.3.2 Alkanethiols

In the following experimental chapters, SAMs of sulphur terminated terpyridine complexes and cyclodextrins are discussed and characterised. The immobilisation of the molecules has been performed either on platinum or gold substrates. However, the most popular and studied SAMs are made of alkanethiols molecules confined on gold surfaces [38, 39, 40] and Figure 1.8 shows a schematic representation of the system. In the last years other metals have been tested as substrate (Pt [41], Ag, Cu [42], Pd [43]) and other molecules as components of the monolayer (sulphides[44], disulphides[45], silanes[46], isonitrile[47], pyridine[48, 49]). Moreover, different techniques have been used to characterise the layers, both electrochemical or spectroscopic[36].

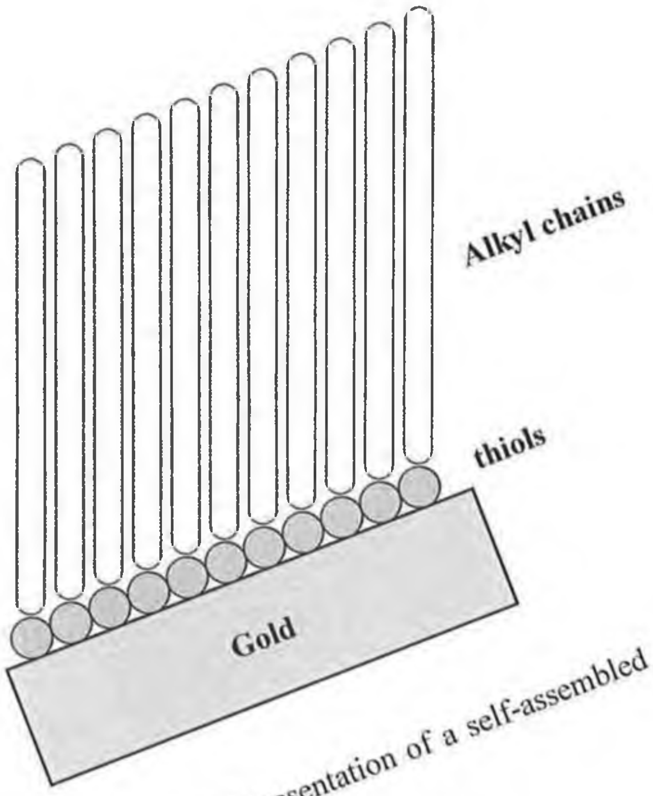

Figure 1.8. Schematic representation of a self-assembled monolayer of alkanethiols on a gold surface

The structure and organisation of the molecules within the monolayers, the lateral interaction, the energy of adsorption, the permeability and possibility of functionalisation of this system have been subject of several studies[43].

The adsorption of alkanethiols is specific and defined as chemisorption but the mechanism of the process has not been clarified[17]. Two possible routes have been proposed for the adsorption process[50]:

$$RS\text{-}H + Au^{\circ}_{n} \rightarrow RS^{-}\text{-}Au^{+} + \tfrac{1}{2}\, H_2 + Au^{\circ}_{n} \qquad (1.9)$$

$$RS\text{-}H + Au^{\circ}_{n} + \text{oxidant} \rightarrow RS^{-}\text{-}Au^{+} + \tfrac{1}{2}\, H_2O + Au^{\circ}_{n} \qquad (1.10)$$

Basically, the SH moiety has to lose an hydrogen to form the RS^{-}-Au^{+} species but it is not well clear whether this happens by the production of H_2 in vacuum (reaction 1.9) or H_2O in solution (reaction 1.10), via reductive elimination reaction of gold hydride or another unknown reaction. Moreover, the presence of thiolate has been shown by XPS[51], FTIR[52], electrochemistry[53] and Raman spectroscopy[54].

More recently Paik *et al.* [55] studied the early stage of adsorption of organosulphur molecules on gold and silver by electrochemical and quartz microgravimetric methods. The potential shifts of the substrate metals, current flowing through the substrates and the surface mass increase observed during the adsorption process were found to support newly proposed electrochemical mechanisms of chemisorption steps. Thiols adsorb on Au and Ag by an anodic oxidation whereas dialkyl disulfides adsorbed through a reaction that results in net cathodic current.

1.3.3 Experimental conditions of deposition

The popularity of the self assembly technique comes from the advantages that it offers in setting the experimental conditions. In fact, the deposition can be carried out at room temperature, under atmospheric pressure, without need of anhydrous or anaerobic conditions. It is enough to expose the substrate to the solution (or vapour) containing the molecules for a certain period of time to allow the assembly to occur. In fact the strength of the bound formed between the sulphur atom and the metallic substrate has been calculated to be in the order of 30 - 40kJmol^{-1} [43] while the net energy of adsorption, considering the bond energies of S-H breaking, S-Au formation and H_2 formation is about -5 kcal mol^{-1} [17, 56]. However, the stability of the layer itself, in terms of energy needed to remove the layer, can be larger than that, since stabilising lateral interactions have to be overcome in order to desorb the layer. Thus, SAMs of thiols are stable over a wide range of electrolyte compositions, potentials windows and temperatures[57].

The choice of the solvent for the deposition is mainly based on the solubility of the molecules, because its nature does not affect the assembly itself. Usually, micro to millimolar concentrations of the molecule are enough to carry out the deposition, affecting more the final homogeneity of the layer[36].

The size of the substrate can be tuned from macro to microscale without any substantial difference in the self-assembly process. Nevertheless, the crystallinity as well as the smoothness of the metal can affect the structure and defect density of the monolayer. Creager *et al.*[58] proved how the microscopic surface roughness influenced the final packing of the layer by comparing layers assembled on wet chemically etched polycrystalline gold electrodes to gold films vacuum evaporated onto heated mica. The blocking properties of the substrates were analysed as shown in Figure 1.9 concluding that defectiveness in the monolayers were strongly influenced by the preparation method of the surface. SEM and STM techniques were used to characterise micro and macroscopic features concluding that only microscopic differences were important in the final assembly.

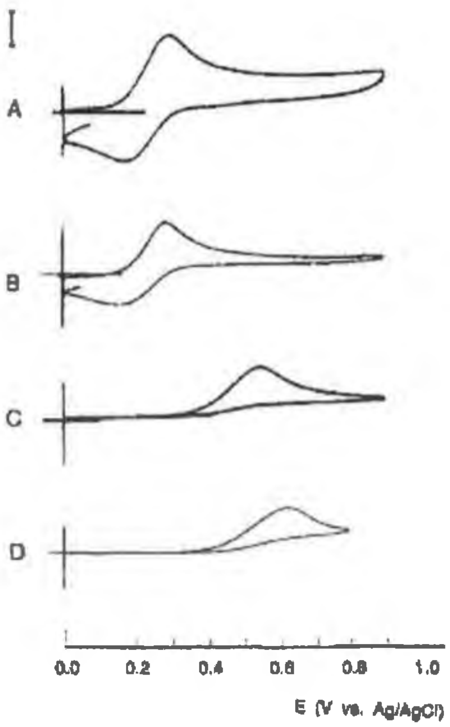

Figure 1.9. CVs of 0.2mM of (hydroxymethyl)ferrocene at gold electrodes coated with a monolayer of $C_{12}H_{25}SH$: A) as polished, B) evaporated onto silicon with chromium underlayer C) etched in concentrated aqua regia D) etched in dilute aqua regia. Adapted from reference 54.

In another contribution Yang *et al.* [59] showed, by electrochemical reductive desorption, how the desorption potentials of alkanethiol monolayers depend on the nature of the crystal face of the substrate, as shown in Figure 1.10. The effect is primarily due to the different electronic charge densities of the single crystal faces upon which the adsorption is performed.

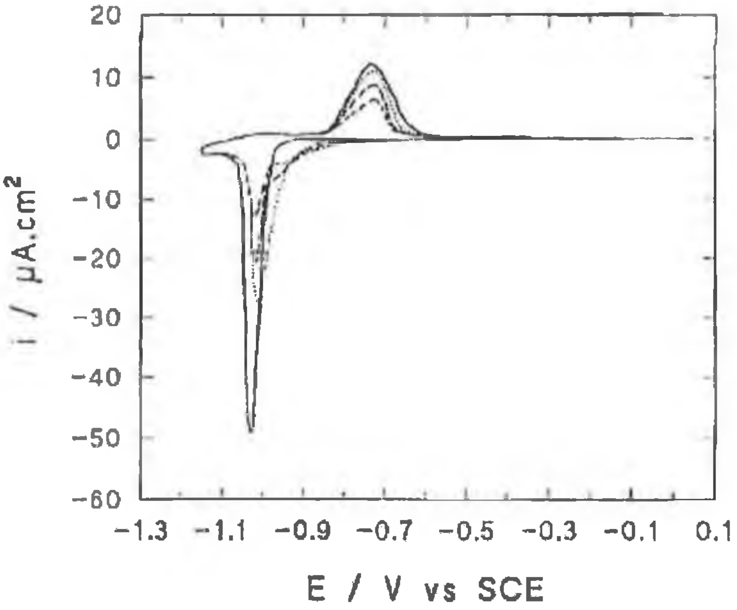

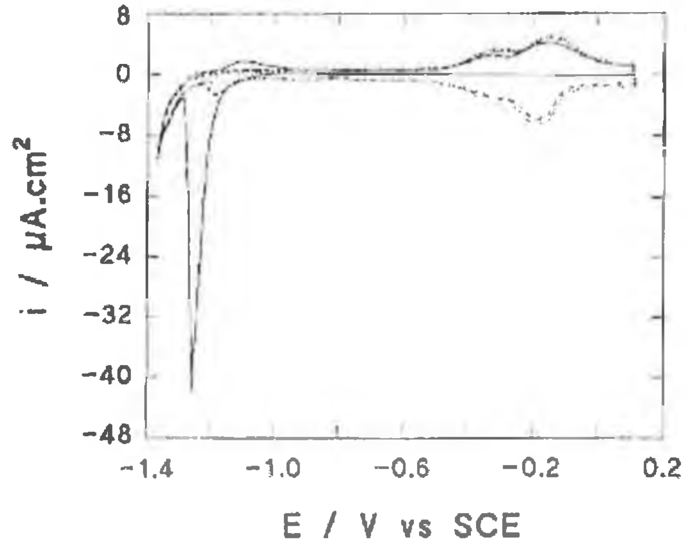

Figure 1.10. CVs of a nonanethiol coated Au(111) (top figure) and Au(110) (bottom figure) electrodes in 0.1M KOH. The first cycle is represented with a solid line, while repetitive scans are represented by dotted lines. Adapted from reference 55.

1.3.4 Electroactive monolayers

The possibilities of varying the chain length and, in particular, of easily introducing functional groups, due to the availability of different ω-terminated thiols (halide, alcohol, aldehyde, amide, carboxylic acid) are other important advantages offered by the self-assembly method. Therefore, SAMs provide a flexible and convenient method for attaching redox centres to electrodes producing *electroactive SAMs* to study electron transfer at nanometer-scale[36].

Besides the electron transfer studies, the redox centres can act as a non destructive probe to characterise the structure of the SAMs, especially in mixed SAMs, or to describe their adsorption/desorption dynamics.

The synthesis of electroactive molecules can be performed before or after their immobilisation. In the first case, the redox centre can be synthesised with a pendant thiol prior to deposition, which is a common strategy followed in literature.

At the other hand, the adsorbed thiols can be coupled via ester or amide bond formation after deposition[60].

Other routes bypass synthetic methods and produce redox active SAMs by means of non covalent interaction between the monolayer and the active probe, *i.e.* host-guest interactions. These two different technologies are the subject of the present thesis. The ease of immobilisation, stability and ideality of SAMs produced by adsorption of electroactive molecules, either covalently and non covalently linked to the sulphur atom, on metal surfaces are discussed. Further characterisation of the specific electroactivity also are presented. The characterisation is often performed by electrochemistry and Raman spectroscopy.

1.3.5 Adsorption dynamics of SAMs

The adsorption of a monolayer involves different steps, such diffusion of the molecule to the substrate, binding of the molecule on the surface, either reversibly or irreversibly, reorganisation of the molecules, which can include surface diffusion, lateral interactions and also desorption[61].

Monitoring the changes of the monolayer surface coverage *vs.* time allows to study the dynamics of the adsorption and determine parameters as the rate constants of the process and the determining step nature, *i.e.* kinetics, diffusion, competition with other molecules.

Bain *et al.*[62] first studied the chemisorption on gold of alkanethiols and found that the adsorption process has two contributions with different kinetics. During the first step, which lasts a few minutes, a disordered monolayer is deposited, while during the second one, that can last for several hours or days, an internal reorganisation of the molecules within the monolayer occurs. While the rate constant of the process is unique, the speed of the deposition itself and the quality of the monolayer are consequences of the solution concentration. By using millimolar solutions of the molecule, highly defective monolayers are deposited in a few seconds while, with micromolar concentrations, a slower less defective deposition is found.

Different fitting models were used in literature to model experimental data and obtain thermodynamics information as the adsorption/desorption rate constant or the free energy of adsorption[27]. Some of these models will be discussed below and applied in experimental Chapters 3 and 4.

For kinetically controlled models, the rate determining step, to reach the final maximum surface coverage, is the kinetics of the binding of the molecules on the surface. In fact, it is possible to calculate, for semi-infinite linear diffusion, the role of the mass transport to the electrode and compare the dynamics of the different steps involved in the adsorption.

The mass transport contribution is calculated, for a defined bulk concentration, in terms of the time needed to diffuse to the surface, enough material as to produce the monolayer at the maximum surface coverage,

$$t = \frac{\delta^2}{\pi D_{soln}} \tag{1.11}$$

where D_{soln} is the diffusion coefficient of the molecule in solution (cm^2/s) and δ is the film thickness (cm), defined as ${}^{\Gamma_{max}}\!/\!{}_{C_b}$, with Γ_{max} in mol cm^{-2} and C_b in mol cm^{-3}. If *t* results smaller than the experimental time required to complete the adsorption, then the mass transport from the bulk to the surface is not rate determining.

1.3.5.1 Kinetically controlled models

A consequence of an adsorption being kinetically controlled is that the concentration of the adsorbing species adjacent to the surface approaches that found in bulk solution and it is constant. Under these conditions, the rate of adsorption is first order in the free sites at the surface:

$$\frac{\partial \Gamma}{\partial t} = k_{ads}(\Gamma_{\max} - \Gamma) \tag{1.12}$$

where k_{ads} is the adsorption rate constant (s^{-1}). The solution of Equation 1.12 describing the variation of the surface coverage with time is therefore[63]:

$$\Gamma(t) = \Gamma_{\max}\left[1 - \exp(-k_{ads}t)\right] \qquad (1.13)$$

If the adsorption has reversible character, another term, $k_{des}\Gamma$, has to be introduced in Equation 1.12, where k_{des} is the desorption rate constant.

When the adsorption requires two adjacent free sites and the adsorbed monolayer is mobile, the second order equation describing the variation of the surface coverage vs. time is the following:

$$\theta(t) = 1 - \frac{1}{k_{ads}t} \qquad (1.14)$$

where θ is the time dependent fractional coverage, $\Gamma/\Gamma_{\max}$ and k_{ads} has the units of $s^{-1}M^{-1}$.

However, competitive, irreversible, first-order parallel adsorption pathways, described by two different binding constant can be representative of the system, *e.g.* two different orientations of the adsorbing molecule.

Adsorption following a two-step mechanism, where weakly bound molecules undergo a surface reorganisation can also be present[64, 65, 66].

Other systems can show mixed behaviour, combining different models. Shen *et al.*[67] described the adsorption of lysozome onto hydrophilic and hydrophobic SAMs, previously immobilised at the surface, using QCM. The adsorption kinetic model included reversible adsorption, irreversible adsorption, desorption and conformational transformation from reversible to irreversible.

However, for instance alkanethiols adsorption has been fully described by simple first order models as Equation 1.12, neglecting the desorption process, even though alkanethiols are known to self-exchange with molecules in solution and diffuse over the substrate surface[68]. In fact, the reversible character of the reaction was usually not visible at the timescale of the adsorption experiment allowing the desorption term to be assumed zero[69].

1.3.5.2 Diffusion controlled model

When the interaction of the molecules with the substrate is fast, diffusion through the bulk to the surface is the rate determining step.

Two main diffusion controlled adsorption types can be used to describe the system. The first is a purely diffusion irreversible model. In this model, the solution adjacent to the surface is completely depleted on the solute that adsorbs and the concentration gradient drives its diffusion from the bulk towards the surface. Therefore, the rate of adsorption is equal to the rate of diffusion[70] and the equation describing the fractional coverage time dependence, θ, is the following:

$$\theta = C_b\left(\frac{D_{so}\ln t}{2}\right)^{1/2} \qquad (1.15)$$

The model assumes that the sticking probability is equal to 1, which is valid for the initial stage of the adsorption. Moreover, this equation does not take into account saturation of the surface.

A diffusion controlled model that incorporates the fraction of covered area has the following differential expression[71, 70]

$$\frac{\partial\Gamma}{\partial t} = C_b\left(\frac{D_{so}\ln}{\pi t}\right)^{1/2}\theta \qquad (1.16)$$

where θ is the fractional surface coverage and can have different configuration and in the following derivation is approximated to $\theta \cong 1 - \frac{\Gamma}{\Gamma_{max}}$. The model assumes that the adsorption has Langmuirian character and it is first order. The integrated equation is then:

$$\Gamma(t) = \Gamma_{\max}\left[1 - \exp\left(-\frac{t}{\tau}\right)^{1/2}\right] \qquad (1.17)$$

where $\tau = \dfrac{\pi\Gamma_{\max}^2}{4D_{soln}C_b^2}$. The model should be applied for systems undergoing a reversible adsorption and at very low surface coverages, *i.e.* when no lateral interactions between the adsorbates exist. However, at the very beginning of adsorption processes the surface coverages are usually low enough to allow Equation 1.17 to be applied.

Combination of kinetically and diffusion control models can also be considered. Hubbard et al.[72] reported on a system with these features, which was fully modelled by Equation 1.13 and 1.17 at different timescales of the experiment. The combination of the two equations was then finally used to fit the experimental data over the whole range of times.

In the following experimental chapters fittings of the data with all the models presented above are shown. The fittings are obtained by minimising the sum squares of the residuals between the theoretical and experimental values and the best fitting parameters are discussed and compared with literature values.

1.3.6 Thermodynamics of Adsorption

The relationship between the amount of substance adsorbed on the electrode, *e.g.* the surface coverage Γ, and the activity in bulk solution, at a given temperature and electrical state of the system, is given by the adsorption isotherm. This description is valid for systems that undergo reversible adsorption, since no model is needed to describe an irreversible system, where the final surface coverage has the same value for all the concentrations.

Langmuir isotherm

The Langmuir isotherm describes equilibrium adsorption when 1) there are no lateral interactions between adsorbed molecules, 2) the limiting surface coverage is dictated simply by the size of the adsorbate, 3) all adsorption sites on the surface are equivalent and 4) the adsorption is fully reversible. The Langmuir isotherm is described by the following equation:

$$\frac{\Gamma}{(\Gamma_s - \Gamma)} = \beta C_b \qquad (1.18)$$

where Γ is the surface coverage at equilibrium (mol cm^{-2}), Γ_S is the saturation surface coverage, β is the adsorption coefficient and C_b is the concentration of the species in the bulk (mol cm^{-3}). Typically, the concentration of the compound in solution is sufficiently low (from milli to micromolar values) that activity effects are negligible. Application of the Langmuir isotherm to experimental data is helpful for obtaining surface coverages of dense monolayer and the adsorption coefficients.

The latter can be used to determine the free energy of adsorption, *i.e.* the difference in free energy between a surface active molecule in solution and in the adsorbed state, according to the following:

$$\beta = \exp\left(-\frac{\Delta G_{ads}}{RT}\right) \qquad (1.19)$$

However, homogeneity which summarises the conditions for a Langmuirian adsorption, is rare. Mercury electrodes come close to having homogenous surfaces. Forster[73] reported on the nearly ideal electrochemical behaviour of 2-hydroxyanthraquinone (2OH-AQ) adsorbed on mercury electrode, showing that the dependence of the surface coverage on the concentration of 2OH-AQ is well fitted by the Langmuir isotherm.

Usually real surfaces have active sites on which the standard free energy of adsorption is high and other less active sites. As the fractional surface coverage increases, the most active sites are occupied first, followed by the less active. Then, lateral interactions start to build up, depending on the nature of the adsorbed species and their average distance apart. Ion-ion interactions are long-range interactions since they decay with the first power of distance. Dipole-dipole interactions decay with r^{-3} while chemical interactions decay with r^{-6} and are only influential at high values of surface coverage. Following the lateral interactions, the voltammetric peaks become broader or narrower than the theoretical value, the formal potential shifts, with changes in the surface coverages and the peak currents do not depend directly on the scan rate. Therefore, the Langmuir isotherm cannot describe the system and another model that takes into account these interactions is needed. *Frumkin isotherm* models the free energy of adsorption as an exponential function of the surface coverage, as expressed by the following equation:

$$\beta C = \frac{\theta}{1-\theta}\exp(g\theta) \qquad (1.20)$$

where $\theta = {}^{\Gamma}\!/_{\Gamma_s}$ is the fraction coverage and g is a parameter that for attractive interactions is negative and for repulsive interactions is positive. It follows that the Langmuir isotherm is a special case of the Frumkin with g equal to zero.

For instance, in contrast to 2OH-AQ monolayers, which showed Langmuirian behaviour, 1-amino-2-sulfonic-4-hydroxyanthraquinone adsorbates exhibit significant lateral interactions, in particular stabilising hydrogen bonding, which requires the Frumkin adsorption isotherm to be used[74].

1.4. Electron transfer kinetics

1.4.1 Marcus theory

Introduction

The study of the heterogeneous electron transfer process across the monolayer/electrode interface is of primary importance in order to characterise the reactivity of interfacial supramolecular assemblies. Monolayers of redox active complexes offer a powerful way to investigate the role of distance, structure and redox composition on the rate and mechanism of the electron transfer because of the ease in tuning their chemical structure and properties.

For homogeneous reactions, changes in the driving force coincides with changes in the temperature or chemical structure of the reactant, which is a more complicated and labour intensive route. At the other side, electrochemistry offers a powerful way of varying the driving force of electron transfer reactions, due to the fact that the external applied potential can be easily changed relative to the formal potential.

1.4.2 Homogeneous electron transfer reactions.

The starting point in describing the electron transfer is to consider homogeneous reactions. Then, the derived model can be applied to heterogeneous systems.
Rate constants can generally be described using the Arrhenius equation which has the following expression[21]:

$$k = A v_n \kappa_{el} e^{-\Delta G^{\neq} / RT} \qquad (1.21)$$

where ν_n is the nuclear frequency factor, κ_{el} is the electronic transmission coefficient, *A* is a precursor equilibrium constant and $\Delta G^{\neq}$ is the free energy of activation. ν_n represents the frequency of attempts on the energy barrier, and is associated with the frequency at which the molecules achieve the appropriate configuration to form the transition state. Therefore, ν_n is generally related to nuclear bond vibrations or solvent motion. κ_{el} is the probability that those molecules, once achieved the transition state, fall into the products configuration and do not fall back into the reactants configuration. *A* represents the ratio of reactant molecules in the reactive position for transition state formation.

Microscopic theories, such as Marcus theory[75, 76] relate $\Delta G^{\neq}$ to structural parameters of the reactants and the medium, in order to have a microscopic expression of the rate constant, in terms of the distance of the redox centre from the surface, the nature of the reactants and the role of the bridging ligand.

It is possible to describe a generic supramolecular assembly with the notation *A-L-B*, where A and B are two redox active centres connected via the ligand bridge L. Then the electron transfer process can be expressed as:

$$\text{A-L-B} \rightarrow \text{A}^{\bullet+}\text{-L-B}^{\bullet-} \qquad (1.22)$$

However, two requirements have to be satisfied in order for the electron transfer to happen.

Firstly, the *Franck-Condon principle*, which states that the electron transfer process is an instantaneous process. Thus, the nuclear configuration of the system does not change during the electronic process. Therefore, reactant and product have to share a common nuclear configuration at the moment of the transfer.

Secondly, since the electron transfer reaction in this case is supposed to be radiationless, and since no energy can be dissipate as heat by vibrational motions, it follows that the internal energy of the system has to be constant during the electronic process. Therefore, the initial state (the energetic level of the electron on the reactant) and the final state (the energetic level of the electron on the product) of the electronic transfer have to be isoenergetic.

The free energy of the system is a multidimensional surface, defined in terms of the nuclear coordinates of the reactant, product and solvent. Among all the different paths that the system can go through, the most favoured is considered, reducing the problem to a single dimension. In this situation, since the internal modes of the A-L-B assembly can be approximated to those of a harmonic oscillator, with an average mode frequency, the equation describing the free energy of the system is simplified to a parabola.

Figure 1.11 shows the free energies *vs.* the nuclear coordinates for the two configurations A-L-B and $A^{\bullet+}$-L-$B^{\bullet-}$:

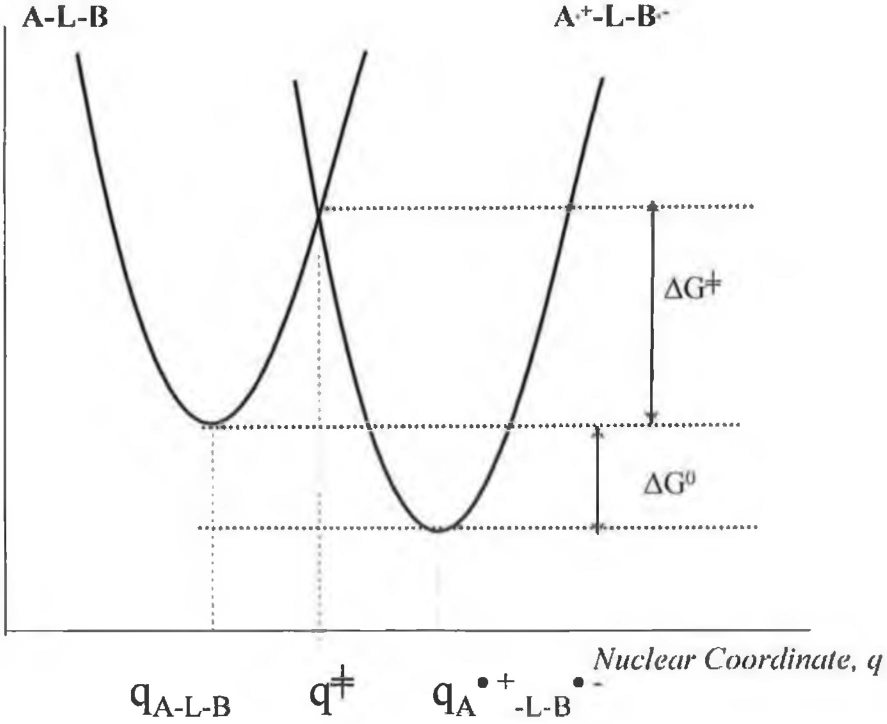

Figure 1.11. Free energies *vs.* nuclear coordinates for the process A-L-B → $A^{\bullet+}$-L-$B^{\bullet-}$

The only point where the above requirements are satisfied is when $q \equiv q^{\ddagger}$ called the *transition state.*

The equations for the two parabolic free energies can be expressed in terms of the nuclear coordinates $q_{A\text{-}L\text{-}B}$ and $q_{A\bullet+\text{-}L\text{-}B\bullet-}$. At the transition state both equations can be used to calculate the energy. Setting the two expressions equal to one another gives an analytical expression for $q^{\ddagger}$ and consequently for the energy of activation $\Delta G^{\ddagger}$:

$$\Delta G^{\ddagger} = \frac{(\Delta G^{\circ} + \lambda)^2}{4\lambda} \tag{1.23}$$

and the electron transfer rate constant expression becomes:

$$k = A\kappa_{el}\nu_n \exp\left[\frac{-(\lambda + \Delta G^{\circ})^2}{4\lambda RT}\right] \tag{1.24}$$

where λ is the *reorganisation energy*, which represents the minimum energy needed to modify the nuclear configurations of the reactant and the solvent to that of the product without transferring an electron. Therefore, increasing the reorganisation energy of a system corresponds to a horizontal distortion of the product free energy in relation to the reactant.

1.4.3 The reorganisation energy λ

The reorganisation energy λ can be separated in two distinct contributions:

$$\lambda = \lambda_{in} + \lambda_{out} \tag{1.25}$$

where λ_{in} and λ_{out} are *the inner and outer sphere* components, respectively.
The inner sphere component, λ_{in}, is the energy associated with changes in bond lengths in the molecule required for the electron transfer to occur, while λ_o is the energy required to change the medium polarisation after that the electron transfer has occurred.
Since many of the molecules used in interfacial supramolecular assemblies undergo negligible changes in the bond lengths during the electron transfer, the inner sphere reorganisation energy often does not contribute significantly to the overall λ and the main contribution is given by the outer sphere component[21]. This last component for homogeneous reactions ha the following expression:

$$\lambda_{out} = \frac{e^2}{4\pi\varepsilon_o}\left(\frac{1}{2R_D} + \frac{1}{2R_A} - \frac{1}{r_{DA}}\right)\left(\frac{1}{\varepsilon_{op}} - \frac{1}{\varepsilon_s}\right) \tag{1.26}$$

where *e* is the electronic charge, ε_o is the permittivity of free space, R_D and R_A are the radii of the donor and acceptor moieties respectively, r_{DA} is the intramolecular distance between donor and acceptor and ε_{op} and ε_s are the optic and static dielectric constants of the medium, respectively.
Both the intramolecular distance and the polarity of the solvent can affect the value of λ_{out}. In fact, by increasing either the distance between the moieties A and B or the polarity of the medium the outer sphere reorganisation energy increases. For heterogeneous reactions where A or B is the electrode surface, Equation 1.26 is slightly different and different contributions are present in literature about the calculation of the outer-sphere reorganisation energy for heterogeneous reactions[77, 78, 79, 80].

1.4.4 Gibbs free energy of activation

Equation 1.23 predicts how $\Delta G^{\ddagger}$ changes with the thermodynamic driving force ΔG° and λ. Variations in the driving force can be thought in a nuclear coordinates scheme as Figure 1.11, as vertical distortion of the free energy surface of the products respect to the reactants. In particular, changing the driving force with respect to a constant value of λ produces three different situation as shown in Figure 12.

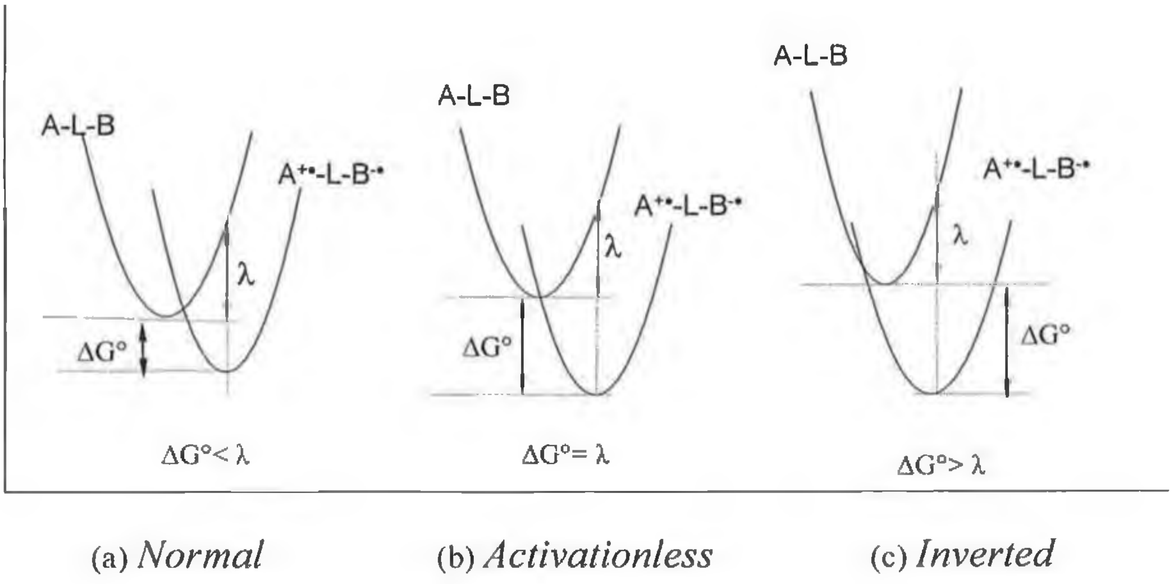

(a) *Normal* (b) *Activationless* (c) *Inverted*

Figure 1.12. Schematic diagram representing the relation between a constant λ and a varying driving force, ΔG°

When $|\Delta G^\circ| < \lambda$ (Figure a) by increasing the driving force, the energy of activation, $\Delta G^{\ddagger}$, decreases with a subsequent increase in the rate constant of the electron transfer reaction as expected from Equation 1.23.

When $|\Delta G^\circ| = \lambda$, (Figure b), $\Delta G^{\ddagger}$ is equal to zero and the rate constant reaches a maximum.

At more negative values of ΔG°, *i.e.* when $|\Delta G^\circ| > \lambda$, $\Delta G^{\ddagger}$ starts to increase despite the large driving force for the reaction and subsequently the rate constant becomes smaller. This range of ΔG° is called the *inverted region*.

1.4.5 Heterogeneous electron transfer reactions

In order to find an expression for the rate for a heterogeneous system, A in the generic supramolecular assembly A-L-B, is now an electrode with a continuous or semi-continuous density of states, instead of the molecular orbitals of the molecular moiety. Therefore, the model described for homogeneous electron transfer reactions can be applied to heterogeneous systems, if changes are introduced as to reflect the metallic behaviour of the electrode.

Three main elementary steps are thought to be involved in the overall electron transfer process for a reactant that is adsorbed at the surface, *i.e.* thermal activation, electronic coupling and the instantaneous electron transfer event itself.

Thermal activation allows the orbitals of the adsorbed molecule to fluctuate around a mean value. Then, when resonance with the electrode energy levels is reached, electron transfer can occur. However, another important factor needs to be satisfied, *e.g.* the electronic coupling between the molecule orbitals and the electrode manifold states. The shorter is the separation between them, the stronger will be the electronic coupling. Finally, the instantaneous electron transfer process can occur. If a bridging ligand connects the electrode surface and the adsorbed molecule, the long-range charge transfer event can happen either via super-exchange[81] or hopping mechanisms. In the first case, the orbitals of the bridging ligand lie outside the resonance with the donor orbitals, usually by ca. 2eV. Therefore, the transferring electron does not directly populate the bridge orbitals. The role of the bridging ligand is to spatially extend the wavefunctions of the reactants, allowing them to couple. In the hopping mechanism, the electron is transferred sequentially through a bridge whose energy levels lie in close resonance with the donor orbitals. The rate of the electron transport may be described as an additive function of each electron transfer step through the bridge.

A metal electrode has a broad energy band of electrons and the electronic coupling, mentioned above between the adsorbed redox couple and the substrate, can occur with any of the occupied electronic state[21, 82]. As for the homogeneous reactions, the electron transfer rate constant is sensitive to the driving force of the charge process, in this case the applied overpotential. However, this sensitivity depends on the extent of the electronic coupling between the reactants, which differentiate systems in adiabatic and non adiabatic, as shown in Figure 1.13.

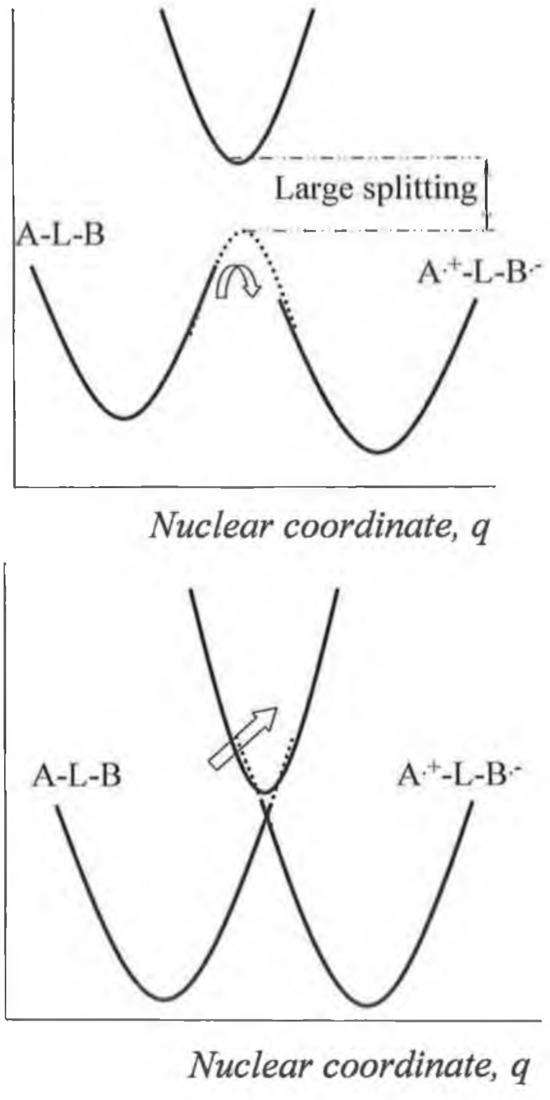

Figure 1.13. Schematic representation of an adiabatic (top figure) and non adiabatic (bottom figure) system

When the electronic coupling is strong, as in the top figure, a splitting larger than k_BT arises at the intersection point. This produces a lower curve, where most likely the system resides, and an upper curve representing an excited state. The system is called *adiabatic*. When the interaction is small, as in the bottom figure, the splitting at the intersection point is less than k_BT. The probability to crossover from the reactant curve to the product one is small and the process is called *non-adiabatic*.

The electronic transmission coefficient κ_{el}, introduced in Equation 1.21, describes the probability that reactant species once achieved the transition state fall into the product configuration. The transfer of an electron between an electrode and a species, held at some distance from the electrode, is considered to be a tunnelling process. Therefore, the probability of the charge transfer decreases with increasing the separation between the electrode and the electroactive species and its value can range between 0 and 1, representing minimum and maximum of tunnelling probability. From Figure 1.14 it is clear that in case of adiabatic systems with a strong coupling, once the transition state has been reached the probability of products being formed is high, close to unity.

At the other side, when the coupling is weak for non adiabatic system, the probability of crossing over to the products configuration is small and κ_{el} <<1. Figure 1.14 illustrates the small probability as a sharp cusp at the intersection between the two potential energy surfaces. The strength of the coupling depends on the overlap between the wave functions of the electrode and the electroactive species, and is expected to decrease exponentially with increasing donor acceptor distance. Hence, varying this distance allows the probability of electron transfer, and so k_{ET}, to be systematically altered [83, 84].

Rearranging Equation 1.21 for adiabatic systems, where κ_{el} is equal to 1, the rate constant expression becomes:

$$k = A\nu_n e^{\left(-\Delta G^{\neq}/RT\right)} \qquad (1.27)$$

and it follows that the rate constant depends only on nuclear parameters, ν_n (Franck-Condon factors).
In contrast, for non adiabatic systems κ_{el} <<1, and electronic factors play a role in the rate constant value. A situation like that occurs when the two reactants are far apart and electronic coupling is weak[85, 86, 87, 88, 89].

In conclusion, classical Marcus theory relates the rate of electron transfer to electronic and nuclear factors. The nuclear terms take into account the dependence of the electron transfer rate on the solvent and species modes while the electronic factors account for the distance dependence and the dependence on the nature of the bridge[61]. Altogether these factors represent the critical parameters that influence the probability of the electron transfer to occur once the driving force is enough to reach the transition state.

1.4.6 Potential dependence of the heterogeneous electron transfer rate constant

A way to decouple the electronic and nuclear factors ($\nu_n\kappa_{el}$) and the energy ($\Delta G^{\ddagger}$) factors in the electron transfer rate constant expression involves measuring electron transfer rate constants at a single temperature over a range of driving forces. With the use of the electrochemistry this is possible by measuring the electron transfer rate constants at different applied overpotentials, η. For adiabatic systems the electron transfer occurs predominantly through states near the Fermi level of the electrode[61] and the electron transfer rate constant is given by the product of the frequency factor and the density of the acceptor states in the molecule D[61]:

$$k(E) = \nu_n D\left(\frac{1}{4\pi\lambda k_B T}\right)^{1/2} \exp\left\{-\left[\frac{(\lambda - E)^2}{4\lambda k_B T}\right]\right\} \qquad (1.28)$$

where λ is the total reorganisation energy. For non adiabatic systems electrons with energies below the Fermi level may be transferred and one needs to sum over all electron energies. The Fermi function describes the distribution of occupied states within the metal at a given temperature as the following

$$n(E) = \left\{\frac{1}{1+\exp[(E-E_F)/k_B T]}\right\} \qquad (1.29)$$

where E is the energy level of an arbitrary state and E_F is the energy of the Fermi level. Therefore Equation X becomes:

$$k(E) = \nu_n N\left(\frac{1}{4\pi\lambda k_B T}\right)^{1/2} \int_{-\infty}^{+\infty} \frac{e^{-\left[(\lambda-E)^2/4\lambda k_B T\right]}}{1+e^{(E-E_F)/k_B T}}\, dE \qquad (1.30)$$

where N is the number of donor states.

The most significant consequences of Equations 1.28 and 1.30 are that they both predict curvature in plots of ln k vs. η. For extremely large driving forces, k no longer depends on overpotential and reaches a maximum value when η is equal to λ, this is equivalent to the *Marcus Inverted Region* seen in homogeneous electron transfer reactions. However, the rate of electron transfer does not decrease with increasing driving force as in homogeneous electron transfer, rather it becomes independent of driving force.

1.5. Electrochemical and spectroscopic techniques

Introduction

A wide range of techniques is available to study kinetics and thermodynamics aspects of electrode processes. Basically, they can be divided in two main categories, *bulk methods*, which deal with phenomena occurring in the bulk of the solution and *interfacial techniques*, which study the electrode-solution interface.

In the present thesis, interest is focused on the study of interfacial properties of supramolecular assemblies. For this reason *potentiostatic techniques,* which belong to the interfacial dynamic techniques, were chosen to characterise the system.

When using the potentiostatic methods, the potential varies as a function of time and the corresponding flowing current in the cell is monitored. The potential can be either stepped, linearly swept or sinusoidally varied from an initial to a final value. To the first class of techniques belong chronoamperometry and chronocoulometry. For the second class the most representative techniques are cyclic voltammetry and linear sweep voltammetry, normal and differential pulse voltammetry while for the third class ac voltammetry and electrochemical impedance spectroscopy are the main techniques.[21]

1.5.1 Potential step techniques

Potential step techniques are widely used to obtain kinetic information about heterogeneous electrode processes. The potential step is the simplest excitation function which can be applied to the working electrode of an electrochemical cell, by stepping instantaneously from an initial potential, at which no net current flows, to a final potential, at which the faradaic process is occurring[21, 90, 91]. The system is monitored as it relaxes towards its new state by either recording the current-time response (chronoamperometry)[92] or the charge-time response (chronocoulometry).
The general shape of excitation and response for a single potential step chronoamperometry experiment in solution are given in Figure 1.14

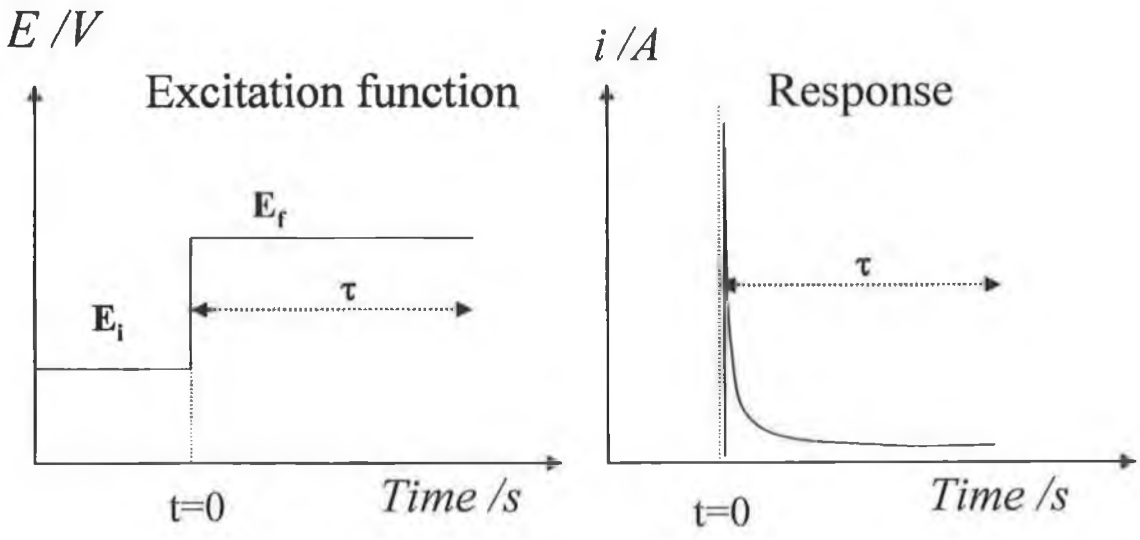

Figure 1.14 Excitation function and general response in solution for single potential step chronoamperometry

1.5.1.1 Solution phase electrochemistry

It is possible to derive an equation describing the current-time profile of a redox species in solution for potential step experiments, by setting the initial and boundary conditions for the experiment.

For instance, a spherical electrode is immersed in an unstirred solution and initially just O (the oxidised form of the redox couple) is present in solution. The concentration of O from the surface of the electrode into the bulk is homogeneous and the potential is initially set as no reduction of O or any other faradaic process can occur.

At time zero the potential is instantaneously stepped to a new value, to fully reduce O present at the surface. If the redox couple is kinetically reversible (Nerstian) the reduction of O reaches, after a certain time, a situation of diffusion controlled state. In this instance, the rate determining step of the process is the mass transfer of the electroactive species at the electrode. A concentration gradient is generated in the solution adjacent the electrode surface, which decreases in time, as well as the current. Under these conditions, the current-time function has the following expression[21]:

$$i = \frac{nFADC_b}{r} + \frac{nFAC_b D_{soln}^{1/2}}{\pi^{1/2} t^{1/2}} \qquad (1.31)$$

where C_b is the concentration of O in the bulk, A is the electrode geometric area, D_{soln} is the diffusion coefficient in the bulk of the oxidised form O and r is the electrode radius. The other quantities have their usual meaning.

Equation 1.31 has two contributions whose contribution varies during the experiment. At short time scales, the time dependent component is dominant and the diffusion field towards the electrode surface can be considered planar. The thickness of the depletion layer is much smaller than the electrode radius and the surface appears to the electroactive species as planar. Under these conditions a $t^{-1/2}$ dependence of the current is found, both for micro and macro electrodes, and follows the decay described by the Cottrell equation. A plot of i *vs.* $t^{-1/2}$ is linear, with a slope proportional to the diffusion coefficient and the bulk concentration of O.

At long time scales, the second term of Equation 1.31 does not contribute anymore to the current, which reaches a steady state value in accord with the following equation:

$$i_{ss} = \frac{nFAD_{soln}C_b}{r} \tag{1.32}$$

The steady state situation is the result of two balanced processes, diffusion and electrolysis. The onset of the steady state for an electrode can be estimated by means of a dimensionless parameter:

$$a = \frac{i_{ss}}{i_{Cottrel}} = \frac{(\pi D_{soln} t)^{1/2}}{r} \tag{1.33}$$

Therefore, for instance, for a 5 mm electrode and a redox couple with a diffusion coefficient in aqueous solution of 1×10^{-5} cm^2s^{-1}, a time of 80 s is required to have a equal to 10, *i.e.* to have $i_{ss} = 10i_t$. Therefore, steady state behaviour is not observed for macroelectrodes at the tens of milliseconds timescale typical of conventional electrochemical experiment. By reducing the radius of the electrode to 5μm, the time for a steady state response is reduced to 80μs, which can fulfil the experiment requirements.

Equation 1.31 shows that the current response is proportional to the flux of redox species at the electrode, which has its maximum at time zero. Therefore, the system at the very beginning of the experiment is kinetically controlled and a value for the heterogeneous rate constant for the electrode reaction can be determined. In fact, other practical problems are involved as the rise time of the potentiostat and the presence of the double layer charging current. This last issue is particularly important because this charging current can totally mask the faradaic current at short times.

1.5.1.2 Surface confined species

The mass transport can limit the potential range over which it is possible to study the kinetics behaviour of the system. In fact, the reciprocal of the rate constant at a particular overpotential gives the timescale over which enough material has to diffuse to the electrode in order to react. Typically, the diffusion coefficients of species in solution are too small to produce enough electroactive material at the electrode surface. Therefore, the use of electroactive monolayers allow this issue to be eliminated.

For instance, an ideal electrochemical reaction involving a surface confined electroactive couple is considered and the potential is stepped, from an initial capacitive value to a final potential where a faradaic reaction is produced. The equation describing the current-time profile has the following expression[87]:

$$i_F = kQe^{(-kt)} \tag{1.34}$$

Equation 1.34 describes a single exponential decay, where *k* represents the apparent heterogeneous rate constant for the overall reaction and Q is the total charge passed during the reaction. Therefore, for an ideal system, where no iR drops are present and an unique rate constant describes the kinetic properties, a plot of *ln i* vs. *t* is linear, with a slope of –*k* and intercept *kQ*.

As discussed in the previous section, a double layer is always set at the electrode-solution interface, which produces a charging current when an external potential is applied which has the following expression[21]:

$$i_c = \frac{\Delta E}{R_u} e^{(-t \;\; R_u C_d)} \tag{1.35}$$

where ΔE is the magnitude of the applied potential step, R_u is the uncompensated cell resistance (Ohm) and C_d the differential capacitance. Equations 1.34 and 1.35 can be resolved if the time constant of the double layer charging is shorter than the faradaic one. In this instance, experimental data are taken and analysed after 5-10 RC constants[93]. Shrinking the size of the electrode and increasing the ionic strength are common strategies utilised to decrease the value of the cell time constant and are fully discussed in the following experimental chapters.

1.5.2 Sweep techniques

1.5.2.1 Cyclic voltammetry

Sweep techniques[90, 21] are useful methods to quickly obtain a general overview and diagnose the redox properties of a redox active molecular system. In fact, it is possible to gain information about potentials, reversibility or adsorption phenomena by analysing the response of the system.

The most widely used technique is *cyclic voltammetry* (CV) which involves sweeping linearly the potential of the electrode from an initial value E_I to a final E_2 at a constant rate. When E_2 is reached the sweep is reversed to reach the initial potential E_I or a new value E_3.

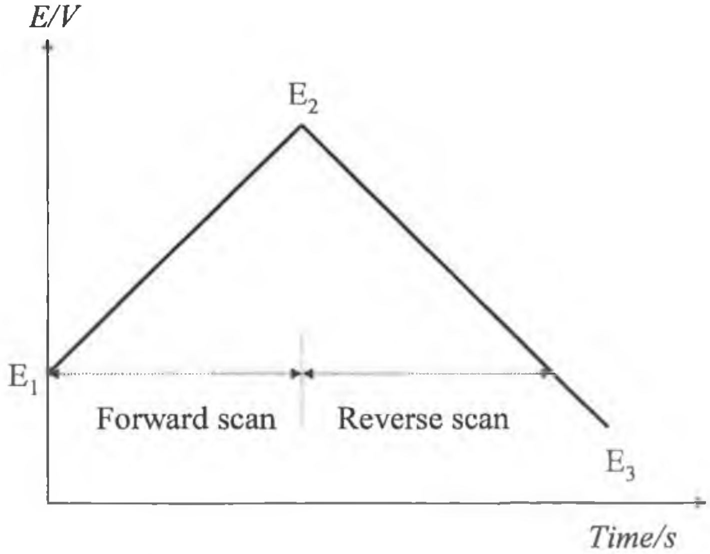

Figure 1.15. Excitation function in cyclic voltammetry

The consequent flowing current has a different profile if the redox couple is dissolved in solution or adsorbed as monolayer on the electrode surface and behaves reversibly or irreversibly.

Solution phase electrochemistry

A quick way to characterise reversibility or irreversibility of a system, together with the diffusion coefficients of the redox centres and formal potentials is solution phase electrochemistry. For instance, a system where only the oxidised form (O) of a redox *reversible* couple is dissolved in an unstirred solution is considered (no R present). The kinetics of the redox couple is fast enough to satisfy at each potential the equilibrium described by the Nernst equation. The starting potential is chosen at the open circuit potential of the system (OCP) and, then, scanned in a reductive direction. When approaching the formal potential of the couple, the reduction reaction of O starts at the electrode surface and a cathodic current is observed. The concentration of R increases, while O concentration decreases, with both concentrations being equal at the formal potential. Then, by further scanning, the concentration of O at the electrode surface approaches zero, while its concentration gradient and therefore the cathodic current reach a maximum. If the potential is still scanned reductively, O molecules sitting at larger distances in the bulk have to diffuse to the electrode surface in order to satisfy the equilibrium dictated by Nernst equation. The depletion layer starts to increase inside the bulk and consequently the gradient of O starts to decrease. At this stage, the system is under diffusion control and the overall behaviour gives rise to a peak shaped current-potential response. By further scanning, the potential reaches values where a steady-state situation is reached. At this stage E is switched and scanned back towards more anodic values. Initially, a cathodic current is still observed due to the very cathodic value of the potential which allows O to be still reduced. Once E becomes sufficiently positive, molecules of R, now accumulated at the electrode surface, start to be oxidised and a peaked shape curve similar to the cathodic (but in the anodic direction) under diffusion control is observed.

A typical CV for an ideally reversible redox couple in solution is shown in Figure 1.16:

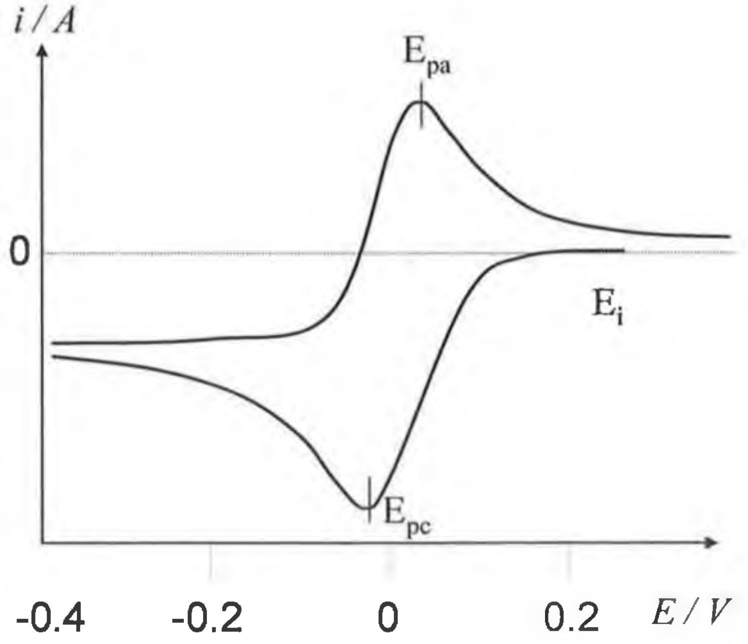

Figure 1.16. Typical cyclic voltammogram for a reversible redox couple in solution

If the diffusion field at the electrode surface is assumed to be planar the Randles-Sevçik equation gives the expression for the peak currents at 25°C under semi-infinite linear diffusion conditions:

$$\left|i_p\right| = 2.69 \times 10^5 n^{3/2} C_b A D_{soln}^{1/2} v^{1/2} \qquad (1.36)$$

where v is the scan rate (Vs^{-1}) and the other parameters have their usual meaning. The square root of the scan rate dependence of the current has an implicit dependence on $t^{1/2}$ which is identical to that of the Cottrell equation. The reversibility of the redox couple is assigned if the conditions listed in Table 1.1 are satisfied.

Table 1.1. Conditions for a reversible redox couple in solution

$\Delta Ep = E_{pc}-E_{pa} = 57/n$ mV
$\mid i_{pa} / i_{pc} \mid = 1$
$i_p \propto v^{1/2}$
E_p independent of v
$\mid E_p - E_{p/2} \mid = 59/n$ mV

Moreover, under reversible conditions, the average of the two peak potentials gives the half-wave potential which is in turn related to the formal potential of the redox couple:

$$E_{1/2} = \frac{E_{pa} + E_{pc}}{2} = E^{0'} - \frac{RT}{2nF} \ln \frac{D_0}{D_R} \qquad (1.37)$$

In fact since usually $D_0 \approx D_R$, it follows that $E_{1/2}$ is a good approximation of the redox formal potential.

Surface confined species

Figure 1.17 shows a theoretical CV for an ideal reversible surface confined redox couple.

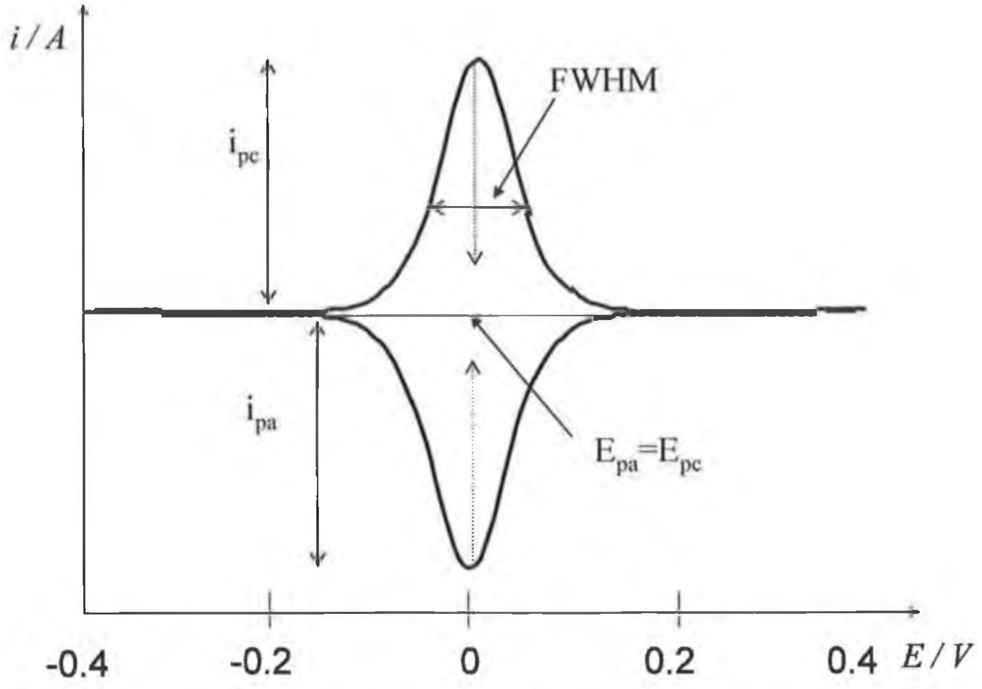

Figure 1.17. Cyclic voltammogram for a reversible surface confined redox couple

The situation is representative for an electroactive monolayer adsorbed at the surface with no molecules dissolved in the electrolyte, or at a very low concentration which does not effect the faradaic response. Since no diffusion takes place, the consequent peak-peak separation is not observed in the anodic and cathodic current maxima, and, therefore, $E_{p,a}=E_{p,c}$. The adsorption sites are considered equivalent and not dependent on the applied potential and the adsorption of the monolayer is strong, in both the reduced and oxidised form.

For instance, a system is considered where, at time zero, just the oxidised form is present, and the potential is swept towards negative values. A consequent cathodic current flows is observed, which rises from the capacitive to a peak value and with further scanning it falls again to the capacitive current. Once more, a peaked shape for the current is obtained and, when the potential scan is reversed, a symmetric shape about x-axis is observed. The equation describing the peak currents is[21]:

$$i_p = \frac{n^2 F^2}{4RT} A\Gamma \, v \qquad (1.38)$$

where Γ is the *surface coverage* (mol cm^{-2}) and n is the number of electrons exchanged during the reaction and A is the electrode area. In contrast with the solution phase CV, the peak current for a surface confined species depends linearly on v.

The area under the wave represents the charge passed during the experiment and it is possible to relate it to the surface coverage of the electrode through the following equation[61]:

$$\Gamma = \frac{Q}{nFA} \qquad (1.39)$$

Another important parameter is the full width at half maximum (FWHM), *i.e.* the total width of the anodic or cathodic wave at half the peak current, which is related to the lateral interactions among the molecules of the monolayer.

Under Langmuir isotherm conditions (where no lateral interactions are experienced) the FWHM for a Nernstian reaction at 25°C is given by:

$$FWHM = \frac{90.6}{n} mV \qquad (1.40)$$

If repulsive lateral interactions are present $FWHM > 90.6/n$ mV while under attractive interactions conditions $FWHM < 90.6/n$ mV.

In the following table the characteristics for an ideal reversible redox active monolayer are summarised.

Table 1.2. Conditions for an ideally reversible electroactive monolayer

$\Delta E_p=0$
$\vert i_{pa} / i_{pc} \vert = 1$
$i_p \ \alpha \ v$
$FWHM = \frac{90.6}{n} mV$
$E_{pa}=E_{pc}=E_{1/2}=E^{\circ'}$

1.5.3 A.C. Techniques

1.5.3.1 Electrochemical Impedance Spectroscopy at the bare electrodes

Electrochemical impedance spectroscopy[90, 21] represents an useful tool for studying the kinetic parameters of a system, together with the characterisation of its resistive and capacitive behaviour. In EIS, the potential imposed on the cell is a sinusoidal signal of angular frequency, ω, of a small magnitude at a constant potential. Therefore, the system is not strongly perturbed and the resulting current is approximately at the steady state. Usually, the recorded output is the magnitude of the *impedance,* a quantity which relates the applied ac potential to the flowing ac current.

The impedance, Z, represents the overall capacitive and resistive behaviour of the cell and relates the two phasors potential and current, **E** and **i**, as follows:

$$\mathrm{E} = \mathrm{i}Z = \mathrm{i}(R_u - jX_c) \qquad (1.41)$$

where R_u is the uncompensated resistance of the cell, X_c is the *reactance* and is the reciprocal of the product ωC_d. Therefore, the impedance can be thought as the sum of a real and imaginary resistance, in a complex notation, as shown in the following equation and Figure 1.18:

$$Z = R_u - jX_c = R_u - j/\omega C_d \qquad (1.42)$$

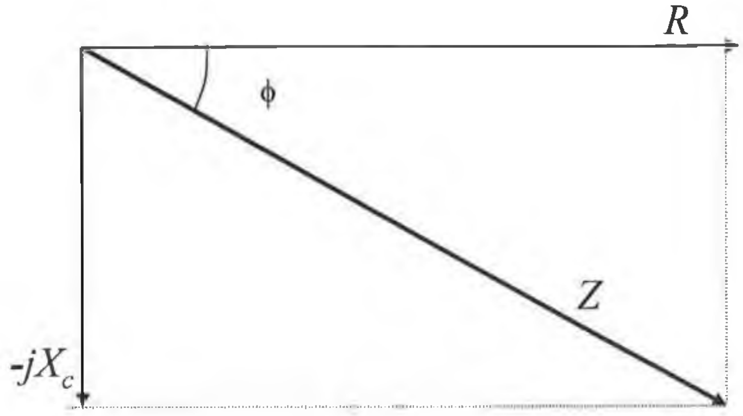

Figure 1.18. Diagram of the real and imaginary components of the impedance

The angle between the two phasors **E** and **i** , called *phase angle*, can be calculated as follows:

$$\tan\phi = \frac{X_c}{R_u} = \frac{1}{\omega R_u C_d} \qquad (1.43)$$

Equation 1.42 shows that the impedance depends on ω and, therefore, by changing the angular frequency it is possible to probe the whole behaviour of the cell.

In principle, any electrochemical cell at any angular frequency can be modelled with a representative circuit of combined capacitors, resistors and inductors which are then related to kinetic parameters of the cell. Different notations are used to display the variation of the impedance with the frequency. In a Bode plot, $\log|Z|$ and ϕ are both plotted against $\log\omega$. An alternative representation, a Nyquist plot, displays Z" (*i.e.* ωX_c) vs. Z' (*i.e.* R) for different ω values.

In the present work, the time constant of cells with bare working electrodes have been measured by EIS. The analysis of the results is carried out by modelling the bare electrode behaviour in a inert electrolyte solution with a RC circuit in series, as shown in Figure 1.19

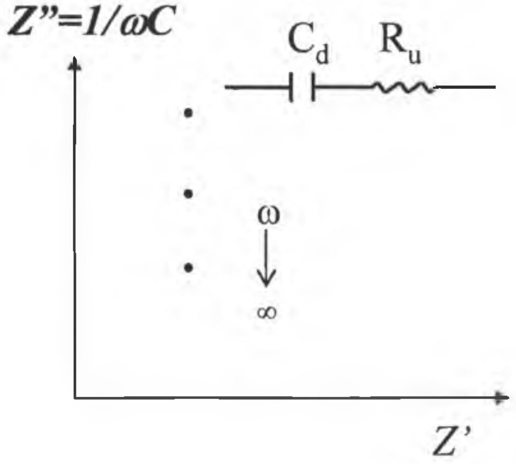

Figure 1.19. Nyquist plot for a bare electrode in an inert electrolyte solution and its modelling circuit of R and C in series.

Since the modelling circuit is in series, the impedance is the sum of the reactance and the resistance, *i.e.* $Z=R_u+1/\omega C_d$. Therefore, at high values of ω, $Z=R_u$ while at low frequencies the capacitive term becomes more important. Ideally, the final Nyquist plot shows a straight line, crossing the Z’ axis at Z’=R. When either a reactive monolayer is added or a redox couple in solution is present the profile in the Nyquist plot is greatly changed. Therefore, more sophisticated and complicated mathematical models are used to interpret the experimental data in terms of electrical circuits[94].

1.5.4 Raman Spectroscopy

Introduction

In Raman spectroscopy an incident light is inelastically scattered by a sample and shifted in frequency by an energy corresponding to its characteristic molecular vibrations. The molecule, hit by the photons, changes its electronic state into a virtual excited state which does not coincide with an electronic transition, and consequently relaxes back in a new vibrational or rotational energy level. The final energy level is smaller than the incident radiation for the Stokes lines and bigger for the anti-Stokes lines, as shown in Figure 1.20.

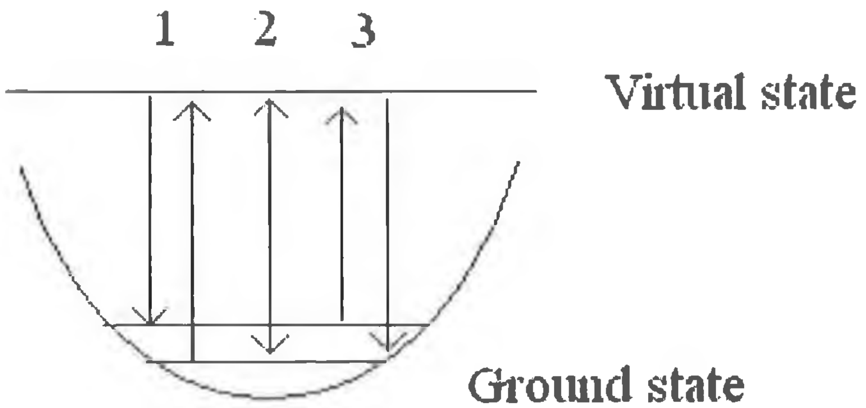

Figure 1.20. Excitation and relaxation to and from virtual states for Stokes (1), Rayleigh (2) and anti-Stokes (3).

However, since only molecules that are in an excited vibrational/rotational energy level can produce anti-Stokes lines and their number is usually small at room temperature, in Raman spectroscopy typically only Stokes lines are measured.

A simple classical electromagnetic field description of Raman scattering can be used to explain many of the important features of Raman band intensities. The dipole moment, **P**, induced in a molecule by an external electric field, **E**, is proportional to the field as shown in Equation 1.44:

$$\mathrm{P} = \alpha \mathrm{E} \qquad (1.44)$$

where α is the polarizability of the molecule and measures the ease with which the electron cloud around a molecule can be distorted. Raman scattering occurs because a molecular vibration can change the polarizability. The change is described by the polarizability derivative, $\frac{\delta\alpha}{\delta p}$, where **p** is the normal coordinate of the vibration. The selection rule for a Raman-active vibration is that a change in polarizability during the vibration has to happen. Therefore, the vibrations of a highly polar moiety, such as the O-H bond, are usually weak since an external electric field can not induce a large change in the dipole moment by stretching or bending the bonds.

Typical strong Raman scatterers are moieties with distributed electron clouds, such as carbon-carbon double bonds. The π-electron cloud of the double bond is easily distorted in an external electric field. Bending or stretching the bond changes the distribution of electron density substantially, and causes a large change in the induced dipole moment.

In general, the intensity of the Stokes Raman scattering is proportional to the square of the induced electric dipole and, therefore, to any electromagnetic field incident on the analyte:

$$I_{RS} \propto E^2 \qquad (1.45)$$

This relation is particularly important in explaining the enhancement of the signal obtained at roughened surfaces as described in the following section.

1.5.4.1 Surface Enhanced Raman Spectroscopy (SERS) and Resonance Raman Spectroscopy (rRS)

Surface enhanced Raman Spectroscopy (SERS)[95] is a selective and sensitive analytical tool that allows detection of molecules adsorbed on nanostructured materials by enhancing the Raman signal. Increases in the intensity of the scattering Raman signal have been observed on the order of 10^4-10^6 and for particular systems as high as 10^6-10^8 [96]. These SERS active substrates are various metallic structures with critical dimensions on the order of tens of nanometres. The most common type of SERS active substrates exhibiting the largest effect are colloidal silver or gold nanoparticles in the 10-150 nm size range, gold or silver electrodes or evaporated films of these metals [97].

It is generally agreed that many factors contribute to the augmentation of the signal, but roughly the enhancement mechanisms are divided into two categories, the *electromagnetic field enhancement* and the *chemical first layer effects*[61]. The latter provides an order or two of magnitude increase in the Raman signal and it is a consequence of interactions between the adsorbed molecules with the substrate, usually electronic coupling. For instance, these interactions can produce resonance Raman effects due to the creation of new metal-molecule charge-transfer electronic transitions.

At the other end, the electromagnetic field enhancement contribution arises from enhanced local optical fields close to the metal surface. When the wavelength of the incident light is close to the plasma wavelength of the metal, conduction electrons in the metal surface are excited into an extended surface electronic excited state called a surface plasmon resonance. Molecules adsorbed or in close proximity to the surface experience an exceptionally large electromagnetic field, and, considering Equation 1.45 their Raman signal is more intense. Vibrational modes normal to the surface are most strongly enhanced.

Closely spaced interacting particles seem to provide extra field enhancement, particularly near the gap sites between two particles in proximity. It follows that roughened materials can produce this type of signal enhancement. Different techniques have been used in order to produce nanostructured roughened surfaces, *i.e.* oxidation-reduction cycles on electrode surfaces[98, 99, 100] vapour deposition of metal particles onto substrates, lithography[96], metal colloids or metal deposition over a deposition mask of polystyrene nanospheres [97,101].

It is also clear that the frequency of the excitation line is important and depends on the characteristic of the roughened surface as well as the type of metal used[102]. It can be inferred then that inhomogeneous roughened surfaces reduces the efficiency of the enhancement, since only a fraction of the substrate will be able to produce enhancement at any given excitation line. Molecules with lone pair electrons or π clouds show the strongest SERS. The effect was first discovered with pyridine[103]. Other aromatic nitrogen or oxygen containing compounds, such as aromatic amines or phenols, are strongly SERS active. The effect can also been seen with other electron-rich functionalities such as carboxylic acids[96].

Raman spectroscopy is conventionally performed with green, red or near-infrared lasers. The wavelengths are below the first electronic transitions of most molecules, as assumed by scattering theory. The situation changes if the wavelength of the exciting laser is within the electronic spectrum of a molecule, *i.e.* when Resonance Raman Spectroscopy (RRS) is performed. In this case, the intensity of *some* Raman-active vibrations increases by a factor of 10^2-10^4.

The signal enhancement observed in SERS depends on the distance of the Raman-active species from the metal surface. While monolayers show superior surface enhancement, there is evidence that SERS may operate at distances of up to tens of nanometers[61]. Moreover, for adsorbed species the selection rules are different and forbidden modes for in normal Raman spectroscopy can be allowed in SERS. Finally, the relationship between the frequencies and intensities of the SERS bands are influenced by the applied potential and the degree of dependence is particular for each considered system.

Conclusions

The self-assembly and molecular recognition techniques seem to offer valid alternative routes to the construction of micro and nanodevices, in particular for the semiconductor industry, which is facing scale down issues.

Molecular electronics, involving chemically designed components, can be tailored and tuned easily to satisfy the particular request of the single device. Therefore, the study of heterogeneous systems as the electrode/electroactive monolayer interfaces is fundamental to understand the advantages that these techniques can offer compared to the traditional lithography method. In particular, the features of the modified interface in terms of electron transfer properties are a key issue. Factors as the distance of the electroactive molecule from the electrode surface, which influence the electronic coupling, and contribution from the medium surrounding the reactive molecule are fundamental. Moreover, the ease of fabrication and the steps constituting the adsorption process are extremely important to understand those factors that drive the formation of the monolayers. Finally, the homogeneity, structure, orientation of the molecules within the monolayer and its stability need to be characterised in order to verify the production of nanometre size systems that can answer the reliability required by the semiconductor industry.

References:

1 Nitzan A., Ratner N., *Science*, **2003**, 300, 1384

2 Tour J. M., *Acc. Chem. Res.*, **2000**, 33, 791

3 Service R. F., *Science*, **2002**, 295, 2398

4 Joachim C., Gimzewski J. K., Aviram A., *Nature*, **2000**, 408, 541

5 Bumm L. A., Arnold J. J., Cygan M. T., Dunbar T. D., Burgin T. P., Jones II L., Allara D. L., Tour J. M., Weiss P. S., *Science*, **1996**, 271, 1705

6 Cygan M. T., Dunbar T. D., Arnold J. J., Bumm L. A., Shedlock N. F., Burgin T. P., Jones II L., Allara D. L., Tour J. M., Weiss P. S., *J. Am. Chem. Soc.*, **1998**, 120, 2721

7 Chen J., Reed M A., Asplund C. L., Cassell A. M., Myrick M. L., Rawlett A. M., Tour J. M., Van Patten P. G., *Appl. Phys. Lett.*, **1999,** 75, 624

8 Reed M. A., Zhou C., Muller J. C., Burgin T. P., Tour G. M., *Science*, **1997**, 278, 252

9 Gittins D. L., Bethell D., Schiffrin D. J., Nichols R. J., *Nature*, **2000**, 408, 67.

10 Gittins D. L., Bethell D., Nichols R J., Schiffrin D. J., *Adv. Mater.*, **1999**, 11, 737

15 Mbindyo J. K. N., Reiss B. D., Martin B. R., Keating C. D., Natan M. J., Mallouk T. E., *Adv. Mater.*, **2001**, 13, 249

17 Ulmann, *An introduction to ultrathin organic films: from Langmuir-Blodgett to Self-Assembly*, Academic Press, San Diego, **1991**

18 Szejtli J., '*Cyclodextrins and their Inclusion complexes'*, Akademiai Kiado, Budapest, **1982**.

19 Tour J. M., Jones II L., Pearson D. L., :Lamba J. J. S., Burgin T. P., Whitesides G. M., Allara D. L., Parikh A. N., Atre S. V., *J. Am. Chem. Soc.*, **1995**, 117, 9529

20 Forster R. J., *Encyclopedia of Electrochemistry*, Eds. Unwin P. A., and Bard A. J., **2003**, Wiley New Yorj, 160-195

21 Allen J.Bard and Larry Faulkner, "Electrochemical *methods: Fundamentals and applications*", **2001**, Second edition, Wiley Ed.

22 Helmoltz H.L.F., *Ann. Physik*, , **1853**, 89, 211

23 Gouy G., *J. Phys .Radium*, **1910**, 9, 457

24 Chapman D.L., *Phil.Mag*, **1913**, 25, 475

25 Stern O., *Z.Elektrochem,* **1924,** 30, 508

26 Hiemenz P., Principles of colloids and surface chemistry, Chapter 11, 3th Edition, Rajagopalan

27 Forster R.J., *Langmuir*, **1995,** 11, 2247

28 Forster R.J., *Anal.Chem,* **1996**, 68 , 3143

29 Smith C.P., White H.S., *Anal. Chem.,* **1993**, 65, 3343

30 Boubour E., Lennox B., *Langmuir*, **2000**, 16, 4222

31 Boubour E., Lennox B., *J. Phys .Chem. B*, **2000**, 104, 9004

32 Schweiss R., Werner C., Knoll W., *J. Electr. Chem*., **2003,** 540, 145

33 Chailiapakul O., Crooks R., *Langmuir*, **1995**, 11, 1329

34 Sabatani E., Rubinstein I., *J. Phys. Chem*., **1987**, 91, 6663

35 Amatore C., Saveant J. M., Tessier D., *J. Electroanal. Chem.,* **1983**, 147, 39

36 Finklea H. O., Self-Assembled Monolayers on Electrodes, *Encyclopedia of Analytical Chemistry*, **2000**, Vol.11, Ed. Meyers R. A., Wiley, Chichester, UK, 10090

37 Walsh D., Keyes T. E., Forster R. J., *J. Phys. Chem. B*, **2004**, 108, 2631

38 Nuzzo R.G., Allara D.L., *J .Am. Chem. Soc.*, **1983**, 105, 4481

39 Porter M. D., Bright T. B., Allara D. L., Chidsey C. E. D., *J..Am. Chem. Soc*., **1987**, 109, 3559

40 Finklea H.O., Avery S., Lynch M., Furtsch T., *Langmuir*, **1987**, 3, 409

41 Zhiyong Li, Shun-Chi Chang, Williams R.S., *Langmuir*, **2003**, 19, 6744

42 Laibinis P.E., Whitesides G., Allara D.L., Yu Tai-Tao, Parikh A.N., Nuzzo R.G., *J. Am. Chem. Soc.,* **1991**, 113, 7152

43 Love J.C., Wolfe D.B., Haasch R.,. Chabinys M.L, Paul K.E., Whitesides G.M., Nuzzo R.G., *J. Am. Chem. Soc.***, 2003**, 125, 2597

44 Katz E., Itzhak N., Willner I., *J. Electroanal. Chem.,* **1992**, 336, 367

45 Nuzzo R. G., Allara D. L., *J. Am. Chem. Soc.,* **1983**, 105, 4481

46 Silberlan P., Leger L., Aussere D., Benattar J. J., *Langmuir*, **1991**, 7, 1647

47 Steiner U. B., Caseri W. R., Suter U. W., *Langmuir*, **1992**, **8**, 2771

48 Brennan J. L., Keyes T. E., Forster R. J., *Langmuir*, **2006**, 22, 10754

49 Brennan J. L., Howlett M., Forster R. J., *Faraday Discussion*, **2002**, 121, 391

50 Ulmann A., *Chem. Rev*., **1996**, 96, 1533

51 Walkzac M. W., Chung C., Stole S. M., Widrig C. A., Porter M. D., *J. Am. Chem. Soc.*, **1991**, 113, 2370

52 Nuzzo R. G., Zegarski B. R., Dubois L. H., *J. Am. Chem. Soc.*, **1987**, 109, 733

53 Li Y., Huang J., McIver R. T. Jr., Hemminger G. C., *J. Am. Chem. Soc.*, **1992**, 114, 2428

54 Widrig C. A., Chung C., Porter M. D., *J. Electroanal. Chem.*, **1991**, 310, 335

55 Woon-kie Paik, Eu S., Lee K., Chon S., Kim M., *Langmuir*, **2000**, 16, 10198

56 Schlenoff J. B., Li M., Ly H., *J. Am. Chem. Soc.*, **1995**, 117, 12528

57 Hitchman J. J., Ofer D., Zou C., Wrigthon M. S., Laibinis P. E., Whitesides G. M., *J. Am. Chem. Soc.*, **1991**, 113, 1128

58 Creager S. E., Hockett L. A., Rowe G. K., *Langmuir*, **1992**, 8, 854

59 D.F. Yang, Wilde C.P., Morin M., *Langmuir*, **1996**, 12, 6570

60 Herrwerth S., Rosendhal T., Feng C., Fick J., Eck W., Himmelhaus M., Dahint R., Grunze M., *Langmuir*, **2003**, 19, 1880

61 Forster, R. J.; Keyes, T. E.; Vos, J. G. "Interfacial Supramolecular Assemblies: Electrochemical and Photophysical Properties", Wiley, New York, **2002**.

62 Bain C. D., Trougthon E. B., Tao Y-T, Evall J., Whitesides G. M., Nuzzo R. G., *J. Am. Chem. Soc.*, **1989**, 111, 321

63 Bertoncello P., Kefalas E. T., Pikramenou Z., Unwin P. R., Forster R. J., *J. Phys. Chem. B.*, **2006**, 110, 10063

64 Fieldne M. L., Claesson P. M., Verall R. E., *Langmuir*, **1999**, 15, 3924

65 Prosser A. J., Retter U., Lunkenheimer K., *Langmuir*, **2004**, 20, 2720

66 Shimazu K., Yagi I., Sato Y., Uosaki K., *Langmuir*, **1992**, 8, 1385

67 Sheng D., Huan M., Chow L.-M., Yang M., *Sensors and Actuators B*, **2001**, 77, 664

68 Damos F. S., Luz R. C. S., Kubota L T., *Langmuir*, **2005**, 21, 602

69 Campbell J. L. E., Anson F. C., *Langmuir*, **1996**, 12, 4008

70 Jung L. S., Campbell C. T., *J. Phys. Chem. B.*, **2000**, 104, 11168

71 Rahn J. R., Hallock R. B., *Langmuir*, **1995**, 11, 650

72 Hubbard J. B., Silin V., Plant A. L., *Biophysical Chemistry*, **1998**, 75, 163

73 Forster R. J., *Anal. Chem.*, **1996**, 68, 3143

74 Forster R. J., Keyes T. E., Farrell M., O'Hanlon D., *Langmuir*, **2000**, 16, 9871

75 Marcus, R. A., *J. Chem. Phys.*, **1965**, 43, 679

76 Marcus R. A., *Ange. Chem., Int. Ed. Eng.*, **1993**, 32, 1111

77 Forster R. J., Faulkner L. R., *J. Am. Chem. Soc.*, **1994**, 116, 5444

78 Forster R. J., Faulkner L. R., *J. Am. Chem. Soc.*, **1994**, 116, 5453

79 Forster R., J., *Inorg. Chem.*, **1996**, 35, 3394

80 Ravenscroft M. S., Finklea H. O., *J. Phys. Chem.*, **1994**, 98, 3843

81 Keyes T. E., Forster R. J., Jayaweera P. M., Coates C. G., McGarvey J. J., Vos J. G., *Inorg. Chem.*, **1998**, 99, 13141

82 Miller R. J. D., McLendon G .L., Nozik A. J., Achmicker W. and Willig F., *Surface electron transfer processes*, VCH, **1995**

83 Balzani V., Juris A., Venturi M., Campagna S., Serroni S., *Chem. Rev.,* **1996**, 96, 759.

84 Bolton J. R., Archer, M. D., "*ET in Inorganic, Organic, and Biological Systems*", Eds. Bolton, J. R., Mataga N., McLendon G., American Chemical Society, Washington D.C., **1999**.

85 Chidsey C. E. D., Bertozzi C. R., Putvinsky T. M., Muijsca A. M., *J. Am. Chem. Soc.*, **1990**, 112, 4301

86 Chidsey C. E. D., *Science*, **1991**, 251, 919,

87 Finklea H. O., Hanshew D. D., *J. Am. Chem. Soc.*,**1992**, 114, 3173

88 Weber K., Hockett L., Creager S., *J. Phys. Chem. B.*, **1997**, 101, 8286

89 Song S., Clark R. A., Bowden E. F., Tarlov M. J., *J. Phys. Chem.*, **1993**, 97, 6564

90 Southampton Electrochemistry Group, *Instrumental methods in Electrochemistry*, University of Southampton

91 Kaifer A. E., Gomez-Kaifer M., *Supramolecular Electrochemistry*, Wiley, **1999**, Chapter 3

92 Wightman R. M., Wipf D. O., in *Electrochemical Chemistry*, Vol. 15, Bard A. J., Ed., Marcel Dekker, New York, **1989**

93 Forster R. J., *Chem. Soc. Rev.*, **1994**, 289

94 Mansfeld F., *Electrochimica Acta*, **1990**, 35, 1533

95 Garrell R. L., *Anal. Chem.*, **1989**, 61, 401A

96 Kneipp K., Kneipp H., Itzkan I., Dasar R. R., Feld M. S., *Chem. Rev.*, **1999**, 99, 2957

97 Moskovits M., *Rev. Mod. Phys.*, **1985,** 57, 783

98 Y. –C. Liu, B. –J. Hwang, W.-J. Jian, *Materials Chemistry and Physics*, **2002**, 73, 129.

99 Cai W. B., Ren B., Li X. Q., She C. X., Liu F. M., Cai X. W., Tian Z. Q., *Surface Science*, **1998**, 406, 9

100 Ren B., Huang Q. J., Cai W. B., Mao B. W., Liu F. M., Tian Z. Q., *J. Electroanal. Chem.*, **1996**, 415, 175

101 Jensen T. R., Malinsky M. D., Haynes C. L., Van Duyne R. P., *J. Phys. Chem. B.*, **2000**, 104, 10549

102 Emroy S. R. Askins W. E., Nie S., *J. Am. Chem. Soc.*, **1998**, 120, 8009

103 Fleischman M., Hendra P. J., Mc Quillian A. J., *Chem. Phys. Lett.*, **1974**, 26, 163

Chapter 2:

Microelectrodes fabrication, synthesis and characterisation of complexes and functionalised β-cyclodextrin

Introduction

In the following chapters the immobilisation and characterisation of cobalt complexes and thiolated β-cyclodextrins (β-CDs) on metal surfaces will be described. Particular attention is dedicated to the adsorption dynamics and electron transfer properties of the assembled monolayers.

The use of metal substrates, such as platinum and gold, allowed the layers to be characterised by electrochemical and spectroscopic methods, including cyclic voltammetry, chronoamperometry, AC voltammetry and Raman spectroscopy. These materials show a high affinity for immobilisation through the sulphur atom, they are stable in a large potential window, both in aqueous and organic solutions and they show enhanced Raman spectra when the substrate is appropriately prepared.

Thiolated cobalt complexes have been studied previously as building blocks for supramolecular structures[1, 2]. However, the studies were focused predominantly on the energetics of immobilisation and not in the dynamics. The present work involved the study and characterisation of tailored molecules for applications in nanotechnology, and in particular in molecular wires, so the major focus was on the electron transfer properties of these monolayers. In this context, the use of microelectrodes is essential in order to probe fast charge transfer kinetics. It is well known that by reducing the dimensions of the electrode surfaces adverse effects, such as ohmic drop, can be significantly reduced and rapid electrode response times achieved [3] [4]. The development of microelectrode technology has significantly broadened the amount of information that can be obtained from electrochemical experiments[5]. Thus, detailed examinations of the kinetics of electrode reactions can be performed at short timescales, revolutionising the understanding of electrode reactions

In the first part of this chapter, the construction and characterisation of platinum microelectrodes are described. The electrodes constructed in this study have radii in the range of 12.5-50 μm, and the response times of these small electrodes are discussed.

In the second part, the synthesis and characterisation of the thiolated cobalt complexes are then described. Complete characterisation of the complexes was carried out using a range of analytical techniques including elemental analysis, mass spectroscopy, UV-Vis spectrophotometry, HNMR, Raman spectroscopy and solution phase electrochemistry.

Thiolated β-CDs are an easy way to modify an electrode surface in order to form a substrate capable of molecular recognition. In the present chapter the characterisation of the gold polycrystalline surface, which acts as a platform for the immobilisation of β-CD-SH molecules, is presented. Complete characterisation of the β-CDs and the including cobalt biphenyl terpyridine complex was carried out again by HPLC, UV-Vis spectrophotometry, HNMR and Raman spectroscopy.

2.1 Platinum Microelectrodes

Introduction

Electrodes with a critical dimension, *e.g.* the radius lying in the range of micrometer, are usually called *microelectrodes*. The successful application of microelectrodes comes from their interesting electrochemical properties that allows fast electrochemical techniques to be used together with a wider range of electrolytic media, not suitable for typical electrodes with millimetre size. Microelectrodes show currents in the range of pico and nanoampere, steady-state responses in the range of microseconds and short RC double layer charging times[3]

During an electrochemical experiment capacitive and faradaic currents flow through the cell and produce a potential that distorts the applied potential by an amount *iR*, the ohmic drop. The nano and pico currents produced at the microelectrodes lower the ohmic drop and allow experiments to be performed in poorly conducting media such as organic solvents. In fact, when a nano current is observed in a cell containing a media with a specific conductance of 0.01 $\Omega cm^{-1}$and an electrode with a radius of 25μm, the potential undergoes a deviation of less than 1 mV, which is not detectable by cyclic voltammetry.

Mass transport

Equation 1.31 in Chapter 1 describes the mass transport for potential step techniques at short and long time scales at an electrode surface.

At short time scales, the diffusion field at the electrode surface can be considered planar and the microelectrode shows a CV with the typical peak-shaped profile characteristic of semi-infinite linear diffusion control. At longer timescales the depletion layer is larger than the electrode and the geometry of the electrode becomes more important. A spherical diffusion field is reached which is more efficient than the planar one. Under these conditions it is possible to observe a steady state response that is only observed at very long times (tens of seconds) with macroelectrodes.

Cell time response

Equation 1.35 describes the current that flows due to the charging of the electrical double layer. The resistance of an electrochemical cell depends on the specific conductance of the medium κ and the radius of the electrode as follows[6]:

$$R_s = \frac{1}{4\pi\kappa r} \tag{2.1}$$

In contrast, the double layer capacitance is proportional to r^2. Multiplying R_s and C_d gives the time cell constant, R_sC_d, which, actually decreases proportionately to the electrode radius. Thus, shrinking the electrode radius produces a smaller cell time constant and a faster electrode response

2.1.2 Microelectrode fabrication

Platinum microelectrodes were constructed using a method previously reported[7], by sealing a fine wire of platinum (Goodfellow Metals, Cambridge, UK) in soft glass. The radii of the microwires used were in the range 12.5-50μm. Soft glass tubing (o.d. 5mm, i.d. 3mm) was cut into pieces of about 6cm in length. One end of the tube was heated in a butane flame, until the tubing partially collapsed, leaving a hole of inner diameter of about 1mm. The tubes were then soaked in a 50:50 milliQ water/nitric acid solution, at 50°C, for several hours to remove any contamination. After cleaning, the tubes were rinsed with milliQ water and then soaked in acetone for 2 hours. Finally, the pieces of tubing were rinsed with milliQ water and oven dried.

An aluminium transition wire (approximately 5 cm in length) was soldered to a piece of copper hook-up wire, stripped of its outer plastic protective covering and bent in zig-zag shape to ensure stability of the wire within the glass tubing. Approximately 3 cm of the microwire was then cut and one end winded around the aluminium wire and soldered. The microscopic wire was then cleaned in a 50:50 milliQ water/nitric acid solution for one hour, rinsed with milliQ water, then soaked in acetone for another hour and finally allowed to dry in air.

The conductivity of the wire assembly was then checked with a multimeter and then passed through the glass tubing, allowing approximately 0.5 cm of the microwire to be exposed through the hole at the end of the tubing. This end was then gently heated in a butane flame until the glass completely collapsed around the microwire, forming a seal between the glass and the microwire. The assembly was then glued to the glass at the end of the copper wire, using an epoxy adhesive and finally capped with a plastic cap. The end of the electrode was then polished using fine sand paper until the end of the electrode appeared flat. The electrode was then allowed to stand in milliQ water overnight to check for any leaks into the electrode body. By performing cyclic voltammetry in 1M $LiClO_4$, before and after the soaking, the leakage could be detected as a substantial increase in the background current. Approximately 90% of the electrodes constructed using this approach were successfully made and were used routinely in electrochemical experiments. The design of the microelectrodes is shown in Figure 2.1

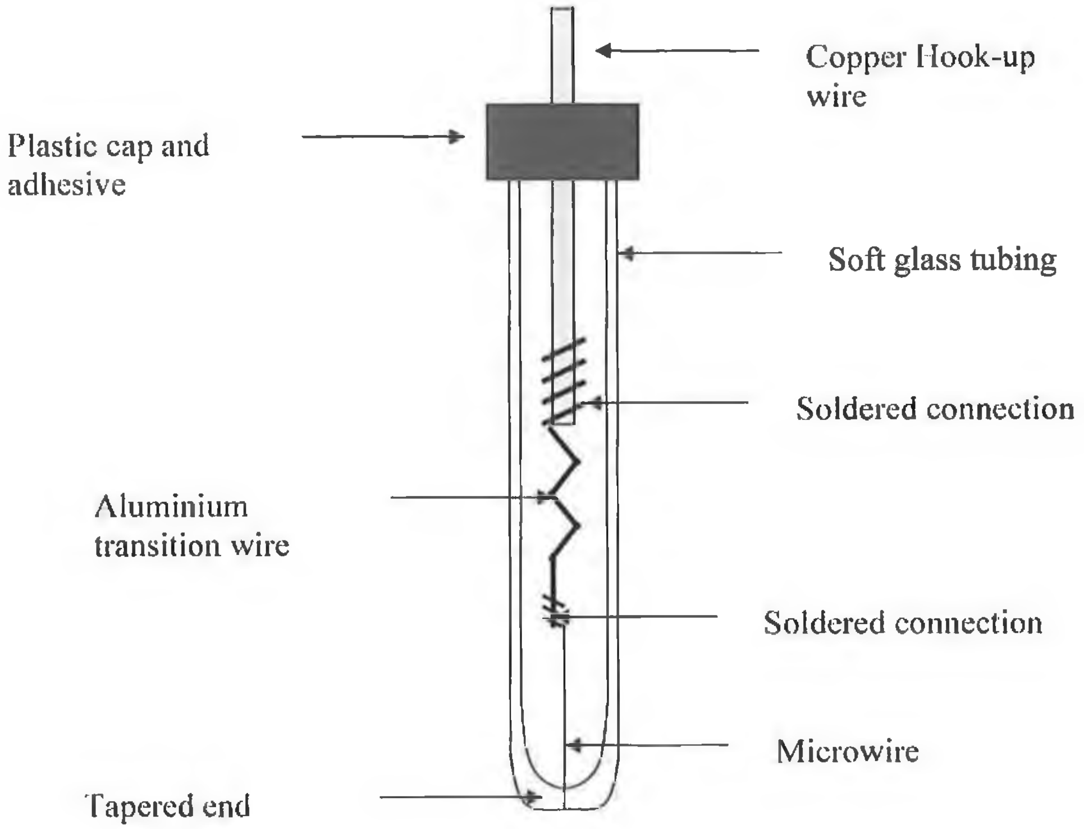

Figure 2.1 Design of the microelectrodes constructed for this study

2.1.3 Electrode polishing

Electrodes that had been successfully sealed were then polished using aqueous slurries of alumina (Buehler, aluminium oxide powder) applied to a felt polishing pad (Struers, OP-Chem). Polishing was carried out by holding the electrode surface against the polishing pad and gently performing "figure of eight" movements with the electrode. Polishing was performed using successively finer grades of alumina, 12.5, 5.0,1.0, 0.3 and 0.05 μm. Between each grade of alumina the electrodes were rinsed thoroughly using milliQ water and then sonicated in milliQ water for 10 minutes.

The progression of polishing was monitored by cyclic voltammetry in 0.5 M H_2SO_4. In this experiment, the reference electrode was a Ag/AgCl, KCl_{sat} aqueous reference, placed in a salt bridge containing the same sulphuric acid solution while a platinum wire was the counter electrode. The salt bridge was used in order to minimise contamination of sulphuric acid solution from the chlorides diffusing from the reference filling solution. Chlorides can react with the metal substrate and affect the voltammetric response. A typical CV for platinum microelectrodes is shown in Figure 2.2

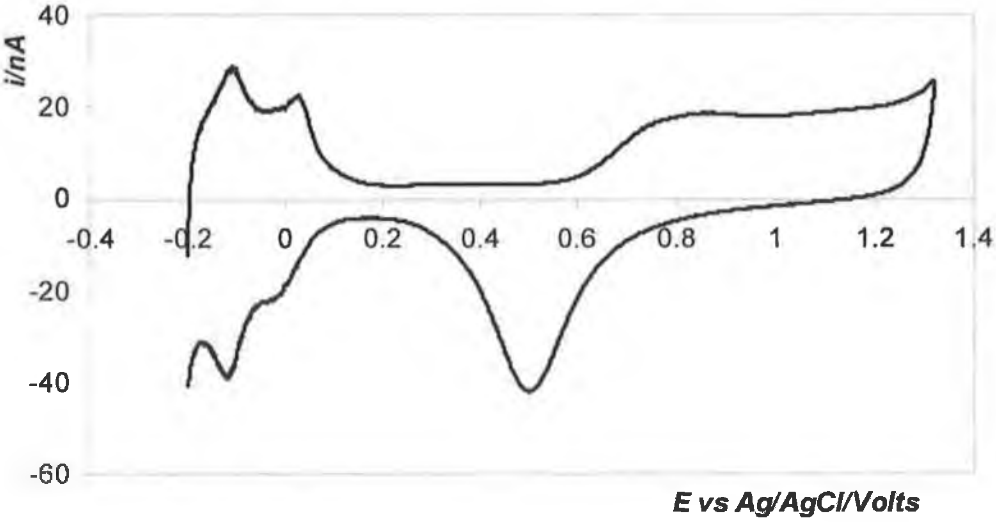

Figure 2.2 CV of a polycrystalline platinum microelectrode (50 μm radius), in 0.5M H_2SO_4 for electrode cleaning. Scan rate: 0.1 Vs^{-1}. Reference electrode: Ag/AgCl, KCl_{sat} in a salt bridge. Counter electrode: platinum wire

In general, the potentials were scanned in a range chosen to form and then subsequently fully reduce a complete oxide monolayer in order to completely remove any adsorbed material. In particular, between 0.7 and 1.0V, the formation of a platinum oxide monolayer is observed, whose profile changes during the scanning. The reverse scan was run from 1.4 to -0.2V to fully reduce the oxide layer around 0.5V. The reductive adsorption peaks for hydrogen are also detected between 0 and -0.2V followed in the reverse scan by the oxidative desorption hydrogen peaks. Limited repetitive scans were performed in this range of potentials until no further change in the oxidation and reduction peaks were observed. A second set of CVs was then run in a smaller potential window. This protocol allowed obtaining a clean electrode and an accurate measure of the charge needed to oxidise just the first layer of the metal surface.

2.1.4 Determination of electrode area

Due to the well characterised formation of oxide monolayers on polycrystalline platinum, the charge passed in removal of these oxide monolayers is routinely used to determine the real or microscopic area of these electrodes[8]. For platinum, hydrogen adsorption from solution may also be used to determine the microscopic area.

The method of oxide reduction for the determination of the real surface area assumes that oxygen is adsorbed at the surface in a mononuclear layer and also that one oxygen atom is attached to one metal atom. Once the contribution from double layer charging has been subtracted, the charge passed during the reduction of the metal oxide layer can be used to calculate the real surface area according to Equation 2.2

$$A_{real} = \frac{Q_r}{Q_s} \tag{2.2}$$

where A_{real} is the microscopic area of the electrode, Q_r is the charge under the surface oxide reduction peak (C) and Q_s is the standard value for the surface oxide charge per unit area for each metal. The reference value for polycrystalline platinum is 420μC cm^{-2}.

The surface roughness of the microelectrodes was calculated by dividing the microscopic area by the geometric area and typical values for the roughness factor were in the range of 1.5-2.1. Some uncertainty arises because of the differing crystal composition of the surface since the charge of desorption depends upon the crystal face of the metal[9].

Once the microscopic area of the electrodes was determined, the electrodes were electrochemically cycled in a capacitive range in 0.5M H_2SO_4, until a time independent background response was observed. In this way complete reduction of any surface oxide and also full desorption of hydrogen were ensured.

2.2 Gold macroelectrodes

The same polishing procedure and electrochemical cleaning described for the platinum microelectrode was followed for the gold macroelectrodes (CH Instruments, 2mm diameter).

Figure 2.3 shows a typical CV, first and last scan, obtained for a gold polycrystalline macroelectrode cycled in 0.5M H_2SO_4:

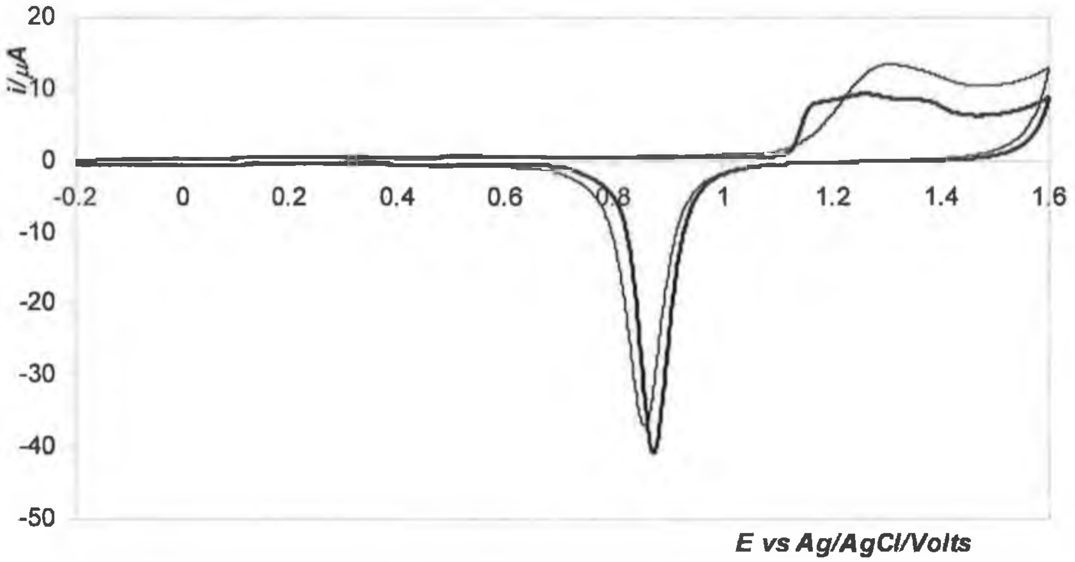

Figure 2.3. CV of a polycrystalline gold macroelectrode (2mm diameter) in 0.5M H_2SO_4 for electrode cleaning, first scan (thin line) and last scan (thick line). Scan rate: $0.1 Vs^{-1}$. Reference electrode: Ag/AgCl, KCl_{sat} in a salt bridge. Counter electrode: platinum wire

Again the potentials were scanned in order to fully oxidise and then fully reduce the gold oxide layer and remove any adsorbed material. Between 1.4 and 1.6 V the peaked profile typical for a polycrystalline gold substrate is observed[10]. The major difference between platinum and gold is the absence for the latter of the adsorption/desorption hydrogen peaks. Therefore, the microscopic area can just be determined with the oxide reduction peak observed at 0.9V, knowing that the specific charge for gold is 390μC cm^{-2} [8]. Typical values for the roughness factor were in the range 1.5-2.2.

2.3 Double layer capacitance and uncompensated cell resistance

As mentioned before, in order to measure the heterogeneous electron transfer rate constant accurately, it is necessary to know the cell time constant. In the following sections, the interfacial capacitance and uncompensated cell resistance as measured by chronoamperometry, AC voltammetry and impedance spectroscopy are reported and discussed as a function of electrode size and electrolyte concentration. The objective is to identify those electrodes with the smallest *RC* constant that will be used as the starting point during the electron transfer determination experiments. Acetonitrile solutions of $TBABF_4$ were tested, since the monolayers behaves ideally in this electrolyte and are stable for several hours.

Materials and instrumentation

Platinum macro (CH Instruments, 2mm diameter) and home-made micro electrodes were mechanically polished as previously described and rinsed with milliQ water. The characterisation was performed in acetonitrile solutions (Sigma-Aldrich, 99.9%) containing oven dried $TBABF_4$ (Sigma-Aldrich electrochemical grade) as electrolyte. A three-electrode electrochemical cell of conventional design was used and all the potentials were quoted *versus* a non-aqueous Ag/Ag^+ reference electrode previously calibrated *versus* the ferrocene/ferrocenium redox couple. The counter electrode was a platinum wire.

Chronoamperometry and AC voltammetry were performed, for macro electrode, using a CH instrument Model 660A potentiostat/galvanostat. EIS was performed for microelectrodes using an impedance spectrum analyzer IM6 BAS Zahner.

For microelectrodes chronoamperometry experiments, a custom-built function two-electrode, generator-potentiostat with a rise time of less than 2 ns was used. The counter electrode was a Pt wire combined with a Ag/Ag^+ reference electrode.

Prior to any experiments the solutions were deoxygenated with oxygen-free argon and a blanket of argon was left over the solution for all the experiments.

2.3.1 Electrolyte concentration dependence for macroelectrodes

Electrochemical impedance spectroscopy determination

In electrochemical impedance spectroscopy, a constant dc potential of 0 V (the OCP) was chosen and the frequency of the ac potential was changed between 1 and 1×10^4 Hz, while the electrolyte concentrations ranged between 0.05 and 0.6 M. Figure 2.4 shows the profile for the phase angle versus the frequency of the ac potential for a platinum macroelectrode in 0.6M $TBABF_4$, in acetonitrile. The conversion of this plot into a graph of imaginary versus real part of the impedance, shown in Figure 2.5, was performed by the CHI software by means of the equations introduced in chapter 1.

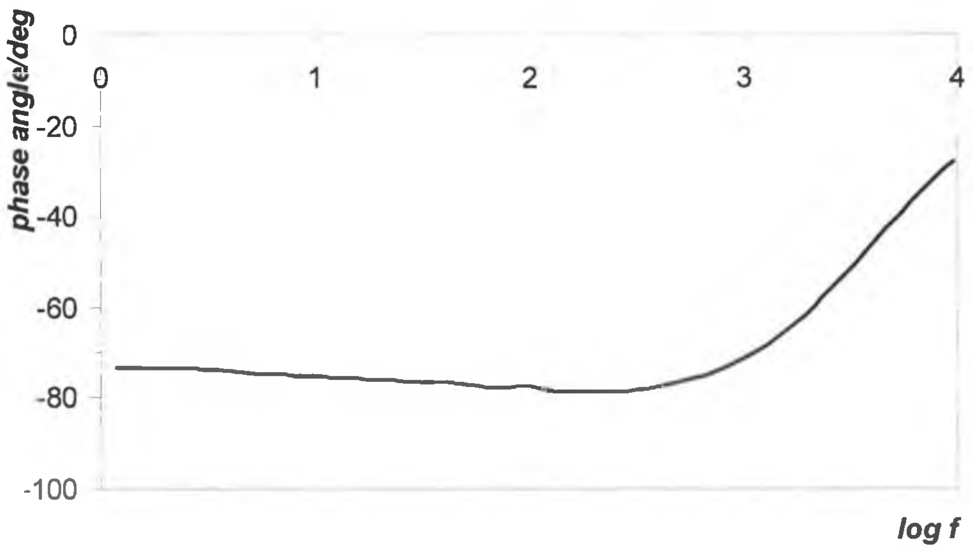

Figure 2.4 Phase angle *versus* log *f* for a platinum macroelectrode (2 mm diameter) at 0.6M $TBABF_4$, in acetonitrile. Frequencies range: 1 to 1×10^4 Hz. Amplitude: 0.005V. Reference electrode: Ag/Ag^+ calibrated vs. Fc/Fc^+. Counter electrode: platinum wire

Figure 2.5 shows the imaginary *versus* the real parts of the impedance for all the concentrations for the platinum macroelectrode

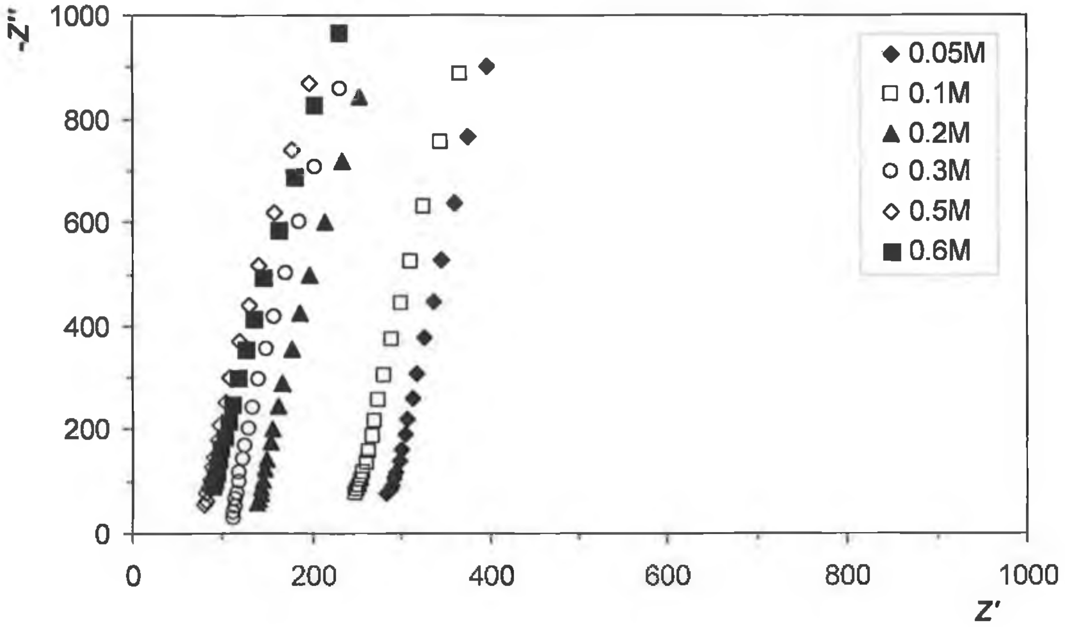

Figure 2.5 Plot of -Z" *vs.* Z' for a platinum macroelectrode at different supporting electrolyte concentrations, $TBABF_4$, in acetonitrile. Frequencies range: 1 to 1×10^4 Hz. Reference electrode: Ag/Ag^+ calibrated vs. Fc/Fc^+. Counter electrode: platinum wire.

The values for the uncompensated cell resistance at the different electrolyte concentrations can be easily extrapolated at –Z''=0, by modelling the impedance profile with best fit linear regressions.

Moreover, rearranging Equation 1.43 gives:

$$Z'' = \frac{1}{\omega C_d} = \frac{1}{2\pi f C_d} \tag{2.3}$$

where f is the frequency in Hz. By plotting Z'' *versus* ω a straight line is obtained, whose slope gives the differential capacitance, C_d. Figure 2.6 shows the straight lines obtained from the results of Figure 2.5 at the different concentrations

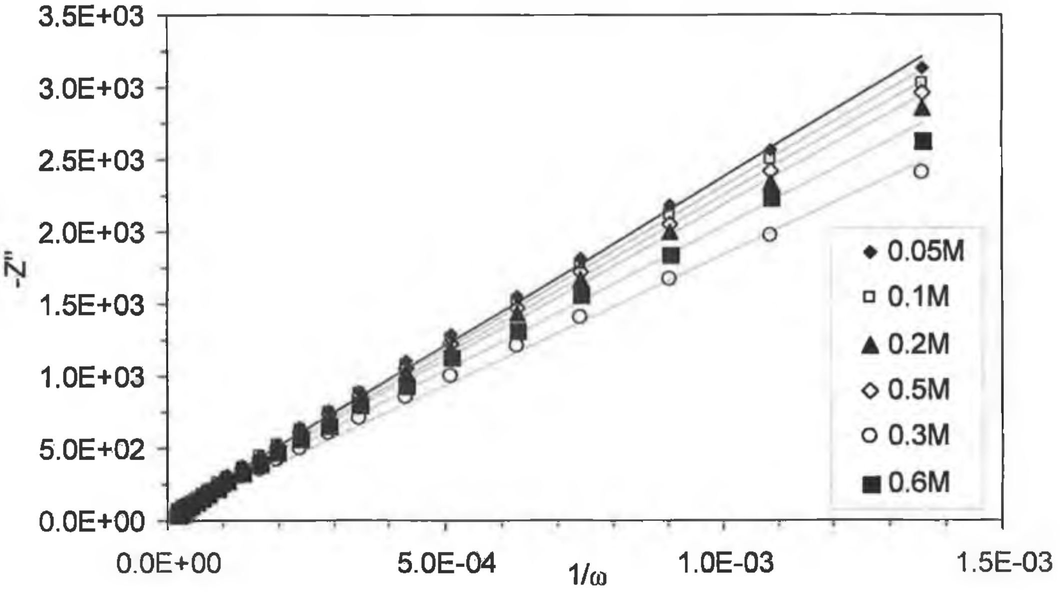

Figure 2.6. Plot of Z" *versus* 1/ω for a platinum macroelectrode (2mm diameter) at different supporting electrolyte concentrations, $TBABF_4$, in acetonitrile. Reference electrode: Ag/Ag^+ calibrated vs. Fc/Fc^+. Counter electrode: platinum wire. The symbols are the data and the straight line are the linear regressions whose slopes give the capacitance of the double layer.

The calculated differential capacitances and resistance are shown in Figure 2.7 for different electrolyte concentrations.

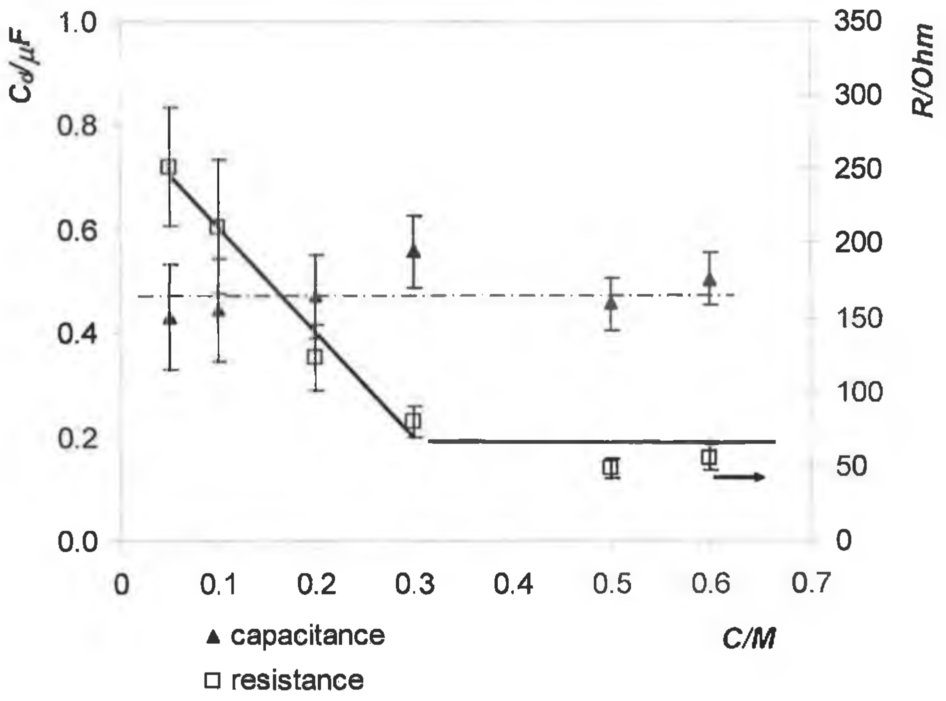

Figure 2.7. Electrolyte concentration dependence of the differential capacitance and resistance by EIS for a platinum macroelectrode at different supporting electrolyte concentrations, $TBABF_4$, in acetonitrile. Reference electrode: Ag/Ag^+ electrode calibrated vs. Fc/Fc^+ redox couple. Counter electrode: platinum wire.

As it can be seen from summarising Figure 2.7 and Table 2.1, C_d does not show any significant electrolyte dependence in the range of concentrations considered. This suggests that the diffuse double layer is compressed for each electrolyte concentration investigated and does not contribute significantly to the overall capacitance.

In Figure 2.7, a linear dependence of the resistance with the electrolyte concentration is visible up to 0.3 M $TBABF_4$, as predicted by Equation 2.1. Further increase of the electrolyte concentration does not decrease the resistance of the system, while a constant plateau value is reached. This phenomenon is probably due to some sort of residual resistance present in the set-up, e.g., a contact resistance in series with the cell resistance.

Table 2.1 summarises the results obtained at different electrolyte concentration in terms of uncompensated cell resistances and double layer capacitances.

Table 2.1 Uncompensated cell resistance and double layer capacitance dependence on $TBABF_4$ concentration in acetonitrile by EIS for platinum macroelectrode

C/M	R_{un}/Ohm	C_d/μF
0.05	252±40	0.43±0.10
0.1	211±45	0.44±0.10
0.2	122±22	0.47±0.08
0.3	80±10	0.56±0.07
0.5	48±7	0.46±0.05
0.6	56±8	0.50±0.05

Chronoamperometry determination

The uncompensated cell resistances and the double layer capacitances for macroelectrodes at different electrolyte concentrations were also determined by chronoamperometry. A typical response is shown in Figure 2.8 and the inset shows the semilog plot:

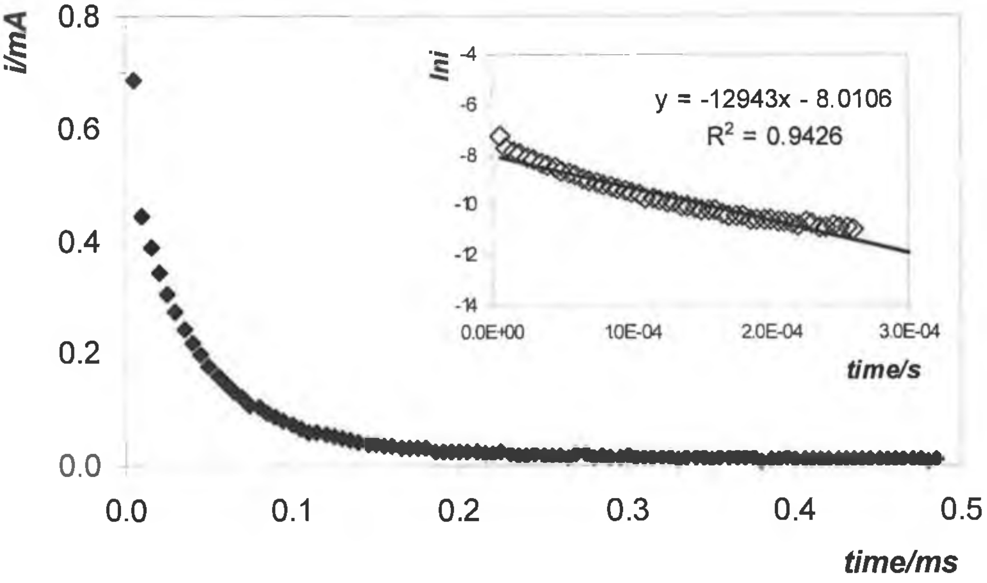

Figure 2.8 Current response from -0.6 to -0.55V for a platinum macroelectrode (2mm diameter) in acetonitrile, 0.6 M $TBABF_4$ in acetonitrile. Reference electrode: Ag/Ag^+ electrode calibrated *vs*. Fc/Fc^+ redox couple. Counter electrode: platinum wire. Potential step: 0.050V for 0.5ms. The inset shows the semi-log current *versus* time response.

As mentioned in Chapter 1 the current flowing after applying a potential step in a capacitive range of potentials can be modelled by the following equation:

$$i_c = \frac{\Delta E}{R_s}\exp(-t / R_s C_d) \qquad (2.4)$$

Using the linearized form of the equation, which is shown in the inset in Figure 2.8, it is possible to calculate the cell time constants, and the individual resistance and differential capacitances. The determined uncompensated cell resistances and capacitances are shown in Figure 2.9 and summarized in Table 2.2.

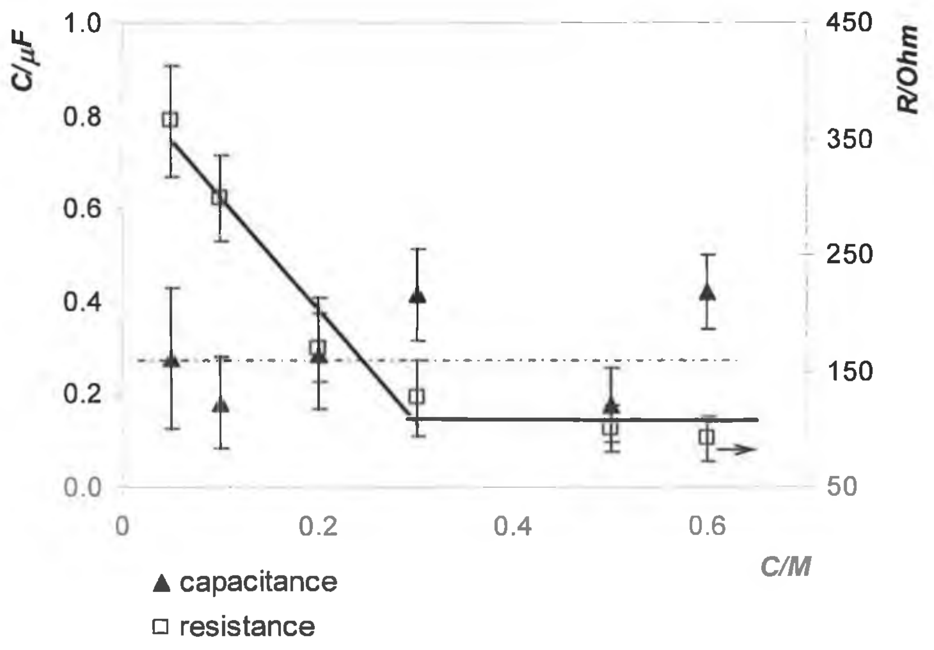

Figure 2.9 Electrolyte concentration dependence of the differential capacitance and uncompensated cell resistance by CA for a platinum macroelectrode (2mm diameter) at different supporting electrolyte concentrations, TBABF$_4$, in acetonitrile. Reference electrode: Ag/Ag$^+$ calibrated *versus* Fc/Fc$^+$ redox couple. Counter electrode: platinum wire.

Table 2.2 Uncompensated cell resistance and double layer capacitance dependence on electrolyte concentration by CA

C/M	*R/Ohm*	*C/μF*
0.05	366±48	0.29±0.15
0.1	299±37	0.20±0.10
0.2	170±30	0.31±0.12
0.3	127±33	0.43±0.10
0.5	100±20	0.18±0.08
0.6	91±20	0.42±0.08

Again, the capacitance does not show a particular dependence on the electrolyte concentration, while the uncompensated cell resistance drops, especially from 0.05 to 0.2M. It is interesting to note that the values obtained by EIS and CA are in good agreement, considering the different techniques and the models used to fit.

Table 2.4 summarises the results in terms of cell time constant, determined either by EIS or CA, at different electrolyte concentrations

Discussion of the results

In Chapter 1 the Debye-Hückel κ parameter was defined and calculated for a range of concentrations, for a 1:1 electrolyte in water and acetonitrile at 25°C. Equation 2.5 shows the expression of κ:

$$\kappa = \left[\left(e^2 / \varepsilon k_B T \right) \sum_i z_{u}^2 n_i^0 \right]^{1/2} \qquad (2.5)$$

where ε is the dielectric constant of the medium, n_i^o is the number of ions at the bulk concentration, e is the charge of the electron, k_B is the Boltzmann constant, T is the absolute temperature and z_i is the charge of the ion taken with the sign. The units of κ are therefore the reciprocal length, then κ^{-1} has the units of length (m) and is usually called the *thickness of the double layer.*

Table 2.3 shows the calculated κ for the range of concentration between 0.05 and 0.6M of $TBABF_4$ in acetonitrile at 25°C.

Table 2.3 Calculated κ^{-1} for different concentrations of $TBABF_4$ in acetonitrile at 25°C

C/M	κ^{-1}/*nm*
0.05	13.6
0.1	9.6
0.2	6.0
0.3	5.6
0.4	4.8
0.5	4.3
0.6	3.9

The major effect of the concentration on κ is evident switching from 0.05 to 0.2 M, when the κ value halves. Further increase of the concentration does not significantly change the diffuse double layer thickness. In Chapter 1, the total double layer was described as made of two contributions defined by the OHP, and therefore the double layer capacitance was also split in two different components, C_H and $C_{diffuse}$, two capacitors in series, representing the capacitance of the charges at the OHP and of the diffuse layer respectively. The typical rules for capacitors in series were applied:

$$C_d^{-1} = C_H^{-1} + C_{diffuse}^{-1} \tag{2.6}$$

where for a 1:1 electrolyte is

$$C_H = \varepsilon_{sol}\varepsilon_0 / x_2$$
$$C_{diffuse} = \kappa \cosh\left({ze\phi_2}/{2k_BT} \right) \tag{2.7}$$

The diffuse layer capacitance, $C_{diffuse}$, depends on the potential and the value of κ while the total capacitance, C_d, is governed by the smaller of the two contributions in Equation 2.7. Therefore, at large electrolyte concentrations $C_{diffuse}$ becomes so large that its contribution to the total capacitance is small and in a plot of C_d versus potential one sees only the constant capacitance of C_H. At small electrolyte concentration a peaked profile is seen, with a minimum at the PZC. Therefore, an interesting way to probe the behaviour of the capacitance and understand its contribution to the *RC* constant of a cell, is to probe the potential dependence of the capacitance at different electrolyte concentrations using AC voltammetry. .

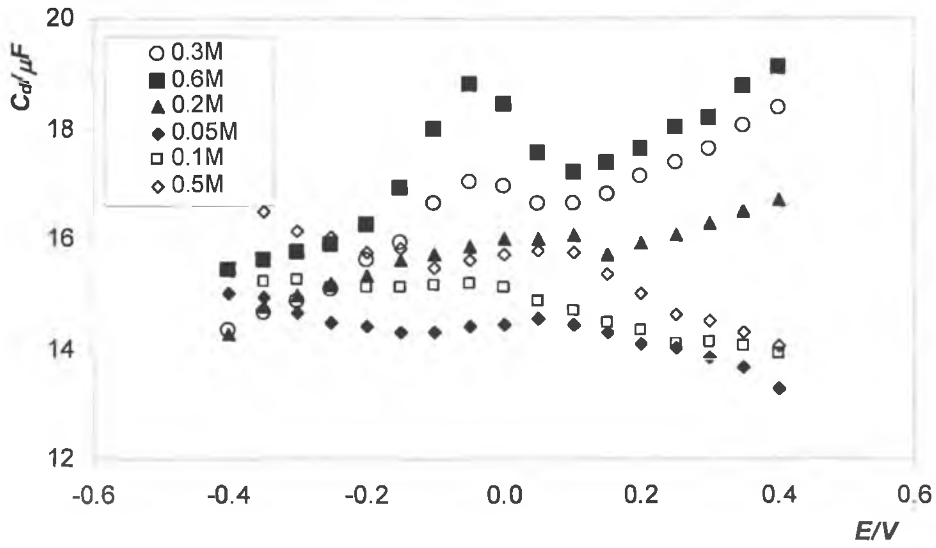

Figure 2.10 Differential capacitance *versus* potential for a platinum macroelectrode (2 mm diameter) at different $TBABF_4$ concentrations in acetonitrile. Reference electrode: Ag/Ag^+ calibrated *versus* Fc/Fc^+ redox couple. Counter electrode: platinum wire.

With the exceptions of 0.6 and 0.3M all of the capacitance values are approximately independent of the applied potential. Moreover, the capacitance values are in the same range for the different concentrations, slightly shifting towards higher values while increasing the concentration. This phenomenon suggests that the double layer is compressed and behaves as a parallel plate capacitor, without really affecting the RC constant value.

The exception showed by 0.6 and 0.3M could be explained with some sort of adsorption of the electrolyte on the surface, phenomenon that is not taken into account in the double layer description by Stern. Another possible explanation could be a reconstruction effect of the polycrystalline surface electrode that can happen during the scanning of the potential[11]. This phenomenon would change the crystallinity of the exposed surface to the contacting electrolyte solution causing a variation of the electrode response. In order to study this possible explanation differential capacitance experiments could be performed with single crystal electrode, since a variation in the surface crystallinity could be detected easier.

Table 2.4 Cell time constants determined either by EIS or CA for different concentrations of $TBABF_4$ in acetonitrile for platinum macroelectrode

C/M	*RC constant/ms by EIS*	*RC constant/ms by CA*
0.05	0.11	0.10
0.1	0.09	0.06
0.2	0.06	0.05
0.3	0.04	0.05
0.5	0.02	0.02
0.6	0.03	0.04

The two techniques show the same trend for the time cell constants. In particular, the shortest cell time constants are obtained when the electrolyte concentration is at least 0.3M. Therefore, in the measurement of the electron transfer, a concentration of 0.6M $TBABF_4$ was selected.

2.3.2 Size dependence : microelectrodes and high speed chronoamperometry

In the following experiments, the size dependence of the cell time constant will be shown and discussed, by comparing the values obtained for macroelectrodes to those determined for microelectrodes at 0.6M. In order to do so, the effect of electrolyte concentration was assessed.

High speed chronoamperometry was carried out by stepping the potential of 0.050V from -0.6 to -0.55V. As for macros, by fitting Equation 2.4, estimations for R and C were calculated at different electrolyte concentrations and they are shown in Figure 2.11

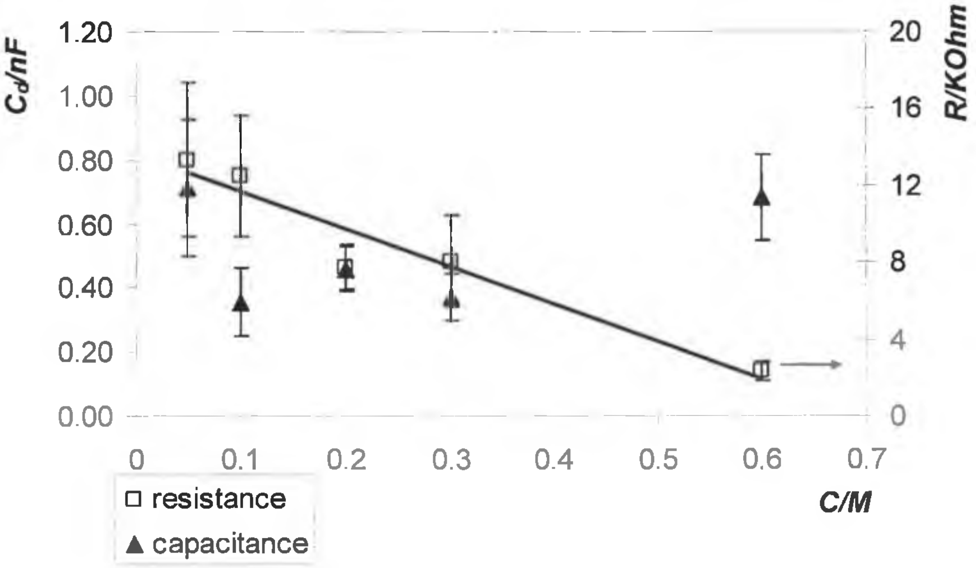

Figure 2.11. Electrolyte concentration dependence of the differential capacitance and resistance by HSCA for a 100 µm platinum electrode at different supporting electrolyte concentrations, $TBABF_4$, in acetonitrile. Reference electrode: Ag/Ag^+ calibrated *versus* Fc/Fc^+ redox couple. Counter electrode: platinum wire.

As it can be seen from the figure, the same trends found for macros are observed for the microelectrodes. In particular, the linearity between the electrolyte concentration and the resistance is well followed. The double layer capacitance drops by three orders of magnitude with respect to the values for macros, while the resistance increases by two orders of magnitude. The overall effect is a net decrease of the cell time constant, from sub millisecond to less than 10μs. This observation is consistent with the theoretical considerations of Section 2.1 where the *RC* is expected to vary with the radius of the electrode, when everything else is kept constant.

Table 2.5 reports the calculated values for *RC* for the whole range of concentrations for the platinum microelectrodes.

Table 2.5. *RC* constants determined by HSCA, for 100 μm platinum electrode at different supporting electrolyte concentrations, $TBABF_4$, in acetonitrile.

C/M	*RC constant/μs*
0.05	9.5±2.0
0.1	4.4±1.2
0.2	3.6±1.1
0.3	3.0±1.3
0.6	1.6±0.7

The values of the reciprocal cell time constants are between 1.05 and $6.2\times10^{5}s^{-1}$. Therefore, electron transfer reactions with rate constants of the order of $10^{5}s^{-1}$ can be measured. In the literature[12], electron transfer rate constants for similar compounds to that described in the present work exhibit rate constants in the range of $10^{4}s^{-1}$. Therefore, it is theoretically possible to measure rate constants using these electrodes.

In order to confirm the values obtained for the time cell constants by HSCA, electrochemical impedance spectroscopy experiments were ran at 0.6M for 100 and 25 micron radius electrodes. The potential chosen was the OCP, and the frequency was ranged from 1×10^{3}Hz to 1×10^{6}Hz.

The results for the EIS are shown in Table 2.6. It can be seen that, for the 100µm electrode, they match the values obtained by the chronoamperometry experiments within 10%.

Table 2.6. *RC* constants at 0.6M $TBABF_4$ acetonitrile solution for a 100 and 25-μ platinum electrode by CA and EIS.

C/M	*electrode diameter (μm)*	*RC/μs by CA*	*RC/μs by EIS*
0.6	100	1.6	1.8
0.6	25	-	0.16

It is interesting to note that by switching from 100 to 25 μm (diameter) electrodes the *RC* constant decreases of one order of magnitude.

In general, the electrode characterisation experiments show that the *RC* constant of a cell does decrease by increasing the electrolyte concentration in a very reproducible way for different sizes of platinum electrodes. The effect of the electrolyte is mainly on the resistance of the system that is generally reduced of one order of magnitude, keeping the size of the electrode constant. Nevertheless, a striking effect is obtained when the electrode dimensions are reduced, changing from 1mm diameter to 50 and 12.5μm radius. The *RC* constants are reduced over four orders of magnitude, due to the small capacitances of the electrodes. Therefore, the best case scenario is represented by an electrolyte concentration of 0.6M and a microelectrode of 12.5μm radius, which allows the electron transfer reactions that occur on the microsecond timescale to be characterised.

2.4 Cobalt terpyridine complexes

Introduction

The cobalt complexes used in the present work are terpyridine complexes of Co^{2+} with different substituents to allow self-assembly or docking with a cyclodextrin host, i.e. benzylthiol and biphenyl. Figure 2.12 shows the structures of the complexes.

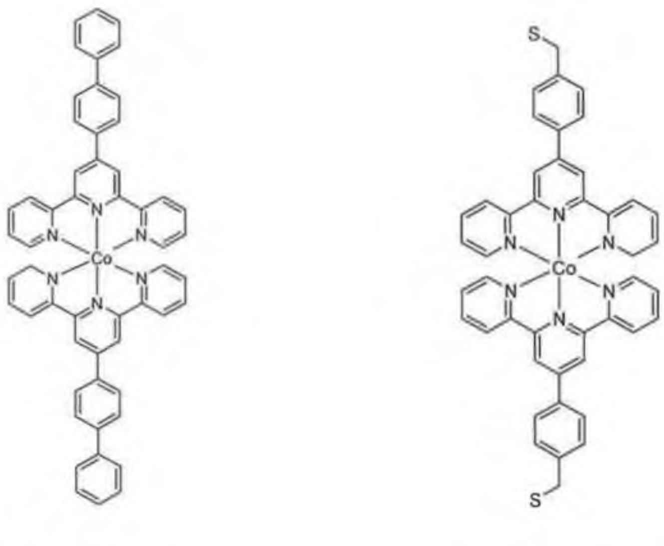

CoTpybip

CoTpySH

Figure 2.12 Molecular structures of bis-biphenyl-2,2':6',2''-terpyridine Cobalt complex (left figure, referred as CoTpybip) and bis-4'-(p-(thiolmethyl)-phenyl)-2,2':6',2''-terpyridine Cobalt complex (right figure, referred as CoTpySH). The molecules are shown without the counter ions and the cobalt metal centre is in the oxidation state 2^+.

In the following chapters bis-biphenyl-2,2':6',2''-terpyridine Cobalt complex and bis-4'-(p-(thiolmethyl)-phenyl)-2,2':6',2''-terpyridine Cobalt complex will be referred as CoTpybip and CoTpySH respectively.

In the following section, the synthesis and characterisation of a series of cobalt terpyridine complexes are described and discussed.

2.4.1 Complexes characterisation

UV-VISIBLE SPECTROSCOPY

UV-Vis spectrophotometry was performed by using a a Hewlett-Packard 342A diode array spectrophotometer. Samples were dissolved in spectrophotometric grade acetonitrile at different concentrations in order to determine the extinction coefficient. Glass cuvettes with a path length of 1 cm were used for all measurements. The minimum slid width was 2nm.

ELECTROCHEMISTRY

Solution phase electrochemistry was performed by cyclic voltammetry using a CH Instruments Model 660 Electrochemical Workstation and a conventional three electrode cell. Platinum polycrystalline macroelectrodes (CH Instruments, 2mm diameter) were used as working electrodes, the counter electrode was a platinum wire and the reference electrode was a Ag/Ag^+ organic reference, previously calibrated *versus* the ferrocene/ferrocenium couple. All experiments were performed at room temperature. The solutions were 0.1M $TBABF_4$ in acetonitrile, deoxygenated with free-oxygen argon.

SOLID STATE RAMAN SPECTROSCOPY

Solid Raman spectroscopy was performed by using Horiba Jobin Yvon HR800UV. The parameters used will be discussed in each section

^{1}H-NMR SPECTROSCOPY, ELEMENTAL ANALYSIS AND ES-MS

^{1}H-NMR was carried out at the University of Birmingham, School of Chemical Science, together with the elemental analysis and ES-MS.

2.5 Synthesis of CoTpySH

The following synthetic procedures were performed in the School of Chemistry at the University of Birmingham and kindly provided for electrochemical studies and Raman spectroscopy.

Synthesis of 4'-(p-(thiolmethyl)-phenyl)-2,2':6',2''-terpyridine

A mixture of ttp-CH_2-Br (540 mg, 1.38 mmol) and thiourea (108 mg, 1.40 mmol) were brought under reflux in dry dioxane (25 ml) for 3 h, resulting in a white suspension. The mixture was cooled down to room temperature, followed by addition of a degassed aqueous solution (5ml) of NaOH (56 mg, 1.50 mmol). The resulting solution was allowed to reflux for 3 hours, and evaporated to dryness. Upon addition of degassed acidified H_2O (20 ml, pH~3-4) a white solid precipitated which was extracted from CH_2Cl_2 (4x100 ml) and dried under vacuum. Yield: 62%.

^{1}H-NMR (300 MHz, $CDCl_3$): δ in ppm 8.73 (s(overlapping), 4H, $H_{6,3'}$), 8.67 (d, *J*= 7.9 Hz, 2H, H_3), 7.87 (m, 4H, $H_{4,o}$), 7.47 (d, *J*= 8.2 Hz, 2H, H_m), 7.36 (m, 2H, H_5), 3.82 (d, *J*= 7.5 Hz, 2H, -CH_2-), 1.82 (t, *J*= 7.5 Hz, 1H, -SH).

ES-MS (MeOH): *m/z* 356 $\{M + H\}^+$, 378 $\{M + Na\}^+$

^{13}C-NMR (75 MHz, $CDCl_3$): δ in ppm 158.7, 158.5, 152.2, 151.6, 144.6, 139.4, 139.4, 131.1, 130.1, 126.3, 123.9, 121.2, 31.2.

Synthesis of CoTpySH

A mixture of $CoCl_2 6H_2O$ (37 mg, 0.155 mmol) and ttp-CH_2-SH (110 mg, 0.31 mmol) was brought to reflux for 30 min.. Following cooling to room temperature and filtration to remove any unreacted solid, addition of excess of NH_4PF_6 (130 mg, 0.79 mmol) led to the precipitation of a pink powder which was isolated by filtration under vacuum and washed with cold MeOH and Et_2O. Recrystallization from MeCN gave the pure compound in 49% yield.

HNMR (400 MHz, CD_3CN): δ in ppm 93.32 (H_6, characteristic fingerprint of low-spin $[Co(terpy)]^{2+}$ species), 54.48, 43.14, 32.58, 14.12, 9.81, 9.36, 8.57.

ES-MS (MeOH): *m/z* 401.2 $\{M - 2PF_6 + MeOH\}^{2+}$, 912 $\{M - PF_6\}^{+}$.

ELEMENTAL ANALYSIS: Found: C, 49.8; H, 3.1; N, 7.8. $C_{44}H_{34}N_6S_2CoP_2F_{12}$ requires C, 49.9; H, 3.2; N, 7.9 %).

In the UV region, bands below 350nm are assigned to the intra-ligand π–π* transitions[13]. The metal to ligand charge transfer band is observed at 510nm, as shown in Figure 2.13. Figure 2.14 shows the extinction coefficient determination.

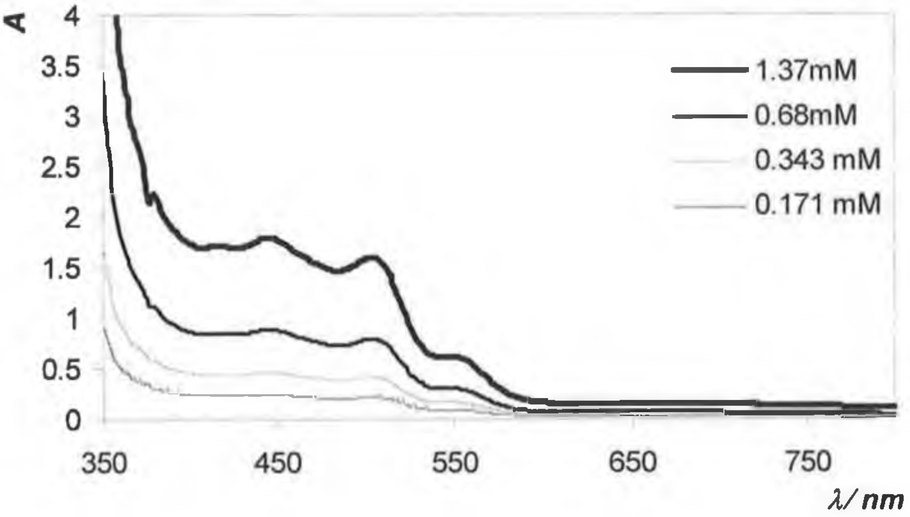

Figure 2.13. Absorption spectra for CoTpySH at different concentrations in acetonitrile.

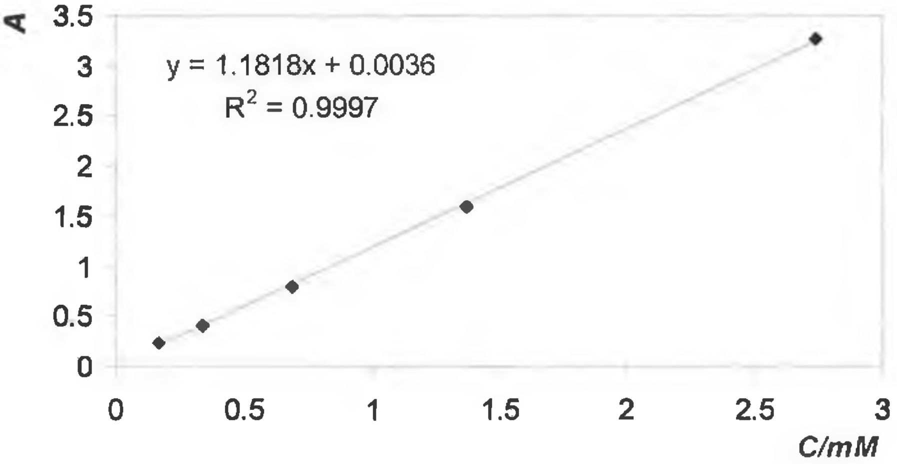

Figure 2.14. Calculation of the extinction coefficient for CoTpySH in acetonitrile for the MLCT at 510 nm.

From the slope of the linear regression the extinction coefficient for the MLCT at 510 nm was calculated to be $1.18 \pm 0.05 \times 10^3 M^{-1} cm^{-1}$. .

2.5.1 Solid state Raman spectroscopy

The preparation of the solid film involved the dissolution of the complex in spectrophotometric acetonitrile at 0.5mM, which was then drop-cast on a platinum surface and allowed to evaporate under argon. The exciting line was 514nm from an argon-ion laser (0.050W) which is resonant with the MLCT optical transition.

Figure 2.15 shows the Raman spectrum obtained for CoTpySH together with the Raman for CoTpy for comparison and assignment of the peaks. Table 2.6 summarises the assignments of the bands.

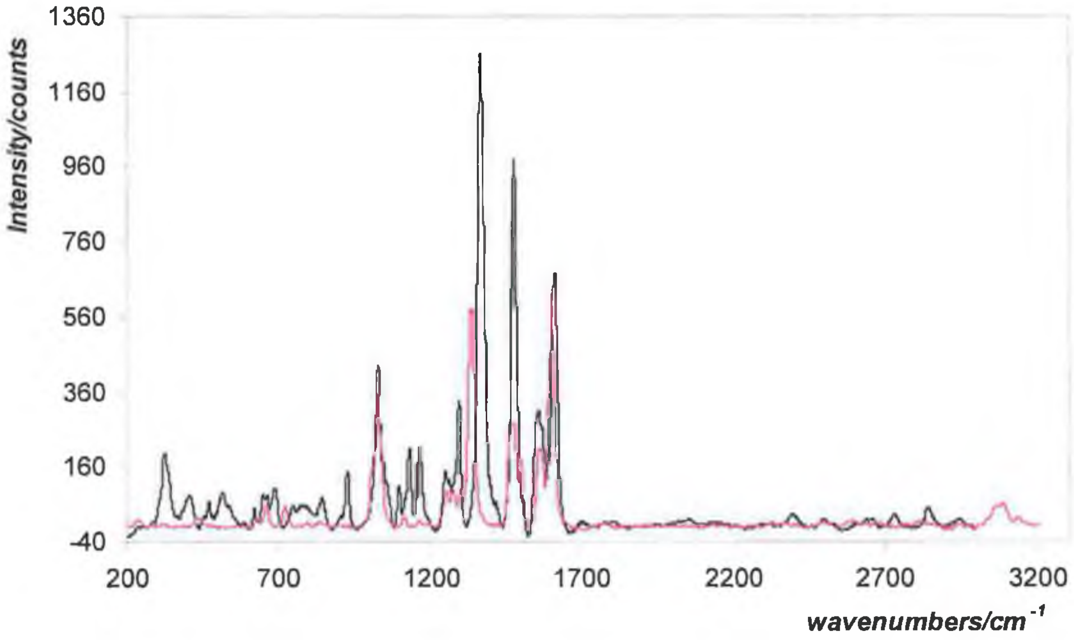

Figure 2.15 Raman spectra (514.5 nm excitation) of a drop cast film of CoTpySH (black line) on a platinum electrode and CoTpy (purple line) on a glass slide

Table 2.7. Assignments for CoTpySH drop cast on a platinum electrode

Wavenumbers/cm^{-1}	***Assignments***
520	Benzene ring mode
640-677	νCS
923	C-SH bending
846	uncertain
1024	βCH terpy mode
1095,1129,1163	Phenyl
1247	CH_2 wagging
1291	CH_2 wagging
1363	Centre py ring mode
1474	Outer py ring mode
1609	Outer py ring mode
2839	νCH_2 aliphatic
2954	νCH_2

It can be seen that no presence of disulfide is detected and that the band at 923cm^{-1}[14] which is completely absent from the CoTpy spectrum suggests the existence of thiols moieties. Moreover, the peaks at 640 and 677 are representative of CS stretching modes. The CH_2 presence is confirmed by the peaks at 2839 and 2954 cm^{-1} and by the wagging modes at 1247 and 1291 cm^{-1}[15, 16]. The presence of the phenyl moiety is confirmed by the peaks between 1095 and 1163cm^{-1} and the ring mode at 520cm^{-1}. Finally, the terpyridine modes are detected at 1024, 1363, 1474 and 1609cm^{-1}. [17, 18, 19] However, compared to the modes of CoTpy they are shifted towards higher energy, probably due to the substitution on the centre pyridine and have different relative intensities. This difference in intensity could be explained by assuming that for the drop cast film on the platinum electrode SERS effect is occurring, affecting the band intensity. Moreover, since both molecules are excited by the same laser line and have similar UV spectra resonance Raman effect is expected to contribute in the same way.

2.5.2 Solution phase electrochemistry

Solution phase electrochemistry experiments were performed for a family of cobalt terpyridine complexes with a general formula $Co(tpy\text{-}R)_2(PF_6)_2$, R=H, pyridyl group or terpy-phenyl-CH_2-SH moiety in order to assign redox processes. The formal potentials and diffusion coefficients were also determined.

Figure 2.16 shows the CV for the Co^{2+}/Co^{3+} redox process for CoTpySH in acetonitrile in the range of the metal based redox processes.

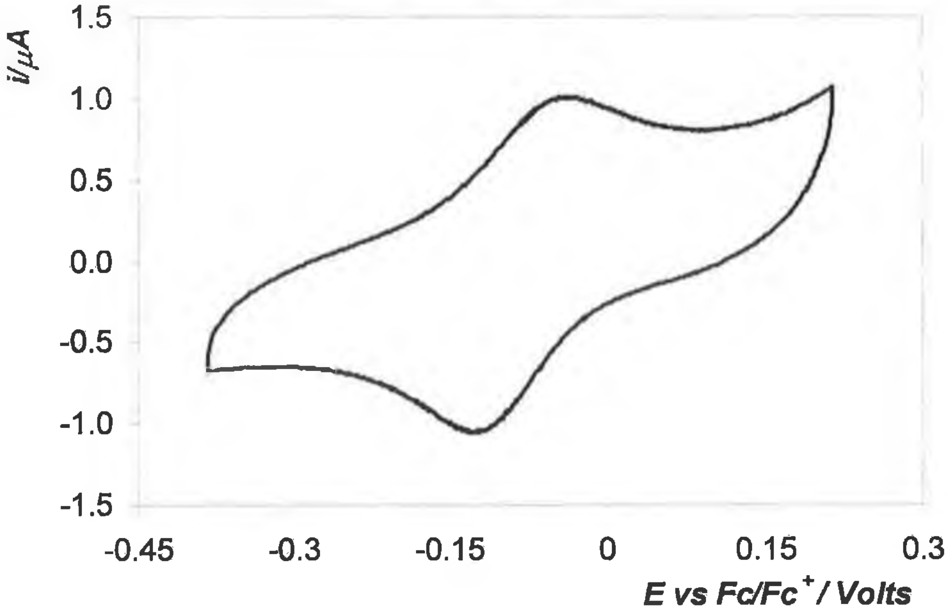

Figure 2.16. Solution phase electrochemistry of CoTpySH in 0.1 M TBABF$_4$ in acetonitrile. Starting potential: OCP, -0.2V. Scan rate: 0.1Vs^{-1}. Reference electrode: Ag/Ag$^+$ calibrated vs. Fc/Fc$^+$. Counter electrode: platinum wire.

It can be seen that a one-electron redox process is observed at –0.081±0.005 V, corresponding to the Co^{2+}/Co^{3+} couple. The peak to peak separation, ΔE_p, is 0.094 V which is somewhat larger than the value 0.057 V expected for a fully reversible single electron transfer process under semi-infinite linear diffusion control. However, ΔE_p and the peak shape do not depend on the scan rate, v, for $0.05 \leq v \leq 5$ Vs^{-1} and a plot of ln i_p *vs.* ln v is linear with a slope indistinguishable from the theoretical value of 0.5. These observations are consistent with a reversible electrochemical reaction involving the $Co^{2+/3+}$ couple.

Diffusion coefficients

Diffusion coefficients for the oxidised and reduced forms of the metal complex were also determined which will be used in the following chapter when the adsorption dynamics of the molecule on the electrode surface will be discussed.

Equation 1.36 describes the relation between the peak current of a species in solution and the square root of the scan rate under planar diffusion conditions. A plot of ip *versus* $v^{1/2}$ has a slope proportional to $C_iD_i^{1/2}$, where D_i is the diffusion coefficient in cm^2s^{-1} of the *i* species and C_i is its bulk concentration in mol cm^{-3}. Equation 1.36 was coupled with steady-state experiments, that were performed using Pt microelectrodes (d=25μm). Equation 1.32 shows that the steady-state current is proportional to the product D_iC_i. Therefore, the ratio between the two quantities D_iC, calculated from the steady-state experiments and $C_iD_i^{1/2}$, calculated from planar diffusion conditions, gives the square root of the diffusion coefficient of the species, $D_i^{1/2}$ as shown below:

$$\frac{D_iC_i}{D_i^{1/2}C_i} \tag{2.8}$$

The values found are listed in the summarising Table 2.7 and they match with literature for related compounds in acetonitrile solutions.[20, 21]

Table 2.8. Electrochemical parameters for CoTpySH dissolved in acetonitrile at room temperature

$E^{\circ\prime}/V$	$\Delta E_p/V$	$D_{Co^{2+/3+}}$ $/cm^2s^{-1}$	$D_{Co^{3+/2+}}$ $/cm^2s^{-1}$
-0.081	0.094	$1.9\pm0.2\times10^{-6}$	$1.1\pm0.4\times10^{-6}$

The values for the diffusion coefficients of the oxidised and reduced form of the redox couple $Co^{2+/3+}$ show that the reduced species is slightly faster than the oxidised form. This difference in the diffusion rate through the bulk could be explained by taking into account solvation phenomena. Those are expected to be stronger for the oxidised form which more likely attracts more solvent molecules than the reduced form. Eventually, the oxidised form has a bigger size than the reduced form and a slower diffusion.

2.6 Synthesis of CoTpybip

Synthesis of [Co(biptpy)$_2$](NO$_3$)$_2$

Biphenyl-2,2':6',2''-terpyridine, biptpy, (150 mg, 0.39 mmol) and cobalt(II) acetate (50.4 mg, 0.20 mmol) were heated to reflux in methanol (113 cm^3) for 15h. The reaction mixture was cooled and a methanolic solution of ammonium hexafluorophosphate added. The resulting precipitate was filtered, dissolved in dry acetone (28 cm^3) and a solution of tetrabutylammonium nitrate (200 mg) in dry acetone (2 cm^3) added to produce a red precipitate which was filtered and washed with diethyl ether to yield [Co(biptpy)$_2$](NO$_3$)$_2$ (139 mg, 73 %) as a dark red solid.

m/z (ES+): 829.2 $[M-NO_3]^+$, 414.6 $[M-2NO_3]^{2+}$.

ELEMENTAL ANALYSIS: Found: C, 68.2; H, 3.9; N, 11.6. C54H38N8O6Co requires C, 68.0; H, 3.9; N, 11.8%).

UV-VIS SPECTROPHOTOMETRY

In the UV region bands below 350nm are assigned to the intra-ligand π–π* transitions and a metal to ligand charge transfer band is observed at λ_{max} of 517nm, as shown in Figure 2.17.

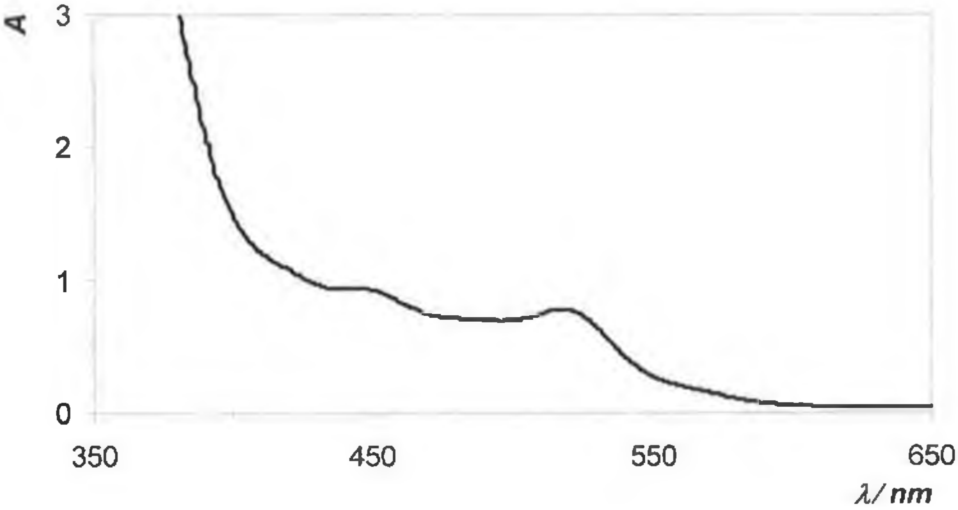

Figure 2.17 Absorption spectra for CoTpybip in acetonitrile at 244μM

From the slope of the linear regression the extinction coefficient for the MLCT at 517 nm is $3.2\times10^3 M^{-1}cm^{-1}$ and for the peak at 444 nm is $3.8\times10^3 M^{-1}cm^{-1}$.

2.6.1 Solid state Raman spectroscopy

The Raman spectroscopy was run on a solid sample on a glass slide. The exciting line was 514nm of 0.050W from an argon-ion laser.

Figure 2.18 shows the Raman spectrum obtained for CobipTpy together with the Raman for CoTpy for comparison and assignment of the peaks. Table 2.9 summarises the assignments of the bands.

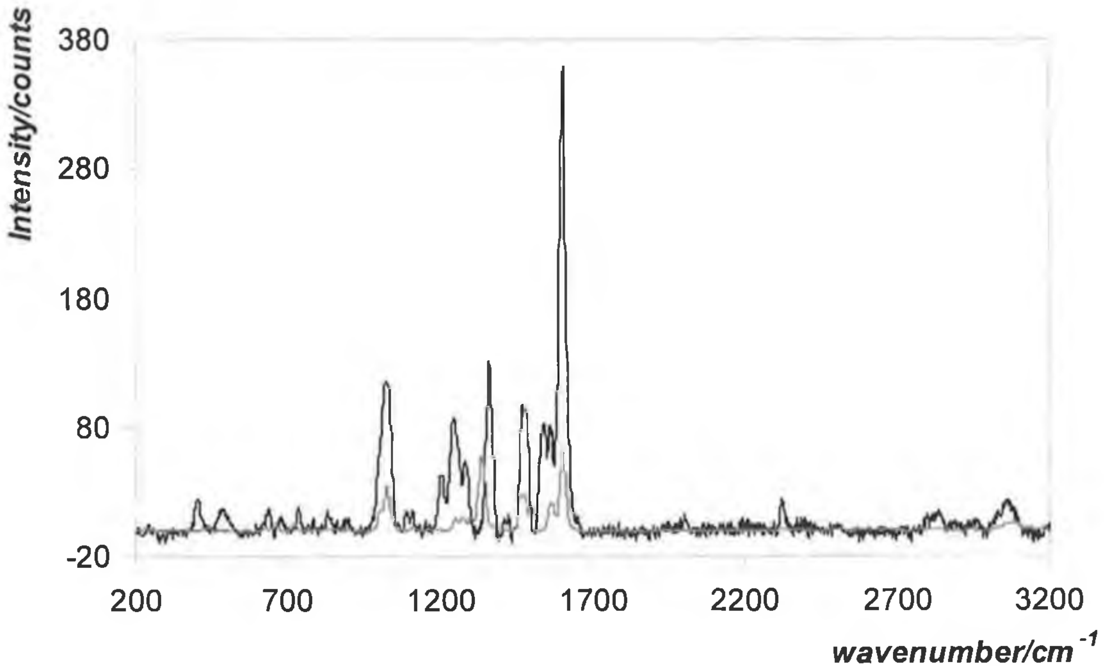

Figure 2.18. Raman spectra (514.5 nm excitation) of solid CoTpybip (black line) and CoTpy (purple line) on a glass slide.

Table 2.9 Assignments for CobipTpy solid powder.

Wavenumbers/cm^{-1}	*Assignments*
1028	βCH terpy mode
1206, 1242, 1277	Biphenyl modes
1357	Centre py ring mode
1471	Outer py ring mode
1602	Outer py ring mode

The modes relative to the terpyridine (1357, 1471 and 1602 cm^{-1}) are visible with a different relative intensity compared to CoTpy. In particular the mode at 1357cm^{-1} is red shifted, probably due to the substitution in 4 position of the central pyridine. The modes between 1206 and 1277 cm^{-1} are likely to be due to the biphenyl substituent[22] and they are completely absent on the CoTpy spectrum.

2.7 *Synthesis of mono-6-deoxy-6-(mercaptopentamethylene)thio-β-cyclodextrin (β-CD-SH)*

The synthetic procedure was performed by Dr. Andrea McNally, School of Chemical Sciences, DCU and kindly provided, following a procedure published by Nelles et al.[23].

The yield and molecular weight are 57% and $C_{47}H_{80}O_{34}S_2$ MW = 1252 g/mol, respectively.

The structures of unmodified beta-cyclodextrinsis are shown in Figure 2.19.

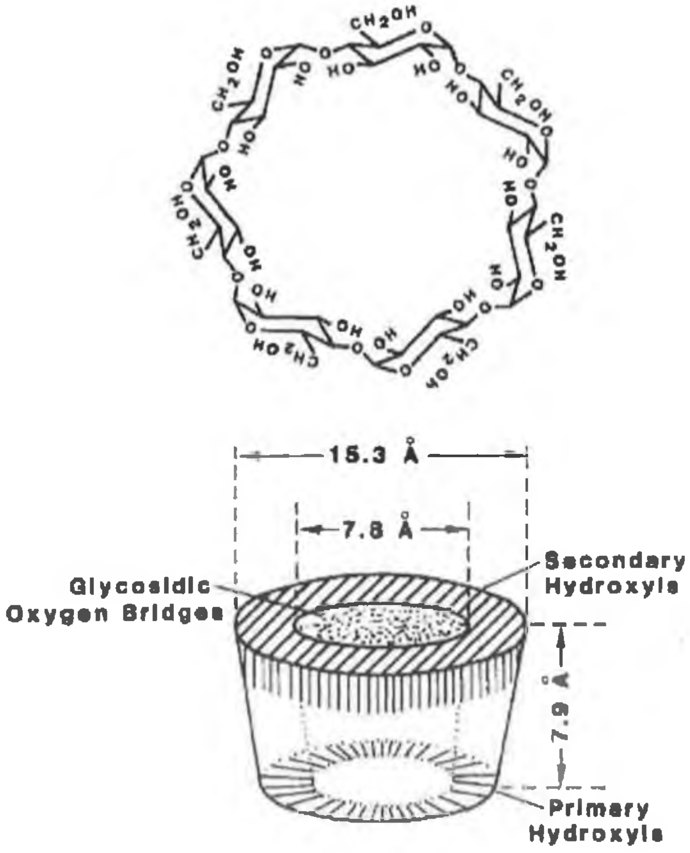

Figure 2.19 Molecular structure and molecular dimension of unmodified beta-cyclodextrins

The modification of the b-CD was conducted on the primary hydroxyls ring and Figure 2.20 show the final structure of the molecule used in the present work:

Figure 2.20. Molecular structure of mono-6-deoxy-6-(mercaptopentamethylene)thio-β-cyclodextrin (β-CD-SH)

ES-MS: Molecular ion peak at m/z = 1257 ([M^+ +H]).

^{1}H-NMR (400 MHz, DMSO) δ $OH_{Glu-2+3}$ 5.6 – 6.0 ppm (m, 14H's), OH_{Glu-6} 4.708 – 4.475 ppm (m, 7H's), H_{Glu-1} 4.827 ppm (m, 7H's), $H_{pentanethiol}$ 1.7 – 1.2 ppm (m, 4H's)

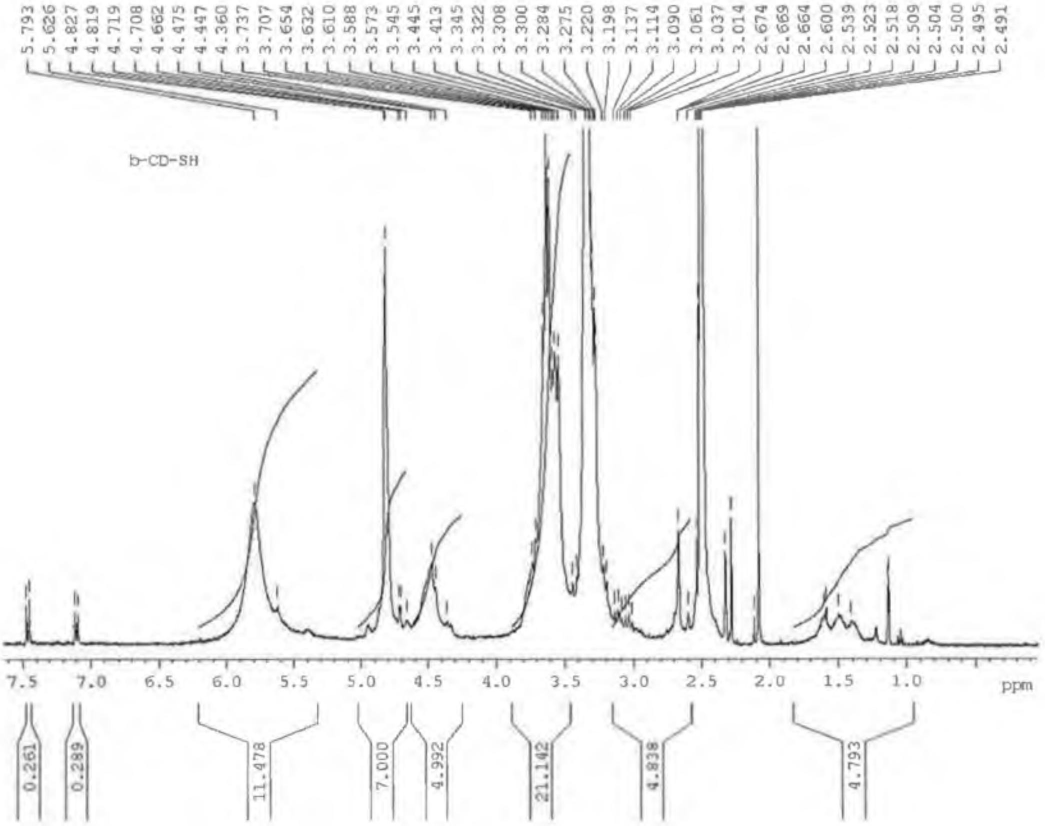

Figure 2.21 ^{1}H-NMR spectrum of β-CD-SH in d_6-DMSO

The spectrum below 3 ppm shows resonances due to the $-CH_2$ and -SH protons of the pentanethiol substituent. This is somewhat obscured by the d_8-DMSO peak at 2.50 ppm. Small peaks are visible at 7.49 and 7.13 ppm, correspond to the –OTs leaving group present as intermediate in the synthetic procedure. Integration of these peaks shows that the –OTs accounts for only 2.06 % of the β-CD-SH.

2.7.1 Solid state Raman spectroscopy

The complex was used as powder and deposited on a silica wafer and then scanned. The excitation line was 632nm which gave the best spectrum. The thiolated modified cyclodextrin is compared in Figure 2.22 to the unmodified β-CD. The parameters used for the acquisition are reported in the figure legend and the assignments summarised in Table 2.10 [24, 25]

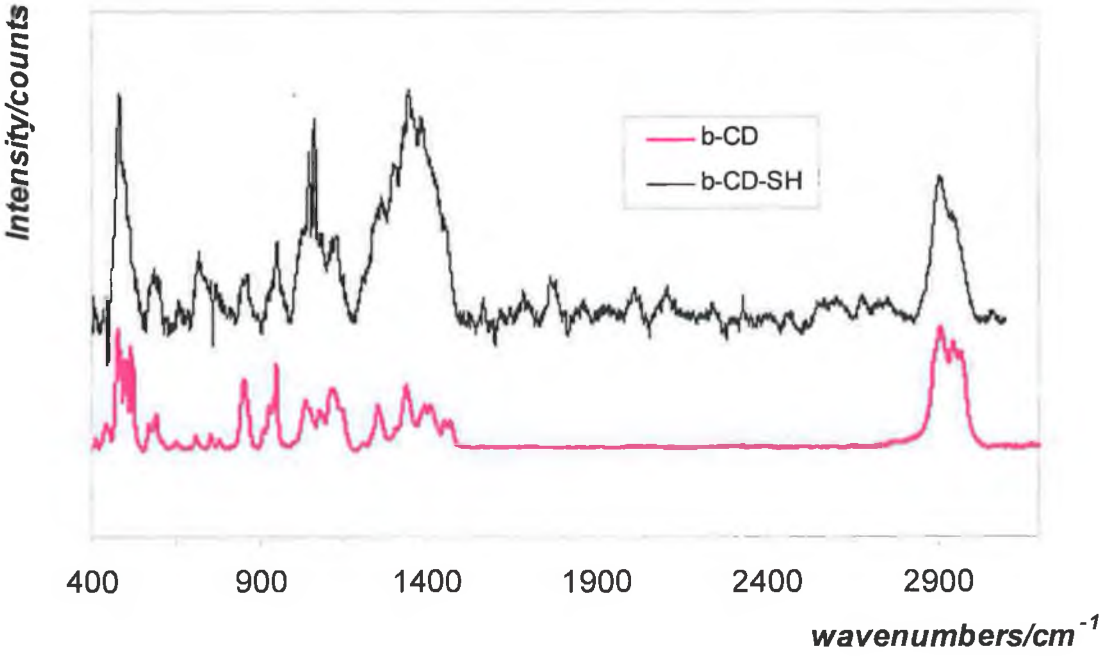

Figure 2.22 Raman spectra (632 nm excitation) of a solid sample of β-CD-SH (black line) and β-CD (purple line) on a silicon wafer. Accumulation parameters : 10s for 40 times . Hole aperture: 300μm, grating: 1800.

Table 2.10. Assignments for β-CD-SH solid powder

Wavenumbers/cm^{-1}	***Assignments***
2929-2912 2929	νCH_2 asymmetric for n-alkanes νOH asymmetric for CD
2861-2849	νCH_2 symmetric n-alkanes
1175-1310	CH_2 twist and rock n-alkanes
1230-1440	Combinations of CH stretching, C-OH deformation and CH_2 deformation modes for carbohydrates
1000-1200	νC-OH and deformation modes
950-1150	νCC n-alkanes
Below 1200	Skeletal and torsional ring modes

The SH modes (stretching, 2590-2560, thiols) and C-S modes (stretching, 740-585, alkyl sulfide) were not detectable[26 27]. However, between 510-525 cm^{-1} the νSS could be covered by the cyclodextrin modes.

Conclusions

The protocol followed for the construction of the microelectrodes proved to be reproducible and effective. The cell time constants for those microelectrodes were successfully measured and exhibited short *RC* constants, giving the possibility of measuring electron transfer rate constants on the microsecond timescale.

The synthesis and characterisation of cobalt terpyridine complexes for self-assembly and inclusion reaction and of thiolated modified cyclodextrins were presented and discussed. The purity of the compounds was confirmed together with the presence of moieties able to self-assemble or to show binding ability with a range of techniques, including solution phase electrochemistry, Raman and UV spectroscopies, HNMR, elemental analysis ES-MS. In particular Raman spectroscopy will be useful as reference for the interpretation and confirmation of the immobilisation of the molecules on the electrode surfaces.

References

1 Maskus M., Abruna H. D., *Langmuir*, **1996**, 12, 4455

2 Maskus M., Abruna H. D., *Abstract of Paper of Am. Chem. Soc.*, **1995**, 210, 352

3 Forster R.J., Chem,. *Soc. Rev.*, **1994**, 289

4 Pletcher D., *Microelectrodes: Theory and Applications*, Eds. Montenegro M. I., Querios, M.A., Daschbach J. L., Kluwer Academic Publishers, **1991**

5 Andrieux C. P., Hapiot P., Saveant J.-M., *Chem. Rev.*, **1990**, 90, 723

6 Newman J., *J. Electrochem. Soc.*, **1970**, 117, 198

7 Xu C., PhD Thesis, University of Illinois at Urbana-Champaign, **1992**

8 Trasatti S., Petrii O. A., *J. Electroanal. Chem.*, **1992**, 327, 353

9 Bard A.J., Faulkner L.R., *Electrochemical methods: Fundamentals and applications*, Second edition, Wiley **2001**.

10 El-Deab M., Sotomura T., Ohsaka T., *J. Electrochem. Soc.*, **2005**, 152, c1

11

12 R. J. Forster, P. J. Loughman, E. Figgemeier, A. C. Lees, J. Hjelm and J. G. Vos, *Langmuir*, **2000**, 16, 7871

13 Juris A., Balzani V., Barigeletti F., Campagna S. Belser P., von Zelewsky A., *Coord. Chem., Rev.*, **1988**, 84, 85

14 Szafranski C.A., Tanner W., Laibinis P.E., Garrell R.L., *Langmuir*, **1998**, 14, 3570

15 Murty K.V.G.K., Venkataramanan M., Pradeep T., *Langmuir*, **1998**, 14, 5446

16 Sant'Ana A.C., Alves W.A., Santos R.H.A., Ferreira A.m.D., Temperini M.L.A., *Polyhedron*, **2003**, 22, 167-1682

17 Zakeeruddin S.M., Nazeerudin M. K., Pechy P., Rotzinger F. P., Humphrybaker R., KalyanasundamramK., Gratzel M., Shklover V., Haibach T., *Inorg. Chem.*, **1997**, 36, 5937

18 Schneider S., Brehm G., Prenzel C. J., Jager W., Silva M. I., Burrows H. D., Formosinho S. T., *J. Raman Spec.*, **1996**, 27, 163

19 Hugot Le-Goff, A., Joiret S., Falaras P., *J. Phys. Chem. B*, **1999**, 103, 9569

20 Pyathi R., Murray R.W., *J. Am. Chem. Soc.*, **1996**, 118, 1743

21 Hjelm J., Handel R.W., Hagfeldt A., Constable E.C., Housecroft C.E., Forster R.J., *Electrochem. Comm.,* **2004**, 6, 193-200

22 Joo S-W., Chung T. D., Jang W. C., Gong M-s., Geum N., Kim K., *Langmuir*, **2002**, 18, 8813

23 M. Weisser, G. Nelles,. P. Wohlfart, G. Wenz, S. Mittler-Neher. *J. Phys Chem.*, **1996**, 100, 17893-17900

24 McNally A., *PhD Thesis* submitted at the Dublin Institute of Technology, **2005**, Chapter 2

25 Lin-Vien D., Colthup N. B., Fately W. G., Graselli J. G., *The Handbook of Infrared and Raman Characteristic Frequencies of Organic Molecules*, Boston Academic Press, **1991**

26 Hill W., Fallourd V., Klockow D., *J. Phys. Chem. B.*, **1999**, 103, 4707-4713

27 Maeda Y., Kitano H., *J. Phys. Chem.* **1995**, 99, 487-488

Chapter 3

Electron transfer across platinum/cobalt terpyridine thiol interface

Introduction

The study of charge transfer processes at molecular and nanoscale has increased significantly in recent years following the interest in nanotechnologies. Nanoscience concerns the study of objects and systems whose at least one dimension is 1-100 nm. The objects studied in this range of sizes are larger than atoms and small molecules, but smaller than the structures typically produced for use in microtechnologies. Optimizing the transfer of electrons over nanometre-scale distances is fundamental to the creation of novel nanoscale devices and to understanding naturally occurring redox processes.[1] The idea of using molecules as elements of computer circuits[2,3], electronic and optical switches,[4,5] sensors,[6] and for charge storage[7] has driven the creation of complex architectures and the identification of building blocks that promote fast electron transfer.[8,9] For example, to compete with near-term semiconducting circuits, approaches need to be developed for the construction of interfacial supramolecular assemblies whose properties, e.g., redox state, can be switched on the nanosecond timescale.

One of the most popular methods used to modify substrates, is the self-assembly of molecules on a surface to produce monolayers, which involves the 2-dimensional interactions between independent building blocks to create a superstructure.[10, 11]. Self-assembled monolayers are themselves nanostructures with a thickness of typically 1-3 nm[12]. They are well-suited for nanoscience because they are easy to prepare, they form on objects of all size and can be easily functionalised.

Among the systems that show self-assembly properties alkanethiols on gold are the most popular and studied, since gold resists oxidation and produces SAMs with low degree of defects[12, 13]. However, the molecules that are believed to have interesting electronic properties are not simple alkanethiols but contain redox sites. Organic molecules containing redox centres whose oxidation number and hence electronic structure can be changed reversibly, show promising functional behaviour when layered between electrical contacts[14], as shown in Figure 3.1 for a nanoparticle attached to gold via alkanethiol bispyridinium[4,15]

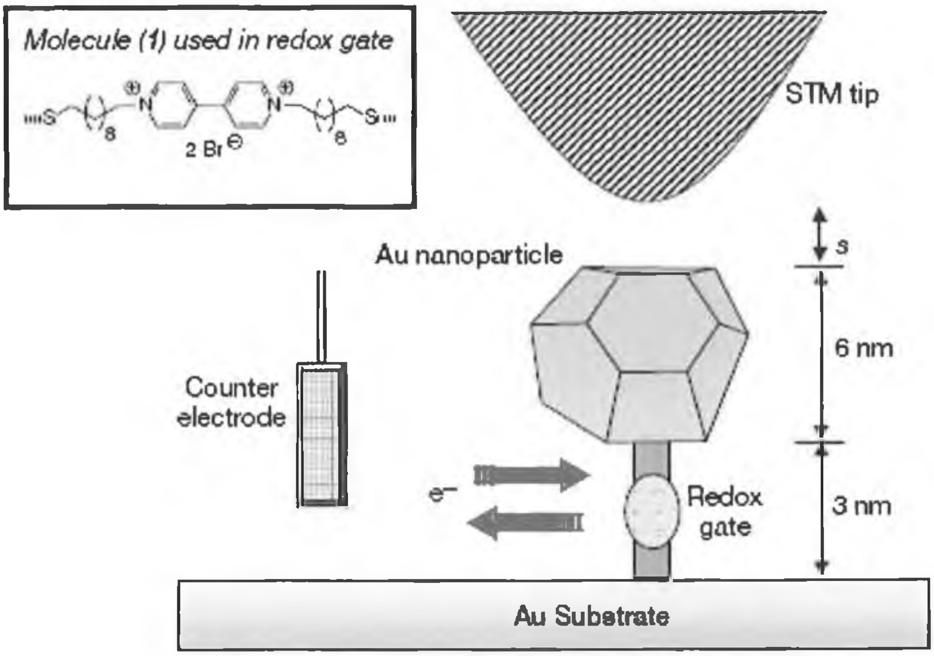

Figure 3.1. Schematic representation of the nanoscopic device. Adapted from reference 15

Among those switchable molecules, organometallic compounds[16], and in particular transition metal complexes with tailored ligands, are the most popular systems, since either the strength or the kinetics of the binding can be controlled and modified[17]. Moreover, the possibility of directing the surface structure at molecular level by carefully tuning the transition metal and ligand natures is probably the most interesting property.

Particular interest has been shown for self-assembled monolayers of transition metal polypyridine complexes. In fact, chelating ligands allow the construction of defined supramolecular architectures and posses an increased stability compared to other bindings, e.g. hydrogen bonding. However, many of the bridging ligands investigated involve flexible linkages to couple the redox centre and the electrode. Such tethers can compromise the collection of mechanistic information about the electron-transfer process since they introduce unnecessary conformational heterogeneity and enantiomers are often present. In contrast, functionalized terpyridine is an attractive approach to the creation of rigid or geometrically constrained linkers.[18] 2,2′:6′,2′′-terpyridine ligands (terpy) are among the heterocycles that have very high binding affinity for transition metal ions such Fe^{2+} and Co^{2+}. Complexation of two terpy ligands can lead to a metal complex which have octahedral coordination geometries and then produce molecules with a linear geometry that facilitates construction of multicomponent linear arrays and molecular wires.[19, 20].

Electrochemical investigations of redox active monolayers provide a powerful insight in the study at nanometre-scale of the effects that distance, chemical structure and composition have on the mechanism and the rate of the electron transfer.[21, 22, 23, 24, 25]. Therefore, cyclic voltammetry and chronoamperometry have been used to characterise the monolayer and its chemical properties.

In the following chapter, the spontaneous adsorption dynamics and interfacial properties of monolayers of $[Co(ttp\text{-}CH_2\text{-}SH)_2](PF_6)_2$, CoTpySH, will be discussed. The electrochemical response of these monolayers is well defined allowing the time dependence of the surface coverage to be monitored and then modelled. Because of their short length, of the order of 10Å, bridging ligands of this type might be expected to support rapid electron transfer across the electrode/monolayer interface.

3.1 Monolayer deposition and electrochemical characterisation

3.1.2 Experimental

Materials and Instrumentation

Cyclic voltammetry was performed using a CH Instrument Model 660 Electrochemical Workstation and a conventional three-electrode cell. Potentials are quoted with respect a home-made Ag/Ag$^+$ organic reference electrode, previously calibrated against ferrocene/ferrocenium redox couple. All experiments were performed at room temperature.

High speed chronoamperometry experiments were performed by using custom-built function two-electrode, generator-potentiostat with a rise time of less than 2 ns. The counter electrode was a Pt wire combined with a Ag/Ag$^+$ organic reference electrode.

The experiments were performed in anhydrous acetonitrile solutions (Sigma-Aldrich, 99.9%) containing oven dried TBABF$_4$ (Sigma-Aldrich electrochemical grade) as electrolyte. The solutions were deoxygenated with oxygen-free argon for 5 min and kept under an argon atmosphere during the experiments.

Monolayer assembly

Platinum microelectrodes of 50 and 12.5 μm radius were used for the electrochemistry. Two protocols were followed as to assemble the monolayer on the platinum polycrystalline microelectrodes, i.e. *ex-situ* and *in-situ*.

For *the ex-situ* immobilization, the deposition solutions were prepared by dissolving CoTpySH in acetonitrile at micromolar concentrations. The platinum microelectrodes were cleaned as described in Chapter 2, washed with milliQ water and then acetonitrile, dried under argon and placed in the deposition solutions overnight. Then, prior to any measurements, they were thoroughly rinsed with acetonitrile in order to wash away any unbound material.

In-situ experiments were performed by exposing the electrochemically cleaned electrodes to micromolar solutions of the complex in acetonitrile with $TBABF_4$ as electrolyte for a period of time longer than one hour. The assembly process was then monitored by cyclic voltammetry of the redox process of the metal centre. The scan rate was kept sufficiently high so the dissolved complex contributed a maximum of 5% to the overall current.

3.1.3 Results

3.1.3.1 In-situ deposition

Figure 3.2 shows the final CV obtained after 2h of immersion of a 50-μm radius platinum electrode in a 10 μM solution of the complex in acetonitrile. The supporting electrolyte is 0.1M $TBABF_4$ and the scan rate is 20 Vs^{-1}:

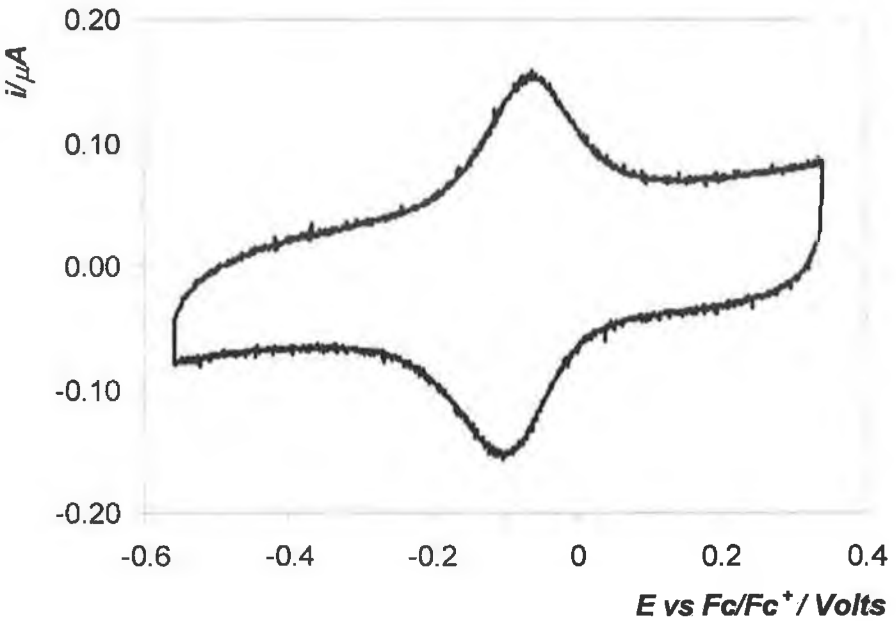

Figure 3.2. *In-situ* CV of the monolayer obtained by immersion of a 50 μm radius platinum electrode for 2h in a 10 μM solution of the complex in acetonitrile, 0.1M $TBABF_4$ as supporting electrolyte. Scan rate: 20 Vs^{-1}. Reference electrode: Ag/Ag^+ calibrated *versus* Fc/Fc^+ redox couple. Counter electrode: platinum wire.

A well defined voltammetric response is observed at E°' equal to –0.082±0.007 V which is assigned to the $Co^{2+/3+}$ redox process, based on the solution phase experiments shown in Chapter 2. The peak currents increase linearly with increasing scan rate, for both the cathodic and anodic waves, as expected for a surface confined species, as shown in Figure 3.3:

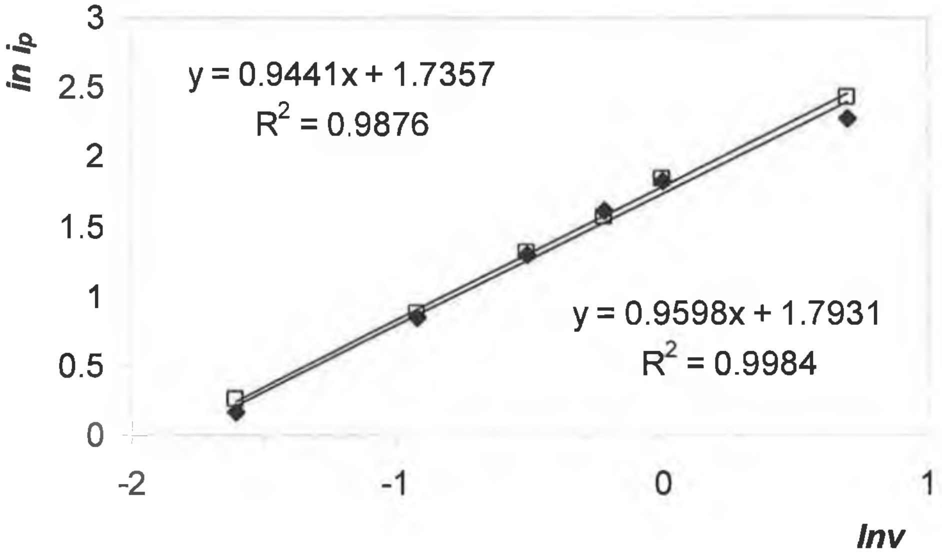

Figure 3.3. Scan rate dependence of the cathodic (black square, bottom regression line) and anodic (open squares, top regression line) peak currents for the $Co^{2+/3+}$ redox process, for the monolayer assembled on a platinum microelectrode, shown in Figure 3.1. The experiment is performed in a complex-free $TBABF_4$ acetonitrile solution. The y-axis display the absolute values of the current.

The peak to peak separation, ΔE_p, is 0.040±0.005 V at $20 Vs^{-1}$ and is invariable with increasing the scan rate up to $50\ Vs^{-1}$, suggesting that the non-zero separation between the potential peaks is not caused by slow heterogeneous electron transfer or ohmic drop. The ratio between the anodic and cathodic peak currents is approximately 1 for the range of scan rates considered.

The FWHM values are 0.135±0.005V and 0.145±0.005V, for the cathodic and anodic waves respectively, instead of the 0.0906 V expected for a single-electron redox process, suggesting the presence of some lateral repulsive interactions between adsorbates. All these considerations suggest that the redox process has a quasi-reversible character.

By integrating the charge under the voltammetric waves a surface coverage of 6.3×10^{-11} and 5.9×10^{-11} $molcm^{-2}$ for the anodic and cathodic peaks respectively, are obtained. Molecular modelling indicates that the projected area of the cobalt complex, adsorbed vertically on the surface, is of the order of 98 $Å^2$. Therefore, under these conditions the surface coverage corresponds to approximately 40% of a close packed monolayer. This maximum coverage is lower than that, $1.2\text{-}1.5 \times 10^{-10}$ $molcm^{-2}$, reported by Abruña for [Co(4′-(5-mercaptopentyl)-2,2′:6′,2″-terpyrindyl)] on gold.[18] However, in their complex, the five carbon alkyl chain attached to the sulphur atom, probably, plays a stabilizing role, leading to a more compact monolayer. The observation that a relatively dense monolayer is formed within 2 hours from a 10 μM solution of the complex is significant and suggests that the thiol moieties interact rapidly with the platinum surface.

In general, these data show that exposure of clean platinum microelectrodes to micromolar concentrations of CoTpySH in acetonitrile leads to the formation of a spontaneously adsorbed monolayer, which behaves quite ideally and in which the heterogeneous electron transfer is relatively fast.

3.1.3.2 Ex-situ deposition

Figure 3.4 shows the profile of the CVs for the *ex-situ* deposition protocol, after an overnight deposition of the cleaned platinum microelectrode in a micromolar solution of the complex in acetonitrile.

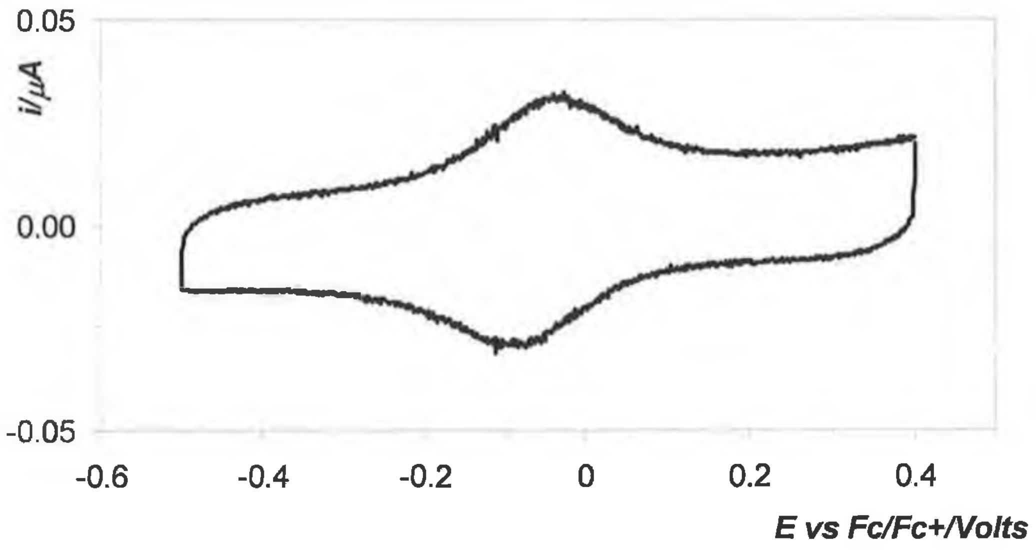

Figure 3.4. CV of the monolayer obtained by immersion of a 12.5 μm radius platinum electrode in a micromolar solution of the complex in acetonitrile for 12 hours. Electrolyte: 0.1M $TBABF_4$. Scan rate: 100 Vs^{-1}. Reference electrode: Ag/Ag^+ calibrated *versus* Fc/Fc^+ redox couple. Counter electrode: platinum wire.

A well defined voltammetric response is observed at E°′ -0.053±0.006 V, which is about 0.030V more positive with respect to the formal potential obtained for the *in-situ* deposition, shown in Figure 3.2. Therefore, after an overnight deposition, the monolayer structure changes by stabilizing its energy, since it results more difficult to oxidise the redox couple. This shifting of the potential peak was also observed during the monitoring of the adsorption for the *in-situ* deposition, as it will be discussed in the next sections. Again, linearity was found for the dependence of the peak currents with the increasing scan rate and the ratio between the cathodic and the anodic peaks was approximately 1 for the range of scan rates considered, as shown in Figure 3.5:

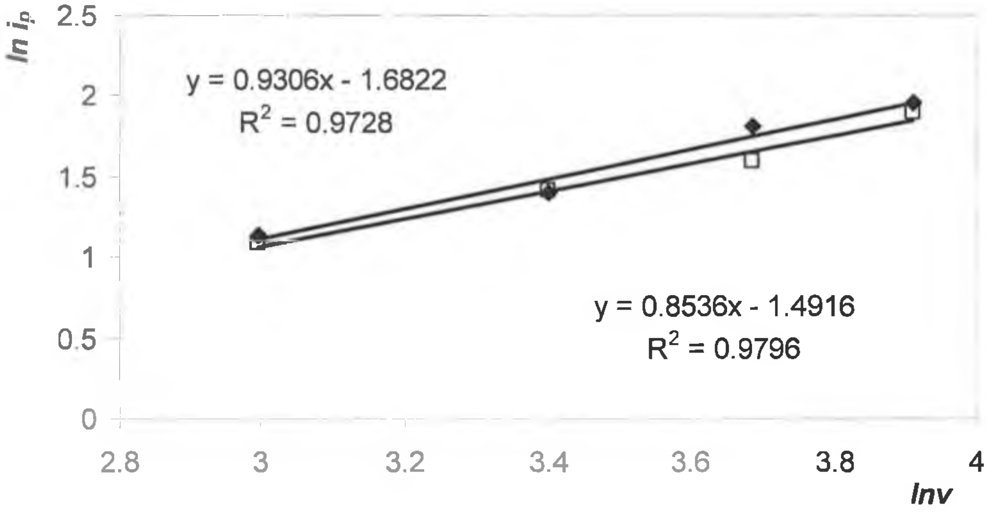

Figure 3.5. Scan rate dependence of the cathodic (black square, top regression line) and anodic (open squares, bottom regression line) peak currents for the $Co^{2+/3+}$ redox process, for the monolayer assembled on a platinum microelectrode following an *ex-situ* deposition. Electrolyte: 0.1M $TBABF_4$. Reference electrode: Ag/Ag^+ calibrated *versus* Fc/Fc^+ redox couple. Counter electrode: platinum wire

A peak to peak separation of 0.044±0.009 V was also determined, which is similar to that found for the *in-situ* protocol, and which did not change by increasing the scan rate up to 500 Vs^{-1} (*vide infra*). The FWHM values are 0.173±0.006V and 0.144±0.005V for the cathodic and anodic peaks, respectively. Therefore, the redox activity of the *ex-situ* deposited monolayer is also considered to be reversible.

However, the surface coverages calculated by integrating the area under the cathodic and the anodic peaks produced a smaller value for the *ex-situ* protocol compared to the *in-situ*, i.e. $3.0\pm0.5 \times 10^{-11}$ mol cm^{-2}. The surface coverage observed here is the same found by Constable and co-workers[26] for structurally similar $[M(terpy)(terpy\text{-}pyridine)]^{2+}$, M is Os or Ru.

Clearly no difference in the voltammetric shapes was observed for the two protocols in terms of ΔEp suggesting that similar electronic properties in terms of electron transfer were found. However, a higher value of FWHM for the cathodic wave was observed leading to the conclusion that stronger repulsive interactions among the molecules in their oxidation state were present for the *ex-situ* deposition. The major difference is the shifting of the formal potential.

A possible explanation relies on the microenvironmental effects that occur during the adsorption. If the adsorption follows a random growth model, shifts in the potential will be expected since, as the surface coverage increases the intermolecular separation will decrease and the molecules will interact with each other. Another contribution can come from the counter ion, in terms of bigger permeability of the *in-situ* assembled monolayer compared to the *ex-situ*. This hypothesis is supported by the increase in the lateral interactions for the *ex-situ* layer.

Another explanation of the difference in the formal potential of the monolayer adrobed either by the *in-situ* or the *ex-situ* protocols, relies on the presence, for the *in-situ* adsorbed monolayer, of molecules which experience physisorption.

Therefore, since those molecules can diffuse over the electrode surface they can show a formal potential closer to the solution phase value.

This explanation, also, takes into account the difference in surface coverages for the monolayer adsorbed by using the two different protocols. More likely the timescale of the experiments are fast enough to measure the electroactivity of those physisorbed molecules before they desorbe and diffuse over the electrode surface.

3.1.4 Desorption of the CoTpySH monolayer in acetonitrile

Desorption experiments were conducted to gain some insight into the structure of the final monolayer, by checking for the presence of multiple desorption peaks and their associated kinetics. The desorption experiment were run in anhydrous acetonitrile solutions containing 0.1M $TBABF_4$ after an overnight exposure of clean electrodes to micromolar solutions of the complex. Desorption of alkanethiols from platinum has not been studied as much as for gold surfaces. However, anhydrous acetonitrile solutions allows to broad the potential window and check a possible desorption of the molecule at very negative potentials together with the presence of the redox processes of the metal centre.

Figure 3.6 shows repetitive scans of a monolayer between 0.4 and -1.8V in 0.1 M $TBABF_4$ anhydrous acetonitrile solution at $2Vs^{-1}$. The electrolyte solution does not contain any dissolved complex.

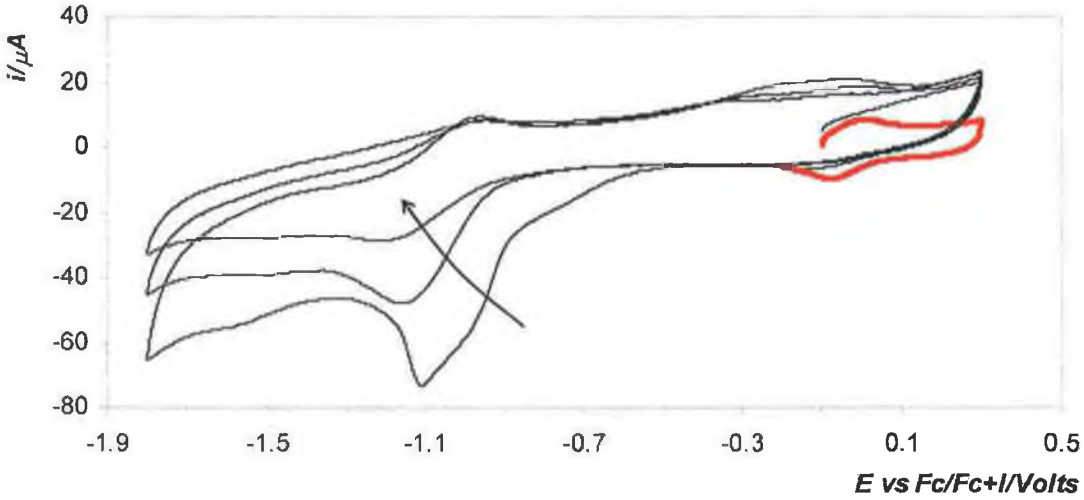

Figure 3.6. Desorption of a monolayer of CoTpySH immobilized on a platinum macroelectrode surface after overnight exposure to a micromolar solution of the molecules in acetonitrile. The electrolyte is 0.1M TBABF$_4$ in anhydrous acetonitrile. Scan rate: 2Vs^{-1}. Reference electrode: Ag/Ag$^+$ calibrated *versus* Fc/Fc$^+$ redox couple. Counter electrode: platinum wire. The red line highlight the oxidation reaction of the metal centre occurred during the first scan. The arrow indicates the time dependence of the peak.

The interpretation of the peaks is complicated by the possible presence of further redox processes, *i.e.* the metal centre reduction from Co^{2+} to Co^{1+}, at around -1.05V and the reductive processes of the terpyridine ligands at more negative values. Figure 3.7 shows how the addition of an anchor group, such as pyridine, to the terpyridine ligand shifts its reduction potentials to more positive values, i.e., it makes the redox process thermodynamically more facile. This phenomenon is likely a consequence of the conjugation and hence higher electron density introduced by the pyridine.

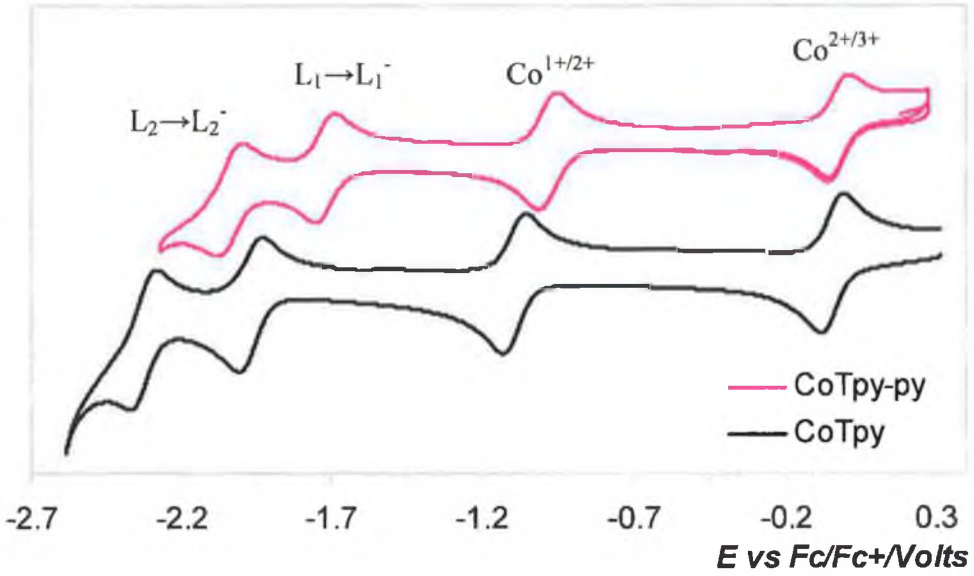

Figure 3.7 Solution phase electrochemistry of CoTpy (black line) and CoTpy-py (purple line) in 0.1M TBABF$_4$ anhydrous acetonitrile solution. Scan rate: 0.5Vs^{-1} starting at the OCP. The working electrode is a polycrystalline platinum macro electrode. Reference electrode: Ag/Ag$^+$ calibrated vs. Fc/Fc$^+$ redox couple. Counter electrode: platinum wire.

By comparing Figure 3.6 to 3.7 the following observations can be made. At first sight the two redox processes observed in Figure 3.6 can be assigned to the metal redox processes shown in Figure 3.6. However, in Figure 3.6 only the oxidation from Co^{2+} to Co^{3+} has ideal behaviour and it disappears after repetitively scanning of the monolayer at negative potentials, suggesting that desorption of the molecule occurs. Furthermore, the peak current of the redox process at -1.1V decreases and changes its shape over time, together with the relative reverse peak at -1.01 V. Moreover, comparing the first red scan in Figure 3.6 to the following ones, it is evident that the capacitive currents changed during the experiment, showing a variation of the double layer structure most likely due to the desorption of the molecule. Finally, by comparing the integrated areas under the peak at -0.83V and -1.1V in Figure 3.6, an order of magnitude difference is obtained, which suggests that baseline correction is needed or overlapping of several redox processes is present. In conclusions, it appears that desorption of the molecule occurs, probably from different energetic sites, producing a quite broad desorption wave.

Further evidence that the redox process at -1.1 V is not involving the cobalt reduction was obtained from solution phase experiment ran over a larger potential window than in Chapter 2, as shown in Figure 3.8.

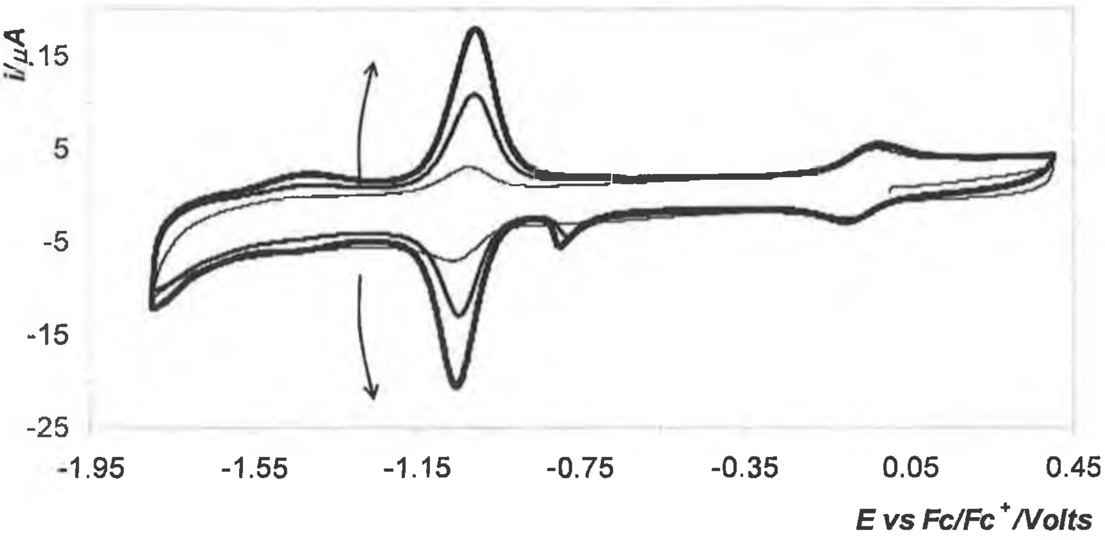

Figure 3.8. Solution phase electrochemistry in the metal and the thiol redox potentials range of CoTpySH in 0.1M $TBABF_4$ acetonitrile solution. Scan rate: $0.5Vs^{-1}$ starting from 0.03V (OCP). The working electrode is a polycrystalline platinum macro electrode. Reference electrode: Ag/Ag^+ calibrated *versus* Fc/Fc^+ redox couple. Counter electrode: platinum wire. The arrows indicate the time dependence of the peak.

In Figure 3.8 the first, the intermediate and the last scans are shown, as to illustrate the changes during the experiment. It is clear that, by continuously scanning, the oxidation of the cobalt metal centre does not change its properties. However, a shift in potential for the formal potential to -0.071V and an increase of about 0.040V in the peak separation is observed compared to the solution phase values discussed in Chapter 2. In particular, a shift to more positive potential was observed for the oxidation of Co^{2+} to Co^{3+}, while the reverse reduction reaction of the probe did not show any particular change. This suggests that some hindrance to the electron transfer involving the oxidation of the molecule is introduced.

By scanning at more negative potentials, the CV profile changed during the experiment. First of all, an increasing pre-peak was observed at -0.75 V, shifting about 0.050V during the experiment. Moreover, the peak currents at -1.05 V become larger and the peak shape changed into a reversible surface confined profile. In fact, a FWHM of 0.117±0.005V and of 0.107±0.005V for the anodic and cathodic wave respectively were obtained, together with ΔEp of 0.035±0.007V. This phenomenon cannot be explained if the redox process at -1.05V is assigned to the cobalt reduction. On the contrary, if one assumes that adsorption of the molecule through the sulphur atom is occurring, the wave can be explained as the reductive desorption and consequent oxidative re-adsorption of the thiolated molecules. This consideration is further confirmed by the areas under the peaks. In each scan the sum of cathodic areas calculated under the peak at -0.75 and -1.045V were equal to the anodic area at -1.010V, suggesting that the pre-peak is indeed involving the reduction of the molecule. Therefore, it is likely that what is observed at -1.05V involves the immobilization of the molecule on the electrode surface, probably by creating multilayers, which produce a blocking layer for the oxidation of the cobalt in solution.

3.2 SERS of the monolayer on platinum

Since the discovery of SERS its applications have been restricted to very few metals such as Ag, Au, Cu that can exhibit an enhancement of the Raman signal up to 10^6 times. However, it is extremely interesting to broad the range of metals that can be used for SERS, primary platinum, which is utilised in many technological processes, due to its catalytic activity and wide polarizable potential window. Unfortunately, it has been shown for decades that rough and smooth platinum surfaces produced very low intense Raman signals, which was often overlapped with bulk Raman bands[27]. The advent of confocal Raman microscopes helped the weak Raman bands of adsorbates on platinum to be improved[28]. Moreover, new roughening techniques showed that an enhancement of the bands intensity could be reached for platinum surfaces and that the signal intensity was influenced by the pre-treatment of the surface itself[29].

3.2.1 Experimental

Further evidence of the presence of the CoTpySH on the platinum surfaces was found by performing *ex-situ* and *in-situ* SERS of the monolayer on platinum polycrystalline macroelectrode. The platinum electrodes were roughened by applying a variation of the protocol proposed by Tian[29 30]. Platinum polycrystalline macroelectrodes (1mm radius) were first cleaned as described in Chapter 2, and then subjected to multi-potential step experiments in 0.5M H_2SO_4. The potential was first stepped for 10s in a positive direction, up to 1.4V and then stepped in a negative direction, down to -0.25V for 2s, for 5-10 minutes. A roughness factor of 5 was then measured. The roughened platinum polycrystalline macroelectrodes were then rinsed with milliQ water, acetonitrile, dried under argon and placed in the micromolar deposition solution of the complex overnight. Prior any measurements the electrodes were rinsed with acetonitrile and dried under argon.

Raman spectra were acquired by using a Horiba Jobin Yvon HR800UV. The excitation was 514nm in order to have resonance effect on the Raman signal together with a weak surface enhancement contribution.

3.2.2 Ex-situ SERS of CoTpySH on roughened platinum electrodes

Figure 3.9 shows the Raman spectrum obtained for a monolayer on a roughened platinum macroelectrode at 514nm together with the Raman spectrum of the solid for comparison.

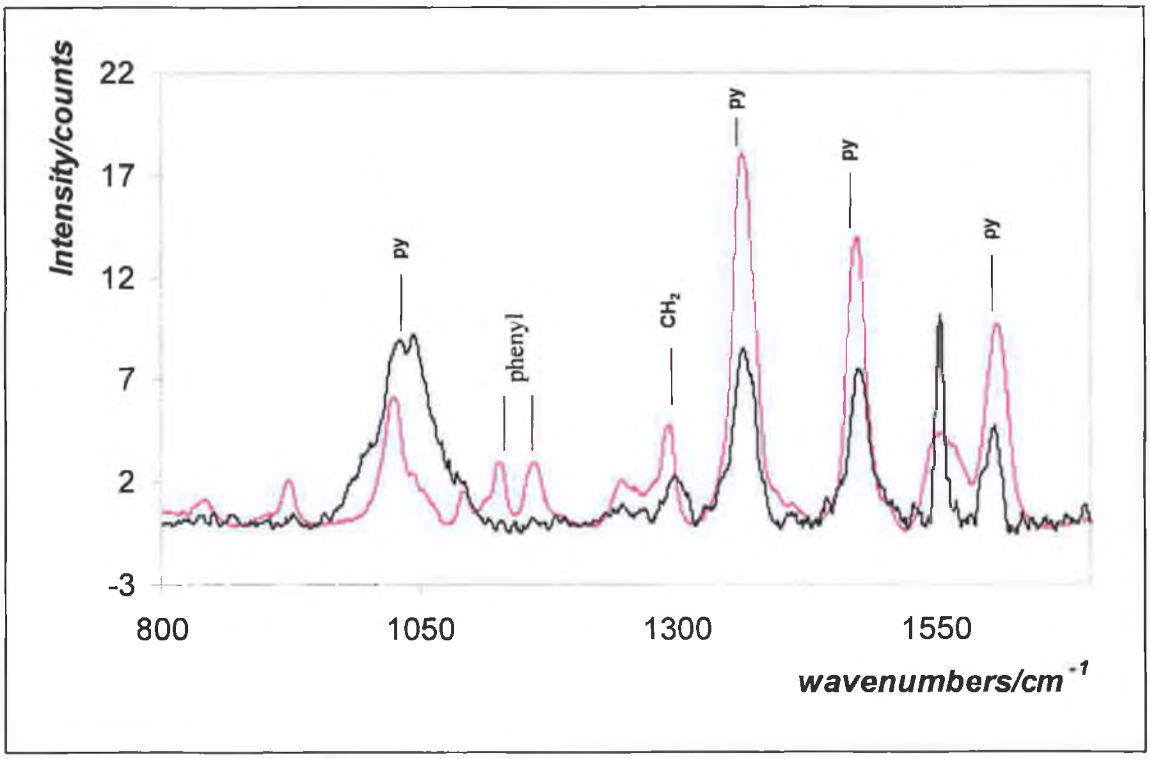

Figure 3.9. *Ex-situ* Raman spectra of CoTpySH monolayer on roughened platinum macroelectrode (1mm radius, black line) and solid powder (purple line) at 514nm. Accumulation: 10s×20times, Hole: 500 μm. Grating: 1800

The presence of the monolayer is confirmed by the peaks in the pyridine ring breathing region. The phenyl peaks between 1100 and 1200 cm^{-1} are not visible. In contrast, the signals due to the terpyridine ligands, enhanced by resonance, are detected and they maintain their relative intensities. Moreover, the peaks at 1247 and 1291 cm^{-1} assigned to the CH_2 wagging are visible and blue shifted in the monolayer spectrum, probably due to the fact that they are close to the surface. In general, these observation are consistent with the molecule adsorbed on the platinum through the sulphur atom even though it is not possible to obtain exact information on the orientation of the molecule. More likely, the disappearance of the phenyl modes suggest that the molecule stretches out from the surface instead of lying on it.

3.3 Adsorption dynamics

Introduction

Monolayer formation involves a small number of fundamental processes, i.e., mass transport to the electrode surface by diffusion of the adsorbate through solution and binding of the adsorbate to the electrode surface. However, the overall sequence may be complicated by additional factors such as reversible binding, surface diffusion, adsorbate reorientation and desorption proceeding in parallel with adsorption[31]. For example, for alkanethiol based monolayers it is well known that formation of the gold- or platinum-thiol bond is essentially irreversible.[32] However, initial adsorption is a rapid process and there is significant mobility of the adsorbates on the surface. At longer times, defects anneal and a more stable, less mobile structure is created.[33,34] By monitoring the time dependence of the surface coverage and fitting these experimental data to appropriate models, an insight into the mechanism of monolayer formation and the relative importance of adsorption kinetics, surface diffusion, and mass transport can be obtained.

Analysis of the surface coverage *versus* time profiles can be used to measure rate constants and obtain a more detailed insight into the monolayer formation mechanism. The surface coverage versus time data obtained at bulk concentrations of CoTpySH ranging from 2.5 to 10 μM have been analysed with a wide range of models (*vide infra*). In each case, the sum square of the residuals between the experimental surface coverages and those predicted by the model were minimised using a gradient search algorithm. A number of models, have been considered in an attempt to model the dynamics of adsorption, leading to a final surface coverage of CoTpySH on platinum: pure diffusion control [35], pure irreversible kinetic control involving a single process [36], mixed diffusion/kinetic control [37], parallel kinetically controlled pathways and a two step mechanism.[38].

A key advantage of electroactive adsorbates is that the time dependent surface coverage can be conveniently monitored using cyclic voltammetry. In particular, the redox activity of the metal centre $Co^{2+/3+}$ was followed. Figure 3.10 shows cyclic voltammograms taken at defined time intervals after a clean platinum microelectrode (50 µm radius) was placed in a 10 µM solution of CoTpySH in acetonitrile, 0.1M $TBABF_4$ at $20Vs^{-1}$.

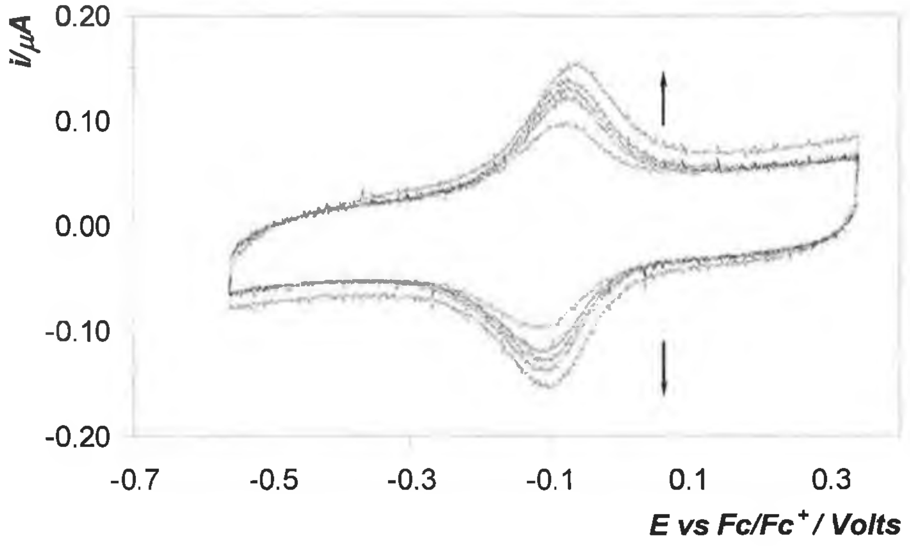

Figure 3.10. Dependence of the cyclic voltammetry response of a 50 µm radius platinum microelectrode following an *in-situ* deposition of a CoTpySH monolayer for 1, 5, 10, 20, 150 minutes. The arrows indicate the increasing time. The bulk concentration of the complex is 10 µM, 0.1M $TBABF_4$. Scan rate: $20Vs^{-1}$. Reference electrode: Ag/Ag^+ calibrated *versus* Fc/Fc^+ redox couple. Counter electrode: platinum wire

These voltammograms clearly show the progressive growth of an electroactive film as evidenced by the growth of the peak corresponding to the Co^{2+}/Co^{3+} redox process. The peak potential for the oxidation reaction, E_{pa}, shifts in a positive potential direction, indicating that it becomes thermodynamically more difficult to oxidize the adsorbate with increasing surface coverage. This behaviour most likely arise because of microenvironmental effects, e.g., a decreasing local dielectric constant as the film forms. Significantly, the peak shape, e.g., the FWHM, does not change during monolayer assembly suggesting that lateral interactions do not change as the surface coverage increases. This behaviour would be expected if the monolayer assembly proceeds by a random growth mechanism as previously found for the *ex-situ* assembled monolayer. It is also noticeable that the interfacial capacitance does not change significantly with increasing surface coverage.

In Figure 3.11 the variation of the surface coverage with time where the bulk concentration is 2.5, 5 and 10 μM in 0.1M $TBABF_4$ acetonitrile solutions at the same scan rates is shown.

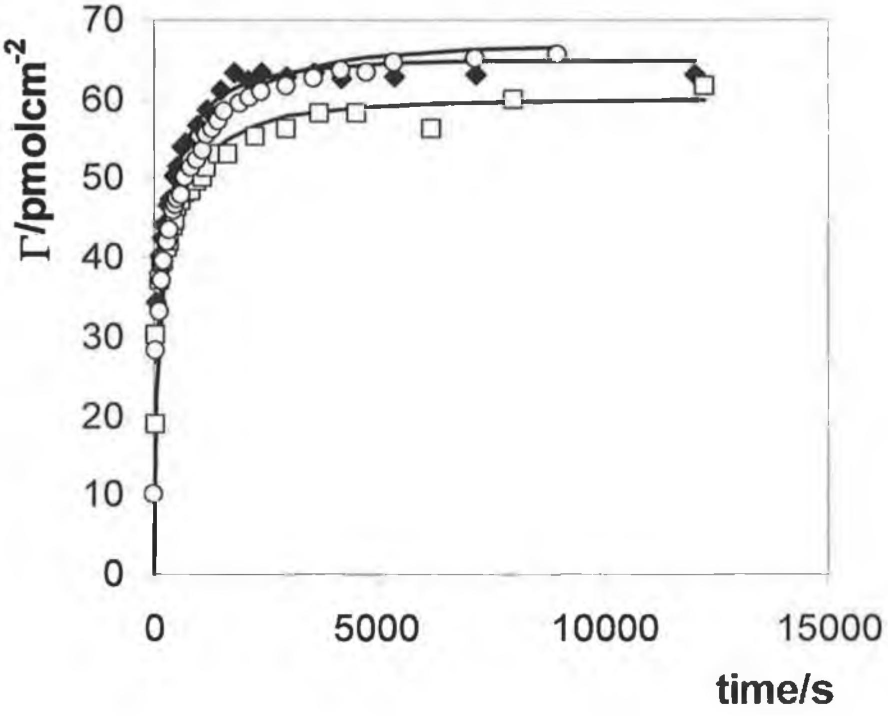

Figure 3.11 Time dependence of the surface coverage where the bulk concentration of CoTpySH is 2.5 □, 5.0 ○ and 10 μM ◆. The solid lines represent the best fits obtained from the diffusion controlled model with a Γ_{max} value of 63±3 pmolcm^{-2} and a diffusion coefficient of 5.5±1.1x10^{-7} cm^{2}s^{-1}.

This figure shows that the surface coverage increases rapidly during the first 40 min following immersion of the electrode for each concentration investigated and reaches a plateau value for times longer than approximately 2 hours. The time required for sufficient material to diffuse from the bulk solution to the electrode surface is given by:

$$t = \frac{1}{\pi D_{Soln}} \left(\frac{\Gamma}{C_B} \right)^2 \tag{3.1}$$

where D_{Soln} is the diffusion coefficient of the complex in solution[31]. The diffusion coefficient has been measured in Chapter 2 and for the redox couple $Co^{2+/3+}$ is 2×10^{-6} $cm^2 s^{-1}$. Therefore, for the lowest bulk concentration investigated, 2.5 μM, the time required for mass transport of sufficient material to form a monolayer under linear diffusion conditions is approximately 100 s, indicating that mass transport to the surface is not rate determining. Significantly, the final surface coverage obtained is independent of the bulk concentration for $2.5 \leq$ CoTpySH ≤ 10 μM suggesting that the complex adsorbs irreversibly. Figure 3.12 shows the correlation plots between theoretical and experimental surface coverages for the various models described in Chapter 1 where the bulk concentration is 2.5 μM, which is also representative for the other concentrations.

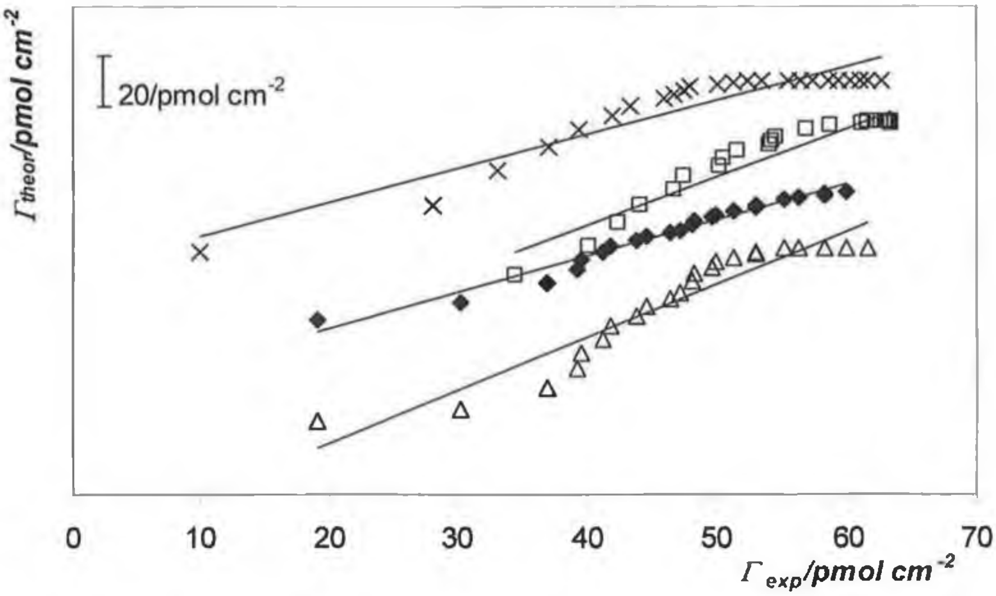

Figure 3.12. Correlation plots of theoretical *vs.* experimental surface coverages using the following models (from top to the bottom): parallel equilibrium, two step adsorption, diffusion controlled adsorption and kinetically controlled adsorption. The modified electrode is a 50 μm radius platinum microelectrode and the bulk concentration of the complex is 2.5μM, 0.1M $TBABF_4$ acetonitrile solution.

The best fit is obtained using the pure diffusion controlled model which gives a direct (slope of 1.09±0.1), unbiased (intercept of -3.0×10^{-12} mol cm^{-2}) correlation between the theoretical and experimental surface coverages. A similar behaviour is observed for the other concentrations explored. The other models either produce biased responses or the residuals depend on the surface coverage. The best fits of this model to the experimental surface coverage *versus* time profiles, over this concentration range, reveal a Γ_{max} value of 63±3 pmolcm^{-2} and a diffusion coefficient of $5.5\pm1.1\times10^{-7}$ cm^{2}s^{-1}. The observation that these best fit parameters are independent of the bulk concentration further suggests the diffusion controlled model appropriately describes the experimental response.

A key observation is that the diffusion coefficient is a factor of approximately 4 times lower than that found for diffusion of the complex in solution. This observation suggests that diffusion of the complex on the electrode surface controls the rate of monolayer assembly. Surface diffusion of alkane thiols has been extensively explored, for example, by Kakiuchi et al. who determined[39] D_{Surf} to be of the order of 10^{-18} cm^2 s^{-1} for undecanethiol and mercaptoundecanoic acid at 60 °C. Weiss et al.[40] found the rate to be lower than 10^{-17} cm^2 s^{-1} for the surface diffusion of thiolate on Au(111) terraces from coalescence of initially isolated domains of $CH_3(CH_2)_{15}SH$ in a mixed SAM with $CH_3O_2C(CH_2)_{15}SH$. Schonenberger et al.[41] observed that holes in a dodecanethiol SAM coalesced at the rate of 0.5-1 nm/min at 90 °C, which corresponds to 1-4 10^{-17} cm^2 s^{-1}. Therefore, while the observed diffusion coefficient is much lower than that associated with diffusion through solution, it is dramatically larger than values previously reported for alkane thiol diffusion on gold. The faster surface diffusion rates observed here most likely arise because the monolayers investigated here are formed on platinum. Moreover, unlike alkane thiols, the complexes investigated here do not undergo stabilizing lateral interactions making them more mobile on the electrode surface.

Thus, it appears that the adsorption mechanism involves a fast initial adsorption step followed by a diffusional process at the surface, e.g., to enable closer packing of adsorbates. It is, perhaps, important to note that while the voltammetry indicates destabilizing lateral interactions, these are rather weak, of the order of 6-8 kJmol^{-1}.

Given that formation of the platinum thiolate bond is exothermic to the order of 40-50 $kJmol^{-1}$, surface diffusion of adsorbates to give a closer packed structure is thermodynamically favourable.

3.4 Electron transfer rate constant determination

In this section the electron transfer rate constant of monolayers of CoTpySH adsorbed on platinum microelectrodes are presented and discussed. In Chapter 2 the *RC* constant of the electrochemical system was determined for bare microelectrodes of 12.5 and 50 μm radius and it was found it was possible to determine rate constants as large as 10^6 s^{-1}. Different methods can be used to determine the rate at which the transfer of electrons occurs.

First, the method introduced by Laviron[42] allows the electron transfer rate constant to be determined from a plot of $\Delta E_p/n$, where ΔE_p is the peak to peak separation and n is the number of exchanged electrons, *versus* the scan rate, when the system is diffusionless and $\Delta E_p > 200/n$ mV. However, in the present work separation due to kinetics effects was not observed at scan rates as fast as 500 Vs^{-1} as shown in Figure 3.13.

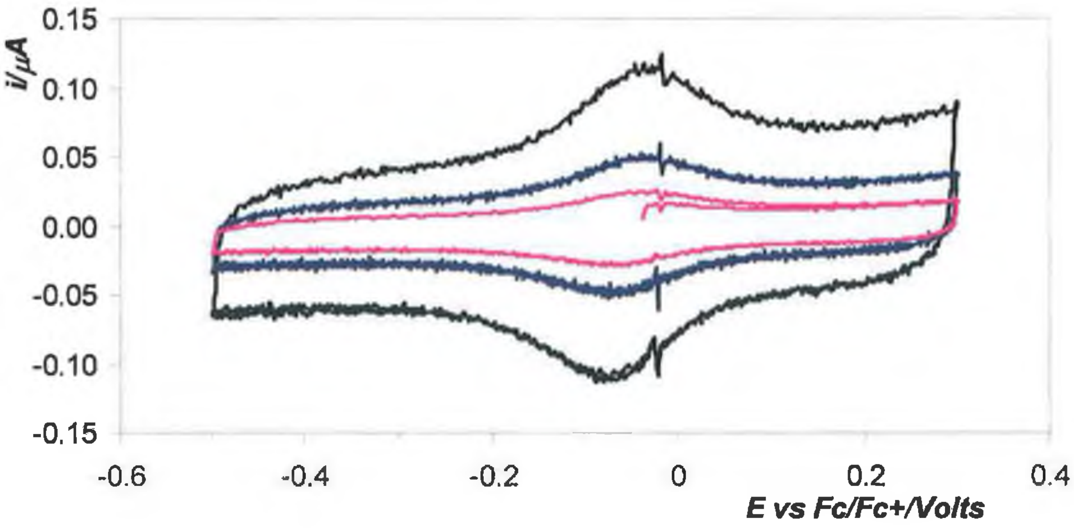

Figure 3.13 CVs of a monolayer of CoTpySH on a platinum microelectrode (12.5μm radius) in 0.6M TBABF$_4$ at 500 Vs^{-1} (black line), 200 Vs^{-1} (blue line) and 100 Vs^{-1} (purple line). Reference electrode: Ag/Ag$^+$ calibrated *versus* Fc/Fc$^+$ redox couple. Counter electrode: platinum wire

It can be seen from the figure that the peak to peak separation does not increase and ΔE_p is 0.04V for $20<v<500$ Vs^{-1}. At 1000 Vs^{-1} the noise overlapping the monolayer did not allow ΔE_p to be accurately determined.

High speed chronoamperometry: acquisition and simulation of the data

Forster[43, 44, 45, 46] used a custom built potentiostat with a rise time shorter than 2 ns for the determination by chronoamperometry of the rate constants of complexes with ligands of similar size to that studied in the present work.

Chronoamperometry is a powerful technique with which to obtain kinetic information. The protocol used here involved stepping the potential from a non faradaic value, set 0.2V away from the formal potential of the redox process, to a potential that is larger than the formal potential of the redox process of at least 0.05V. The amplitude of the potential step was kept constant at 0.5V and therefore the capacitive contribution to the current decay was also constant, assuming the capacitance of the monolayer independent on the applied potential. The overpotential, η, was varied. This protocol assures that the contribution from the reverse rate constant to the overall measured rate is minimised. The consequent flowing current was then monitored during time and analysed to obtain kinetic information.

Usually, two current decays, which arise from the double layer charging and the faradaic currents flows, can be time resolved, because they have different time constants. In particular the *RC* constant is shorter than that of the faradaic process, and analysis of the data only after 5-10 *RC* is desired.

Simulations of the expected experimental transients can be performed in order to decide whether a 50 or 12.5 μm radius microelectrode best suits the rate constant determination. In fact, the current decay for an electroactive monolayer is a function of the rate constant at a particular overpotential, η, and Q, the charge that undergoes the redox reaction which is related to the surface coverage. Therefore, although it is suitable to use small electrodes in order to minimise the *RC* constant contribution, for slow heterogeneous electron transfer rate constants, a high surface charge is required for the faradaic transient to be detected.

In Chapter 1, the equations describing the current decays following a potential step for the double layer charging and a redox active monolayer were introduced. Simulation of the two decays can be performed varying the electrode size (50 and 12.5 μm radius), k° (between 10^3 and 10^4 s^{-1}), the applied overpotential (between 0.05 and 0.2V) and keeping constant the surface coverage and the potential step. Both the electrodes showed two distinct decays for the capacitive and faradaic currents for overpotentials bigger than 0.05V, at faster (10^4 s^{-1}) and slower (10^3 s^{-1}) standard rate constants. Figure 3.14a and b show the simulations obtained at η equal to 0.180V, supposing an *RC* constant the same as at the bare electrode. This is the worse case scenario since more likely the *RC* constant is lowered by the presence of the monolayer that decreases the capacitive contribution.

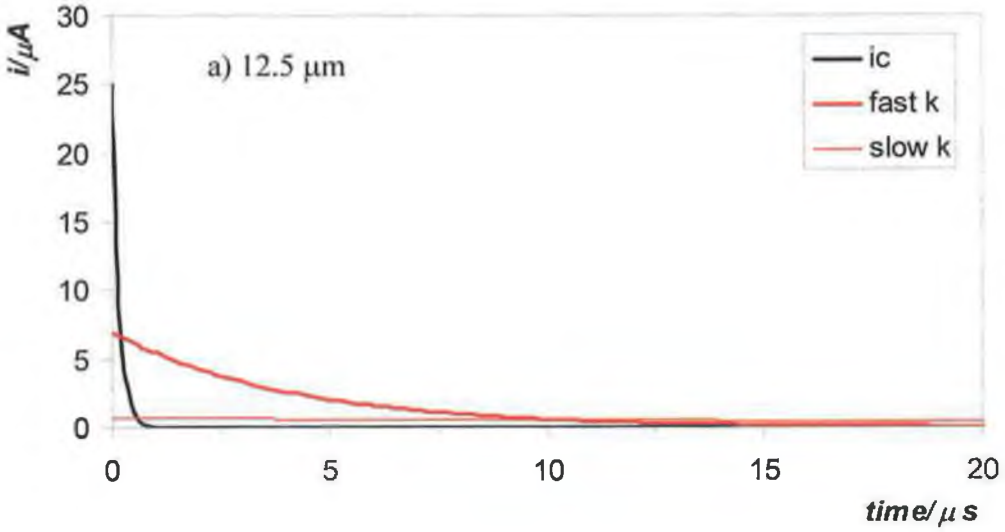

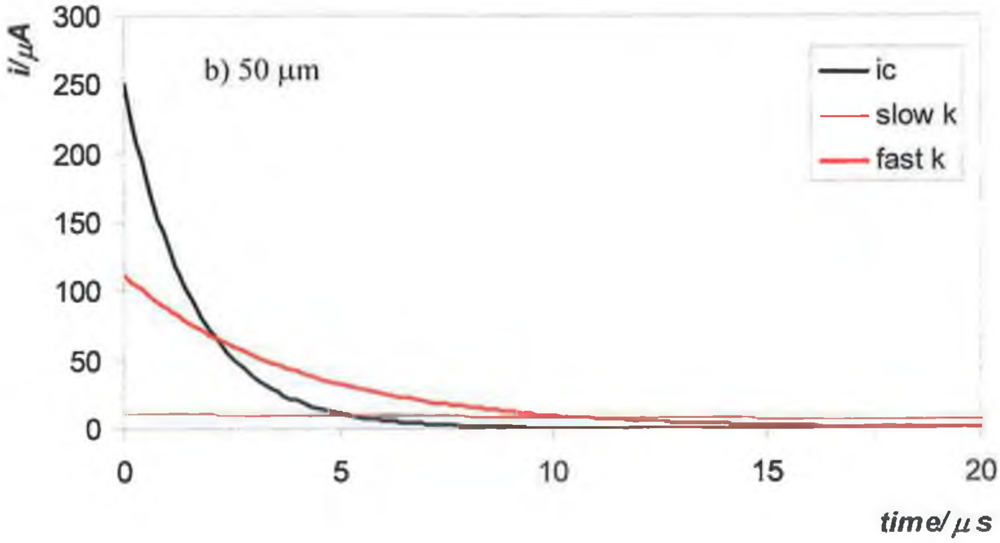

Figure 3.14 Simulations for a 12.5μm (a, top graph) and 50μm (b, bottom graph) for the capacitive and faradaic decays at overpotential of 0.180, for k° in the order of 10^3 s^{-1}(thin red line, slow k) and 10^4 s^{-1}(thick red line, fast k). Potential step: 0.5V. *RC* constants: 0.16μs for plot **a** and 1.6μs for plot **b**. The capacitive decay is plotted as a black line.

However, experimentally better results were obtained with 50 μm radius microelectrodes, since usually higher surface coverages were achieved and a better signal to noise ratio was obtained. Therefore, the determination of the electron transfer was performed by chronoamperometry with 50μm radius platinum electrodes in 0.6M $TBABF_4$.

Figure 3.15 shows a typical experimental decay following an applied overpotential of 0.180V for a 50 μm radius platinum microelectrode modified with CoTpySH,.

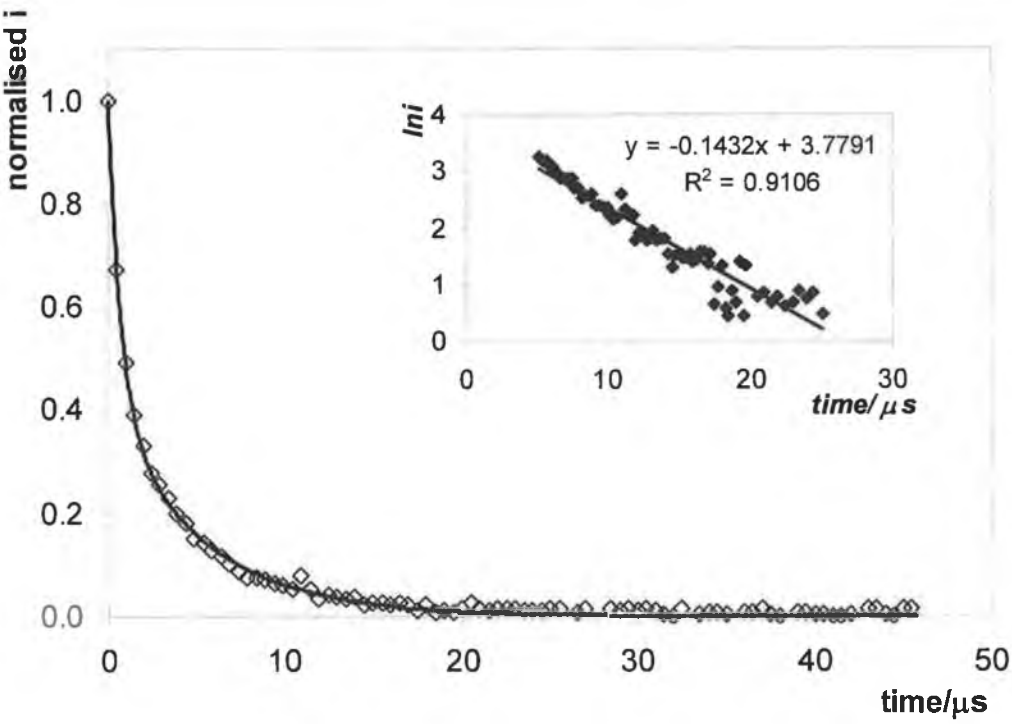

Figure 3.15 Current response (◇) for a 50 μm radius platinum microelectrode modified with a CoTpySH monolayer following a potential step of 0.5V where the overpotential η was 0.180V. The solid line is the best fit double exponential decay. Fitting parameters: k= $1.92\times10^5 s^{-1}$ and k_{RC}= 1.44×10^6 s^{-1}. The inset shows the semilog current vs. time response for the Faradaic current decay corresponding to oxidation of the Co^{2+} centres after 5*RC*. The supporting electrolyte is 0.6M $TBABF_4$ in acetonitrile. Reference electrode: Ag/Ag^+ calibrated versus Fc/Fc^+ redox couple. Counter electrode: platinum flag. Cell set up: two electrode cell with the reference and the counter combined.

The solid line confirms that the experimental response is adequately described by a double exponential decay arising from double layer charging and faradaic electron transfer at short and long times, respectively. The inset shows semilog graph, lni *vs.* t, where the slope is the electron transfer rate constant, k, at a defined overpotential and the intercept is ln kQ. For the experiment shown in Figure 3.15 the heterogeneous electron transfer rate constant, k, was calculated to be $1.4\pm0.9\times10^{5}\ s^{-1}$ and the *RC* of $1\pm0.5\ \mu s$. From the semilog plot, the charge associated with the electron transfer is calculated to be ca. 75% of the charge determined by cyclic voltammetry. Moreover, no deviations from linearity are observed at short time scale indicating that uncompensated cell resistance, which would cause the rate constant to evolve in time, is insignificant. Therefore, ca. 75% of the surface confined molecules are redox active on a microsecond scale and show a single rate constant and thus a similar microenvironment.

After the chronoamperometry experiment the presence and stability of the monolayer was checked and successfully recorded, indicating that the 25% of "inactive" monolayer is not due to desorption of the molecules from the surface, as shown in Figure 3.16

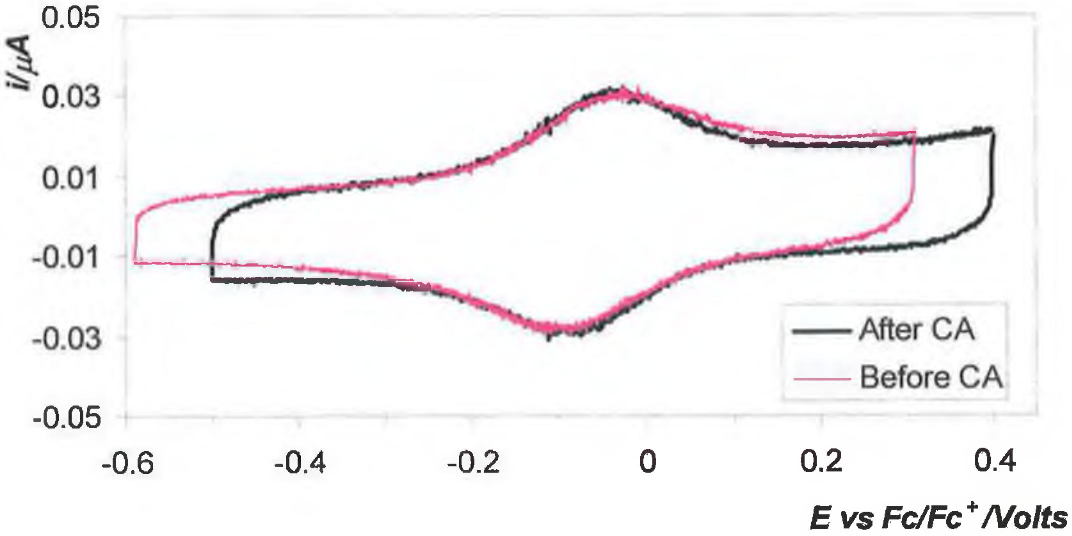

Figure 3.16 CVs of the monolayer before and after the chronoamperometry experiment in 0.6M $TBABF_4$. Scan rate: 5 Vs^{-1}. Reference electrode: Ag/Ag^+ calibrated versus Fc/Fc^+ redox couple. Counter electrode: platinum flag.

3.4.2 Potential dependence of k

Potential dependent electron transfer experiments may allow the reorganization energy and electronic coupling effects to be deconvoluted for these terpyridine based monolayers and calculate a value for k°.

Overpotentials ranging from 0.120 to 0.200 V were applied and the corresponding rate constants measured. The current decays were recorded and fitted as described in the preceding section and a plot of k *vs.* η for the oxidation process of $Co^{2+/3+}$was obtained as shown in Figure 3.17.

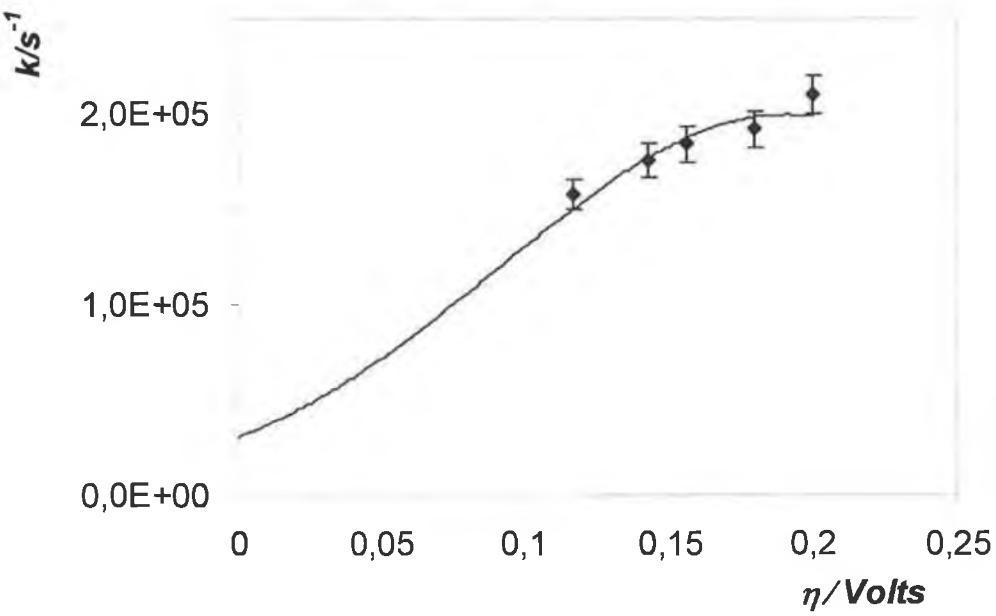

Figure 3.17. k vs. η plot for a CoTpySH monolayer adsorbed on 50 μm radius platinum microelectrode. The supporting electrolyte is 0.6M $TBABF_4$. Potential step: 0.5V. Overpotential: from 0.120 to 0.2V. The solid curve represents the best fit derived from the Marcus model, where λ=0.19V and pre-exponential factor is 2.4 $x10^4$ s^{-1}. The extrapolated standard heterogeneous rate constant is $3.06\pm0.03x10^4$ s^{-1}.

It is perhaps important to note that Figure 3.17 is a different representation of the dependence of the rate constants on the applied overpotential than that presented in a Tafel plot. For the data presented here, the ln k dependence of the conventional Tafel plot obscures the very weak potential dependence of k. The maximum applied overpotential was chosen to be 0.2V, since at higher values the corresponding k was faster than the *RC* constant of the cell for the 50 μm radius electrode.

In Chapter 1 the expression for Marcus equation, relating the rate constant to the driving force was described. The potential dependent rate of electron transfer for adiabatic systems at a certain overpotential, η,and temperature, T, is expressed by[47]:

$$k(\eta) = \frac{2\pi}{\hbar\sqrt{4\pi k_B \lambda}} H^2 e^{\frac{(\lambda-\eta)^2}{4\lambda k_B T}} \tag{3.2}$$

where H is the matrix coupling element, which quantifies the electronic interaction of the redox orbitals and the metallic states. The experimental data were then fitted with Equation 3.2, leaving as freely adjustable parameters λ, the total reorganization energy, and the matrix coupling element H and minimizing the sum square of the residuals between the experimental and theoretical data.

The fitting procedure gave λ equal to 0.191eV, or 18.5 kJ mol^{-1}, and H equal to 0.22 kJ mol^{-1}. The fact that the electronic element is less than 1 kJ mol^{-1} is supportive of considering the system being adiabatic and it is in good agreement with literature values for compounds with similar ligand length [48, 49]. The extrapolated standard heterogeneous rate constant was $3.06\pm0.03\times10^4$s^{-1}. Significantly, this rate constant is in the same order of magnitude of that found for [Os(bpy)$_2$ 1,2-bis(pyridyl)ethane]$^{2+}$ where the electron transfer distance is similar to that of the terpyridine complex investigated here but the electron transfer is highly non-adiabatic[50, 51, 52]

As mentioned in Chapter 1, the reorganization energy, λ, is made of two contributions, the inner, λ_{in}, and outer , λ_{os}, sphere energies. Under Marcus theory λ_{os}, has the following expression [49, 53] in kJ mol^{-1} for an heterogeneous electron transfer process:

$$\lambda_{os} = \left(\frac{e^2 nN}{8\pi\varepsilon_0}\right)\left(\frac{1}{a} - \frac{1}{r}\right)\left(\frac{1}{\varepsilon_{op}} - \frac{1}{\varepsilon_s}\right) \tag{3.3}$$

where N is the Avogadro's number, a is the radius of the redox centre(5.6 Å) [18], *n* is the number of electrons, ε_0 is the vacuum dielectric constant (8.85×10^{-12} C^2/Jm), r is reactant-image distance, and ε_{op} and ε_s are the optical and static dielectric constants of the medium around the redox centre. In the following calculations, the imaging effects will be neglected, i.e. $r\rightarrow\infty$. Therefore, an estimation of λ and discussion of the results obtained from Figure 3.17 can be performed.

A calculation of the static dielectric constant ε_s is possible by knowing the *RC* constant of the system which can be obtained from the fitted transients with the double exponential equation. At 0.6M $TBABF_4$ the effective contribution to the total capacitance comes predominantly from the monolayer, since the diffuse double layer is compressed. Therefore, ε_s is given by:

$$\varepsilon_s = \frac{dC_{dl}}{\varepsilon_0} \tag{3.4}$$

where *d* is the ligand length (10Å)[50] The double layer capacitance, C_{dl}, was calculated to be 2.1×10^{-6} F cm^{-2} and, therefore, ε_s was equal to 2.4. The optical dielectric constant can be calculated as the squared value of the refractive index of the medium, which for acetonitrile is 1.344. By substituting those values in Equation 3.3, λ_{os} is 17.2 kJ mol^{-1}.

The agreement between this value and that obtained by fitting the Tafel plot is good and similar to what found in literature[22] by Chidsey, and it suggests that the activation energy of the process is mainly controlled by the reorganization of the medium surrounding the molecule. Therefore, the breaking of the conjugation due to either the bonds between the phenyl moiety and the terpy or the phenyl and the CH_2 does not seem to play a significant role in the electron transfer rate as well as the nature of the heteroatom bonding to the metal surface.

Conclusions

Monolayers of $[Co(ttp\text{-}CH_2\text{-}SH)_2]^{2+}$ on platinum were prepared which are extremely stable and exhibit close to ideal reversible electrochemistry. A particular advantage of terpyridine complexes is that they enable supramolecular assemblies to be built in a highly linear manner in the direction perpendicular to the electrode surface.

The adsorption mechanism monitored *in-situ* involves rapid adsorption of the complex followed by a rate limiting surface diffusion that ultimately yields monolayers in which the surface coverage is 40% of that expected for a close packed assembly. The adsorption of the molecule is irreversible and controlled by diffusion of the molecule on the surface. The rate of surface diffusion is approximately 10 orders of magnitude higher than that found for alkane thiols on gold indicating that the interaction of the Cobalt thiol complexes with platinum is substantially weaker and reflecting the fact that there are destabilizing interactions between the cobalt complexes compared to stabilizing lateral interactions in the case of conventional alkane thiols. These electrostatic repulsive interactions, together with their inherent linearity, is likely to lead to highly ordered structures on the molecular scale.

The dynamics of electron transfer are the same order of magnitude expected for short chain ligand with a heterogeneous electron transfer rate constant, k°, of $3.06\pm0.03\times10^{4}\ s^{-1}$ and a reorganization energy controlled by the solvent contribution.

References

1 Adams D. M, Brus L., Chidsey C. E. D., Creager S., Creutz C., Kagan C. R. Kamat P. V., Lieberman M., Lindsay S., Marcus R. A. J., *J. Phys. Chem. B*, **2003**, 107, 6668.

2 Park J. W., Pasupathy A. N., Goldsmith J. I., Soldatov A. V., Chang C., Yaish Y., Sethna J. P., Abruña H. D., Ralph D. C., McEuen P. L., *Thin Solid Films*, **2003**, 438, 457.

3 Park J., Pasupathy A. N., Goldsmith J. I., Chang C., Yaish Y., Petta J. R., Rinkoski M., Sethna J. P., Abruña H. D., McEun P. L., Ralph D. C., *Nature*, **2002**, 417, 722.

4 Gittins D. I., Bethell D., Schiffrin D. J., Nichols R. J., *Nature*, **2000**, 408, 67.

5 Sortino S., Di Bella S., Conoci S., Petralia S., Tomasulo M., Pacsial E. J., Raymo F. M., *Adv. Mater*, **2005**, 17, 1390.

6 Gooding J. J., Mearns F., Yang W., Liu J., *Electroanalysis*, **2003**, 15, 81.

7 Chao L., Fan W., Straus D. A., Lei B., Asano S., Zhang D., Han J., Meyyappan M., Zhou C., *J. Am. Chem. Soc.*, **2004**, 126, 7750.

8 Hjelm J., Handel R. W., Hagfeldt A., Constable E., Housecroft C. E., Forster R. J., *Inorg. Chem.*, **2005**, 44, 1073.

9 Hjelm J., Handel R. W., Hagfeldt A., Constable E., Housecroft C. E., Forster R. J., *Phys. Chem. B*, **2003**, 107, 10431-10439.

10 Ulmann A., *An introduction to ultrathin organic films: from Langmuir-Blodgett to Self-Assembly*, Academic Press, San Diego, **1991**

11 Finklea H. O., *Encyclopedia of Analytical Chemistry*, Vol. 11, Ed. R. A. Meyers, Wiley, Chichester, UK, **2000**, 10090.

12 Love C.J., Estroff L.A., Kriebel J.K., Nuzzo R.G., Whitesides G.M., Chem. Rev., **2005**, 105, 1103

13 Finklea H. O., Self-assembled monolayers on electrodes, in *Encyclopedia of analytical chemistry*, **2000**, Vol.11, R.A. Meyers (Ed), Wiley, Chichester, UK, 10090

14 Feldheim D.L., Keating C.D., *Chem. Soc. Rev.*, **1998**, 27, 1

15 Gittins D. L., Bethell D., Nichols R J., Schiffrin D.J., Adv. Mater., **1999**, 11, 737

16 Yu H., Luo Y., Beverly K., Stoddart J.F., Tseng H.-R., Heath J., R., *Angew. Chem.. Int. Ed.. Engl.,* **2003**, 42, 5706

17 Kalyanasundaram,K. *Photochemistry of Polypyridine and Porphyrin complexes*, Academic Press: London, U.K. **1991**

18 Maskus M., Abruña H. D., *Langmuir*, **1996**, 12, 4455.

19 Collin J.-P., Gavin P., Heitz V,. Sauvage J.-P., *Eur. J. Inorg. Chem.*, **1998**, 1, 1.

20 Haider J. M., Chavarot M., Weidner S., Sadler I., Williams R. M., De Cola L., Pikramenou Z., *Inorg. Chem.*, **2001**, 40, 3912.

21 Chidsey C. E. D., Bertozzi C. R.,. Putvinsky T. M, Muijsca A. M., *J. Am. Chem. Soc.*, **1990**, 112, 4301.

22 Chidsey C. E. D., *Science*, **1991**, 251, 919.

23 Finklea H. O., Hanshew D. D., *J. Am. Chem. Soc.*, **1992**, 114, 3173.

24 Walsh D. A., Keyes T. E., Forster R. J., *J. Phys. Chem. B., **2004***, 108, 2631.

25 Benniston A. C., Chapman G. M., Harriman A., Mehrabi M., Sams C. A., *Inorg. Chem.*, **2004**, 43, 4227.

26 Figgemeier E., Merz L., Hermann B. A., Zimmermann Y. C., Housecroft C. E., Gu1ntherodt H.-J., Constable E. C., *J. Phys. Chem. B,* **2003**, 107, 1157

27 Maeda T. Sasaki Y., Horie C., Osawa M., *J. Electron. Spectrosc. Relat, Phenom.*, **1993**, 381, 6465

28 Tabaksblat R., Meier R. J., Kipp B. J., *Appl. Spectroscop.*, **1992**, 46, 60

29 Ren B., Huang Q. J., Cai W. B., Mao B. W., Liu F. M., Tian Z. Q., *J. Electroanal. Chem.*, **1996**, 415, 175

30 Cai W. B., Ren B., Li X. Q., She C. X., Liu F. M., Cai X. W., Tian Z. Q., *Surface Science*, 1998, 406, 9

31 Forster R. J., Keyes T. E., Vos J. G., *Interfacial Supramolecular Assemblies*, Wiley Ed.

32 Bain C. D., Troughton E. B., Tao Y.-T., Evall J., Whitesides G., Nuzzo R. G., *J. Am. Chem. Soc.*, **1989**, 111, 321.

33 Porter M. D., Bright T. B., Allara D. L., Chidsey C. E. D., *J. Am. Chem. Soc.* **1987,** 109, 3559.

34 Nuzzo R. G., Zegarski B. R., Dubois L. H., *J. Am. Chem. Soc.* **1987,** 109, 733.

35 Bard A. J., Faulkner L. R., *Electrochemical methods: Fundamentals and Applications*, Second Edition, Ed. Wiley

36 Langmuir I., *J. Am. Chem. Soc.*, **1917**, 39, 1848.

37 Shen D., Huang M., Chow L. M., Yang M., *Sens. and Actuat. B.*, **2001**, 77, 664.

38 Prosser A. J., Retter U., Lunkenheimer K., *Langmuir,* **2004,** 20, 2720.

39 Kakiuchi T., Iida M., Gon N., Hobara D., Imabayashi S., Niki K., *Langmuir,* **2001,** 17, 1599.

40 Stranick S. J., Parikh A. N., Tao Y.-T., Allara D. L., Weiss P. S., *J. Phys. Chem.,* **1994,** 98, 7636

41 Schonenberger C., Jorritsma J., Sondag-Huethorst J. A. M., Fokkink G., *J. Phys. Chem.,* **1995,** 99, 3259.

42 Laviron E., *J. Electroanal. Chem.*, **1979**, 101, 19

43 Forster R. J., *J. E. Chem. Soc.*, **1997**, 144,1165

44 Forster R. J., *Inorg. Chem.*, **1996**, 35, 3394

45 Forster R. J., Faulkner L. R., *J. Am. Chem. Soc.*, **1994**, 116, 5444

46 Forster R. J., Keyes T. E., *J. Phys. Chem. B*, **1998,** 102, 10004

47 Forster R. J., Loughman P. J., Keyes T. E., *J. Am. Chem. Soc.,* **2000,** 122, 11948.

48 Walsh D. A. Keyes T. E., Hogan C. F., Forster R. J., *J. Phys. Chem. B.*, **2001,** 105, 2792

49 Forster R. J., O'Keilly J. P., *J. Phys. Chem.* , **1996**, 100, 3695

50 Forster R. J., Loughman P. J., Figgemeier E., Lees A. C., Hjelm J., Vos J. G., *Langmuir,* **2000**, 16, 7871.

51 Forster R. J., Faulkner L. R., *J. Am. Chem. Soc.*, **1994**, 116, 5444

52 Brennan J. L., Howlett M., Forster R. J., *Faraday Discussions*, **2002**, 121, 391

53 Finklea H. O., Hanshew D. D., *J. Am. Chem. Soc.*, **1992**, 114 (9), 3173

Chapter 4

Immobilisation and characterisation of beta-thiol cyclodextrins on gold electrodes

Introduction

Host-Guest chemistry

In the wide field of nanotechnology, the host-guest chemistry is an attractive route for building up supramolecular architectures using non-covalent interactions in a way that allows the properties of the final system to be tuned. The method involves a 'host' molecule which includes, totally or in part, by non-covalent forces, a 'guest' molecule to produce a 'host-guest' complex. The non-covalent supramolecular interaction is based on a range of attractive and repulsive forces, which are dictated by the properties of the individual components.

Commonly the host is a large molecule or aggregate such as an enzyme or synthetic cyclic compound possessing a well defined, sizeable, central cavity. Some well-studied examples of host molecules are calixarenes[1], crown ethers[2] and cyclodextrins[3]. The guest may be an ionic species, an organic or a more complex molecule, such as a hormone or neurotransmitter. Among all the hosting molecules cyclodextrins (CDs) seem to be the most important ones because they are semi-natural products, produced from a renewable natural material by an enzymatic reaction, they are fairly inexpensive, due to the high yields of production and they show low toxicity and therefore can be consumed by humans.

CDs have the capability of accommodating molecules of the size of one-two benzene rings in their cavities, while larger molecules, that have sided chains of comparable size, are partially included. CDs are cyclic oligosaccharides, prepared by the enzymatic degradation of starch, most commonly comprising of six, seven or eight D-glucopyranoside units (α, β, γ respectively) linked by a 1,4-glycosidic bond. Due to their conformation, they form hydrophobic cavities lined by the glycoside oxygen bonds, which are responsible for the ability of the CDs to include hydrophobic molecules.

The inclusion phenomenon essentially involves substitution of the included water molecules with a less polar guest. Interaction of the relatively non-polar guest molecule with an imperfectly solvated hydrophobic cavity of the CD is an energetically favoured process. The driving forces leading to the inclusion complexation by cyclodextrins include electrostatic, Van der Waals and hydrophobic interaction, hydrogen bonding, relief of conformational strain, exclusion of cavity–bound high-energy water and charge-transfer interaction.[4 5 6].

The inclusion of a guest, G, is a thermodynamic equilibrium process with an association constant, K, given by the relationship:

$$\begin{gathered} CD + G \leftrightarrow CD.G \\ K = \frac{[CD.G]}{[CD][G]} \end{gathered} \tag{4.1}$$

Self-assembled monolayers of thiolated CDs

Coupling the ability of the CDs for molecular recognition with assembly techniques is a powerful route to produce sensors able to recognize and quantify molecules in aqueous solutions[7].

SAMs are highly organised at the molecular length scale, the most studied of which involves the immobilisation of molecules through a sulphur atom onto gold surfaces. When the self-assembled molecule is able to bind and therefore recognise other molecules, a strong and versatile modified surface for sensing can be built up. Given that the supporting materials are noble metals the assemblies can be characterised by a wide range of techniques, including electrochemistry.

In the present work, mono-6-deoxy-6-(mercaptopentamethylene)thio-β-cyclodextrin was self-assembled on gold polycrystalline surfaces through the pentanethiol moiety, in order to produce modified substrates able to perform molecular recognition and ultimately build up supramolecular architectures at the interface. The modified CDs studied to date, typically α and β, primarily involve modification on the primary side of the CD cavity with sulphur containing moieties such as thiolate. Upon surface attachment, the wider opening of the CD receptor will face the adjacent solution, which should facilitate binding of solution species inside the cavity. Again, the utilisation of mono-thiolated CDs seems to be more promising in terms of packing and low defect density in the monolayer rather than multi-thiolated CDs[8]. This is mainly due to the higher degree of rotational freedom that the cavity experiences when assembled on a surface and therefore the molecules within the monolayer are able to interact and pack closely.

The surface coverage, the extent of lateral interactions among the β-CDs constituting the monolayer, and the orientation of the cavities will be discussed extensively in the following sections.

4.1 Experimental

Instrumentation

Cyclic voltammetry and AC voltammetry were performed using a CH Instrument Model 660 Electrochemical Workstation and a conventional three-electrode cell. All solutions were deoxygenated thoroughly prior any experiment using oxygen free argon, and a blanket of argon was maintained over the solutions during all experiments. Potentials are quoted with respect a home-made Ag/AgCl, KCl_{sat} aqueous reference electrode, previously calibrated against standard laboratory calomel reference electrode. All experiments were performed at room temperature.

Monolayer assembly

The electrodes were cleaned are described in Chapter 2, then rinsed with milliQ water and placed, as quickly as possible in a daily fresh micromolar solution (from 100 to 200μM) of the β-CD-SH and soaked overnight. The solutions were prepared by dissolving β-CD-SH in milliQ water and then sonicated for 10 min. The solubility[1] in water of β-CD is known to be 0.012M at 25°C

4.2 Description of the β-CD layer

4.2.1 Reductive desorption

It is well known that the surface coverage of alkanethiols monolayers can be determined by reductive or oxidative desorption[9] of the adsorbed thiolated layer. The electrode reaction for the reductive desorption of monolayer films at alkaline pH (pH>11), where the experiment can be performed at accessible potentials, can be described by the following Equation:

$$H^+ + AuS(CH_2)_mCH_3 + ne^- \rightarrow Au(0) + HSC(CH_2)_mCH_3 \qquad (4.2)$$

Porter *et al.*[9] first reported on the determination of the surface coverage of adsorbed alkanethiols at evaporated gold electrodes. The technique was based on the measurement of the charge passed for the reductive desorption (Equation 4.2b) of the gold-bound thiolate layer, assuming that one electron was needed to reduce one gold-sulphur bond, i.e. n=1. The experiment was performed in 0.5 M KOH in a potential window between -0.2 and -1.2V, imposed by solvent reduction. For dodecanethiols a sharp voltammetric peak was observed at -1.1 V *vs.* Ag/AgCl. The applicability of this method was evaluated by using ferrocene terminated thiols and by comparing the surface coverages obtained by reductive desorption to the values calculated from the ferrocene/ferrocenium redox process.

Similar approach was extended by Rojas *et al*[7] to thiolated CDs, *i.e.* for the reductive desorption of Per-6-thio-β-CD in 0.5 M KOH solution adsorbed on gold bead electrodes. As shown in Figure 4.1, a large peak at –0.95V *vs.* SSCE was attributed to the reductive desorption of the layer.

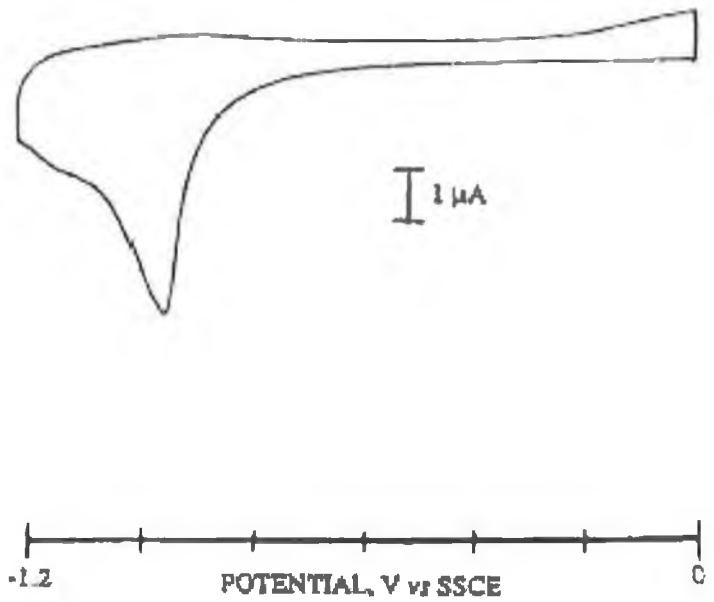

Figure 4.1. Reductive desorption of Per-6-thio-β-CD in 0.5 M KOH solution adsorbed on gold bead electrodes, derivatised by overnight exposure to a 1.0 mM solution of the cyclodextrins in DMSO/H_2O (60:40 v/v). Scan rate 0.1 Vs^{-1}. Adapted from ref. 9.

By assuming Equation 4.1 applies, they calculated a surface coverage of 75% of a full-packed monolayer, supposing that six Au-S bonds were broken. No data were presented regarding the crystallinity of the gold substrate.

However, in another contribution Yang *et al.*[10] reported on the desorption and adsorption kinetics of nonylmercaptan on gold single crystal electrodes, showing a substantial dependence of the desorption potential on the substrate, pH and scan rate. Thiols deposited on polycrystalline gold surfaces showed multi-peaks when reductively desorbed that agreed well with the potentials found for the thiols adsorbed on each single crystal gold films. In particular, CVs of a nonanethiol-coated Au(111) in 0.1 M KOH showed a symmetric, sharp, reductive current at -1.04V (*vs.* SCE) while, when Au(110) was used as electrode the reductive peak was found at -1.27V. Finally, as shown in Figure 4.2, on polycrystalline faces, two main reductive current peaks were seen at potentials corresponding to the value measured on the Au(111) surface (-1.04V) and close to the value for Au(110). These differences were thought to be partially related to the different surface charge densities of the different single crystal faces that play a role in the reductive desorption of the molecule.

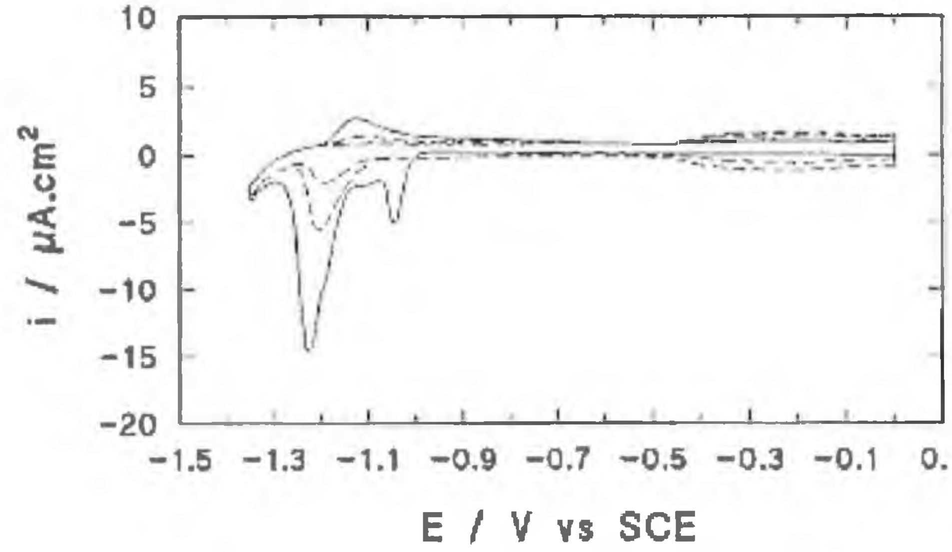

Figure 4.2. Reductive desorption of a nonanethiol modified gold polycrystalline electrode in 0.1 M KOH at 0.2Vs^{-1}. Solid line, first cycle; dashed lines second and third cycles. Adapted from ref. 10.

In the present work, reductive desorption cyclic voltammograms of mono-6-deoxy-6-(mercaptopentamethylene)thio-β-cyclodextrin layers (denoted β-CD-SH) on polycrystalline gold macro electrodes were run in 0.5 M KOH solutions, in a potential window between the OCP and -1.4 V in order to measure the surface coverage of the layers. Figure 4.3 shows the resulting CV.

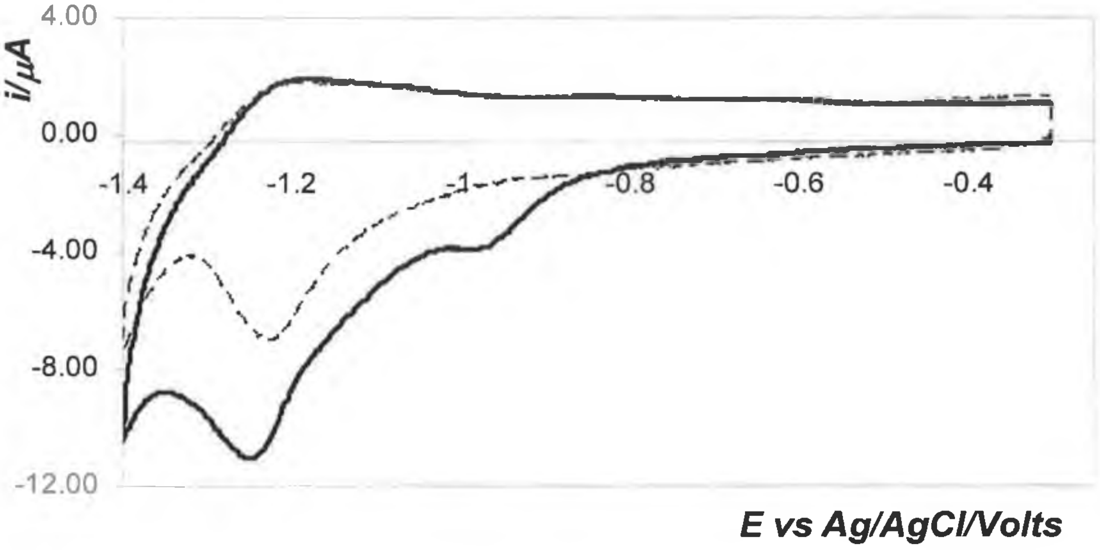

Figure 4.3. Reductive desorption in 0.5 M KOH of β-CD-SH monolayer adsorbed on a gold polycrystalline macroelectrode (2 mm diameter). Solid line: first cycle, dashed line: second cycle. Scan rate: $0.1 Vs^{-1}$. Reference electrode: Ag/AgCl, KCl_{sat} in a salt bridge. Counter electrode: platinum wire.

It is perhaps useful to split the description of the experiment in two sections, referring to the first and second cycle respectively.

In the first scan, two main reductive peaks are visible at -0.95 and -1.25V *vs.* Ag/AgCl, together with an anodic re-adsorption peak at around -1.2V. The anodic peak is broad and ill-defined, most likely because it is distributed over a larger range of potentials[11, 9] By comparing Figure 4.3 to Figure 4.2 it is clear that desorption of the β-CD-SH layer occurs at the same potentials as for nonanethiol monolayers. Thus, the presence of the β-CD as head group does not affect the interactions within the alkyl chains in the layer which controls the desorption potentials.

The FWHM for the reductive peak at -1.25V has a mean value of 0.091±0.010V, which is an ideal value for a surface confined species that undergoes a one electron Nernstian redox process. The peak at -0.95V has a FWHM of 0.130±0.010V, indicating some repulsive interactions between the molecules within the monolayer.
The difference in volts between the two peaks is around 0.3V, which is ca. 26 kJ mol^{-1} in terms of the free energy of adsorption. In well-packed alkanethiols monolayers, the alkyl chains are able to interact through the methylene CH_2 group, gaining a stabilising energy of 4-8 kJ mol^{-1} per CH_2 [12]. In the present work, the alkyl chain attached to the beta-cyclodextrin is made of 5 carbons whose lateral interaction, possible when the molecule adsorbs on a particular crystalline face, could account for the difference in potentials observed in the CV. The fact that the peak at -1.25V has an ideal value for FWHM is a further evidence of these interactions among the molecules.

In the second cycle the peak at -0.95V disappears while the peak at -1.25V still shows an electrochemical signal, although it is shifted to more positive potentials. The shift in potentials of the peak at -1.25V can be explained by assuming that the polycrystalline gold surface is constituted of contacting islands of Au(110) and Au(111). In this scenario the desorption of the molecules adsorbed on Au(111) produce destabilised edges at the Au(110) patches. Moreover the surface coverage of the peak at -0.95V is ca. 20-25% of the value obtained from the -1.25V peak. Therefore, desorbing a small amount of thiols from Au(111) can produce a less stable monolayer whose desorption potentials shift positively. During the desorption experiments, either single or multiple waves were recorded and it was not unusual to observe very broad peaks, sometimes barely detectable, even though other control experiments showed good blocking towards external probes (vide infra). The occurrence of reductive desorption at intermediate potentials is not unusual and Boubour *et al* [13] and more recently Calvente *et al.* [14] have reported on potential-induced gating of self-assembled monolayers. In the Calvente contribution, the monolayers were first adsorbed and were then subjected to chronoamperometry experiments. The applied potential was chosen between the deposition and the desorption values and held for times long enough to exceed a defined t_{max}, exclusive to each type of alkanethiols, generally within 2 minutes. Then, reductive desorption experiments showed that these monolayers have become progressively more disordered and unstable and they ultimately desorbed. Again, Yang *et al.* [15] reported on a spontaneous desorption process of alkanethiols adsorbed on gold, by STM and AFM imaging, revealing and confirming that the process mainly initiates at defect sites and then propagate in the ordered domains.

4.2.2 SERS of the modified polycrystalline gold macroelectrodes.

The presence of the monolayer and the dependence of its structure on the applied potential were probed by performing SERS at the modified gold polycrystalline electrodes. The Raman experiments were performed either *ex-situ*, with the monolayer dried in argon and scanned in air, or *in-situ*, in an aqueous solution of 0.2M Na_2SO_4, with Ag/AgCl, KCl_{sat} as reference electrode and a platinum wire as a counter electrode. Figure 4.4 shows the *ex-situ* SERS of the β-CD-SH monolayer on roughened gold polycrystalline electrode, at 632nm excitation line together with the Raman spectrum of the powder, for comparison.

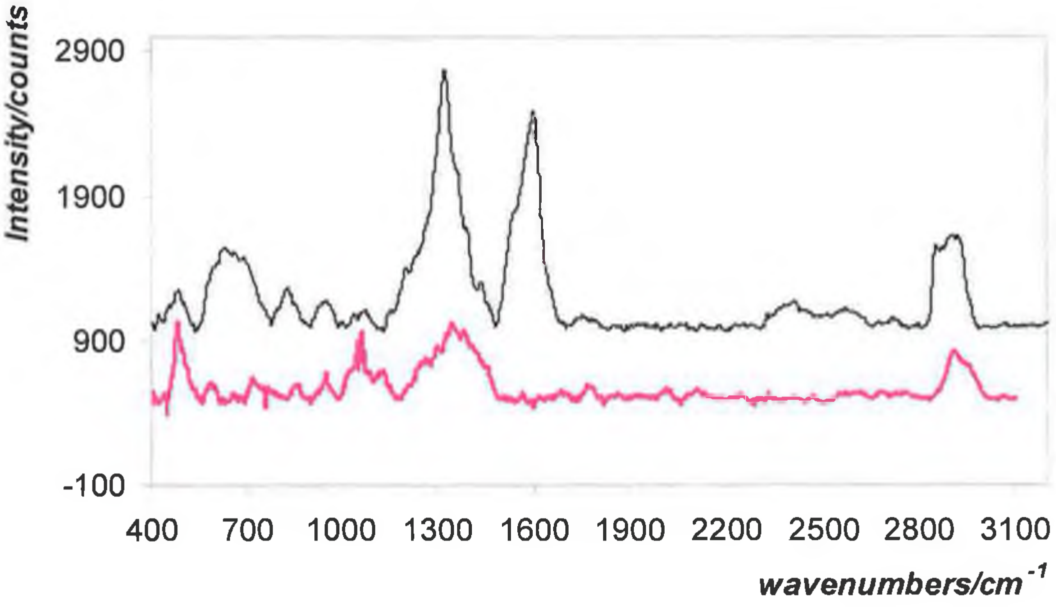

Figure 4.4. *Ex-situ* SERS of β-CD-SH monolayer on roughened polycrystalline gold macroelectrode (2mm diameter, black line) and Raman of solid powder on glass (purple line) at 632nm.

The assignments of the bands are the same as described in Section 2.6 for the solid powder. It can be seen that the modes relevant to the cyclodextrin are present on the gold surface, supporting the fact that the cyclodextrins are effectively adsorbed on the gold. Moreover, the signal is in general stronger than the response from the solid powder on glass due to enhancement factors. Since no absorption is observed for the CDs in the UV-Vis region, the 632nm excitation will enhance the signal thorough the surface enhancement effect. Therefore, the orientation of the molecule on the surface will allow some particular modes to be enhanced, giving information about the structure of the monolayer.

By comparing the spectra shown in Figure 4.4 some differences are visible. First, at 2869 cm^{-1} a peak in the monolayer spectrum is visible, which is absent for the solid and can be assigned to the symmetric $\nu(CH_2)$ of the alkyl chain. The range between 1200 and 1400 cm^{-1} is assigned either to twisting and rocking of CH_2 in the alkyl chain or the cyclodextrin modes and therefore, the intense peak at 1326 cm^{-1} is probably a combination of different modes. In the region between 500 and 1000 cm^{-1} a better resolution of the cyclodextrin modes is observed with respect to the solid powder, in particular in the range between 500 and 700 cm^{-1}, which is assigned to the CS modes. These observations are consistent with an adsorption of the thiolated β-cyclodextrin through the sulphur atom, with the pentane chain close to the surface. The broad and intense peak at 1604 is not well understood, since no double bonds are present in the molecule and the signal is completely absent in the spectrum of the solid powder. Figure 4.5 shows the effect of a contacting electrolyte solution on the Raman response of the monolayer.

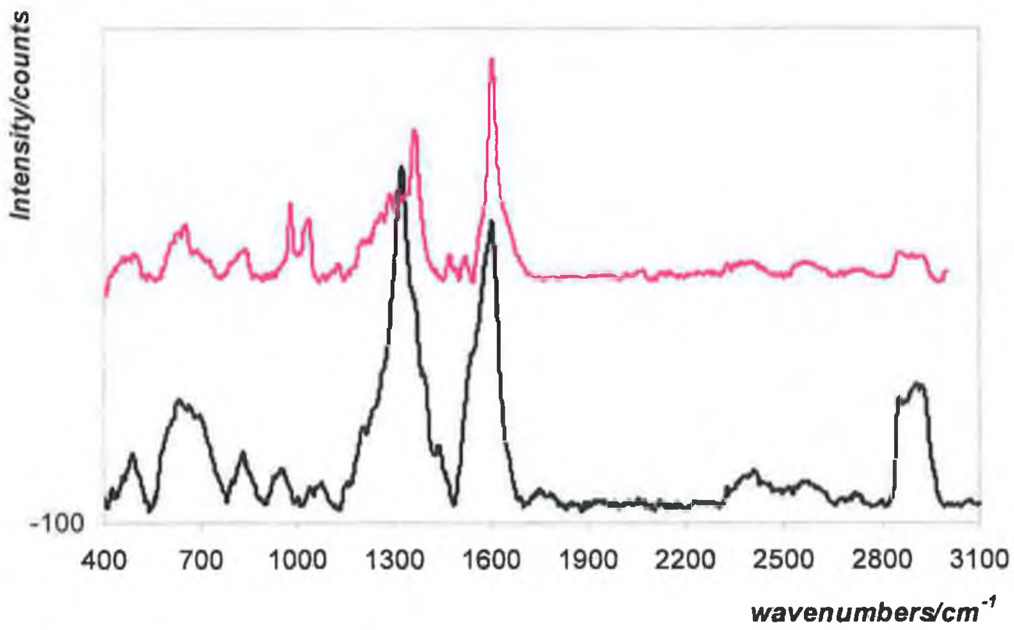

Figure 4.5. *In situ* (purple line) and *ex-situ* (black line) SERS of β-CD-SH on roughened gold polycrystalline macroelectrode (2mm diameter) at 632 nm. For the *in-situ* experiment, the electrolyte solution is an aqueous 0.2M Na_2SO_4. Reference electrode: Ag/AgCl, KCl sat. Counter electrode: platinum wire

In the *in-situ* measurements, the Raman spectra confirm that the monolayer is present. The modes at 2869 cm^{-1} are still visible, confirming that the CDs are likely oriented with the alkane chain closer to the surface. However, the profile in the range between 1200-1000 cm^{-1} changes, with peaks more intense and better defined that can be assigned to CH_2 modes. This could be explained by the presence of a contacting aqueous solution that causes the thiolated cyclodextrins to fully extend off the electrode surface.

Effect of the applied potential on SERS spectra

The applied potentials were chosen in order to be more positive and more negative than the OCP (0V). The external potential was applied by connecting a CHI potentiostat-galvanostat workstation to the cell containing the modified electrode. The potential was stepped and the consequent flowing current monitored. When the current reached a plateau the Raman experiment was started and the spectra accumulated. Figure 4.6 shows the effect of the applied potential on the monolayer structure in 0.2M Na_2SO_4. The peak at 920 cm^{-1} is due to the electrolyte, Na_2SO_4, and can be used as internal reference to discuss the relative intensities of the peaks at the different potentials.

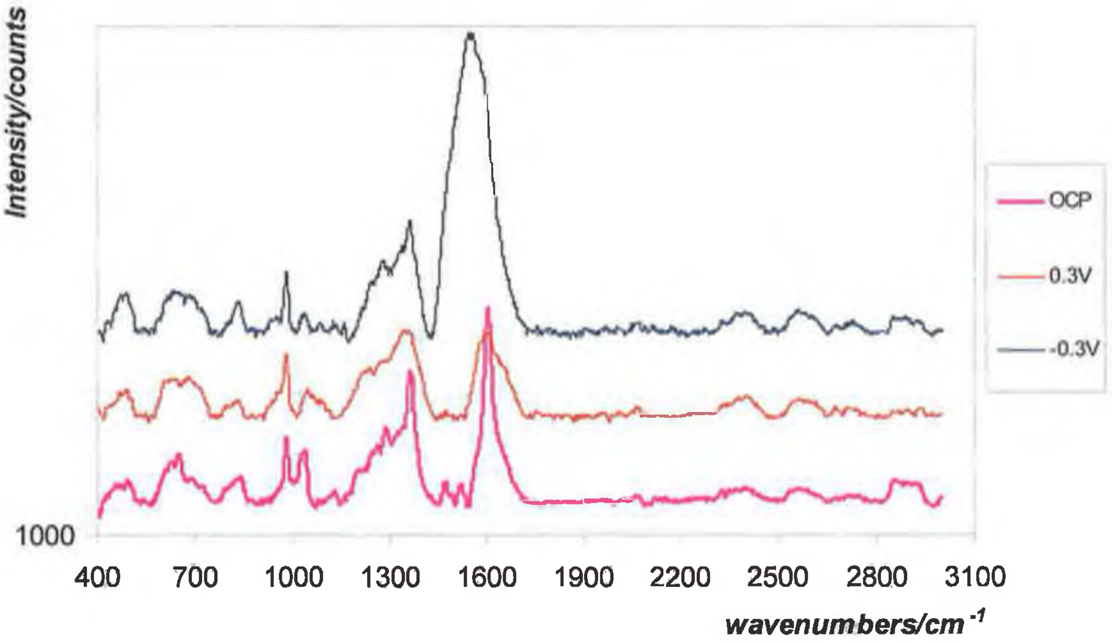

Figure 4.6 *In situ* SERS of β-CD-SH on roughened gold polycrystalline macroelectrode (2mm diameter) at 632 nm at OCP (0V, purple line), 0.3V (red line) and -0.3V (blue line) in an aqueous 0.2M Na_2SO_4. Reference electrode: Ag/AgCl, KCl sat. Counter electrode: platinum wire.

The intensity of peaks between 2869 and 2920 cm^{-1} changes by switching from the OCP, at 0V, to -0.3 and 0.3V, while the profile between 1200 and 1500 cm^{-1} does not show any particular change. The peak at 1015 cm^{-1} become less intense and defined by applying an external potential, while the peak at 1604 decreases at 0.3V and is extremely intense at -0.3V and red shifted. Moreover, a peak at 850cm^{-1} is better defined at -0.3V compared to the OCP. These observations are consistent with an effect of the applied potential on the whole structure of the adsorbed monolayer, since vibrations of either the alkyl chain or the cyclodextrin head are affected. Therefore, the experiments suggest that by applying an external potential 1) the monolayer is still present at the interface, 2) there is an internal reorientation of the molecules within the monolayer, as supposed from the results obtained with cyclic voltammetry which is reversible. However, it is not possible to quantify by Raman spectroscopy the reorientation of the molecules within the monolayer in detail.

4.2.3 Surface coverage determination by reductive desorption

As suggested first by Schneider[11] and later by Yang[10], the charge associated with the desorption of a monolayer consists of capacitive and faradic contributions. The calculation of the faradic charge, Q_f, was performed by subtracting the charge due to the double layer charging, Q_{cap}, from the total charge under the reductive peaks, Q_r:

$$Q_f = Q_r - Q_{cap} \tag{4.3}$$

The electrochemical reductive desorption charge determination is significantly complicated by the simultaneous passage of double layer charging current during the desorption process. Moreover, the capacitive charge has two contributions, the double layer charge of the coated electrode and the charge associated to the diffuse layer of the uncoated electrode.

Assuming that the coated electrode behaves as a pure capacitor, then, the charge accumulated by scanning from potential E_1 to potential E_2, before the desorption potential, can be expressed as:

$$Q_c = C_c(E_2 - E_1) \tag{4.4}$$

where Q_c is the capacitive charge for the coated electrode (C), C_c is the capacitance of the film (F) and E_1 and E_2 are the initial and final potentials (V).

Similarly, for an uncoated electrode the following equation can be used:

$$Q_u = \sum_{i=1}^{n} C_i dE \tag{4.5}$$

where dE is the potential step of the experiment (0.05 V) and C_i is the differential capacitance of the uncoated electrode at each step *i* (F). Therefore, performing AC voltammetry experiments, for coated and uncoated electrodes, allows the total capacitive charge, Q_{cap} to be determined.

As described in Chapter 2 it is possible to convert impedance measurements into capacitance values, by means of Equation 2.3. A frequency of 962 Hz was imposed to the ac potential, at which the behaviour of the cell is purely capacitive. The amplitude was 0.005V for the ac potential and a potential step of 0.050V for the dc potential. Figure 4.7 shows the results obtained for an uncoated electrode scanned between -0.7 and -1.4V and a coated electrode from 0 to -0.5V, in 0.5 M KOH:

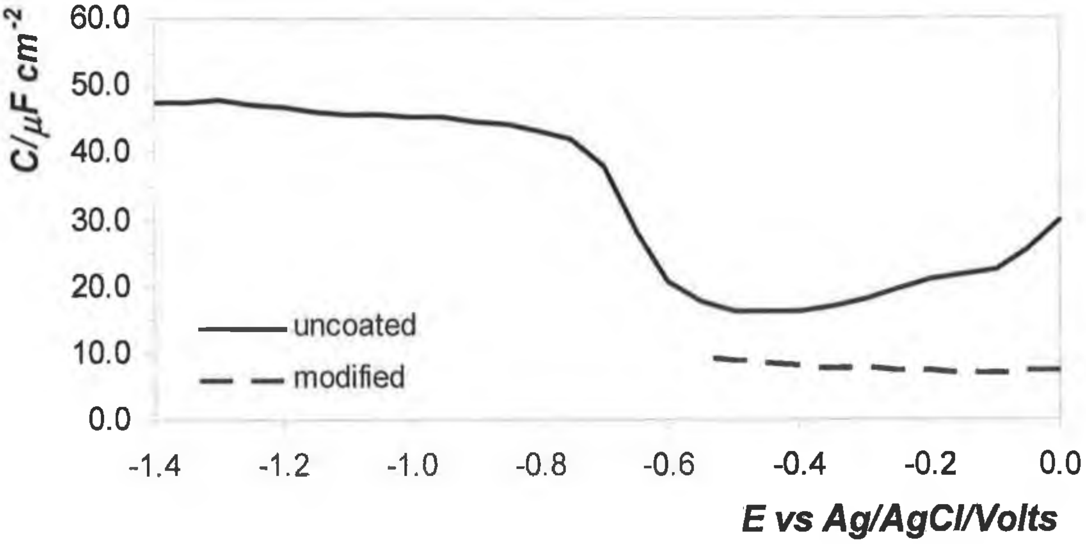

Figure 4.7 AC voltammetry of an uncoated (top) and a coated (bottom) gold polycrystalline macroelectrode (2 mm diameter) in 0.5 M KOH with frequency = 962Hz, amplitude= 0.005V and potential step= 0.05V.

It is clear, from Figure 4.7, that the assumption of treating the coated electrode as a pure capacitor is appropriate, since its capacitance profile is potential independent, in the range observed. Moreover, as expected, the capacitance of the modified electrode with an organic layer is lower than the value for the unmodified electrode, when in contact with an electrolyte. As it can be seen from Figure 4.7, the capacitance of the modified electrode in the range of potentials between 0 and -0.5V is about 50-60% lower than the capacitance of the uncoated electrode.

By applying Equation 4.5, the capacitive charge for the uncoated electrode was calculated to be 26±6 μC cm^{-2}, in the range of potentials between -0.7 and -1.4V. For the coated electrode, the capacitive charge value in the same range of potentials was extrapolated from the values obtained between 0 and -0.5 V by applying Equation 4.4, resulting in a value of 4.8±0.8μC cm^{-2}, which is in a good agreement with literature values for modified interfaces[10]. In order to calculate the final capacitive charge, the contributions from the coated and the uncoated capacitive charge at each potential should be determined. However, it is not possible to obtain this information from the CV and, therefore, assumptions need to be made. From Figure 4.3, it is clear that the current profile in the desorption range of potentials does not behave as expected for an ideal capacitor, since the baseline shows a decrease indicating that the double layer capacitance tends towards the bare electrode value as desorption proceeds. Thus, the final faradaic charge, Q_f, can be calculated by subtracting the capacitive charge of the uncoated electrode from the integrated area under the two reductive peaks, Q_r. The surface coverages are determined by applying the following equation.

$$\Gamma = \frac{Q}{nFA} \qquad (4.6)$$

Assuming n=1 a mean value for Γ was calculated to be $1.6 \pm 0.9 \times 10^{-10}$ mol cm^{-2}. The large uncertainty reflects the difficulties associated with accurately measuring the baseline as well as differences in the desorption peak shapes and potential.

In the literature**Error! Bookmark not defined.** the outer diameter of the β–CD is reported to be 15Å, which gives a projected area of 176Å^2 per molecule and a surface coverage of 8.11×10^{-11} mol cm^{-2} for a hexagonal full-packed monolayer. Alternatively, the average experimental surface coverage gives a value for the projected area of 104 Å^2. Values for the surface coverages in literature for short alkanethiols, such as mercaptobutanol and mercaptohexanol are 7.5×10^{-10} and 9×10^{-10} mol cm^{-2} respectively. Thus, it appears that although the alkanethiols have surely an effect in the structure and orientation of the β-CD head group, they cannot pack as closely as in the absence of the β-CD. Weisse *et al.*[16] reported on the determination, by optical methods, of the surface coverage and orientation for mono-thiolated and mixture of multi-thiolated cyclodextrins derivatives on gold substrates. They developed a model for the organisation of the cyclodextrins derivatives in the chemisorbed films which is shown in Figure 4.8.

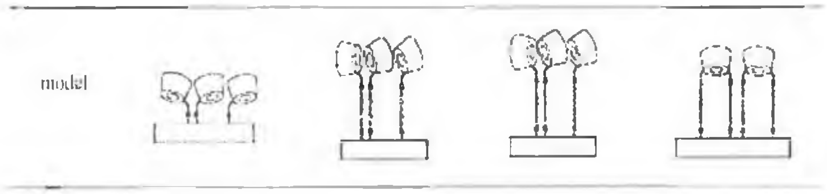

Figure 4.8. Models for the structure of the chemisorbed cyclodextrins films for mono and multi-thiolated derivatives. Adapted from ref 16.

In this model, the beta-cyclodextrin tori are located as an outermost layer on top of the spacers and the spacers are oriented perpendicular to the surface. The spacers in the monothiolated derivatives give freedom to the cyclodextrin tori to align themselves in the top layer, optimising intermolecular hydrogen bonding. The packing density of the tilted cyclodextrins tori increases with increased spacer length. When the spacer is more than one carbon, the tori orientation is not as in the hexagonal closed packed model but more likely in a brick packing model, whose surface coverage is 1.9×10^{-10} mol cm^{-2} [17].

The spacer used in the present work was shorter than the ones reported previously, which allows the CD to orientate in an intermediate situation between a hexagonal and brick packed monolayer. Moreover, the desorption potentials suggest that the monolayer is constituted of at least two diverse structures, which show different lateral interactions within the alkyl chains and likely allow different orientations of the β-CD tori. Finally, Schneider *et al.* [18] showed how the assumption that the reductive desorption of alkanethiols from a surface requires one electron per sulphur atom may not be accurate. By coupling cyclic voltammetry with quartz microbalance experiments they showed a large discrepancy between the amount of material lost during the reductive desorption experiment, as calculated from the charge with n=1, and the mass change monitored with the EQCM. These arguments suggested that a fairly large fraction of the electrochemistry charge must be due to double layer charging and that n could have values different than integer[19, 20].

4.3 Impedance characterisation: the double layer capacitance

Introduction

Reductive desorption is a useful method for measuring the surface coverage but it is destructive. Another way to estimate the surface coverage and defectiveness of the β-CD-SH layer is the monitoring of the blocking behaviour towards an external redox active probe and/or the change in the double layer capacitance after the monolayer adsorption. In the following section, these two techniques are compared to the desorption technique in order to find a correlation that allows them to be used as screening tests.

Since thiol CD monolayers are not electroactive, a way to check the presence of the layers on the substrate surfaces is to monitor the change in the double layer capacitance following the adsorption of the layer. As explained in Chapter 1, when a monolayer of an insulating molecule is adsorbed at the surface of the electrode, the double layer capacitance of the modified electrode drops, due to the fact that the electrolyte molecules are displaced and the dielectric constant of the contacting phase decreases.

Experimental

In section 4.1 the preparation of the substrate, gold polycrystalline macro electrodes, was described. After polishing with alumina and electrochemically cleaning in sulphuric acid, the electrodes were rinsed with milliQ water and the capacitances for the bare electrodes were checked in a daily fresh 0.2 M Na_2SO_4 aqueous solution from -0.5 to 0.5V. Sodium sulphate was chosen as electrolyte for the capacitance measurements because of the low binding constant of sulphate with β-CD. Chamberlain *et al.* [21] reported on the electrostatically-induced inclusion of anions in CD monolayers on electrodes. By monitoring the interfacial capacitance with different electrolytes they found that the larger and more strongly solvated anions like SO_4^{2-}, F^- and H_2PO^{4-} were excluded.

After measuring the capacitance of the bare surfaces, the electrodes were rinsed with copious amount of milliQ water and placed in the deposition solution. The results for six electrodes are shown in Figure 4.9 together with the values obtained at the bare surfaces. Capacitance measurements were performed by AC voltammetry technique. A low frequency of 123 Hz was used. At this frequency the behaviour of the cell is purely capacitive, previously checked by EIS at the OCP. An amplitude of 0.005V was set for the ac potential and a potential step of 0.050V for the DC potential.

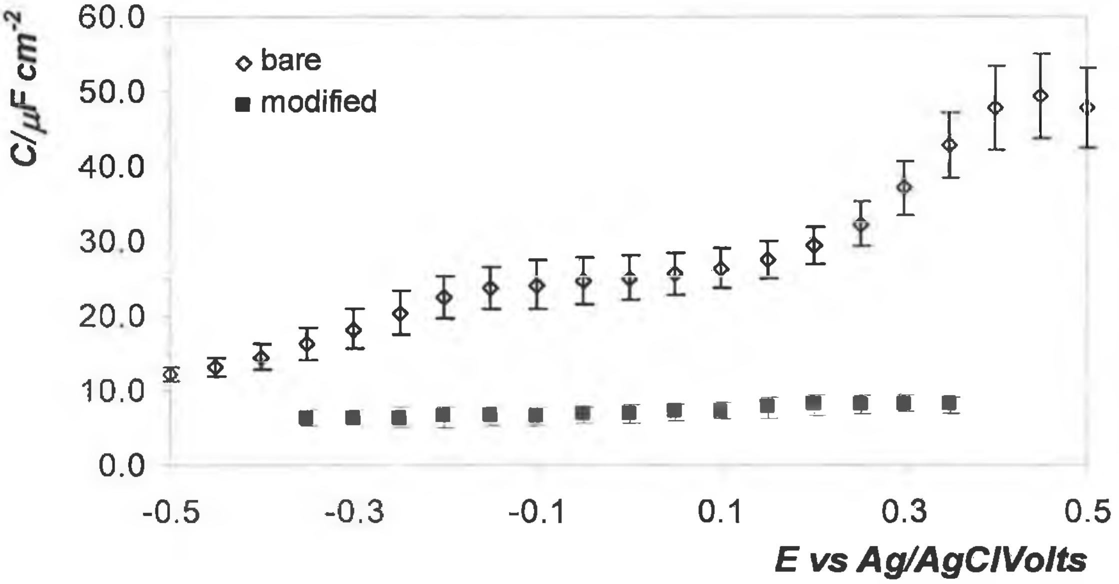

Figure 4.9 Capacitance measurements for bare (top) and β-CD-SH modified (bottom) gold polycrystalline macro electrodes in a 0.2M Na_2SO_4 aqueous solution. AC voltammetry parameters: Amplitude(V)=0.005, Potential step(V)=0.050, Frequency=123Hz. Reference electrode: Ag/AgCl, KCl sat in a salt bridge. Counter electrode: platinum flag.

Figure 4.9 clearly shows that the bare electrode does not behave as a pure ideal capacitor, since the double layer capacitance changes with the applied potential. This is due to reorientation, adsorption or desorption of the electrolyte molecules at different potentials, showing a maximum in the capacitance at 0.3V. The error bars are significant reflecting the heterogeneity of the bare surfaces, probably due to the protocol followed in their preparation, which does not allow a microscopic control of the substrate, and therefore their possible different reactivity.

For the modified electrodes, a drop between 60-87% in the capacitance values can be observed, as expected when an organic film is adsorbed at the surface. The behaviour of the double layer is more similar to an ideal capacitor in the checked range of potentials, being less affected by the applied potential and showing a flat profile. This is mainly due to the fact that the electrolyte molecules cannot reach the electrode surface and undergo reorganisation, changing the double layer structure. The modified electrodes behave as blocked electrodes against the sodium sulphate molecules and limited permeation is observed. The error bars are significantly smaller for the modified electrodes than for the bare electrodes, suggesting that a final similar situation is reached on electrode surfaces with different initial capacitances. This result is somewhat expected since the adsorption of the β-CD-SH is a chemisorption process that likely to displace any weakly bound adsorbates.

The capacitance drop can then be used as a qualitative description of the adsorption, as a preliminary screening to check the presence of the monolayer on the electrode surface. Monitoring the dynamics of adsorption could then give a better insight on the factors dominating the self-assembly.

4.4 Adsorption dynamics

Introduction

As discussed in Chapter 1 the adsorption of a monolayer involves different steps, such diffusion of the molecule to the substrate, binding of the molecule on the surface, either reversibly or irreversibly, reorganisation of the molecules, which can include surface diffusion, lateral interactions and also desorption.

The adsorption of thiols on gold surfaces has been proved to be an irreversible process i.e. a covalent bond is formed between the thiol and the gold substrate. However, initial adsorption is a rapid process and there is significant mobility of the adsorbates on the surface. At longer times, defects anneal and a more stable, less mobile structure is created. By monitoring the time dependence of the surface coverage, the mechanism of the adsorption can be understood, and the contribution of each process, can be determined.

As previously mentioned, the formation of non-electroactive monolayers can be monitored by capacitance measurements. i.e. by monitoring the change in the double layer capacitance when an organic film is forming. EIS is a powerful technique that allows following the profile of the impedance of a system vs. time. Then, as described in Chapter 2, the imaginary part of the impedance is used to calculate the capacitance of the system.

Experimental

The measurements were performed at the OCP of the cell in order to avoid any effect of the potential on the adsorption dynamics. A frequency of 123Hz was chosen together with an amplitude of the AC voltage of 0.005V and a deposition time from 3h to 1 day. The polycrystalline gold macroelectrodes were polished and electrochemically cleaned as previously described. Then, they were placed in a freshly prepared 0.2M Na_2SO_4

solution and left to equilibrate in the free β-CD electrolyte solution in order to reach a plateau and therefore a stable initial situation for the adsorption to be studied. Figure 4.10 shows the results for a polycrystalline gold macroelectrode in a 90μM aqueous solution of β-CD-SH, 0.2M Na_2SO_4 for a deposition time of 3h. This figure reveals that the rate of capacitance decrease drops dramatically for deposition times longer than about 2,000 s. However, a true constant plateau is not observed.

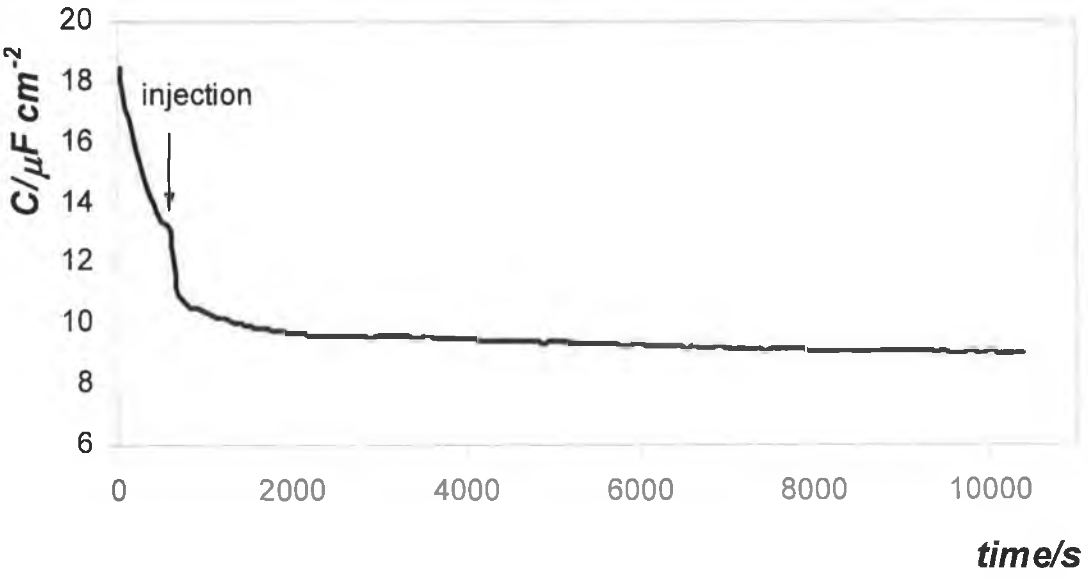

Figure 4.10. Capacitance measurements *vs.* time for a bare polycrystalline gold macroelectrode, in a 90μM aqueous solution of β-CD-SH, 0.2M Na_2SO_4. EIS parameters: E = OCP, Amplitude(V)= 0.005, Frequency= 123Hz. Reference electrode: Ag/AgCl, KCl_{sat} in a salt bridge. Counter electrode: platinum flag.

In order to apply the fitting models it is necessary to convert the capacitance values into θ, fraction of surface coverage.

A linear relation between capacitance and surface coverage is assumed[22] and the following equation is applied:

$$\theta = \frac{(C_i - C_t)}{(C_i - C_f)} \qquad (4.7)$$

where C_i is the capacitance at the injection time, C_t is the capacitance at each time and C_f is the capacitance at the end of the experiment (F). Figure 4.11 shows experimental θ *vs.* time profiles and best fits obtained to various adsorption models..

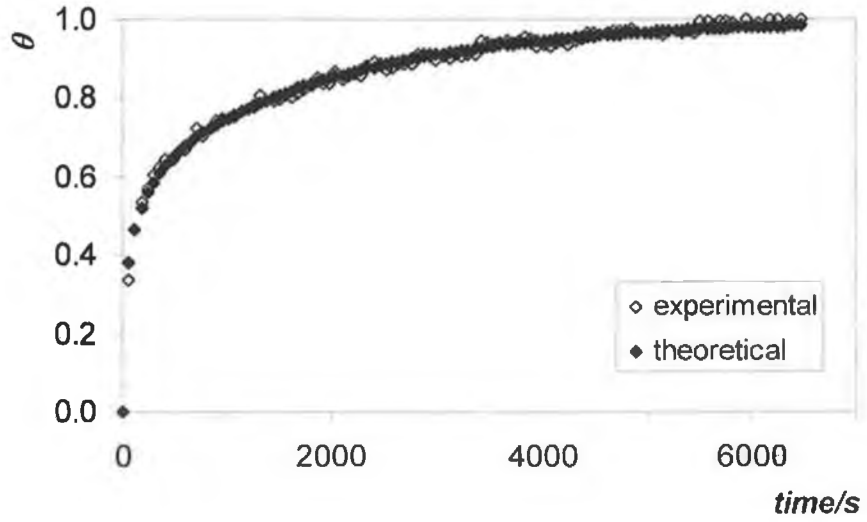

Figure 4.11. Variation of θ with time for a gold polycrystalline macroelectrode in a 100 μM aqueous solution of β-CD-SH, 0.2M Na_2SO_4; experimental (open squares) and fitted values (black squares, model 6, double exponential). Reference electrode: Ag/AgCl, KCl sat in a salt bridge. Counter electrode: platinum flag.

4.4.1 Curve Modelling

It can be seen that the adsorption process has two main components, one very fast which develops in the first 30 minutes and a second one, with a smaller rate constant. This two-stage assembly process yields an equilibrium surface coverage after approximately 3h.

A number of models sourced from literature were fitted to the experimental data[22 23 24]

1. kinetically controlled Langmuir model
2 diffusion controlled Langmuir model
3 second order kinetically controlled model
4 Purely diffusion controlled adsorption
5 Elovich adsorption model
6 A double exponential combining 1 and 2

The following Table summarise the equation describing the models:

Model	***Equation***
Kinetically controlled Langmuir model	$\Gamma(t)=\Gamma_{\max}\left[1-\exp(-k_{ads}t)\right]$
Diffusion controlled Langmuir model	$\Gamma(t)=\Gamma_{\max}\left[1-\exp\left(-\frac{t}{\tau}\right)^{1/2}\right]$
Second order kinetically controlled model	$\theta(t)=1-\frac{1}{k_{ads}t}$
Purely diffusion controlled adsorptionl	$\theta(t)=C_b\left(\frac{D_{so\ln}t}{2}\right)^{1/2}$
Elovich adsorption model	$\Gamma(t)=\Gamma_{\max}\left[1-\exp(-k_{ads}t)^{\exp(-E/RT)}\right]$
Combined double exponential	$\theta(t)=1-\left[a\exp(-k_{ads}t)+(1-a)\exp\left(-\frac{t}{\tau}\right)^{1/2}\right]$

Models 1,2 and 6 are essentially the same ones applied for the adsorption dynamics of CoTpySH on platinum in Chapter 3 and discussed in Chapter 1. For these three models an irreversible statistical adsorption with no following desorption is assumed. In model 1 the limiting step is the rate of adsorption and in model 2 the mass transport of the molecule to the surface. Model 4 is a purely diffusion system which does not take into account saturation of the surface, and therefore it cannot properly describe the system. Model 5 is essentially model 1 corrected by a factor which takes into account an energy barrier E before binding. The model supposes that the energy increases with increasing the surface coverage, due to increasing lateral interactions. However, Weisser *et al.*[24] found values for this energy for mono and multi-thiolated β-CDs on gold surfaces to be in the range from 0 to 1.8 kJ/mol, which essentially reduces model 5 to model 1.

For each model, the sum square of the residuals between the experimental θ, fractional coverages, and those predicted by the theoretical models was minimised, by having as freely adjustable parameters the rate constants and pre-exponential factors.

Figures 4.12a, b and c show the correlation plots for the best fittings obtained from three of the models:

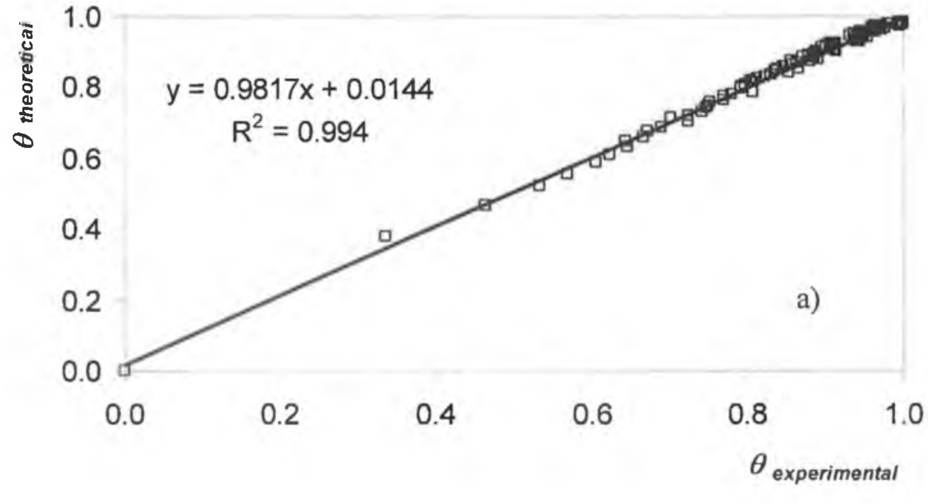

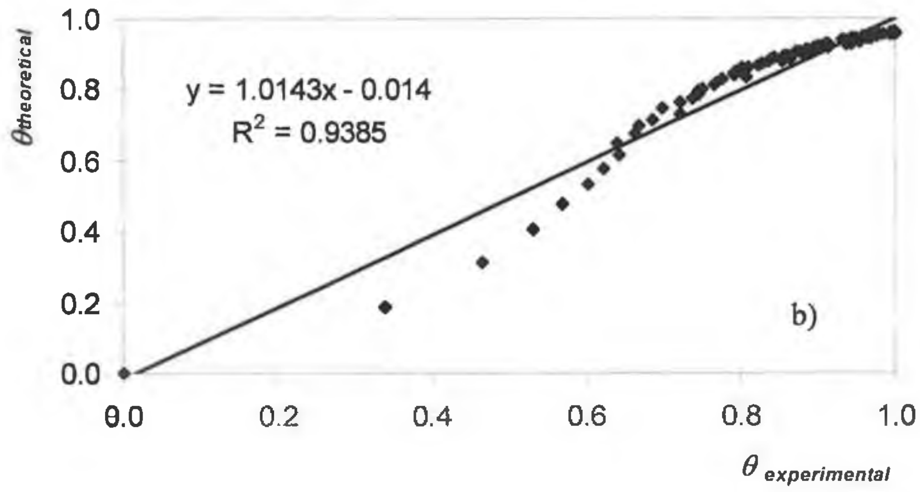

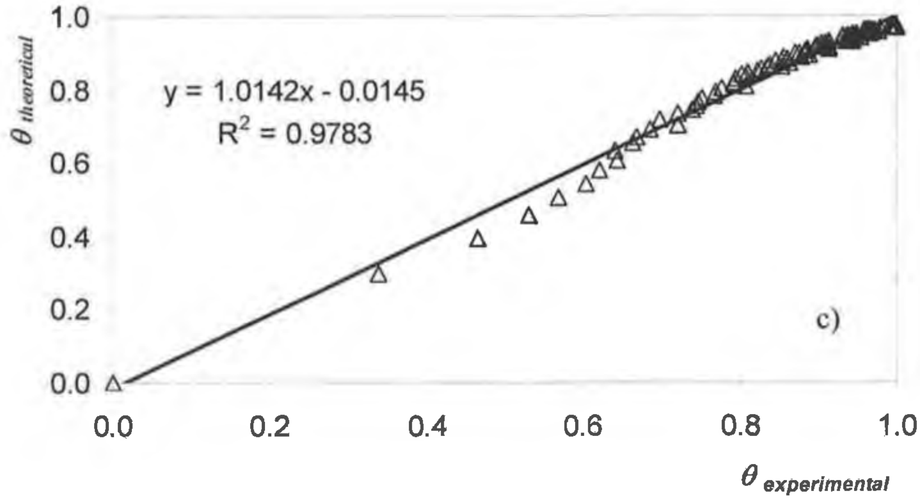

Figure 4.12. Correlation plots between the experimental θ and the best fitted values for double exponential model (model 6, open squares), second order (black squares, model 3) and diffusion controlled model (model 2, open triangles). The black lines are the linear regressions for the three models.

It can be seen that the combination of a Langmuirian diffusion and kinetically controlled adsorption models gives the best results, with a $R^2 = 0.9879$, a slope very close to unity (0.9816) and small intercept (0.15). The fitting equation is the following:

$$\theta = 1 - \left(A\exp\left(-\kappa_K t\right) + \left(1 - A\right)\exp\left(-\kappa_d t^{1/2}\right)\right) \tag{4.8}$$

where A is a pre-exponential factor, κ_K (s^{-1}) is the apparent rate constant for the kinetic controlled adsorption process and κ_d ($s^{-1/2}$) is the rate constant for the diffusion controlled adsorption. The pure diffusion control adsorption is the second model that fits the data properly, suggesting that the reaction has a main diffusive character. Table 4.1 summarises the values for κ_K and κ_d for models 6 and 2.

Table 4.1. Rates of adsorption for models 6 and 2

C/μM	**Model 6**		**Model 2**
	κ_K/s^{-1}	$\kappa_d/s^{-1/2}$	$\kappa_d/s^{-1/2}$
105	2.5×10^{-4}	0.093	0.051
100	4.9×10^{-4}	0.121	0.045
90	2.5×10^{-4}	0.109	0.048

Values for the diffusion coefficient can be calculated by using the mean value of the surface coverage determined in the previous section, knowing that:

$$D = \frac{k_d^2 \Gamma^2 \pi}{4C^2} \tag{4.9}$$

where C is the concentration of β-CD-SH (mol cm^{-3}) and D is the diffusion coefficient ($cm^2\ s^{-1}$). By means of the fitted κ_d values from model 6, D was calculated to be $2.5\pm0.7\times10^{-8}\ cm^2s^{-1}$, which is two orders of magnitude smaller than the value found by Simova *et al.*[25] at 300K for a cyclodextrin concentration of 0.001M in aqueous solutions.

Therefore, as found for CoTpSH in Chapter 3, the diffusion process considered in this model is more likely interfacial rather than through the solution to the electrode surface. This consideration is also supported by the timescale of the adsorption process. In fact, the time required for mass transport of sufficient material to form a monolayer under linear diffusion conditions when the concentration is 90μM and supposing D is 2.6×10^{-6} cm^2 s^{-1}, is less than 1s, indicating that mass transport to the surface is not rate determining. The molecules are therefore thought to diffuse to the electrode surface from the bulk and then diffuse over the electrode surface where they undergo an internal reorganization. The fact that, likely, different crystalline faces constitute the surface is supportive of a mechanism of interfacial diffusion.

Therefore, the adsorption has an irreversible character which is interfacial diffusion controlled and kinetically controlled at different timescales of the experiment.

4.5 Blocking behaviour

Introduction

The main goal in blocking experiments is to understand the roles played by different charge transfer processes that operate whenever a freely diffusing redox species encounters a monolayer coated electrode, namely long-range electron transfer, permeation across the film and charge transfer at the pinholes. Long-range electron transfer, tunnelling, is usually observed at well packed, defect-free and stable alkanethiols monolayers and usually shows a strong dependence on the alkyl chain. As previously shown, the presence of a bulky head group as the β-CD does not allow the alkyl chains to closely pack. Evidence for ion permeation into short alkanethiols monolayers was reported by Porter *et al.*[26], showing the dependence of the differential capacitance on the hydrocarbon chain length and nature of the supporting electrolyte.

Here, two different redox couples $K_4Fe(CN)_6$ and $Co(tpy)_2(PF_6)_2$ with different solubility properties were used as external probes in blocking experiments. The hydrophilic $K_4Fe(CN)_6$ should exhibit greater blocking by the layer since the only way to approach the surface is through defects . The hydrophobic $Co(tpy)_2(PF_6)_2$ could not undergo permeation into the CD cavity.

The blocking experiments were performed in 0.2M Na_2SO_4, at which pH (ca. 7) the CDs are neutral[10] and therefore the electrostatic contribution to the blocking behaviour should be minimized.

4.5.1 Cyclic voltammetry of $K_4Fe(CN)_6$

$K_4Fe(CN)_6$ is a well known probe[27 28] which undergoes reversible one electron, outer sphere redox reactions in aqueous solutions at bare electrodes. The k° is sufficiently small to produce reversible, quasi-reversible and irreversible responses under accessible conditions. A 2 mM solution of $K_4Fe(CN)_6$ in 0.2M Na_2SO_4 was prepared. Cyclic voltammetry from -0.1 to 0.5 V was performed at different scan rates, ranging from 0.1 to 5 Vs^{-1}, for the bare and β-CD-SH modified gold polycrystalline electrodes. For further reference a nonanethiol modified electrode (denoted C_9S/Au) was also tested. Figure 4.13 shows the normalized current profiles recorded at 0.1Vs^{-1} where the starting potentials are the OCPs.

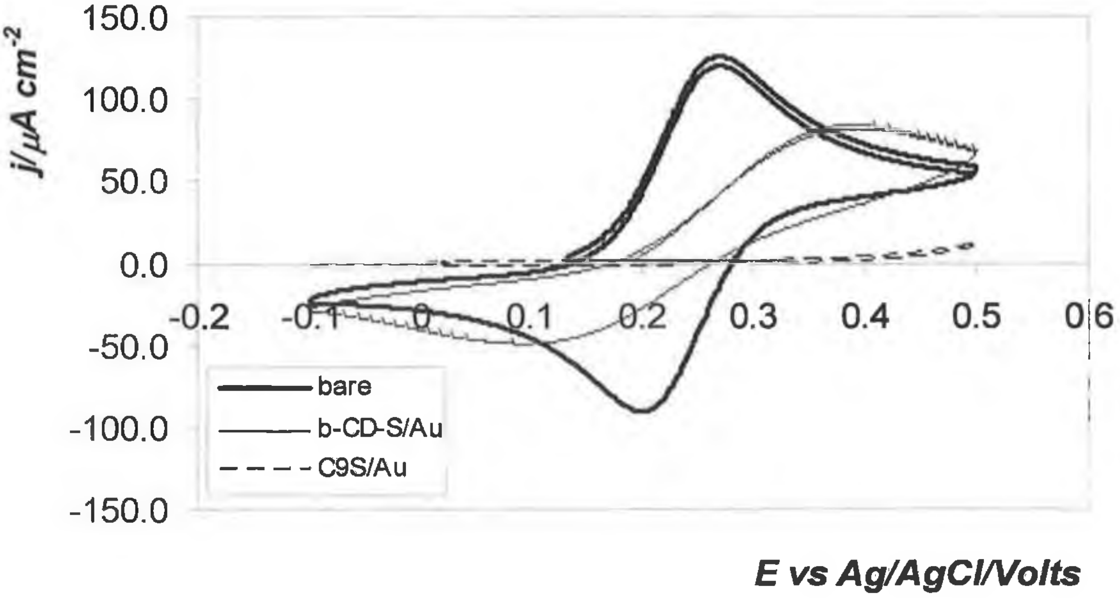

Figure 4.13. Cyclic voltammetry of an aqueous 2mM $K_4Fe(CN)_6$ in 0.2M Na_2SO_4 of a bare (black line), β-CD-SH (thin line) and C_9SH (dashed line) modified gold electrodes. The starting potentials are the OCPs. Scan rate $0.1 Vs^{-1}$. Reference electrode: Ag/AgCl, KCl_{sat}. Counter electrode: platinum wire.

Two limiting cases are visible in Figure 4.13. At the bare gold electrode $Fe(CN)_6^{4-}$ undergoes a reversible oxidation from Fe^{2+} to Fe^{3+} at a potential of 0.235V. The peak-to-peak separation is 0.070±0.005 V which is very close to the ideal value of 0.057V for a one-electron redox reaction under semi-infinite linear diffusion control.

At the opposite extreme, exponential-like voltammograms are obtained at C_9S/Au electrode. The layer is so compact and insulating that the electron transfer rate is dramatically slower. This behaviour is expected when the redox probe remains at the solution side of the monolayer. In particular, the current profile, up to 0.35V, is capacitive while the steadily increasing currents from 0.35 to 0.5V are attributed to tunnelling across the alkanethiol monolayer.

Between these two limiting situations, the β-CD-S/Au electrode shows an intermediate behaviour, with a drop in the peak currents together with a shift in peak potentials with respect to the bare electrode. The peak-peak separation increases up to 0.323V. The shift suggests that the phenomenon is due to slower kinetics of electron transfer. In fact the electron transfer is hindered by the presence of the β-CD-SH layer but can still occur at overpotential of ca. 0.150V. The high currents obtained, as compared to the results obtained for C_9S/Au, indicate that some penetration of the redox probe occurs at layer, due to the presence of defects or the nature itself of the layer, which allows for a closer approach of the probe to the electrode surface. The CVs are highly reproducible suggesting a reproducible monolayer structure.

4.5.2 Stability of the layers: timescale

Cyclic voltammetry of the layers was performed in 2 mM $K_4Fe(CN)_6$ in 0.2M Na_2SO_4 by repetitively cycling (every 2, 5 and 20min) between -0.05 and 0.5V at 0.2V s^{-1} for 1h. Some of the layers showed a certain level of permeation and Figure 4.14 shows the results for 1h cycling.

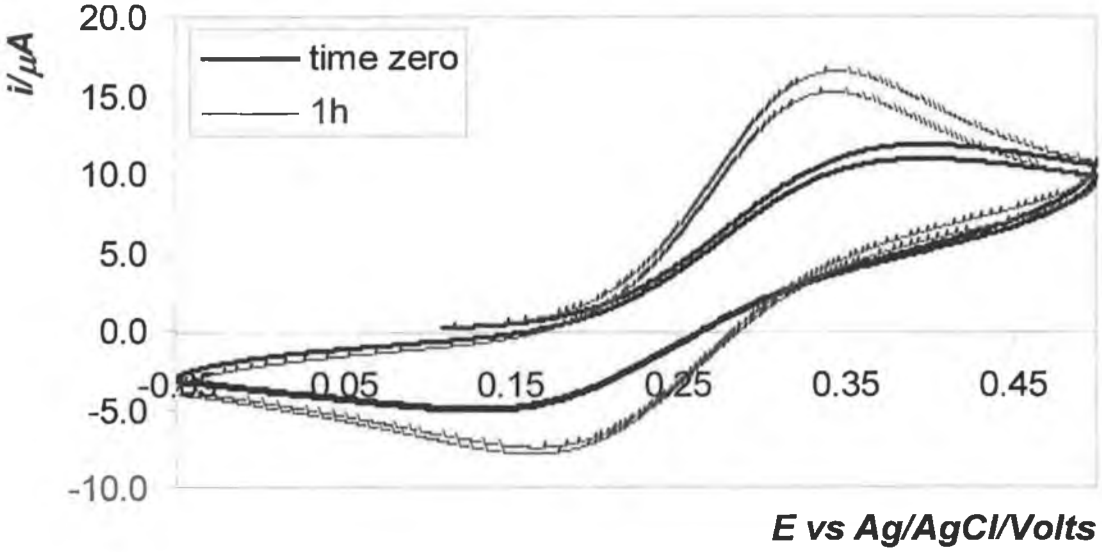

Figure 4.14. Cyclic voltammetry of an aqueous 2mM $K_4Fe(CN)_6$ in 0.2M Na_2SO_4 of β-CD-SH modified gold electrodes at time zero (black line) and after 1h of cycling (thin line). The starting potentials are the OCPs. Scan rate $0.2Vs^{-1}$. Reference electrode: Ag/AgCl, KCl_{sat}. Counter electrode: platinum wire.

By comparison of Figures 4.14 and 4.13 it can be seen that the potentials shift back towards the reversible values and the currents increased and become more peaked after repetitive cycling. The peak-peak separation comes back to 0.180V and the anodic overpotential drops to 0.070V. This is a consequence of some sort of permeation of the redox probe which is more pronounced for the Fe^{2+}oxidation state, which is more hydrophobic. However, permeation affects the layer partially since the final CV after one hour of cycling are still more similar to those expected for a blocked interface than for a bare electrode. Reductive desorption experiments were ran after 1h cycling in 0.5M KOH to check the presence of thiol layers and Figure 4.15 shows the results.

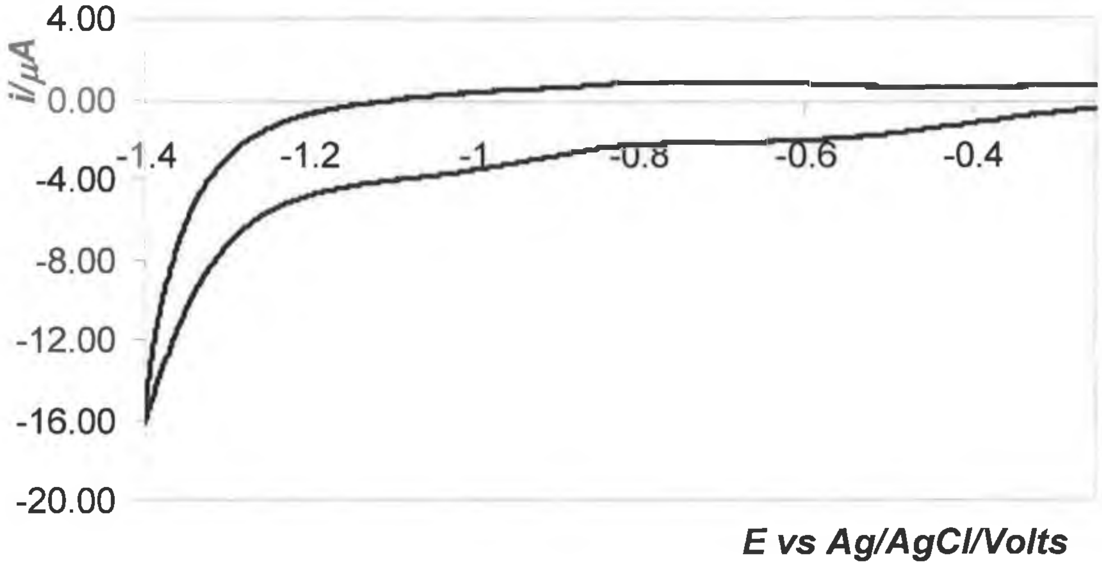

Figure 4.15 Reductive desorption in 0.5M KOH of β-CD-SH monolayer on polycrystalline macroelectrode after 1h cycling in 2mM $K_4Fe(CN)_6$, 0.2M Na_2SO_4. Scan rate: $0.1Vs^{-1}$. Reference electrode: Ag/AgCl, KCl sat in a salt bridge. Counter electrode: platinum wire.

In general the reductive peak magnitude was noticeably reduced, sometimes hardly detectable, together with a shift of the peak potentials to more positive values, around -1V and -0.6V. The decrease of the peak currents together with the shift in potentials suggests that some instability was introduced in the layers, due to repetitive scans. It was not possible to determine the surface coverages of the layers and therefore to say if the cycling triggered desorption of the thiol molecules or just introduced disorder and instability.

The stability experiment shows how the time scale of the inclusion experiment is of primary importance in order to guarantee the presence of the β-CD-SH layer on the electrode surface.

4.5.3 Stability of the layers: potential window

Capacitance measurements were performed by AC voltammetry technique, at a frequency of 123Hz, amplitude of 0.005V and a potential step of 0.050V, by progressively increasing the positive potential from 0.4 to 0.6V. Figure 4.16 shows the profiles of C *vs.* E.

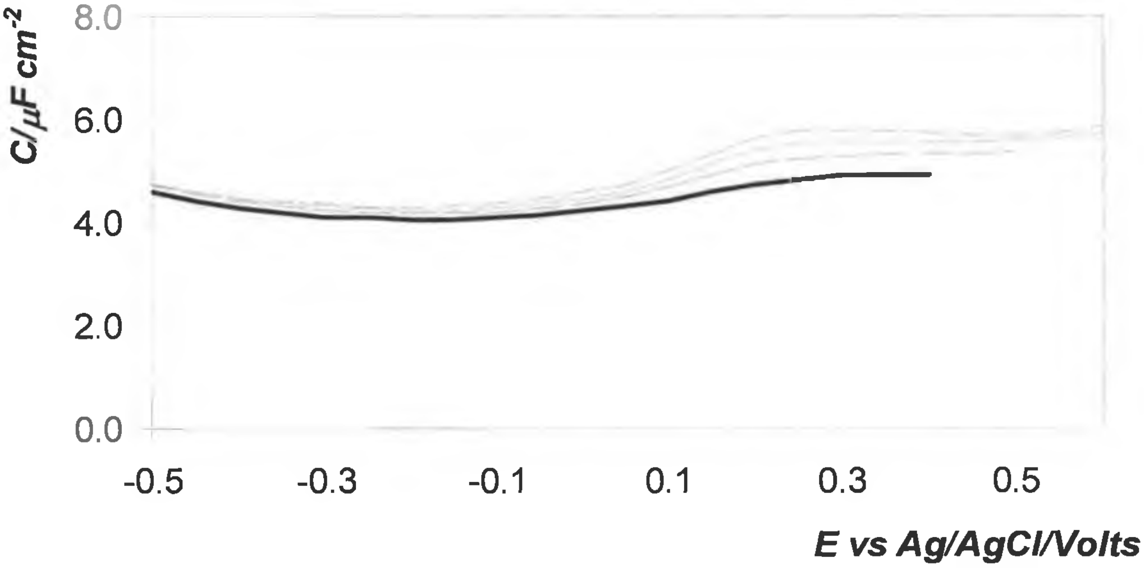

Figure 4.16. Capacitance measurements for β-CD-SH modified gold polycrystalline macro electrodes in 0.2M Na_2SO_4 aqueous solution from -0.5 to 0.4V (black line), from -0.5 to 0.5V (dashed line) and from -0.5 to 0.6V (dotted and dotted-dashed line. AC voltammetry parameters: Amplitude(V)=0.005, Potential step(V)=0.05, Frequency=123Hz. Reference electrode: Ag/AgCl, KCl sat in a salt bridge. Counter electrode: platinum flag

As it can be seen, increasing the positive range of potentials by 0.2 V produces an overall increase of the capacitance of ca. 1μF cm^{-2}. By comparing Figure 4.16 to the bare electrode capacitances in Figure 4.9 in the range of potentials between 0.4 and 0.5V, it can be said that this change is almost negligible, being slightly bigger than the error bars magnitude. Therefore, gold oxidation, which is supposed to start at 0.6V and to destabilise the monolayer, does not have a major effect on the adsorbed β-CD molecules, in the timescale of the experiment. Thus, when monitoring the inclusion reaction a potential window of ca. 1V, from -0.5 to 0.6V, can be used without desorbing the CD monolayer.

4.5.4 Cyclic voltammetry of $C(Tpy)_2(PF_6)_2$

The blocking behaviour towards a more hydrophobic redox couple,$[Co(tpy)_2](PF_6)_2$, (denoted CoTpy) was also tested. The probe was chosen due to its similar geometry and physical properties to the complex to be used for the inclusion reaction. However, CoTpy should not include in the β-CD cavities since its diameter is bigger than the CD cavity size[29]. Again, the hydrophilicity of the probe and then the permeability features of the layer have been tested. Micromolar solutions (ca. 500μM) in 0.2M Na_2SO_4, 90:10 milliQ water/acetonitrile were prepared, by dilution of millimolar solutions of the probe in pure acetonitrile. Figure 4.17 shows the CVs obtained at the bare and β-CD modified polycrystalline gold macroelectrodes at $0.1Vs^{-1}$.

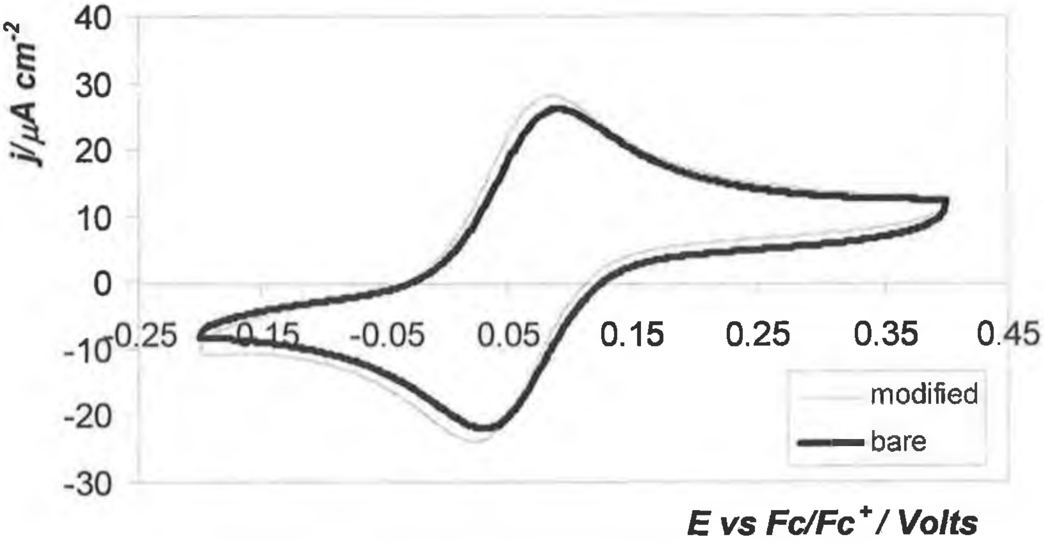

Figure 4.17. Normalised cyclic voltammetry of a 500μM $Co(tpy)_2(PF_6)_2$, 0.2M Na_2SO_4, 90:10 milliQ water/MeCN for a bare (thick line) and β-CD-SH (thin line) modified gold macro electrodes. The starting potentials are the OCPs. Scan rate: $0.1Vs^{-1}$. Reference electrode: Ag/AgCl, KCl_{sat}. Counter electrode: platinum wire.

At the bare electrode the redox couple shows a reversible behaviour, with ΔE_p= 0.062±0.005 V and $E^{\circ\prime}$= 0.061±0.005 V. Significantly, reversible voltammetric waves were also detected at the β-CD-S/Au electrode. In particular, ΔE_p= 0.061±0.005V and $E^{\circ\prime}$= 0.054±0.005 V. At the modified electrode the currents are slightly *enhanced*, while the formal potential is shifted of less than 0.010V towards more negative values. Since both the anodic and cathodic peak potentials are shifted, the effect likely has a thermodynamic rather than a kinetic character and oxidation of the probe is somewhat easier at the modified surface rather than the bare. The rate of electron transfer at the β-CD modified interface appears to be relatively large since the ΔE_p does not change, by changing the scan rate from 0.010 to 0.5 V/s.

In order to check if permeation occurs or if cycling in the presence of the cobalt complex induces disorder or desorption, reductive desorption experiments were run after the blocking experiments. These experiments did not show any particular difference from the results obtained for the desorption of fresh monolayers. Therefore, by cyclic voltammetry it was not possible to check the actual permeation of the molecule through the layer.

Future work could involve the study of the blocking experiment at different time scales and at different probe concentrations, in order to define the limits of the phenomenon.

4.6 Defects characterisation and surface coverage determination by blocking experiments

Introduction

The defects at a modified electrode can be thought as an array of microelectrodes and therefore the theory developed for this system can be used to describe their properties[30, 31, 32].

Consider a one-electron redox reaction in an unstirred solution where only one species, A, is present at time zero:

$$A \overset{k^0,\alpha}{\leftrightarrow} B + e^- \qquad (4.10)$$

where k° is the standard heterogeneous electron transfer rate constant (cm s^{-1}) and α is the transfer coefficient. Initially only species A is present and, by increasing the potential, A is oxidised to B and a depletion (or diffusion) layer grows around each individual disc. The shape and magnitude of the CV are then dependent on different factors, the size of the diffusion layer *vs.* the size of the defects, ϕ, and the distance between the individual defects, d.

Then four situations can happen as shown in Figure 4.18:

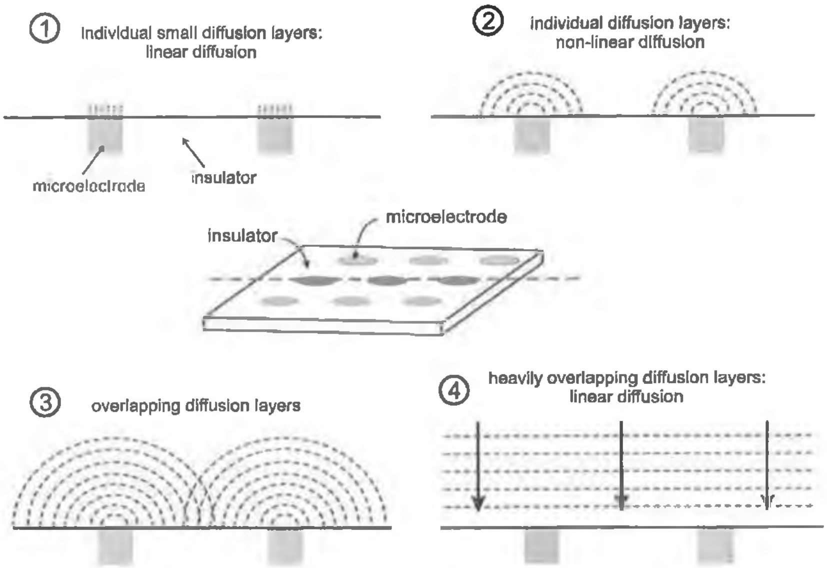

Figure 4.18. Schematic diagram of the four situations of a diffusion profile for an array of microelectrodes/defects. Adapted from ref. 30

In situation 1, at very short time scales, the diffusion layer thickness, δ, is smaller than the size of the defects resulting in a linear diffusion profile. The resulting CV is a scaled-down macroelectrode response. In situation 2, δ is larger than ϕ but not enough to cause two adjacent diffusion layers to overlap. The diffusion layer has a radial profile and the resulting CV is the response of an individual microelectrode multiplied by the number of the defects on the surface. Arrays, like situations 2, produce scan rate independent CVs with steady-state characteristics, for a certain range of scan rates. In situation 3, two adjacent profiles start to overlap and peak currents and scan rate dependence start to appear in the CV as the response becomes controlled by semi-infinite linear diffusion. Finally in situation 4 the diffusion fields overlap completely and linear diffusion predominates.

In terms of modelling the CV response, situation 1 and 4 can be described by planar diffusion methods, while situation 2 can be described by the 2-dimensional microdisk problem. Situation 3 is more complicated since it includes contributions from both radial and linear diffusion..

Amatore *et al.*[33] analysed the four categories for an evenly spaced array of disk-shaped microelectrodes of uniform radii embedded in an insulating plane. They found expressions for the CV shape in terms of two dimensionless parameters A and B, which depend on k°, the scan rate, the fractional coverage, Θ.[34] They reported on limiting cases like reversible CVs, irreversible CVs, with k°_{app} given by the product of k° and (1- Θ), and plateau currents which are independent of scan rate. Switching from one situation (CV shape) to the other is, then, a consequence of the interplay between the scan rate, d, ϕ and the concentration of the redox probe.

4.6.1 CVs simulation

Simulations of the CVs obtained at the bare and modified electrodes at different scan rates were performed by CHI660A software.

Figures 4.19 and Figure 4.20 show the results for a bare and a modified macro electrode respectively at 0.2V/s in a 2mM $K_4Fe(CN)_6$,0.2M Na_2SO_4 solution under semi-infinite linear diffusion conditions.

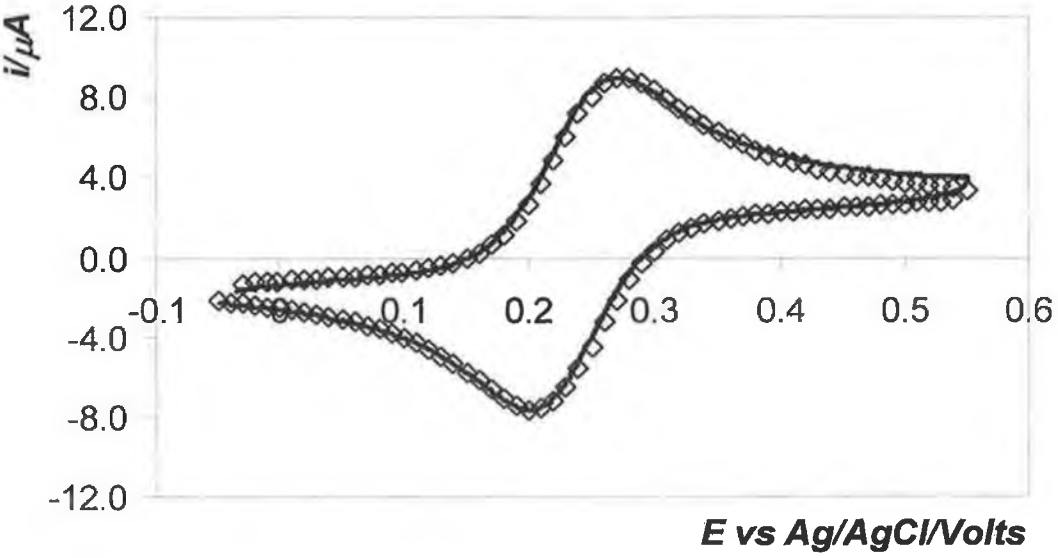

Figure 4.19. Experimental (solid line) and simulated (open squares) CV for 2mM $K_4Fe(CN)_6$,0.2M Na_2SO_4 solution at a bare electrode at 0.2 V/s. Reference electrode: Ag/AgCl, KCl sat in a salt bridge. Counter electrode: platinum wire.

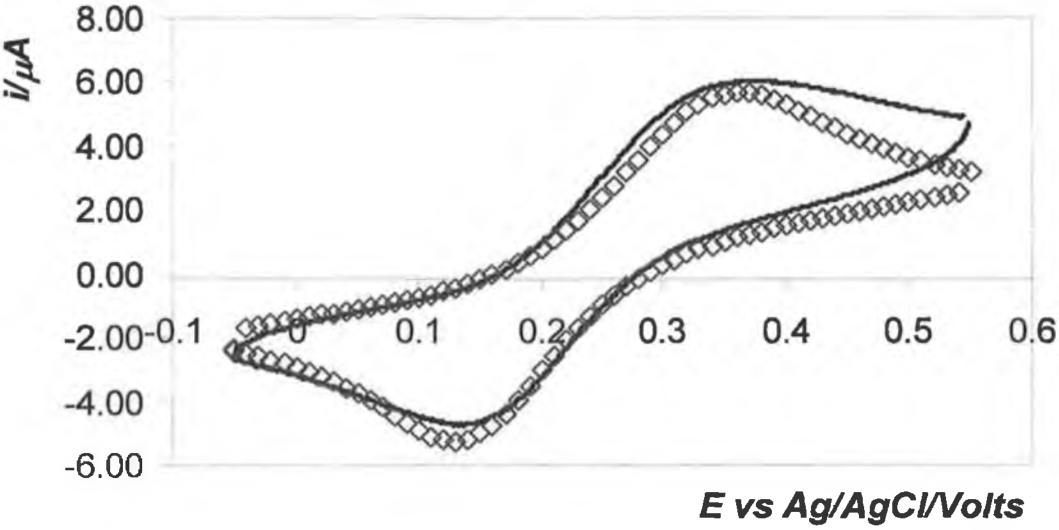

Figure 4.20. Experimental (solid line) and simulated (open squares) CV for 2mM $K_4Fe(CN)_6$,0.2M Na_2SO_4 solution at a modified electrode at 0.2 V/s. Reference electrode: Ag/AgCl, KCl sat in a salt bridge. Counter electrode: platinum wire

For the bare electrode, as shown in Figure 4.19, where the diffusion is assumed to be planar and the reaction is reversible in the experiment time-scale, the agreement between the experimental data and the fitting is good.

For the modified electrodes, as shown in Figure 4.20, the agreement between theory and experiments is poorer, because the fitting program does not take into account the contribution from radial diffusion. Particularly defect free layers could be obtained showing blocking behaviour at 0.010V/s. The simulation could not be performed for such packed monolayers and the surface coverages were then calculated by reductive desorption. However, in general, a good correlation between the blocking experiments and the values obtained by desorption was found, allowing to chose those electrodes that exhibited good blocking.

Table 4.2 summarises the parameters used to simulate the bare and two modified electrodes, denoted as mod1 and mod2. The fitting values reproduce very well the bare electrode in a range of scan rate between $0.010Vs^{-1}<v<1Vs^{-1}$ while for the modified electrodes the range is $0.1Vs^{-1}<v<0.5Vs^{-1}$.

Table 4.2. Simulation parameters for bare and modified electrodes in a 2mM $K_4Fe(CN)_6$,0.2M Na_2SO_4.

	$k°/$ cm s^{-1}	$E°/V$	α	$C_{Fe^{2+}}$ /M	$D_{Fe^{2+}}$ / $cm^2\ s^{-1}$	$D_{Fe^{3+}}$ / $cm^2 s^{-1}$	*Area*/cm^2	C_{dl} / μF
bare	9×10^{-3}	0.238	0.5	0.00135	8.5×10^{-7}	9×10^{-7}	0.064	1.2
Mod1	4.2×10^{-4}	0.235	0.55	0.00135	1×10^{-6}	1×10^{-6}	0.052	1.2
Mod2	8.2×10^{-4}	0.235	0.5	0.00135	1×10^{-6}	1×10^{-6}	0.1	1.3

The k° values for the bare electrode is in good agreement with literature values[35]. The diffusion coefficients were calculated as previously described in Chapter 3 and a value of 8.4×10^{-7} cm^2 s^{-1} was obtained for both the reduced and oxidized forms. These values are in excellent agreement with the simulated values. The simulated microscopic areas were compared to those calculated from the reductive peaks in the cleaning CV, which are 0.058 cm^2, 0.062 cm^2 and 0.15 cm^2 for bare, mod1 and mod2 respectively. It can be seen that the matching between experimental and simulated values is in the order of 10-30%. As previously mentioned, the apparent heterogeneous electron transfer rate constant can be related to the standard rate constant by the following equation:

$$k^0_{app} = k^0(1-\Theta) \tag{4.11}$$

where Θ is the fraction of covered area. Application of Equation 4.11 gives values for Θ of 0.953 and 0.911 for mod1 and mod2 respectively, assuming k° value from Table 4.2. When the blocking was observed at 0.02V/s the simulation gave a $k_{app}=3\times10^{-4}s^{-1}$, which in terms of $\Theta=0.992$[36]. The corresponding surface coverages calculated by reductive desorption has a mean value of 1.6×10^{-11} mol cm^{-2}. Thus, the blocking seems to be an efficient and non destructive technique to estimate the packing of the monolayer.

4.6.2 Size and distribution of the defects

In principle, by knowing the fraction of covered area it is possible to describe in terms of size and distribution the defects of a monolayer[36]. Again, assuming evenly spaced array of disk-shaped microelectrodes of uniform radii embedded in an insulating plane, pinhole parameters can be estimated from CVs, by determining the scan rate at which peak current is not longer linear with the square root of the scan rate, i.e. switching from a planar diffusion to a radial diffusion.

Figures 4.21a and b show the shape of the CV at different scan rates when switching from planar diffusion to a situation where contribution from radial diffusion is visible with the typical S-shaped CV.

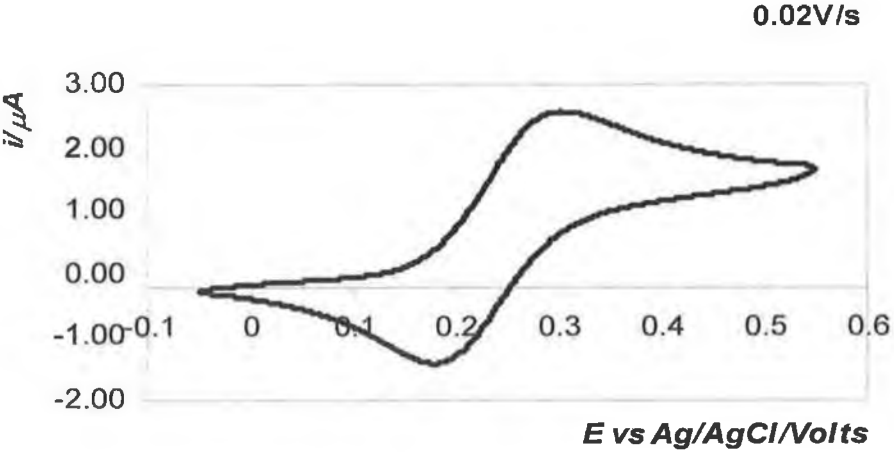

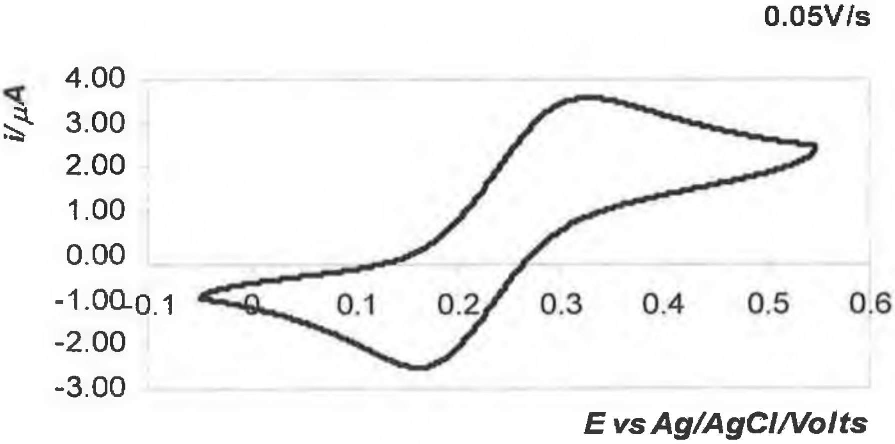

Figure 4.21a. Cyclic voltammograms of 2mM $K_4Fe(CN)_6$,0.2M Na_2SO_4 solution at a modified electrode at 0.02 (top) and $0.05Vs^{-1}$(bottom). Reference electrode: Ag/AgCl, KCl sat in a salt bridge. Counter electrode: platinum wire

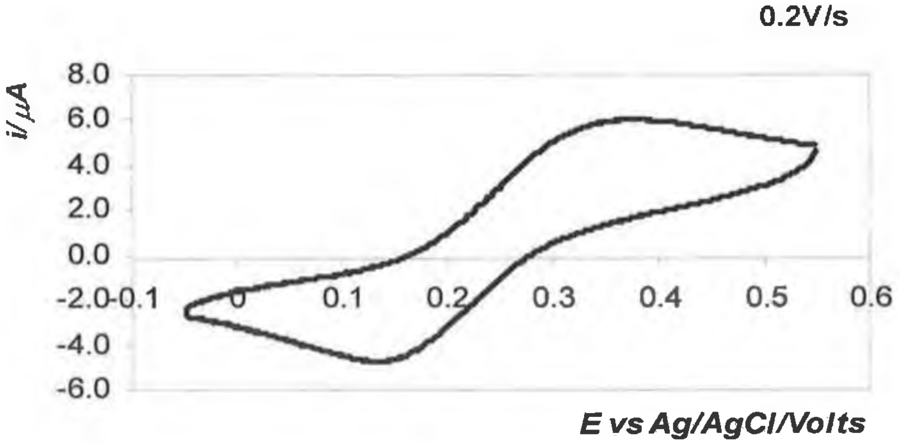

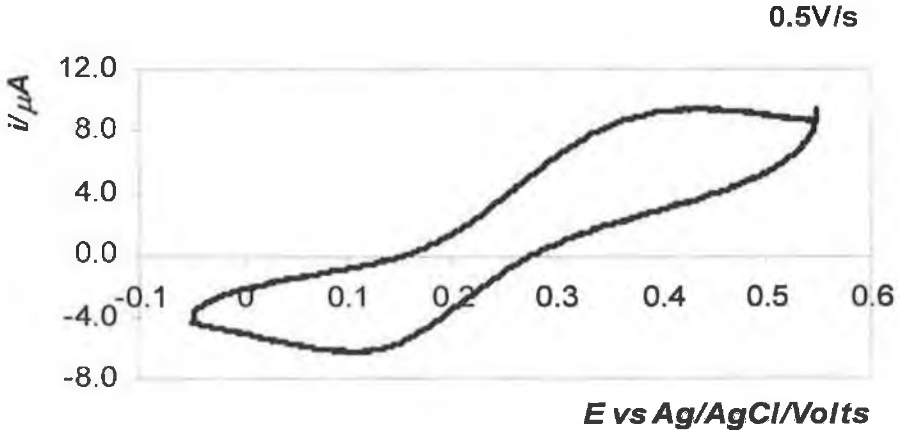

Figure 4.21b. Cyclic voltammograms of 2mM $K_4Fe(CN)_6$,0.2M Na_2SO_4 solution at a modified electrode at 0.2 (top) and 0.5 Vs^{-1}(bottom). Reference electrode: Ag/AgCl, KCl sat in a salt bridge. Counter electrode: platinum wire

The equations describing this method are the following:

$$d \approx \frac{\left(\frac{DRT}{Fv_{max}} \right)^{1/2}}{2.22(1-\Theta)^{-1/2}} \qquad (4.12)$$

$$\phi = d(1-\Theta)^{1/2} \qquad (4.13)$$

where the parameters have the meaning previously described.

Figure 4.22 shows the plot of log i_{peak} *vs.* log v for mod 1.

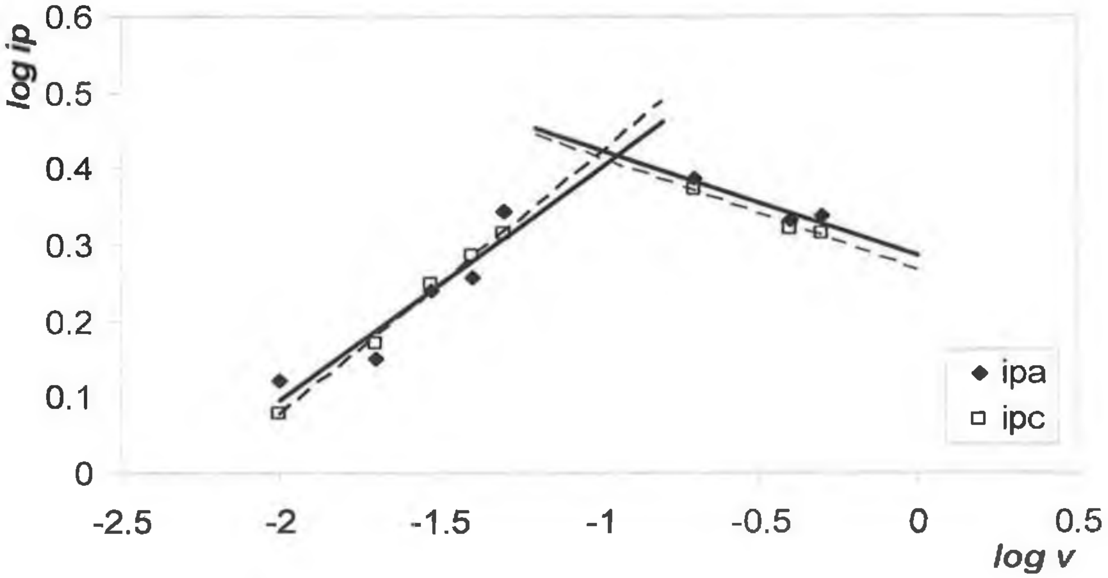

Figure 4.22. Graph of log i_p *vs.* log v for an aqueous 2 mM $K_4Fe(CN)_6$,0.2M Na_2SO_4 solution at a modified β-CD-SH gold electrode for the anodic (black square) and cathodic (open square) showing the switch from a planar to a radial diffusion situation.

It can be seen that the slope of the two linear regression changes. Ideally, radial diffusion should give a log i_p independent on the scan rate, while a decrease is observed. This is mainly due to the difficulty in placing the baseline in the experimental CVs which shown a shape similar to situation 3 rather than 2. The intersection of the two linear regressions is v_{max} and its value is 0.11V/s. Substituting Θ (0.95) and v_{max} in Equations 4.12 and 4.13, a distance between the defects of 500nm and a diameter of 108nm are calculated, ten times the outer diameter of the β-CD-SH. However, these numbers should be treated cautiously since no proof of the evenly distribution of the defects and uniformity of the radius was found. Moreover accurately determining the CV baseline is challenging.

Conclusions

In the present chapter the formation and characterisation of modified gold polycrystalline macroelectrodes with β-CD-SH was shown. The monolayer appears to be well packed, most likely with a mixed character between a hexagonal and brick packed monolayer conformation. Small size defects were detected with blocking behaviour experiments performed with $K_4Fe(CN)_6$. The layer results sensitive to the hydrophilicity of the probe and stable over a wide potential window and timescales of hours.

Therefore the layers results suitable for molecular recognition of electroactive probes in aqueous solutions.

References:

1 Steed J.W., Atwood J.L., *Supramolecular Chemistry: A Concise introduction* , New York, Wiley, **2000**

2 Ciba Foundation Symposium 158, *Host-Guest molecular interactions-from Chemistry to Biology*, Wiley-Interscience, **1991**

3 SemLyen J.A., *Large Ring Molecules*, Wiley and Sons, **1996**

4 Szejtil J., '*Cyclodextrins and their Inclusion complexes'*, Akademiai Kiado, Budapest, **1982**.

5 Leu L., Qing-Xiang G.. *Journal of Inclusion Phenomena and Macrocyclic Chemistry* **2002,** 42,1

6 Ramamurthy V., '*Photochemistry in Organized and Constrained Media*', V. Ramamurthy, Ed., VCH Publishers, Cambridge, UK, **1991**, p. 319.

7 Rojas M.T., Koniger R., Stoddart J. F., Kaifer A. E., *J. Am. Chem. Soc*., **1995**, *117*, 336

8 Henke C., Steinem C., Janshoff A., Steffan G., Luftmann H., Sieber M., Galla H. J., *Anal. Chem*., **1996**, 68, 3158

9 Walczak M. M, Popenoe D. D., Deinhammer R. S., Lamp B. D., Chung C., Porter M. D., *Langmuir*, **1991**,*7* ,2687

10 Yang D.F., Wilde C.P., Morin M., *Langmuir*, **1996**, *12*, 6570

11 Schneider T., Buttry D., *J. Am. Chem. Soc*., **1993**, *115*, 12391

12 Lavrich D. J., Wetterer S. M., Bernasek S. L., Scoles G., *J. Phys. Chem. B*., **1998**, 102, 3456

13 Boubour E., Lennox R. B., *J. Phys. Chem B*, **2000**, 104, 9004

14 Calvente J. J.,Lopez-Perez G., Ramirez P., Fernandez H., Zon M.A., Mulder W. H., Andreu R., *J. Am. Chem .Soc*., **2005**, 127, 6476

15 Yang G., Amro N. A., Starkewolfe Z. B., Liu G., *Langmuir*, **2004,** 20, 3995

16 Weisser M., Nelles G., Wohlfart P., Wenz G., Mittler-Neher S., *J. Phys. Chem*., **1996**, 100, 17893

17 Nelles G., Weisser M., Back R., Wohlfart P., Wenz G., Mittler-Neher S., *J. Am. Chem. Soc.*, **1996**, 118, 5039

18 Schneider T. W., Buttry D. A., *J. Am. Chem. Soc.*, **1993**, 115, 12391

19 Schultz J. W., Wetter K. J., *J. Electroanal. Chem.*, **1973**, 44, 63

20 Swathirajan S., Brukenstein S., *Electrochim. Acta*, **1983**, 28, 865

21 Chamberlain R. V., Slowinska K., Majda M., *Langmuir*, **2000**, 16, 1388

22 Subramanian R., Lakshminarayanan V., *Electrochimica Acta*, **2000**, 45, 4501

23 Dannenberger O., Buck M., Grunze M., *J. Phys. Chem. B.*, **1999**, 103, 2202

24 Weisser M., Nelles G., Wohlfart P., Wenz G., Mittler-Neher S., *J. Phys. Chem.*, **1996**, 100, 17893

25 Simova S., Berger S., *J. of Incl. Phenomena and Macrocyclic*, **2005**, *53,* 163

26 Porter M. D., Bright T. B., Allara D. L., Chidsey C. E. D., *J. Am. Chem. Soc.*, **1987**, 109, 3559

27 Conway B. E, Currie J. C., *J. Electrochem. Soc.*, **1978**, 125, 257

28 Finklea H. O., Self-Assembled Monolayers on Electrodes, in *Encyclopedia of Analytical Chemistry,* **2000**, Vol. 11, R. A. Meyes (Ed), Wiley, Chichester, UK, 10090

29 Maskus M., Abruna H. D., *Langmuir*, **1996,** 12, 4455

30 Amatore C., Saveant J-M., Tessier D., *J. Electroanal. Chem.*, **1983**, 147, 39

31 Davies T. J., Compton R. G., *J. Electroanal. Chem.*, **2005**, 585, 63

32 Finklea H. O., Snider D., Fedyk J., *Langmuir*, **1993**, 9, 3660

33 Amatore C., Saveant J.-M., Tessier D., *J. Electroanal. Chem.*, **1983**, 147, 39

34 Bard J. A., Faulkner L. R., *Electrochemical methods: Fundamentals and applications,* Second edition, Ed. Wiley, Chapter 14.

35 Sabatani E., Rubinstein I., Maoz R., Sagiv J., *J. Electroanal. Chem.*, **1987**, 219, 365

36 Sabatani E., Rubinsteun I., *J. Phys. Chem.* **1987**, *91*, 6663

Chapter 5:

Inclusion reaction of CoTpybip in the immobilised β-CD cavities

Introduction

The need of miniaturised devices capable of directional motion of electrons and energy, in particular for the semiconductor industry, has triggered the generation of molecule-based functional devices. In particular, the study of the integration of those molecular components into well-ordered assemblies with a well-defined supramolecular architecture has been investigated extensively. Such devices require control of molecular orientation and organisation at the nanometre scale, and, therefore, it is of primary importance to study molecules and methods that allow assembling multicomponent nanostructures.

Traditional molecular electronics based attempts have relied on either covalently linked low molecular weight systems or polymers[1]. However, complexity in the synthetic procedure or lack of spatial control of individual molecular units together with inefficiency of mass transfer often limits systems of this kind. Alternative "bottom up" strategies for forming supramolecular assemblies involve the deposition of thin films and layers by Langmuir-Blodgett method (LB), which has the disadvantage of requiring particular instrumentation and being labour intensive[2]. Crespo-Biel *et al.*[3] reported on the utilisation of layer by layer deposition (LBL) to form multivalent supramolecular host-guest interactions between dendritic guest molecules and host-modified gold nanoparticles. However, with this technique is not easy to control the stability towards interpenetration of the single layers.

A more versatile and promising route is to mimic the self-assemblies present in living systems that are capable of directional control of electron transfer and energy[4, 5]. Artificial systems that mimic the properties and the functions of the biosystems can be developed based on the immobilisation of molecules able to interact non covalently with other redox/photoactive active molecules, which have a defined geometry in order to build up molecular wires.

Figure 5.1 schematically shows the idea of a molecular wire, where a transition metal complex acts as the active part of the wire, by switching its redox state, and the CDs and the linkers direct the self-assembly onto the surface. Moreover, functionalised CDs are ideal hosts because of their selective complexing properties, aqueous solubility and ability to self-assemble.

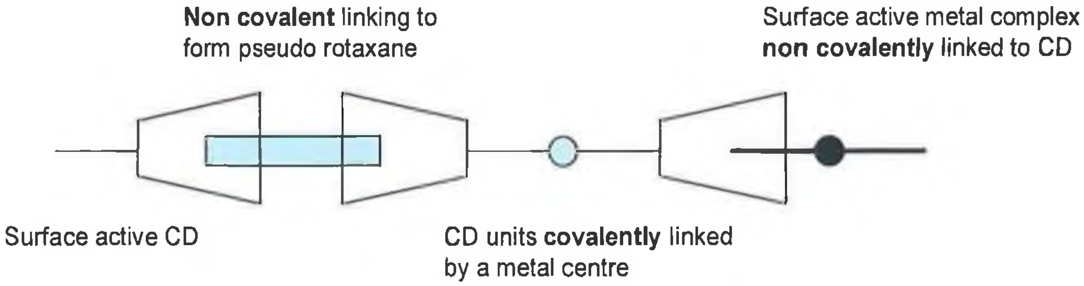

Figure 5.1 Schematic representation of a molecular wire

As previously described, cyclodextrins have the ability of forming inclusion complexes with hydrophobic molecules. The number of reported inclusion complexes with CDs in solution and immobilised on a surface has been increasing over the years. Rojas *et al.*[6] first reported a CV investigation of well organised and defined molecular cavities confined on a gold surface that were able to include molecules dissolved in solution. The probe in solution was a ferrocene redox couple, capable of including into the β-CD cavities. Since then, other authors reported on the characterisation with electrochemistry of the inclusion of small molecules able to completely or partially penetrate the cavity, e.g. ferrocene [7, 8, 9, 10] and cobaltocenium derivatives [11, 12], organic molecules [13] [14](adamantyls[15, 16], quinones[17, 18] and anthraquinones[19], benzyls, phenols, alkyl chains[20, 21]) . However, as previously mentioned, the guests used for the present work are molecules with a defined linear geometry such as the terpyridine complexes characterised in Chapter 3.

Some studies on the ability of terpyridine complexes to perform directional light-induced charge separation energy transfer have been carried out successfully in solution[22]. In the case of osmium terpyridine biphenyl complexes, the biphenyl moiety allowed the molecule to include, constructing modular systems that showed higher flexibility rather than polymetallic systems of donor/acceptor units. Therefore, in this work a similar compound, cobalt terpyridine biphenyl, CoTpybip, was chosen as an electrochemically active guest molecule. The design of the metalloguest was carefully chosen as explained below.

First, cobalt terpyridine complexes show accessible formal potentials in aqueous solution at a gold electrode, as shown in Chapter 3 for a family of CoTpyL, where L is an including tail such as diphenyl or adamantyl. In the case of inclusion of the cobalt terpyrydine complex the tail has to be hydrophobic in order to interact with the cavity of the β-CD. Moreover, the size of the tail needs to take into account the cavity dimension. Aromatic biphenyls have been proved to strongly interact with β-CD in solution[22].

In the following sections, the ability of β-CDs molecules immobilised on gold to bind CoTpybip present in the contacting solution is reported using electrochemistry. The amount of included complex and the thermodynamic constant of the inclusion process is also discussed. Further characterisation by Raman spectroscopy has also been performed. Control experiments at the bare gold electrodes will complete the characterisation of the process.

5.1 Experimental

Instrumentation

Cyclic voltammetry was performed using a CH Instrument Model 660 Electrochemical Workstation and a conventional three-electrode cell. All solutions were deoxygenated thoroughly prior to measurement using oxygen free argon, and a blanket of argon was maintained over the solutions during all experiments. Potentials are quoted with respect a home-made Ag/AgCl, KCl_{sat} aqueous reference electrode, previously calibrated against a standard laboratory calomel reference electrode. All experiments were performed at room temperature.

Raman spectroscopy was performed using an Horiba Jobin Yvon HR800UV . The acquisition was carried out *ex-situ* after washing the electrode with copious amount of milliQ water and drying it under argon. Acquisition parameters are listed in the relative section.

Complex formation

CoTpybip was synthesized and characterised at the School of Chemical Science in Birmingham and used as received.

The medium in which the host-guest complex formation takes place is important, since it influences the inclusion equilibrium process in both directions. In fact, as described in Chapter 1, the inclusion process can be simply thought as the substitution of the solvent (typically water) included in the cavities by a less polar guest. CoTpybip is a hydrophobic probe that is soluble in acetonitrile. However, solutions with high water content are needed for the inclusion process, in order to enhance the affinity between the CD cavity and the molecule itself. In fact, as reported by Osella *et al.*[23] regarding the inclusion of ferrocene into β-CD cavities in mixtures of water and an organic co-solvents, the increase of the acetonitrile presence from 0 to 10% produced a small decrease in the binding properties (ca. from 4×10^3 to 3×10^3 M^{-1}).

Previous studies were performed at the School of Chemical Sciences in Birmingham, on the complexation in solution between permethylated beta-cyclodextrins and M-bipTpy, where M is Ir, Os, by HNMR, circular dichroism, microcalorimetry and luminescence spectroscopy. The following conclusions were made:

1) the amount of acetonitrile does not have to exceed 10%.
2) the inclusion happens through the secondary side of the CDs due to dipole coupling effects
3) just the terminal phenyl ring of the biphenyl tail is included in the cavity.[24]

In the present work, in order to probe the affinity of the cavities of the β-CD-SH monolayers for the redox probe, modified electrodes were exposed to solutions of CoTpybip and cyclic voltammetry was performed. In particular, the redox process involving the metal oxidation Co^{2+} to $Co^{/3+}$, was monitored and the characteristic for a reversible redox process for a surface confined species checked.

The following experimental conditions were used based on the conclusion cited above. Millimolar solutions of CoTpybip in anhydrous acetonitrile were first prepared. Then, aliquots of the stock solution were diluted, by dropwise addition of milliQ water, to produce micromolar concentrations of the redox probe with a final water/acetonitrile ratio of 90/10. These deposition solutions were then used in two different protocols for the inclusion process with the modified electrodes, i.e. *ex-situ* and *in-situ* inclusions.

In-situ inclusion involved dipping the modified working electrodes in micromolar solutions of CoTpybip, containing 0.2M Na_2SO_4 The association was monitored using high scan rate CVs in order to limit the diffusive contribution. The electrodes were not removed at any stage from the deposition solutions. In the presence of the electrolyte the solubility limit of the probe was approximately 40 μM, at which the solution was non-turbid and stable for about 10 minutes.

Ex-situ monitoring of the inclusion process involved dipping the β-CD-S/Au electrodes in micromolar solutions (90:10 milliQ water/acetonitrile) of the cobalt complex for different deposition times. Subsequently the electrodes were washed with milliQ water and checked in 1M $LiClO_4$ solutions. The high electrolyte concentration was needed to "freeze" the equilibrium set in the deposition solution, creating a highly ionic and hydrophilic environment.

5.2 Molecular recognition

5.2.1 In-situ inclusion

For the *in-situ* inclusion monitoring, the modified β-CD electrodes were prepared as described in Chapter 4 and then placed in a cell containing micromolar solutions of the complex in 90:10 milliQ water/acetonitrile, 0.2M Na_2SO_4 as supporting electrolyte. Four different concentrations were used, namely 5, 10, 20 and 40 μM.

The reproducibility of the experiment is an issue of primary importance. Unfortunately, it has been shown in Chapter 4 that during the immobilisation of the β-CD-SH on gold, it is not possible to control and direct their orientation and packing. However, it is possible to characterise the CD films. Moreover, it was shown how scanning the layer for long times could introduce some disorder in the layer itself, probably through desorption of some molecules, which reduces the probability of the inclusion. It is also important to note that hydrophobic probes in aqueous solution can exhibit a significant tendency to physically adsorb on the electrode surface. Therefore, fast scan rates for short times were used in the following experiments. Figures 5.2 shows representative CVs for a β-CD-S/Au consecutively immersed in 5, 10, 20 μM solution of the complex, 90:10 milliQ water/acetonitrile, 0.2M Na_2SO_4. Between each experiment the β-CD modified electrodes were rinsed with acetonitrile to completely remove any included molecule which would affect the achieving of equilibrium. The corresponding Gaussian fitted background corrected CVs, are shown in Figure 5.3. The background correction was performed in Excel by fitting the best baseline to the data and then subtracting it from the experimental data. The background corrected CVs were then fitted with a Gaussian equation in Origin 6.0, which minimises the Chi square value between experimental and theoretical data. The potential peak and the FWHM were left as freely adjustable parameters. The discussion of the results will be based on Figure 5.3. This data processing was needed due to the small magnitude of the peaks related to the inclusion process compared to the capacitive current.

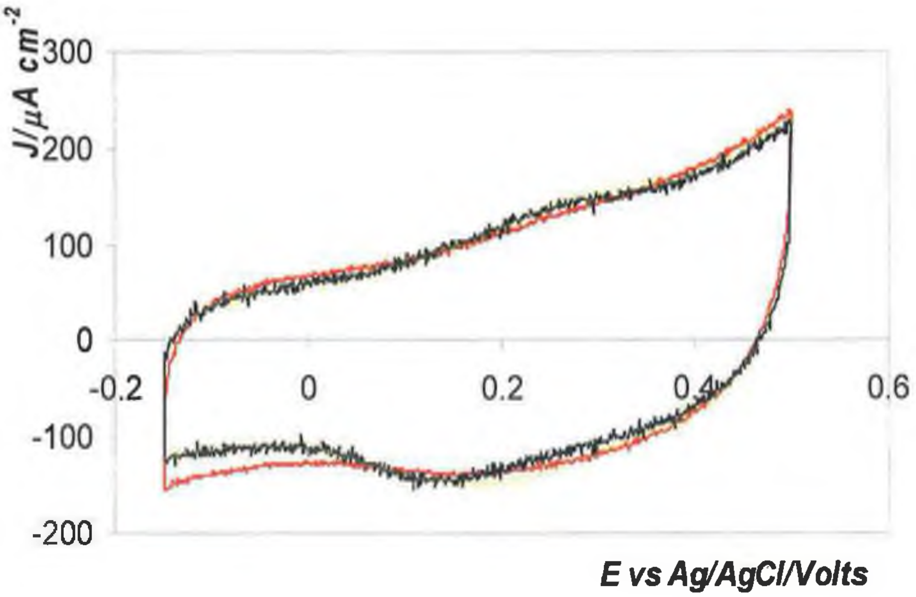

Figure 5.2. CVs of β-CD-S/Au electrode immersed in a 5μM (red line), 10μM (black line) and 20μM (yellow line) solutions of the complex, 90:10 milliQ water/acetonitrile, 0.2M Na_2SO_4. Scan rate: $10Vs^{-1}$. Reference electrode: Ag/AgCl. Counter electrode: platinum wire.

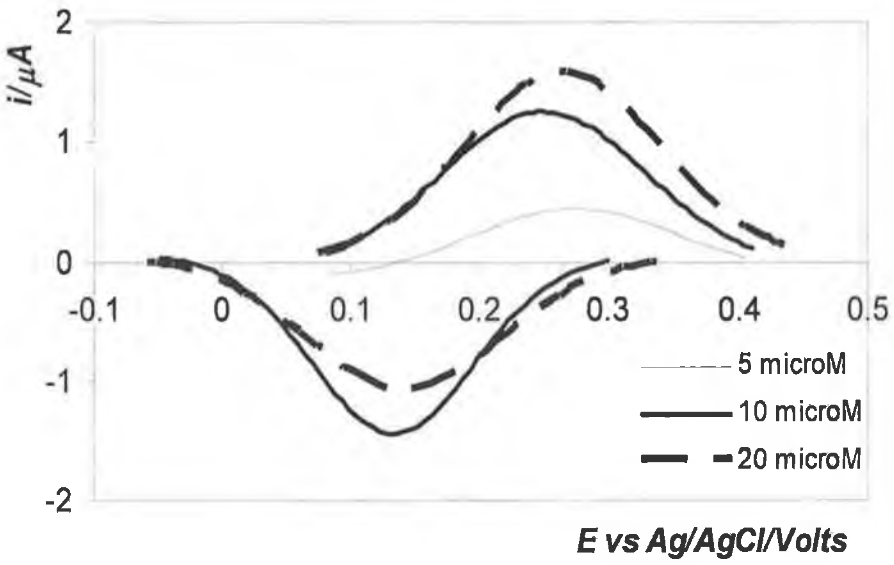

Figure 5.3. Gaussian fitted background corrected CVs of a β-CD-S/Au electrode immersed in a 5μM (thin line), 10μM (black line) and 20μM (dashed line) solutions of the complex, 90:10 milliQ water/acetonitrile, 0.2M Na_2SO_4. Scan rate: $10Vs^{-1}$. Reference electrode: Ag/AgCl.. Counter electrode: platinum wire.

A way to check the occurrence of the inclusion process between a redox probe and cavities in solution by electrochemistry is to monitor the shifting of the potential peaks of the redox process with respect to the values in absence of the binding cavities. In fact, in the literature[12 25 26] the shift to more positive potentials was used to indicate that the complexation had occurred between electrochemically reversible redox probes and β-CDs in solution, together with a drop in the peak current values. The interpretation of the phenomenon was based on the different environment that the redox probe experiences when in solution or in the cavity of the β-CD. Since the cavity represents a more stable system for the hydrophobic probe in the reduced state, the consequent oxidation is more difficult and requires higher energy and therefore more positive potentials. In the literature, shifts spanned between 0.010 to 0.1V and a decrease in the current was also observed as a consequence of the inclusion[6, 25, 26]. In fact, since the included complex was assembled in solution, it was characterised by smaller diffusion coefficients, compared to the free complex, which produced smaller currents. In the present case, the peak currents do not decrease since the cavities are confined on the surface and the probe can diffuse as normal. Therefore, only the shift in potentials can be checked.

More interestingly, in another contribution Rowe *et al.* [27] showed how the formal potential of a surface confined thiol terminated ferrocene shifted to more positive potentials when the chain length of the surrounding alkanethiols was increased. While the distance from the electrode of the redox probe was constant, the environment changed creating a more stable situation for the ferrocene neutral molecule as shown in Figure 5.4.

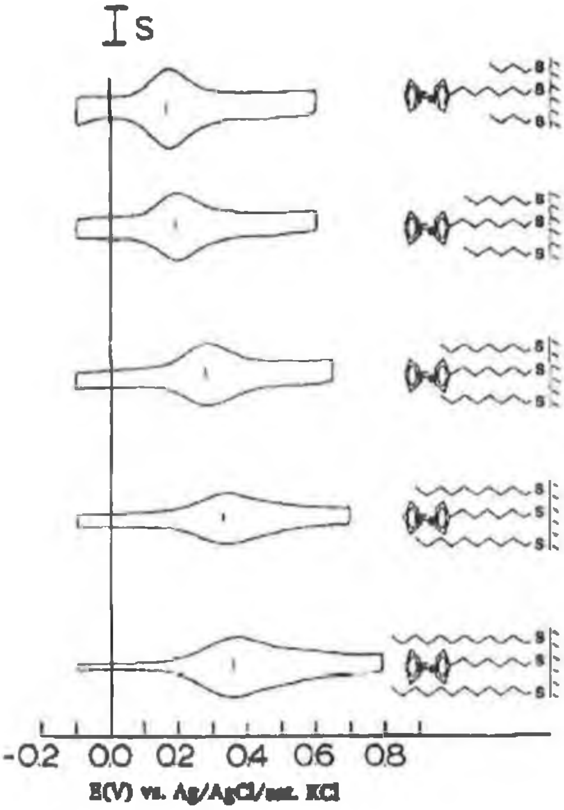

Figure 5.4. CVs in 1M HClO4 of electrodes coated from ethanol solutions containing (Fc)C6SH and n-alkanethiols: A) butane thiols, B) n-hexanethiol C)n-octanethiol D) n-decanethiol E)n-dodecanethiol. Scan rate 100mV/s, S=1μA, coverage for each voltammograms is 2.4×10^{-11} mol cm^{-2}. Adapted from reference 28

They explained the phenomenon as an increased free energy that must be overcome to force the electrogenerated ferrocenium ion to reside in this quite non-polar, poorly solvating environment. In particular, they observed a shift in potential ranging from 0.050 to 0.200V when switching from a C4 to a C12 alkyl chain. The fact that the formal potential shifted even when the probe was partially buried in the surrounding layer, is supportive of the results discussed below for our probe.

In Figure 5.3, redox processes are visible for the modified electrodes immersed in 10 and 20 μM solutions, while at 5 μM just the anodic wave is detectable. The anodic and cathodic potentials are 0.263±0.012V and 0.137±0.005V, respectively and the formal potential is 0.197±0.008V. If compared to the formal potential of the *in-situ* control experiments shown in Section 5.3, performed at the bare electrodes, the formal potential of the cobalt oxidation results shifted to more positive values. In particular, both the anodic and the cathodic waves move, suggesting that this effect is not due to kinetics but to thermodynamics issues. The shift is about 0.050V, ca. 5 kJ mol^{-1} which is in the order of magnitude of weak interactions, e.g. Van der Waals forces that are needed to compensate the change in the oxidation state. Considering literature values, the magnitude of the shift is supportive of a partial inclusion of the probe into the cavities, likely through the biphenyl moiety while the terpyridine ligand is partially interacting with the cavity.

Further evidence of an actual inclusion is obtained by considering the blocking experiment conducted in Section 4.4.4. For those experiments, CoTpy, which does not have biphenyl moieties, was used as probe in solution and its electron transfer properties characterised by CV at the bare and β-CD-S/Au electrodes. It was found that the probe behaved reversibly in the same way over the two different electrodes, showing just a small shift to more negative potentials for the modified surface. Since CoTpy is unable to include in the cavities, due to its size, the signal observed in Figure 4.17 could only come from the probe in solution undergoing a reversible redox reaction most likely through the β-CD cavities. Similar considerations can be obtained by comparing Figures 5.2 and 5.9. It is clear that CoTpybip acts differently at the β-CD-S/Au and bare electrodes and in particular that at the modified electrode the physisorption is suppressed, and, therefore that diffusion to the electrode surface is blocked. Therefore, the redox process observed in Figure 5.2 at higher potentials is considered to be associated with the included complex.

The presence of cathodic and anodic waves is a proof of an actual electronic communication through the CDs between the metal centre and the electrode. However, the electron transfer does not look rapid in the timescale of the experiment since a peak to peak separation of about 0.130V is present. If the included complex is considered as a surface confined species which is reversibly adsorbed at the electrode surface, undergoing an ideally reversible redox reaction, a zero separation between the two peaks should be observed. It is not clear if the peak to peak split was due to kinetics effects, because a scan rate dependence experiment was extremely affected by iR drop and no reliable information could been obtained.

A more detailed analysis of the amount of the included complex *vs.* its bulk concentration allows the binding constant to be estimated, as discussed in the following section, and compared to the values obtained in solution for similar compounds. In Figures 5.2 and 5.3 the profiles obtained for the modified electrodes immersed in a 40 μM solution are not shown due to precipitation of the CoTpybip in solution that affected the resulting CV.

5.2.2 Estimation of the binding constant

By integrating the area under the peaks in Figure 5.3, surface coverages for the oxidised and reduced forms can be calculated and therefore the association constant for the equilibrium between the probe in solution and the immobilised form can be estimated. Table 5.1 summarises the values of the surface coverages *vs.* bulk concentrations.

Table 5.1 Surface coverages and formal potentials for the included CoTpybip-β-CD-S/Au in 0.2M Na_2SO_4, 90:10 milliQ water/acetonitrile

C/μM	Γ_a/pmol cm^{-2}	Γ_c/pmol cm^{-2}	E°′/V
5	24	-	0.279[a]
10	54	48	0.191
20	63	43	0.201

[a] Refers to the anodic peak potential since the cathodic wave is not visible

In order to estimate the binding constant, a mechanism for the process has to be postulated, which considers the rates of the electron transfer and of the association and dissociation processes and the different parameters that direct them. In fact different pathways can be thought happening during the oxidative electrochemical experiment as shown in Figure 5.5

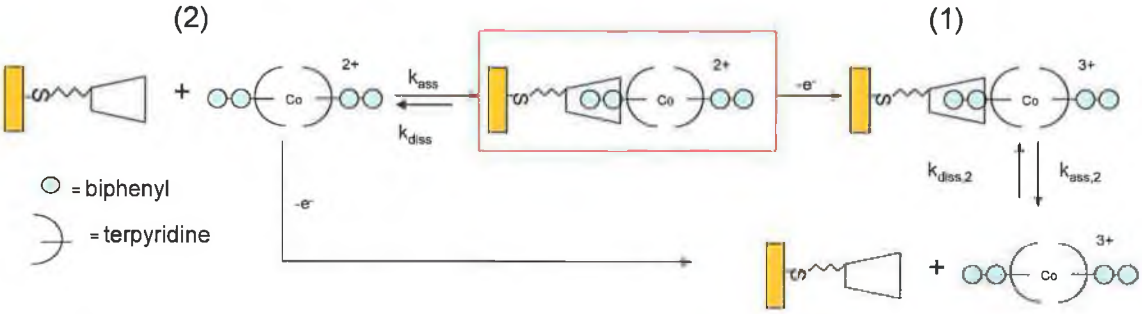

Figure 5.5 Schematic representation of the possible mechanism for the oxidative electrochemical experiment.

The red box is the starting situation where the cobalt complex is included in the cavities and it is in equilibrium with the redox probe dissolved in the contacting electrolyte solution at the OCP. Then, when an external potential is applied pathway 1 or 2 can follow, depending on the rates of the electron transfer and of the dissociation/association processes of the assembly as well as the affinity of the produced oxidised molecule for the cavity.

In the literature**Error! Bookmark not defined.**[13,28] a wide range of values for the association and dissociation rate constants is reported which varies from 2.8 to 5.2×10^7 $M^{-1}s^{-1}$ and from 0.01 to 1.3×10^5 M^{-1} s^{-1} for the association and dissociation of the assembly processes respectively. Also it has been reported a strong dependence of these constants on the structure of the guest molecule. Moreover, a general two-step equation has been thought to be representative of the complexation reaction as shown in Equation 5.1

$$P + CD \underset{k1,b}{\overset{k1}{\leftrightarrow}} P - CD^* \underset{k2,b}{\overset{k2}{\leftrightarrow}} P - CD \qquad (5.1)$$

where P is the redox probe in solution and CD is the cyclodextrin cavity and k1 and k2 are the forward rate constants and k1b and k2b are the backwards. The first step is the association between the probe and the CD to form a transient complex, P-CD*, which then relaxes to the isomeric included assemble, P-CD. The second step involves solvation changes.

Wang et al.[25] supposed that the oxidation of cobaltocene to cobaltocenium could only occur after dissociation from β-CD, since the oxidised form would lead to a more unstable situation. Nevertheless, in their work the cobaltocene was completely included in the cavity, while in the present work the included moiety is just the terminal phenyl of the biphenyl tail. The last assumption is consistent with the shift in potentials observed of about 0.050V. Therefore, the oxidation of the metal centre in the complex should not dramatically change the properties of the included moiety, allowing direct oxidation of the included complex. Moreover, the assembly studied by Wang was in solution where the electron transfer is limited by diffusion, while the supramolecular assembly is now immobilised on a surface, where the electron transfer occurs at faster rates. Therefore, in Figure 5.3 and Table 5.1 the smaller surface coverage for the reduction of the included complex simply reflects the affinity of the more hydrophilic oxidised molecule for the bulk rather than the CD cavity. Pathway 1 was, then, supposed to represent the redox process occurring at the electrode when scanning at positive potentials, and Equation 5.1 allows the binding constant for the reduced form to be estimated.

$$K_{ass} = \frac{[CobipTpy - \beta - CD - S/Au]^{2+}_{surf}}{[CobipTpy]^{2+}_{sol}[\beta - CD - S/Au]_{surf}} \qquad (5.2)$$

In Chapter 4 the surface coverage of the β–CD-SH was calculated to be $1.6 \pm 0.9 \times 10^{-10}$ mol cm^{-2}. Substituting the values from Table 5.1 in Equation 5.2, K_{ass} is $2.78 \pm 0.7 \times 10^{4}$ M^{-1}.

Haider et al.[22] report on a binding constant between $[Os(biptpy)(tpy)]^{2+}$ and metallo-beta cyclodextrins *in solution* of 2×10^{4}M^{-1}. The binding constant is in the same order of magnitude of the constant found in solution, suggesting that the immobilisation does not affect the thermodynamics of the process. Similar conclusions were provided by Rojas[6] when the inclusion of ferrocene into β-CD cavities was monitored. However, they treated the inclusion process as a reversible adsorption process and they fitted the surface coverages *vs.* concentration profile with a Langmuirian equation:

$$\frac{\Gamma}{\Gamma_{max} - \Gamma} = K_{ass}C \qquad (5.3)$$

where Γ is the surface coverage at each single concentration and Γ_{max} is the saturation surface coverage (mol cm^{-2}), which in our case corresponds to occupation of all the cavities. With this method, the determination of the actual surface coverage of the surface confined CDs is not needed and can be left as a freely adjustable parameter. By fitting the data in Table 5.1 with Equation 5.3, a binding constant of 7.6×10^{4} M^{-1} and a saturation surface coverage of 1.08×10^{-10} mol cm^{-2} were obtained. It is interesting to note that a good agreement between the fitted value for the saturation surface coverage and the value from the desorption experiment ($1.6 \pm 0.9 \times 10^{-10}$ mol cm^{-2}) of the cyclodextrins was found. This consideration is supportive of the fact that the protocol followed in Chapter 4 for the determination of the confined cyclodextrins is correct and that they are able to accommodate guests. The free energy of association is calculated to be ca. 25 kJ mol^{-1} which is in the order of magnitude expected for hydrophobic interactions.

An interesting phenomenon was recorded during the scanning. The redox activity increased by decreasing the time between the scanning, reaching a maximum stable value. When the system was left quiet, the redox activity decreased back to the starting situation. This phenomenon suggests an on/off condition for the system that was detected in each experiment. Probably, the application of a potential is a further parameter that triggers the inclusion process, more likely by varying the cavities orientation. The potential dependence of the structure of the β-CD monolayer was shown in Chapter 4. In particular, a change in the Raman spectrum was recorded when a potential step was applied with a different final potential value, suggesting an orientation effect of the molecules within the monolayer.

The effect of the applied potential on the orientation and self-organisation of reversibly adsorbed β-CDs on gold single crystal was also reported by Ohira *et al.*[29] [30]. Interestingly, they monitored by STM the organisation of CDs in nanotubes structures in a specific potential window and consequently disruption of the order outside those potentials.

In general, *in-situ* inclusion seems to occur at the modified β–CD-S/Au electrodes with CoTpybip, with an association constant comparable to those found in solution for related complexes. The inclusion is reversible and likely potential controlled and is detectable down to 5μM concentration of the probe. Moreover, a further proof of the amount of immobilised CDs on the surface was possible by fitting the inclusion data.

5.2.3 Ex-situ inclusion

The *ex-situ* inclusion experiment was conducted in order to monitor the possibility of removing the modified electrodes from the deposition solution and, by consecutive dipping steps in solutions containing CDs or guests molecules, building up molecular wires. The preparation and characterisation of the modified β-CD-S/Au electrodes was discussed in Chapter 4. Once prepared the electrodes were cycled with $K_4Fe(CN)_6$ to check their blocking properties, rinsed with milliQ water and placed in micromolar solutions of the complex, 90:10 milliQ water/acetonitrile, and monitored after one hour and overnight deposition.

Prior to any electrochemical measurements, the electrodes were thoroughly rinsed with milliQ water and subsequently checked in a free complex 1 M $LiClO_4$ solution. Figure 5.6 shows the background corrected CVs obtained for a modified gold polycrystalline macroelectrode immersed sequentially in 10, 20 and 40 μM solution of the probe, 90:10 water/acetonitrile and scanned at $0.5 Vs^{-1}$ after 1h deposition.

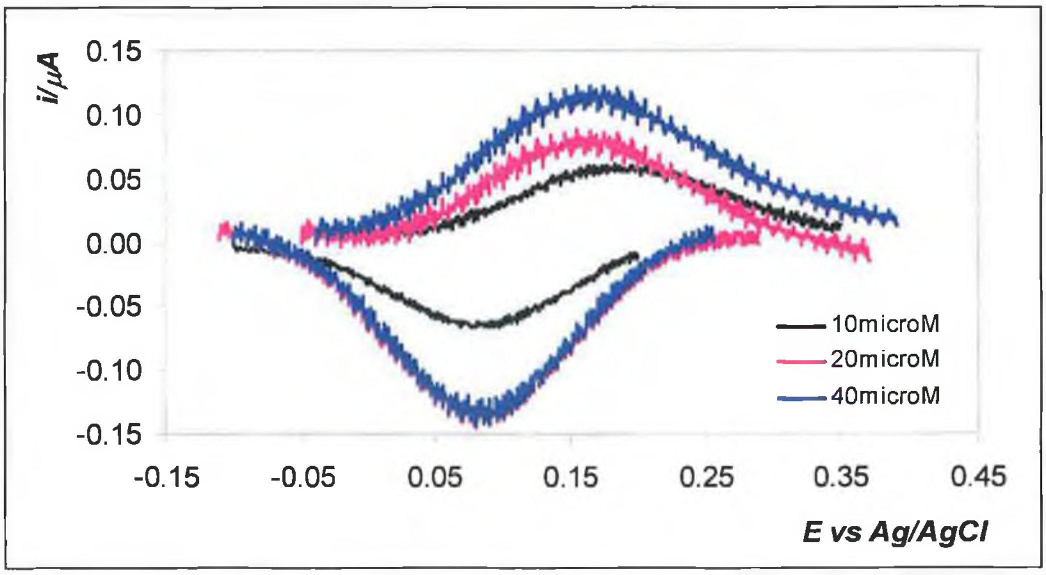

Figure 5.6 Background corrected CVs of a β-CD-S/Au polycrystalline macroelectrode (2 mm diameter) immersed subsequently in 10 (black line), 20 (purple line) and 40 μM (blue line) solutions of the probe, 90:10 water/acetonitrile after 1h deposition. Electrolyte: 1M $LiClO_4$. Scan rate: $0.5 Vs^{-1}$. Reference electrode: Ag/AgCl. Counter electrode: platinum wire

The following table summarises the characteristic values for the CVs at the different concentrations after 1h deposition.

Table 5.2 Surface coverages and formal potentials for the included CoTpybip-β-CD-S/Au, from the *ex-situ* deposition

C/M	E_c/V	E_a/V	$E^{\circ\prime}/V$	$FWHM_c$ $/V$	$FWHM$ $_a/V$	$\Gamma_a/$ $pmolcm^{-2}$	$\Gamma_c/$ $pmolcm^{2}$
10μM	0.084±0.004	0.185±0.009	0.134±0.005	0.132±0.013	0.153±0.005	2.1/3.4	1.8/4.4
20μM	0.084±0.002	0.171±0.013	0.127±0.008	0.145±0.013	0.142±0.024	2.7/6.1	4.7/6.3
40μM	0.091±0.011	0.181±0.011	0.143±0.002	0.141±0.005	0.170±0.008	4.0/7.5	4.6/6.5

For the surface coverages two representative results are reported to shows the trends of the values but the difficulty in the reproducibility

The discussion of the results obtained with the *ex-situ* inclusion is more complicated, since the reproducibility was affected by the washing step and, therefore, only a qualitative description is presented. First, it is interesting to note that even after copious washing a redox process was observed that followed a trend, *i.e.* the surface coverage of the probe increased with the concentration in solution. However, the surface coverages are about one order of magnitude smaller than what found for the *in-situ* inclusion. A very rough estimation of the binding constant is therefore around $1.0 \pm 0.3 \times 10^3$ M^{-1}, an order of magnitude smaller than the *in-situ*.

As previously discussed, the shift in formal potential is an indication of inclusion. However, from the table it is clear that the values for the formal potential are scattered with a highest value of 0.143±0.002V, which is about 0.020V shifted respect to the *ex-situ* control experiment ran at the bare electrode (*vide infra*). In particular the standard deviations for the peak potentials are around 10% the values. Apparently, it is not possible to undoubtedly say that inclusion occurred at the modified electrode by electrochemistry, since presence of the precipitated complex on the electrode surface, due to the washing step, can affect the final response.

To further investigate the occurring of the inclusion, Raman spectroscopy was ran and the results will be discussed in the following section.

5.2.4 Raman spectroscopy of the ex-situ included complex

An additional attempt to monitor a possible *ex-situ* inclusion was performed by running *ex-situ* Raman spectroscopy of the electrode and comparing the result with the Raman of the solid powder of the CoTpybip and of the empty β-CD monolayer on gold, as shown in Figure 5.7. The modified electrode was a smooth electrode, the same used for the electrochemistry, washed with milliQ water and dried under argon prior to the measurement. Therefore, not a strong enhancement due to surface roughness was expected. The presence of the CoTpybip and the cyclodextrin layer was checked by scanning the wavenumbers in different energy ranges, between 900 and 1700 cm^{-1} for the terpyridine modes and between 2700 and 3100 for the alkyl chain attached to the cyclodextrins. Both the molecules were successfully detected and the assignments of the modes were based on the lists discussed in Chapter 2. The following table summarises the results of Figure 5.7.

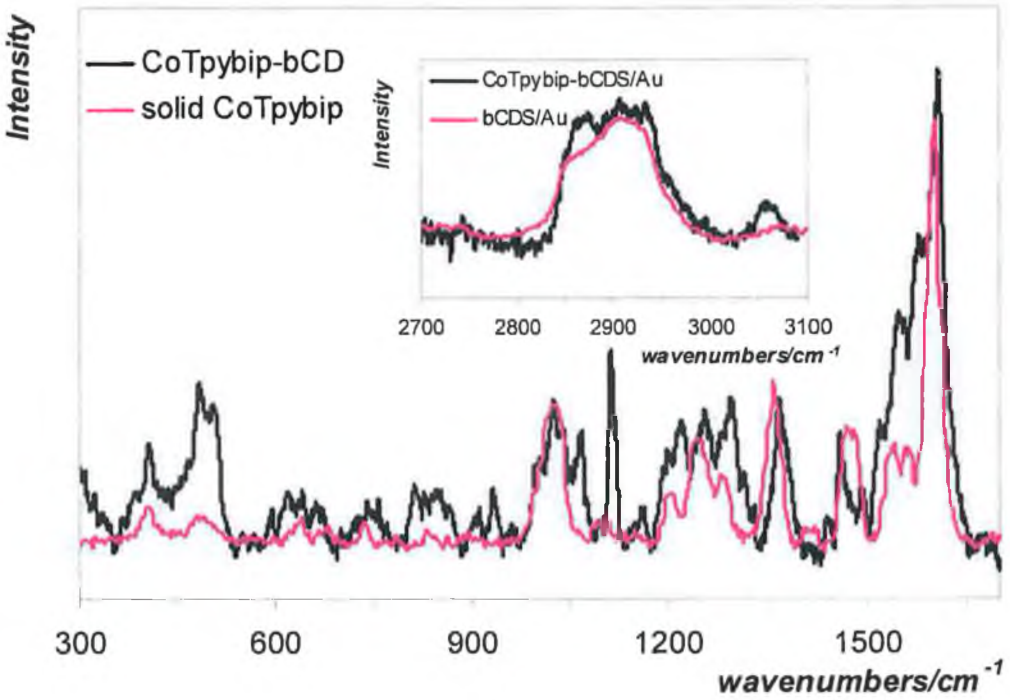

Figure 5.7. *Ex-situ* Raman spectra of CoTpybip-β–CD monolayer on smooth polycrystalline gold macroelectrode (2 mm diameter, black line) and Raman of solid powder of CoTpybip (purple line) in the breathing ring region of the terpyridine ligand. The inset shows *ex-situ* Raman spectra of the included monolayer (black line) and of the empty β-CD monolayer (purple line). Acquisition parameters are: Line: 632nm. Grating: 1800. Hole: 500. Accumulation: 10s×20 times.

Table 5.3 Comparison between Raman shifts for the CoTpybip solid and included in the cyclodextrin layer

CoTpybip solid/cm^{-1}	*CoTpybip-β–CD/cm^{-1}*	*Assignments*
1028	1028	Terpyridine mode
1206	1206 and 1224	Biphenyl mode
1242	1247 and 1258	Biphenyl mode
1277	1284 and 1297	Biphenyl mode
1357	1368	Centre py mode
1471	1459	Outer py mode
1539	1546	Biphenyl?
1602	1608	Outer py mode

It is interesting to note that either the modes for the terpyridine or the biphenyl are shifted, likely because their vibrational modes are affected by the cavity.
The main shifts are observed for the biphenyl modes which are between 16 and 20 cm^{-1} while the terpyridine modes shifts range between 6 and 12 cm^{-1}. Moreover, the vibrations relative to the overall terpyridine remains constant at 1028 cm^{-1}.

Furthermore, in Figure 5.7, the biphenyl modes show peaks with usually a shoulder at smaller wavenumbers, which are close to the values observed for the solid sample. This suggests that some of the molecules present at the electrode surface indeed have precipitated from the solution during the washing step but that the included complex is also present and it is not entirely washed away. Therefore, the mixed behaviour observed with the electrochemistry can be associated with both physically adsorbed and included molecules.

The vibrations of the cyclodextrin hosting the probe are not shifted if compared to the spectrum obtained for the free monolayer, βCD-S/Au in the inset of Figure 5.7. However, the relative intensities change, in particular for the CH stretching modes at 2936 and 2911 cm^{-1} compared to the CH stretching of the alkyl chain at 2864 cm^{-1}. Therefore, the inclusion has some effects also on the monolayer vibrations. Again, the reproducibility is a key issue due to the difficulties of controlling the effects on the monolayer of the washing step.

In general, the *ex-situ* inclusion occurs and it is possible to qualitatively monitor the presence of the included complex, especially by means of Raman spectroscopy. The washing step seems to play a key role in the quantitative determination of the inclusion process, since some complex can be precipitated on the surface.

5.3 Characterisation of CoTpybip at a bare electrode surface

5.3.1 Experimental

Control experiments were run with bare polycrystalline gold macroelectrodes and micromolar solutions of the cobalt complex in order to check and characterise any possible physisorption process of the molecule on the bare electrode surfaces. The control experiments were also run *in-si*tu and *ex-situ.*

5.3.2 Ex-situ control experiment

For the *ex-situ* protocol two different concentrations were used, 10 and 100 μM, in 90:10 milliQ water/acetonitrile. The protocol followed was the same used for the *ex-situ* inclusion at the β-CD modified electrodes described in Chapter 3. The modified electrodes left in the cobalt complex solution, were first rinsed with copious amount of milliQ water and then checked in an oxygen free 0.1M $LiClO_4$ solution after 30, 60 and 120 min and overnight deposition.

Figures 5.8a and b show the change in time of the control experiment for a bare gold electrode immersed in a 10μM solution of the complex in 90:10 milliQ water/acetonitrile

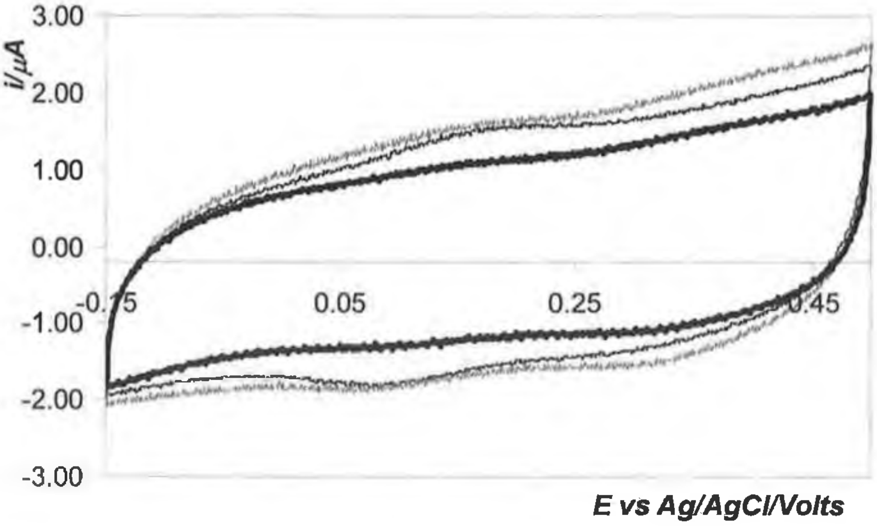

Figure 5.8a. CV of a bare polycrystalline gold macro electrode left in a 10μM solution of the complex, 90:10 milliQ water/acetonitrile after 30 min (thin line), 60 min (shaded line) and 120min (thick line) and washed with milliQ water prior the measurement. Scan rate: $0.5Vs^{-1}$. Electrolyte: 0.1M $LiClO_4$. Reference electrode: Ag/AgCl. Counter electrode: platinum wire

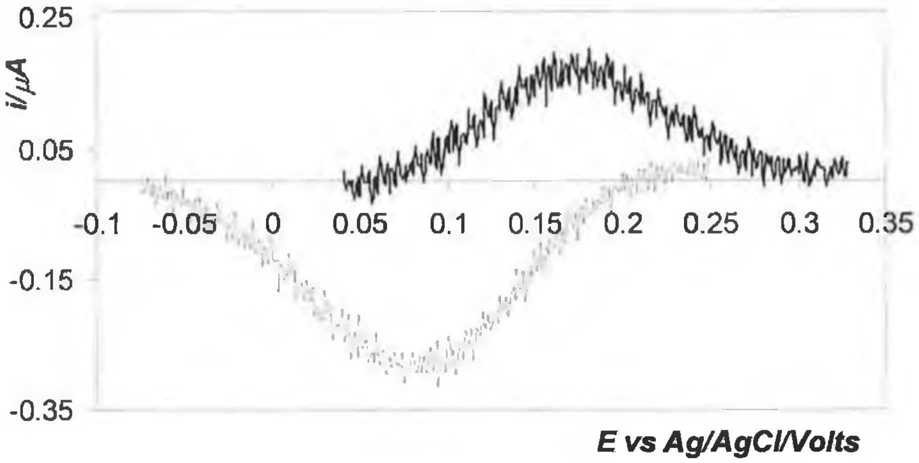

Figure 5.8b. Background corrected CV of a gold polycrystalline macroelectrode left in a 10 µM solution of the complex, 90:10 milliQ water/acetonitrile for 30 min and washed with water. Electrolyte: 0.1M $LiClO_4$. Scan rate: $0.5Vs^{-1}$. Reference electrode: Ag/AgCl. Counter electrode: platinum wire

In the first scan, recorded after 30min in the deposition solution, a redox process is just about visible and from the background corrected CV, shown in Figure 5.8b, it is possible to calculate the $E^{\circ\prime}= 0.126\pm0.005V$, $\Delta E_p=0.100V$ and FWHM of $0.146\pm0.008V$ and $0.113\pm0.010V$ for cathodic and anodic waves respectively. A scan rate dependence experiment showed linearity between the peak current and the scan rate, for $0.1<v<0.5Vs^{-1}$, with a slope of 0.9973 and $R^2=0.997$. This kind of correlation is typical of surface confined species. The surface coverage at 30 min deposition time was $1\pm0.01\times10^{-11}$ $molcm^{-2}$ and $9.4\pm3.2\times10^{-12}$ $molcm^{-2}$, for the anodic and the cathodic waves respectively, which are *larger* than the values found for the experiment conducted with the modified electrodes. After 60min in the deposition solution and washing with milliQ water, the surface coverage decreases and is not visible anymore after 120min. Altogether these considerations are consistent with the molecule weakly physisorbed on the electrode surface, since repetitive washings with milliQ water reduced the surface coverage.

The *ex-situ* control experiments showed that the molecule can adsorb weakly on the bare electrode surface, probably by weak forces which evolve and change during time and washing. As previously showed, the washing step does not have the same effect on the surface coverage for the modified electrodes, since a trend where the surface coverages increased with the bulk concentration was observed. This suggests that the interactions of the probe with the bare and the modified electrodes are different. In particular, CoTpybip seems to experience a stronger interaction with the β-CD-S/Au which is also concentration dependent.

5.3.3 In-situ control experiment

As for the *ex-situ* protocol, the *in-situ* protocol at the bare electrodes was the same used for the β-CD modified electrodes. Three different concentrations of the cobalt complex in 90:10 milliQ water/acetonitrile were used, namely 1, 5 and 10 μM, with 0.01M Na_2SO_4 as electrolyte. Between each deposition the electrodes were thoroughly rinsed with acetonitrile to completely remove any physisorbed material.

Figure 5.9 shows the background corrected CV for a 5μM solution of the complex, 90:10 milliQ water/acetonitrile, 0.01M Na_2SO_4, at $0.5Vs^{-1}$ which is representative for the concentrations investigated.

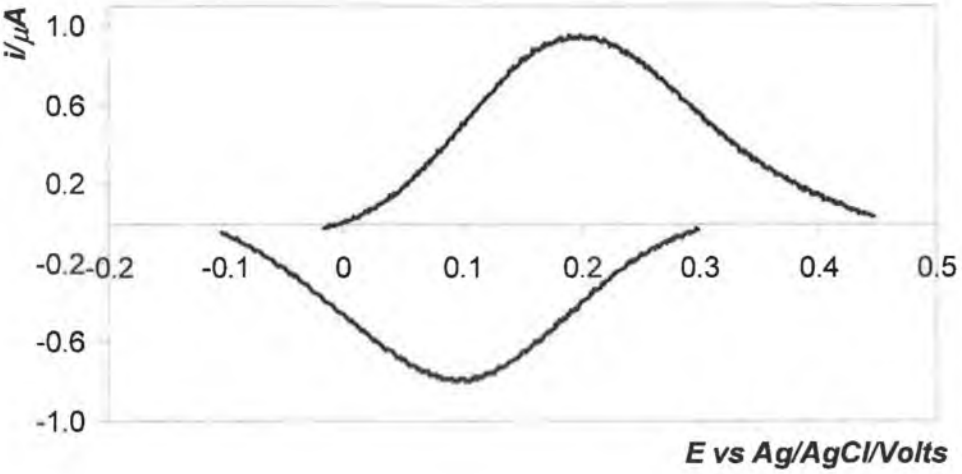

Figure 5.9 *In-situ* background corrected CV of a gold polycrystalline macroelectrode scanned in a 5 μM solution of the complex, 90:10 milliQ water/acetonitrile, 0.01M Na_2SO_4 as electrolyte. Scan rate: $0.5Vs^{-1}$. Reference electrode: Ag/AgCl. Counter electrode: platinum wire

A redox process is visible in the range of potentials assigned to the oxidation of the cobalt complex and, from Figure 5.9, it is possible to calculate the $E^{\circ\prime} = 0.147\pm0.003V$, $\Delta Ep=0.053\pm0.011V$ and FWHM of $0.193\pm0.019V$ and $0.216\pm0.017V$ for cathodic and anodic wave respectively. A scan rate dependence experiment showed linearity between the peak current and the scan rate, even for low scan rates as $0.5<v<1Vs\text{-}1$, with a slope of 0.9213 and $R^2=0.97$. Again as previously found for the *ex-situ* inclusion altogether these characteristics are consistent with a surface confined species with a more negative formal potential compared to the included complex.

The surface coverages for the oxidation of the physisorbed molecule have been found bigger than that values for the included complex, ranging from 84, 67 and 67 pmol cm^{-2} for 1,5 and 10 μM solution respectively. The corresponding cathodic surface coverages were 28, 60 and 59 pmol cm^{-2}. The main observation is that the surface coverage vs. bulk concentration does not follow any trend, probably being triggered just by the applied potential.

It is interesting to note that the formal potential for the *ex-situ* and *in-situ* control experiments are shifted of about 0.020V, probably due to the different charge density at the surface of the bare electrode. In fact, while in the first case the adsorption is performed at the OCP in the second scenario an external potential is applied. This consideration suggests that indeed some sort of electrostatic interaction controls the adsorption of the molecule at the bare surface.

In general the *in-situ* control experiments suggest that electrostatic physisorption of the molecule is present for the bare electrode in the same range of concentrations used for the inclusion experiment. However, the features of the CVs obtained are different either in terms of formal potential or surface coverage, suggesting that what is observed for the *in-situ* inclusion experiment is effectively the complexation of the cobalt complex in the CD cavity.

The overall conclusions of these control experiments is inconclusive in the sense that clearly physisorption occurs at bare electrodes but that this process differs from that found for the monolayer coated electrodes.

Conclusions

The inclusion process of CoTpybip into the cavities of β-CD-SH molecules immobilised on a gold surface was successfully characterised for the *in-situ* protocol, allowing the binding constant to be estimated. The value obtained is in good agreement with literature values for the same process in solution. A mechanism for the redox reaction was supposed, with a direct oxidation of the molecule included in the cavities, followed by the setting of a new equilibrium between the oxidised form at the electrode and in the bulk. The electron transfer needs to be fully characterised. However, there is evidence that the heterogeneous electron transfer rate constant is smaller than that found for the CoTpySH discussed in Chapter 2.

The adsorption of the probe at the bare electrode was also characterised and showed different characteristics to the included complex, allowing physisorption and the inclusion process to be distinguished. Raman spectroscopy was particularly useful for the characterisation of the *ex-situ* inclusion, where the washing step caused the probe to precipitate on the electrode surface.

In general, the first step for the construction and characterisation of molecular wires was therefore achieved, showing that the 1) inclusion process can be characterised *in situ* and 2) by taking off the electrode from the deposition solution the included complex is still available for a bottom up construction of molecular wires.

References:

1 Barigeletti F., Flamigni L., *Chem Soc. Rev.*, **2000**, 29, 1

2 Ulman A., *Chem. Rev.*, **1996**, 96, 1533

3 Crespo-Biel O., Dordi B., Reinhoudt D. N., Huskens J., *J. Am. Chem. Soc.*, **2005**, 127, 7594

4 Service R. F., *Science*, **2002**, 295, 2398

5 Lehn J.-M., *Supramolecular Chemistry, Concepts and Perspectives*, VCH, Weinheim, Germany, **1995**

6 Rojas M. T., Königer R., Stoddart J. F., Kaifer A. E., *J. Am. Chem. Soc.*, **1995**, 117, 336

7 McCormack S., Russel N., Cassidy J. F., *Electrochim. Acta*, **1992**, 37, 1939

8 Matsue T., Evans D. H., Osa T., Kobayashi N., *J. Am. Chem. Soc.*, **1985**, 107, 3411

9 Strelets V. V., Mamedjarova I. A., Nefedova M. N., Pysnograeva N. I., Sokolov V. I., Pospisil L., Hanzlik J., *J. Electroanal. Chem.*, **1991**, 310, 179

10 Komura T., Yamaguchi T., Noda K., Hayashi S., *Electrochim. Acta*, **2002**, 47, 3315

11 Wang H., Mendoza S., Kaifer A. E., *Inorg. Chem.*, **1998**, 37, 317

12 Gonzalez B., Cuadrado I., Alonso B., Casado C. M., Moran M., Kaifer A. E., *Organometallics*, **2002**, 21, 3544-3551

13 Szejtli J., '*Cyclodextrins and their Inclusion complexes*', Akademiai Kiado, Budapest, **1982**.

14 Weisser M., Nelles G., Wenz G., MittlerNeher S., *Sensors and Actuators B.*, **1997**, 38, 58

15 Cromwell W. C., Bystrom K., Eftink M. R., *J. Phys. Chem.*, **1985**, 89, 326

16 Michalke A., Janshoff A., Steinem C., Henke C., Sieber M., Galla H. J., *Anal. Chem.*, **1999**, 71,2528

17 Maeda Y., Fukuda T., Yamamoto H., Kitano H., *Langmuir* , **1997**, 13, 4187

18 Lee J. Y., Park S. M., *J. Phys. Chem. B.*, **1998**, 102, 9940

19 Shamsipur M., Yari A., Sharghi H., *Spectr. Acta A.*, **2005**, 62,372

20 Chan J., Dong S., *J. Electronala. Chem.*, **1997**,440,

21 Castronuovo G., Niccoli M., *J. Inclus. Phenom. And Macrocyclic Chem.*, **2005**, 53, 69

22 Haider J. M., Chavarot M., Weidner S., Sadler I., Williams R.M., De Cola L., Pikramenou Z., *Inorg. Chem.*, **2001**, 40, 3912

23 Osella D., Carretta A., Nervi C., Ravera M., Gobetto R., *Organometallics*, **2000**, 19, 2791

24 Pereira Silva M. J. J., *PhD Thesis* submitted at the University of Birmingham, **2005,** Chapter 2

25 Wang Y., Mendoza S., Kaifer A.E., *Inorg. Chem.*, **1998**, 37, 317

26 Matsue T., Evans D.H., Osa T., Kobayashi N., *J. Am. Chem. Soc.*, **1985**, 107, 3411

27 Rowe G. K., Creager S. E., *Langmuir*, **1991**, 7, 2307

28 Connors K. A., *Chem .Rev.*, **1997**, 97, 1325

29 Ohira A., Ishizaki T., Sakata M., Taniguchi I., Hirayama C., Kunitake M., *Colloids and Surfaces*, **2000**, 169, 27

30 Ohira A., Sakata M., Taniguchi I., Hirayama C., Kunitake M., *J. Am. Chem. Soc.*, **2003**, 125, 5057-5065

Chapter 6

Conclusions and Future Work

The focus of this thesis has been the construction and characterisation of monolayers assembled on metal nobles surfaces via covalent and non-covalent bonds, able to perform electron transfer reactions. The importance of finding alternative routes for the construction of nanodevices for different applications and, in particular, for the semi-conductor industry, has driven the study of new techniques capable of producing molecular size devices.

It has been shown in Chapter 3 and 4 that the self-assembly technique allows monolayers of surface active metal complexes to be formed on either platinum or gold. However, monolayers in which the orientation of the individual adsorbates and highly stable monolayers are required for molecular electronics applications. With this in mind, terpyridine complexes were utilised in Chapter 3 as building blocks since they show perpendicular orientation to the electrode surface, probed with SERS. The geometry of the terpyridine ligand together with some repulsive interactions between the molecules within the monolayer appears to allow highly ordered structures to be built. However, they are less dense than a full-packed monolayer, but still can provide 10^{13} molecules/cm^2 compared to 10^8 density achieved by state-of-the-art nanolithography.

Electron transfer properties are of course of great importance in the production of molecular wires and GHz or better switching frequencies are required. The possibility of transferring electrons from and to the electrode surface was investigated in Chapter 3 for the terpyridine complexes. It was found that the rate constant of the process is in the order of magnitude of related complexes ($3.06 \pm 0.03 x104$ s^{-1}) and it is controlled by weak electronic coupling to the electrode surface. Significantly, despite the direct coupling to the electrode surface, and the short electron transfer distance, the electron transfer rate is at least two orders of magnitude slower than conventional semiconductors.

Future work could involve the link of the immobilized sulphur terpyridine complexes with other sulphur terminated molecules, producing a disulfide bond, with extremely ordered geometry, which is able to conduct electrons over higher distances. The mediation of the first immobilized monolayer for the electron transfer involving the overlying multilayers would be of primary importance, in particular in terms of nature of the metal redox centre and of the bridging ligand (conjugation, length).

Chapter 4 and 5 dealt with the immobilisation of redox active molecules through a non-covalent interaction, in particular the host-guest properties of β-cyclodextrins. Again the structure, packing and orientation of the immobilised β-CDs was probed,. It was found that the nature (crystallinity) of the substrate greatly controls the final packing of the molecules, producing islands of different type of aggregation, where the lateral interactions have different contributions. In particular, when applying a varying external potential, the molecules appeared to change their orientation within the monolayer. However, the change is reversible, rendering the whole system interesting for different applications.

Probably the most interesting results is the effective *partial* inclusion of redox active molecules in the cavities of the immobilised β-CDs, probed either with electrochemistry or SERS. The inclusion was demonstrated to be reversible and, in some extent, potential controlled. In fact, as to best of our knowledge, the characterisation by electrochemistry of the inclusion of molecules into the cavities of β-CDs involved only molecules, as ferrocene or cobaltocene, which showed *complete* inclusion into the hosting cavities. This approach did not allow other hosts to be linked to the included species which is a key step in building up molecular wires.

Future work could involve the study of the nature of hosts and guests with a higher equilibrium constant, which allows confining a bigger number of molecules (adamantyl and cyclodextrins) on the surface. The study of the electron transfer timescales of such a supramolecular system is, then, fundamental to understand the effective utilisation of those assemblies as molecular electronics.

Acknowledgements

I don't really know where to start from...it was a very interesting, painful and unforgettable experience…not only in terms of work, but also in terms of people that I've met and experiences that I couldn't have done back in Italy…

First of all, I would like to thank Prof. Robert Forster for the opportunity he gave me and his guide and experience during these last almost 4 years and Prof. Han Vos for his support.

And then of course all the people that have walked with me on this emerald island, comforting me when I was sad and partying with me when I was happy!!
In DCU the list is endless and surely I'll forget somebody, so don't take any offence, you're anyway in my thoughts..
Starting from the people who "live or lived" in S102: Johan, Martin, Lynn, Darragh, Colm, Eoin, Emmet, Jennifer, Almut, Javed
Going to Postdocs and postgraduate in Robert and Tia's group (Oh, Jaysus, so many..): Yann, Uju, Gavin, Andrea, Deirdre, Stephen…
And then all the other friends, spread around the campus: Tony, Lynda, Adriano, Nicola, Yuliya, Anna, Keith, Alan, Bill…

All the people from SUSANA project..

Stefania you have a special place…

Finishing with the no-nerd friends (no chemists!!): Xavier, Isabelle, Alix, Gwen, Alwin, Monica, Torsten..

Enrico, my soulmate..

And myself..and Ireland..